Magnetorheological shock absorbers:

Modelling, design, and control

by

David Craig Batterbee

Submitted for the degree of Doctor of Philosophy

November 2006

The University Of Sheffield.

Department of Mechanical Engineering

Supervisors: Dr N.D. Sims and Dr R. Stanway

SUMMARY

Magnetorheological (MR) fluids enable the rapid and continuous alteration of flow resistance via the application of a magnetic field. This unique characteristic can be utilised to build semi-active dampers for a wide variety of vibration control systems, including structural, automotive, and aeronautical applications. As an example, MR fluids could enhance the performance of aircraft landing gear, which are subject to widely varied and unpredictable impact conditions with conflicting damping requirements.

In this thesis, a numerical sizing methodology is developed that enables the impact performance of MR landing gears to be optimised. Using real data provided by landing gear manufacturers, the sizing methodology is applied to both lightweight aircraft, and large-scale commercial jets in order to demonstrate scalability. For both aircraft types, results indicate that the peak force and the severity of fatigue loading can be enhanced over a wide range of impact conditions. However, it is shown that MR landing gears can be heavier than passive systems. To validate the numerical approach, a prototype MR landing gear shock strut is designed, fabricated, and tested. Good correlation between the model and experiment is demonstrated, particularly for low velocity excitations.

MR dampers exhibit highly non-linear force-velocity behaviour. For landing gear impacts, it transpires that this behaviour can be used to an advantage, where it is shown that an acceptable performance can be obtained using open-loop control i.e. with a constant magnetic field. However, this non-linear behaviour is highly undesirable for other scenarios (e.g. an aircraft taxiing), and as a consequence, the choice of an effective control strategy remains an unresolved problem. A further aim of this thesis is therefore to develop effective control techniques for broadband excited MR vibration systems.

Through an extensive series of numerical and experimental investigations, case studies representative of the general single-degree-of-freedom and two-degree-of-freedom vibration isolation problem are presented. In the experiments, the hardware-in-the-loop-simulation method is adopted, which provides an excellent means to bridge the gap between theory and practice when the behaviour of a specific component is complex. Here, the MR damper is physically tested, whilst the remainder of the structure is simulated in real-time. The results demonstrate that the chosen control strategy can provide significant performance benefits when compared to more commonly used strategies and equivalent passive systems. Furthermore, the control strategy is shown to be insensitive to factors such as the type of input excitation.

ACKNOWLEDGEMENTS

I would like to thank my supervisors, Dr Neil Sims and Dr Roger Stanway, for their help and support throughout this project. I am most grateful to Dr Neil Sims for his technical guidance, and for the numerous opportunities he has made available e.g. conference trips, future research posts.

I would also like to thank everyone from the department who have aided this research, particularly Mike Rennison and Jamie Booth for their help with the design and manufacture of the test facility, Bob Mills, John Goodliffe and John Wilkinson for assisting with electrical design aspects, Pae Huyanan for helping with computer problems, as well as the secretarial and administrative staff.

This research was made possible by the support of the EPSRC and the European Commission under project reference No. FP6-502793 (The ADLAND project). I would also like to acknowledge the ADLAND partners, especially Messier Dowty and the Polish Institute of Aviation for providing the landing gear data, and the Fraunhofer Institute for supplying the MR fluid.

Finally, I would like to give thanks for the support of my partner Hannah, my family and friends, and all those who have worked along side me in the office.

TABLE OF CONTENTS

NOMENCLATURE

a	Amplitude of sine wave signal
a_{1o}	Outer cross-sectional area of the cylinder containing gas
a_{2i}	Piston area
a_{2o}	Outer cross-sectional area of the cylinder that seals against the piston head
a_o	Cross-sectional area of a passive orifice
A	Energy absorbed by the shock strut
A_1	Cross-sectional area of the bobbin core
A_2	Cross-sectional area of the flux return
A_3	Cylindrical area at the interior of the bobbin flange
A_c	Cross-sectional area of the copper wire
A_f	Pole area of the fluid
A_s	Pole area of the valve material
b	Mean annular circumference of the valve
B	Feedback gain
B_f	Magnetic flux density in the fluid
B_s	Magnetic flux density in the valve material
c	Tyre constant
C	Road surface fitting constant
C_d	Discharge coefficient
C_p	Passive damping coefficient
C_{post}	Post yield damping coefficient
C_{pre}	Pre-yield damping coefficient
C_w	Damping coefficient of the tyre
d	Mean valve diameter
d_p	Orifice diameter of the passive valve
D	Set-point gain of the linearised system
D_{max}	Maximum shock strut displacement during an impact
D_p	Piston head diameter
$D_{v_{max}}$	Shock strut displacement at the maximum piston velocity
D_{IS}	Set-point gain of the fully active skyhook system
D_{ISm}	Set-point gain of the fully active modified skyhook system
D_{MR}	Set-point gain of linearised skyhook system
D_{MRm}	Set-point gain of the linearised modified skyhook system
D_{SAS}	Set-point gain of the ideal semi-active skyhook system
D_{SASm}	Set-point gain of the ideal semi-active modified skyhook system
f	Frequency
F	Actual damping force
F_d	Set-point damping force
F_g	Gas spring force
F_h	Hydraulic damping force
$F_{h_{max}}$	Maximum damping force requirement of the landing gear
F_{max}	Maximum shock strut force during an impact
F_s	Shock strut force

F_t	Tyre force
F_y	Yield force
g	Acceleration due to gravity ($9.81 ms^{-2}$)
G	Feedforward gain
$G(s)$	Transfer function of the yield stress response
h	Valve gap height
h_c	Coil height
H_f	Magnetic field strength in the fluid
H_s	Magnetic field strength in the valve material
I	Current
I_{OL}	Constant current level of the open-loop system
I_1	Initial current
I_2	Final current
I_{max}	Switching current of the on/off controller
k	Linear stiffness of the fluid
K	Vehicle suspension stiffness
K_{iso}	Stiffness of SDOF mass-isolator
K_w	Linear tyre stiffness
l	Length of individual valve
l_a	Active valve length
l_c	Length of wire
l_p	Length of the passive valve's orifice
l_t	Total length of the multi-staged valve
L	Lift
L_c	Inductance of the coil
L_s	Length of flux path through the valve material
m_1	Mass representing fluid inertia
m_2	Mass of piston head
m	Gas exponent
m_p	Distributed mass of aircraft
m_v	Mass of valve
m_w	Mass of wheel and tyre assembly
M	Mass of SDOF mass-isolator
M_c	Mass of vehicle
n	Number of individual valves/stage number
N	Number of turns
p	Power
P	Pressure
P_1	Fluid pressure in chamber 1
P_2	Fluid pressure in chamber 2
P_a	Gas pressure
P_{a0}	Initial gas pressure
Q	Volume flow rate
Q_i	Volume flow rate into control volume
Q_{i1}	Volume flow rate into chamber 1
Q_{i2}	Volume flow rate into chamber 2

Q_{max}	Maximum valve flow rate during impact
Q_o	Volume flow rate out of control volume
Q_{o1}	Volume flow rate out of chamber 1
Q_{o2}	Volume flow rate out of chamber 2
r	Tyre exponent
R_c	Resistance of coil
Re	Reynolds number
Re_c	Critical Reynolds number
s	Laplace operator
$S(\psi)$	Displacement power spectral density of road surface
t	Time
t_a	Bobbin core radius
t_b	Bobbin flange height
t_d	Instant of time when shock strut deflects
v	Fluid volume
v_{10}	Initial fluid volume in chamber 1
v_{20}	Initial fluid volume in chamber 2
v_a	Gas volume
v_{a0}	Initial gas volume
V	Piston velocity
V_c	Horizontal vehicle velocity
V_{max}	Maximum piston velocity
V_{sink}	Aircraft sink velocity
w	Road surface exponent
w_c	Coil width
W	Aircraft weight
x	Displacement of the shock strut
x_1	Displacement of the mass representing fluid inertia
x_2	Displacement of the piston head
x_b	Displacement of the base
x_c	Displacement of the vehicle mass
x_m	Displacement of the isolated mass
x_r	Road surface height
x_w	Displacement of the wheel mass
X	Distance along the mean valve radius
z	Displacement of SDOF impact system
z_p	Displacement of distributed aircraft mass
z_w	Displacement of wheel and tyre assembly
$\ddot{z}_{cr}$	Critical acceleration that causes shock strut deflection
α	Modified skyhook weighting parameter
β	Bulk modulus of fluid
χ	Quasi-steady MR damping function
δ	Dimensionless valve length
Δm_f	Extra mass of fluid
ΔP_{l_i}	Pressure drop across the inactive valve length
ΔP_{l_a}	Pressure drop across the active valve length

ΔP_0	Zero-field pressure drop
ΔP_{max}	Maximum valve pressure drop (Active + inactive)
Δt	Time delay associated with the actuator dynamics
ΔQ	Net volume flow rate
ϕ	Magnetic flux
ϕ_f	Magnetic flux in the fluid
ϕ_s	Magnetic flux in the valve material
Φ	Volume fraction of iron particles
φ	Phase associated with the actuator dynamics
$\dot{\gamma}$	Shear rate
λ	Control ratio
μ	Viscosity of MR fluid
μ_0	Magnetic constant ($4\pi \times 10^{-7}$ H/m)
ρ	Density of hydraulic oil
ρ_{MR}	Density of MR fluid
σ	Resistivity of copper
τ	Time constant
τ_y	MR fluid yield stress
$\tau_{y_{max}}$	Maximum MR fluid yield stress
ψ	Wave-number
ζ	Damping ratio
ζ_{min}	Minimum damping ratio

ABBREVIATIONS

ADLAND	European project name – 'Adaptive landing gear for improved impact absorption'
CBA	Car Body Acceleration
ER	Electrorheological
FEA	Finite Element Analysis
GM	General Motors
HILS	Hardware In the Loop Simulation
LSL	Large Scale Levered
LST	Large Scale Telescopic
LVDT	Linear Variable Displacement Transducer
PSD	Power Spectral Density
NASA	National Aeronautics and Space Administration
RMS	Root Mean Square
SDOF	Single Degree Of Freedom
SWS	Suspension Working Space
WCF	Wheel Contact Force
2DOF	Two Degree of Freedom

CHAPTER 1. INTRODUCTION

The theory of vibration within an engineering context has been studied for over a century [1, 2]. This early research was fuelled by the need to understand and hence better control the vibrations in machines and structures (such as rotating shafts, turbine blades, buildings and bridges), which were ever increasing in size and complexity [2]. The original solutions described by Timoshenko [2] and Den Hartog [1] were often based upon the use of passive devices such as the addition of springs, dampers and/or masses. However, achieving a desirable performance over a wide range of excitation conditions was soon recognised as a problem [1]. This 'passive' limitation led to the development of active and semi-active systems, which can alter their suspension characteristics in response to sensed variables [3]. One of the most novel methodologies to date incorporates the use of smart fluids, which can be used to build semi-active devices. Such fluids enable the rapid and continuous alteration of flow resistance via the application of an electric or magnetic field [4].

In what follows, the relative merits of passive, active, and semi-active vibration control methodologies are described with particular emphasis on the use of 'resilient isolation' [5] or suspension systems. This will serve to highlight the significant benefits that can be gained by employing smart fluids in such systems. Particular attention is given to aircraft landing gear and vehicle suspensions, which are the key systems investigated in this thesis. The introduction concludes with some background information, and the outline and objectives of the present research.

1.1 The relative merits of passive, active, and semi-active suspensions

Passive suspensions are the most frequently adopted solution to vibration control. This is due to their inherent simplicity, reliability and low cost. To give just a few examples, passive suspensions are utilised in automobiles, aircraft, locomotives, and buildings [5]. As shown in Figure 1-1, passive systems typically comprise masses, springs and dampers, which are "passive" in the sense that a power source is not required [6]. Thus, the suspension elements can only store and dissipate energy associated with local relative motions. Moreover, this energy cannot be controlled, as the suspension properties remain fixed for all time. This characteristic represents the passive system's most significant shortfall, as the suspension parameters will only be optimal for specific conditions [7]. Therefore, where structures are subject to a wide variety of excitation conditions, performance will suffer.

As an example, aircraft landing gears are subjected to a wide range of impact conditions due to variations in sink speed, angle of attack and mass. The landing gear must be able to absorb sufficient energy in severe impacts or crash landing scenarios in order to minimise structural damage. To accommodate this requirement, the performance for more common (i.e. less severe) impacts will be compromised, and this will reduce the aircraft's structural fatigue life and increase levels of passenger discomfort. Furthermore, the damping requirements during taxiing conflict with the impact phase of landing. For example, a low damping rate is required such that the full stroke of the shock absorber is utilised in the face of high velocity impacts [8]. During taxiing, a high damping rate is required in order to accommodate the lower velocity excitations and thus prevent excessive heave and pitch motions [8]. Similar performance trade-offs exist for vehicle suspensions. Large variations in road surface conditions, vehicle mass,

and driving style result in conflicting suspension configurations that provide optimal performance. For example, Sharp and Hassan [7] showed that to obtain good performance over many different road surfaces with a fixed suspension working space, wide variations in the suspension parameters are required. Another classic performance trade-off can be explained by comparing sports cars with conventional family vehicles. Whilst sports cars have stiff suspensions to maximise handling, this degrades the ride quality. On the other hand, family cars have softer suspensions to improve passenger comfort, but this is at the detriment of road holding [3]. Clearly, such performance conflicts cannot be overcome with passive suspension elements.

To overcome the limitations described above, considerable attention has been paid to active suspension systems [9-14], which began to be developed most notably in the 1950's and 60's [3]. Typically, a hydraulic actuator is used to both supply and dissipate energy to and from the vibrating structure. Here, electro-hydraulic servo-valves control the flowrate of high-pressure fluid that is pumped into and out of the actuator. Consequently, using appropriate sensors and control logic, significant vibration performance can be achieved over wide ranging excitation conditions.

As an example, McGehee *et al.* [9] presented an experimental investigation of an active landing gear, and demonstrated that the initial decelerating force during touchdown could be reduced by 32% under certain conditions. In passenger vehicles, Crolla noted that an active system could enhance ride comfort by 35% [15]. However, in the same article, Crolla also pointed out that the development of active vehicle suspensions has been "dropped". This is due to the associated high cost, power consumption, weight and complexity, which significantly outweigh the potential performance enhancements.

For example, Csere [16] noted that the Nissan Infinity active suspension was $5500 more expensive than a conventional suspension, 202lbs heavier, and absorbed 3-5 horsepower. Again, due to the increased weight, cost and complexity, active landing gears have not been introduced onto production aircraft [8], in spite of the significant research developments in this field [9, 10, 17-19].

Semi-active systems offer an attractive compromise between passive and active suspensions. Such systems provide a means to control energy storage and/or dissipation. However, unlike active systems, semi-active devices cannot increase the energy of the system, thus the power requirements are significantly lower. Furthermore, their performance can approach that of fully active systems [7, 20], whilst their weight, cost and complexity is potentially more comparable to passive devices.

Arguably, the most significant semi-active control policy to date was described by Karnopp, *et al.* [6]. The concept was based on work by Bender, *et al.* [21], where linear optimal control theory was used to derive the optimum control force for a single-degree-of-freedom (SDOF) system. It transpired that this optimum force could be realised by the series combination of linear passive elements shown in Figure 1-2. This is called skyhook damping, as in most practical cases it is not possible to connect the damper to an inertial reference [6]. The performance advantages of skyhook damping are illustrated in Figure 1-3, which shows typical transmissibility plots for SDOF systems. In contrast to a passive system (Figure 1-3(a)), skyhook control enables the significant attenuation of the resonant peak without degrading the high frequency response (Figure 1-3(b)).

To emulate the skyhook configuration, an active system is required to generate the necessary force inputs. However, Karnopp [6] described how this policy could be implemented in a semi-active manner, by adopting what is commonly referred to as a clipped optimal approach. Essentially, a semi-active damper generates the skyhook force when there is a requirement for energy dissipation. As shown in Figure 1-4(a), this occurs when the skyhook force has the same direction as the relative velocity across the damper. When an energy input is required, the semi-active device produces no force at all, or (at least) the level of energy dissipation is minimised.

Various semi-active dampers have been proposed, which are often controlled by altering the geometry of the oil flow passages or orifices. Karnopp [6] proposed the electro-hydraulic device shown in Figure 1-5, which enabled the separate control of compressive and rebound forces using solenoid operated poppet valves. Cebon *et al.* [22] investigated a valve adjustable semi-active damper for lorry suspensions. These authors pioneered the hardware-in-the-loop-simulation (HILS) method, which enabled various controller designs to be investigated experimentally. Here, the semi-active damper was physically tested with a hydraulic actuator, whilst the remainder of the vehicle was simulated in real-time. Using realistic road excitations and a skyhook-based controller, it was shown that vehicle body accelerations could be reduced by 22% over an optimally damped passive system [22].

Semi-active damping has also been investigated for aircraft landing gear. Ghiringhelli [23] used an electro-hydraulic servo-valve to alter the orifice shape during the impact phase of landing. The device was shown to outperform an equivalent passive system with an optimised orifice. Maemori *et al.* [24] used a stepping motor to rotate a

"control tube" that altered the flow passages during landing impacts. In another study, Krüger [8] numerically investigated the control of semi-active landing gears for aircraft taxiing manoeuvres. A time constant of 25ms was used to account for the control valve dynamics, although the actuation methodology was not addressed. In that study, Krüger demonstrated reductions in RMS vertical cockpit acceleration of up to 40%.

Despite the significant advantages associated with reduced power consumption, semi-active devices utilising variable orifice methods are still potentially unfeasible. For example, they require a large number of moving parts, and components are often similar to those used on active systems (e.g. electro-hydraulic valves). Consequently, they can be as complex, costly and bulky as active devices. Smart fluids on the other hand, provide an excellent, and arguably the most superior means to provide vibration control. Such fluids permit semi-active damping via alteration of the fluid properties rather than the flow geometry. Their key advantages are as follows:

- The fluid properties can be rapidly and reversibly changed using a low power electrical source. For example, the smart fluid shock absorber produced by Delphi (known as MagneRide [25]) has a peak power of 20W, and the RMS value is just a small fraction of this [26].

- The response times, which are typically under 10ms, are faster than other semi-active shock absorbers [26].

- Smart fluid devices are fairly straightforward to design within the constraints of existing passive designs.

- No small moving parts are required. Carlson [26] noted that Delphi's MagneRide shock absorber has 60% fewer parts than their previous electro-mechanical semi-active damper system.

In conclusion, the cost-effectiveness and simplicity of smart fluid devices could approach that of passive systems, unlike other active/semi-active systems. Combining this with their potential to provide performance benefits that approach active systems, smart fluids are clearly a superior solution to vibration control. The above factors have contributed to the significant commercial success of smart fluid devices, [26-28], which has not been experienced by any other active/semi-active system.

At this stage, it is appropriate to give a more detailed description of smart fluids, which is dealt with in the next section.

1.2 Smart fluids

There are two main classes of smart fluid – the first exploits the electrorheological (ER) effect, and the second utilises the magnetorheological (MR) effect. ER fluids comprise micron-sized semi-conducting particles dispersed in an insulating oil. On the other hand, MR fluids consist of micron-sized magnetisable particles (typically iron) suspended in a non-magnetisable liquid such as mineral oil, silicone oil or water. Microscopically, when the appropriate field is applied (magnetic or electric), polarisation causes the formation of particle chains as illustrated in Figure 1-6(a). The strength of these chains, which is determined by the intensity of the applied field, provides an increased resistance to flow. In macroscopic terms, this increased resistance exists in the form of a controllable yield stress, which is much like a Bingham plastic as shown in Figure 1-6(b). It is this yield stress phenomenon that can be utilised

to build highly controllable semi-active devices such as dampers, clutches, actuators, and brakes etc. In the "Field-Off" condition, the response is often approximated to that of a Newtonian fluid i.e. where the shear stress is linearly proportional to the shear rate (see Figure 1-6(b)).

Although practical ER fluids were produced over twenty years ago [29, 30], a mass-produced device is yet to be seen in the market. Considerable developments in MR fluid technology occurred nearly a decade later [28], yet they have had significant commercial success, most notably in the automotive industry. For example, General Motors have featured MR shock absorbers on many of their Cadillac and Corvette vehicles since 2002 [26]. The reason for this present difference in commercial viability is largely associated to the fluid properties.

ER fluids have lower controllable force levels and require very high voltages in order to generate electric fields of up to 6kV/mm [4]. Also, ER fluids have a narrow working temperature range (typically between 15°C to 90°C [31]), which makes them unsuitable in hostile environments. As an example of how this has restricted commercialisation, the use of ER fluids in the aerospace industry was ruled out, owing to a reluctance to provide the necessary voltages [4]. Furthermore, the extreme temperatures associated with high aircraft altitudes would have provided an additional barrier. In contrast to ER devices, MR fluids can be powered by a low voltage source and can operate between -40°C to 150°C [28]. Consequently, they are far better suited to aerospace applications, and the more recent developments in MR fluids have lead to a renewed interest in this field.

Despite the present success of MR fluids, a wide variety of control strategies are in use (either experimentally or commercially) and as yet, there is no consensus on how best to perform automatic control. This is primarily due to the inherent non-linear behaviour of smart fluid devices, which can be observed by considering the simplified behaviour shown in Figure 1-6(b). This behaviour makes the goal of tracking a prescribed force demand a challenging task, which has often led to the development of relatively complex semi-active controllers.

1.3 Background, objectives and outline

A significant part of the present research has been carried out under the European ADLAND project [32] – 'Adaptive landing gear for improved impact absorption'. The ADLAND partners have investigated the feasibility of incorporating various semi-active devices within aircraft landing gear. One key method involves the design of aircraft shock absorbers incorporating MR fluids, which is a key focus of this thesis. MR fluids were chosen (rather than ER) due to their superior commercial potential, particularly for aerospace applications as outlined in Section 1.2.

The feasibility of MR landing gears will depend on whether specific design and packaging requirements can be met, since space and weight are vital design considerations. Consequently, one key aim of the present research is:

To develop and experimentally validate effective device design and sizing procedures for MR landing gears subject to packaging constraints.

The design methodology will primarily focus on the impact phase of an aircraft's landing. Here, the landing gear loads are at their largest and most unpredictable levels,

thus the effect on the load and fatigue life of structural components is most significant. Furthermore, the methodology must consider the effects of fluid compressibility and high velocity flow, which are particularly significant in an impact scenario. Open-loop control studies will also be performed to illustrate the potential of MR landing gears to adapt to a wide range of impact conditions.

As described in Section 1.2, the choice of an effective control strategy in MR suspension systems remains an unresolved problem. A further key aim of the present thesis is therefore:

To develop effective closed-loop control methodologies that can overcome the inherent non-linearity of MR dampers.

This thesis will focus on two general case studies – (1) a broadband excited SDOF mass-isolator, and (2) a 2DOF mass-isolator subject to realistic roadway excitations. Such configurations are highly representative of vehicle suspensions and aircraft taxiing manoeuvres.

The thesis is organised as follows. Chapter 2 presents a review of the literature, which serves to highlight the novelty of this thesis. This begins with a history of smart fluids, and a description of the various configurations of device. The key modelling formats and control methodologies are then described, paying particular attention to flow mode damping devices similar to that used in this research. Due to the significant landing gear focus of this thesis, the literature review concludes with a detailed history of aircraft shock absorber design.

In Chapter 3, the MR landing gear design methodology is described. Using real data provided by landing gear manufacturers, the methodology is applied to both lightweight aircraft, and large-scale commercial jets in order to demonstrate scalability. To validate the numerical approach, a prototype MR landing gear shock strut is designed, fabricated, and tested, which is the subject of Chapter 4. Here, the purpose built damper test facility that was used to perform the experiments is also described.

In Chapters 5 and 6, the focus is moved away from the specific problem of landing gear applications, and the more general issue of closed-loop control is considered. This is relevant to aircraft taxiing scenarios and the ride characteristics of automotive vehicles.

In Chapter 5, a control methodology is described that overcomes the inherent non-linear behaviour of smart fluid devices. This methodology is illustrated numerically through a series of investigations of SDOF and 2DOF structures. In Chapter 6, experiments are performed in order to further validate the efficacy of the control approach. The HILS approach is adopted, where a commercial MR damper is physically tested and the remainder of the SDOF and 2DOF structures is simulated in real-time. Finally, Chapter 7 presents the key conclusions of this research and some suggestions for further work.

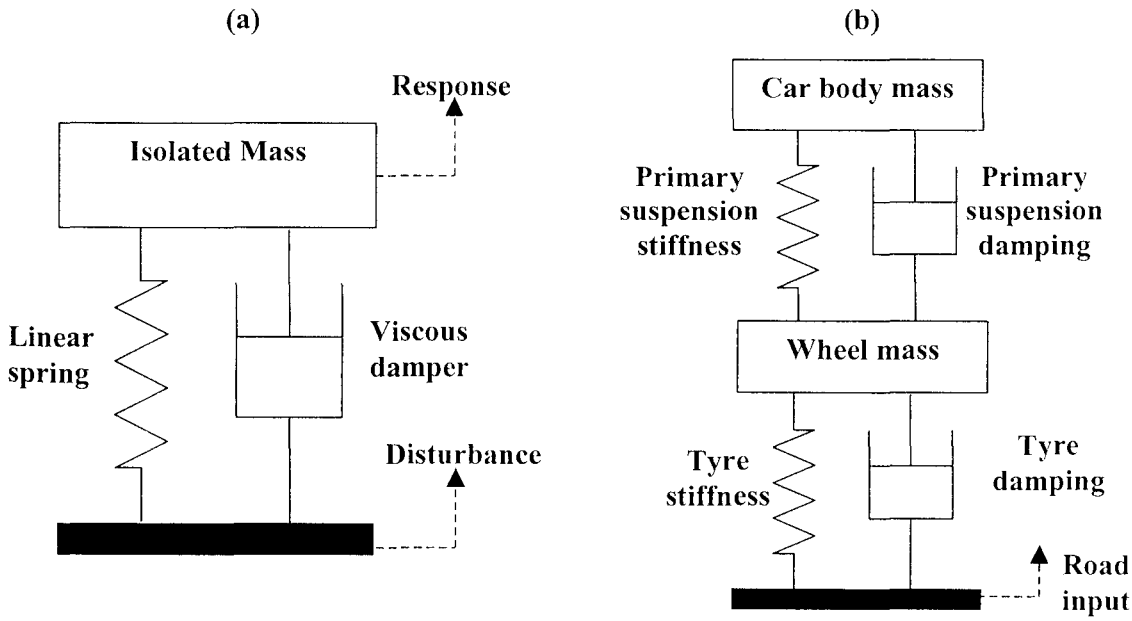

Figure 1-1: Passive suspension configurations. (a) Single-degree-of-freedom mass-isolator and (b) two-degree-of-freedom "quarter car" suspension model.

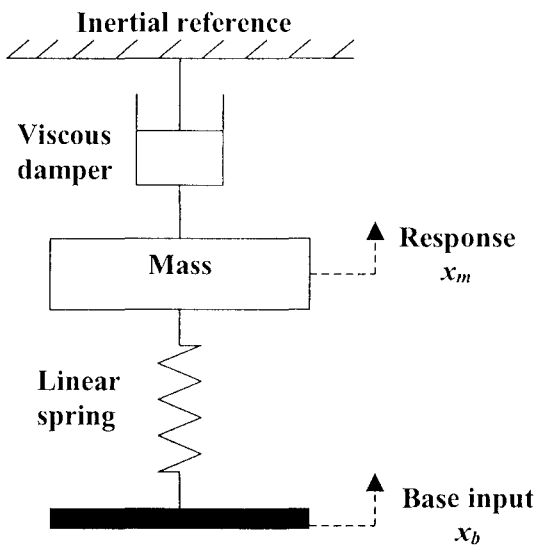

Figure 1-2: The skyhook control principle [6].

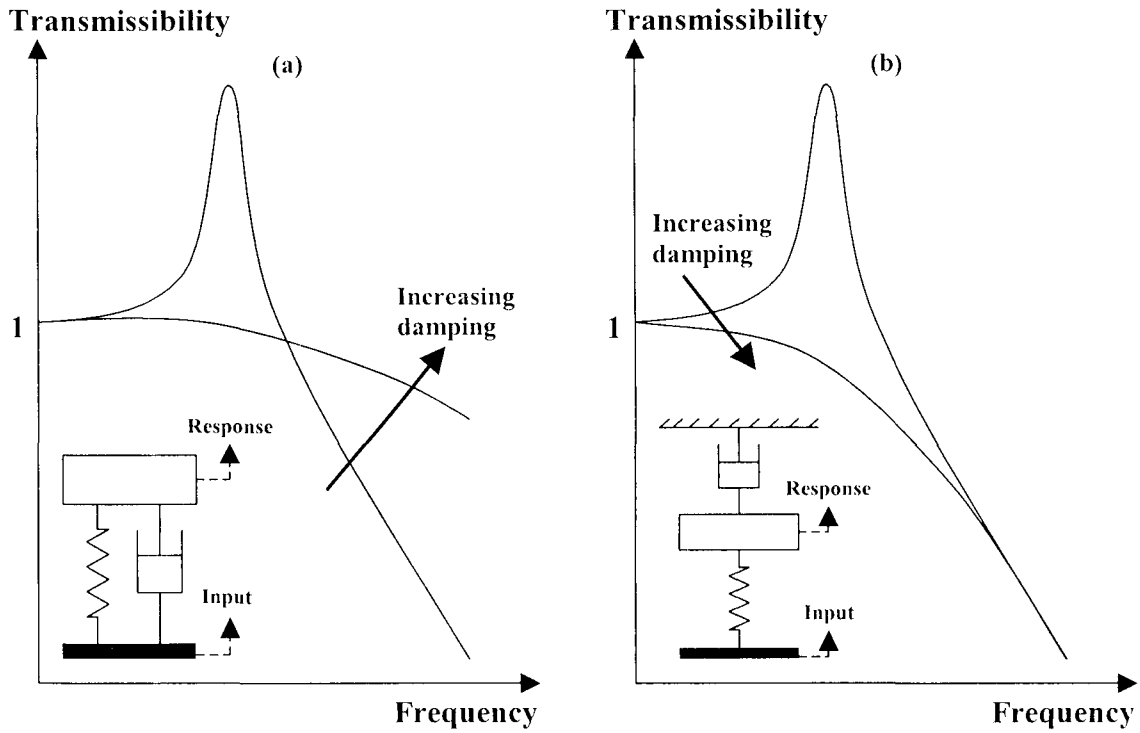

Figure 1-3: Transmissibility plots for (a) passive and (b) skyhook SDOF systems.

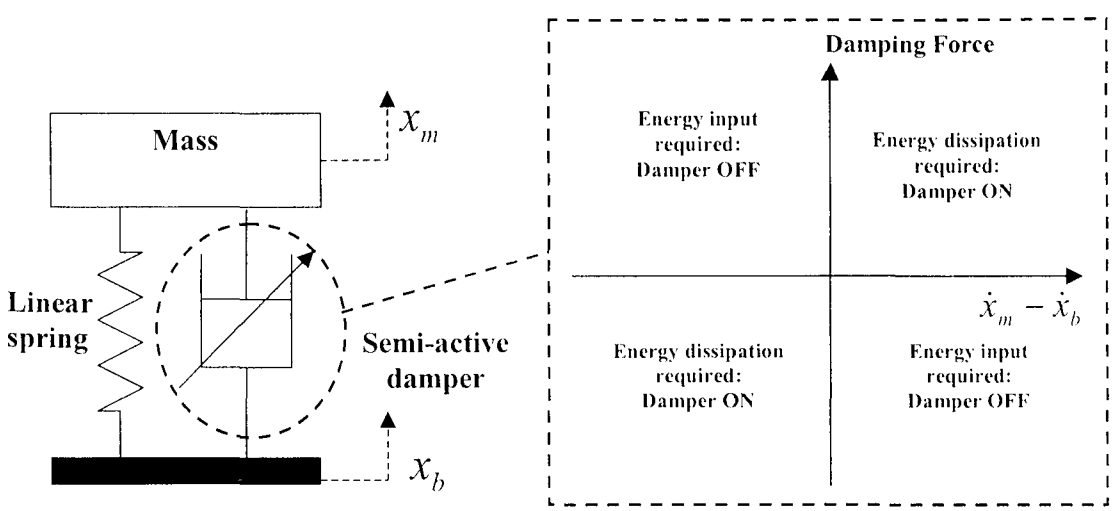

Figure 1-4: The semi-active clipped optimal approach.

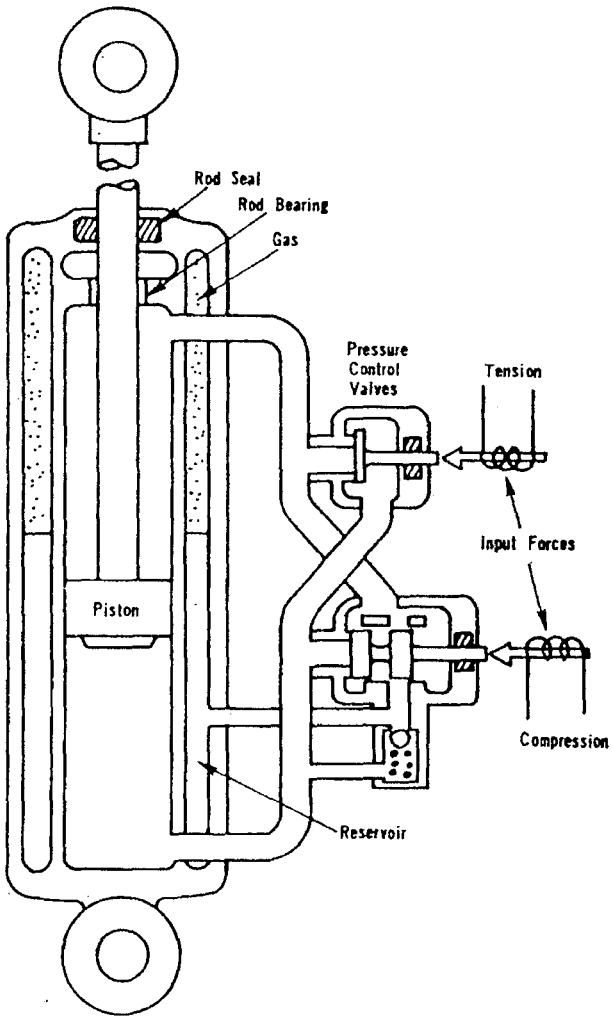

Figure 1-5: The electro-hydraulic semi-active damper proposed by Karnopp, *et al.* [6].

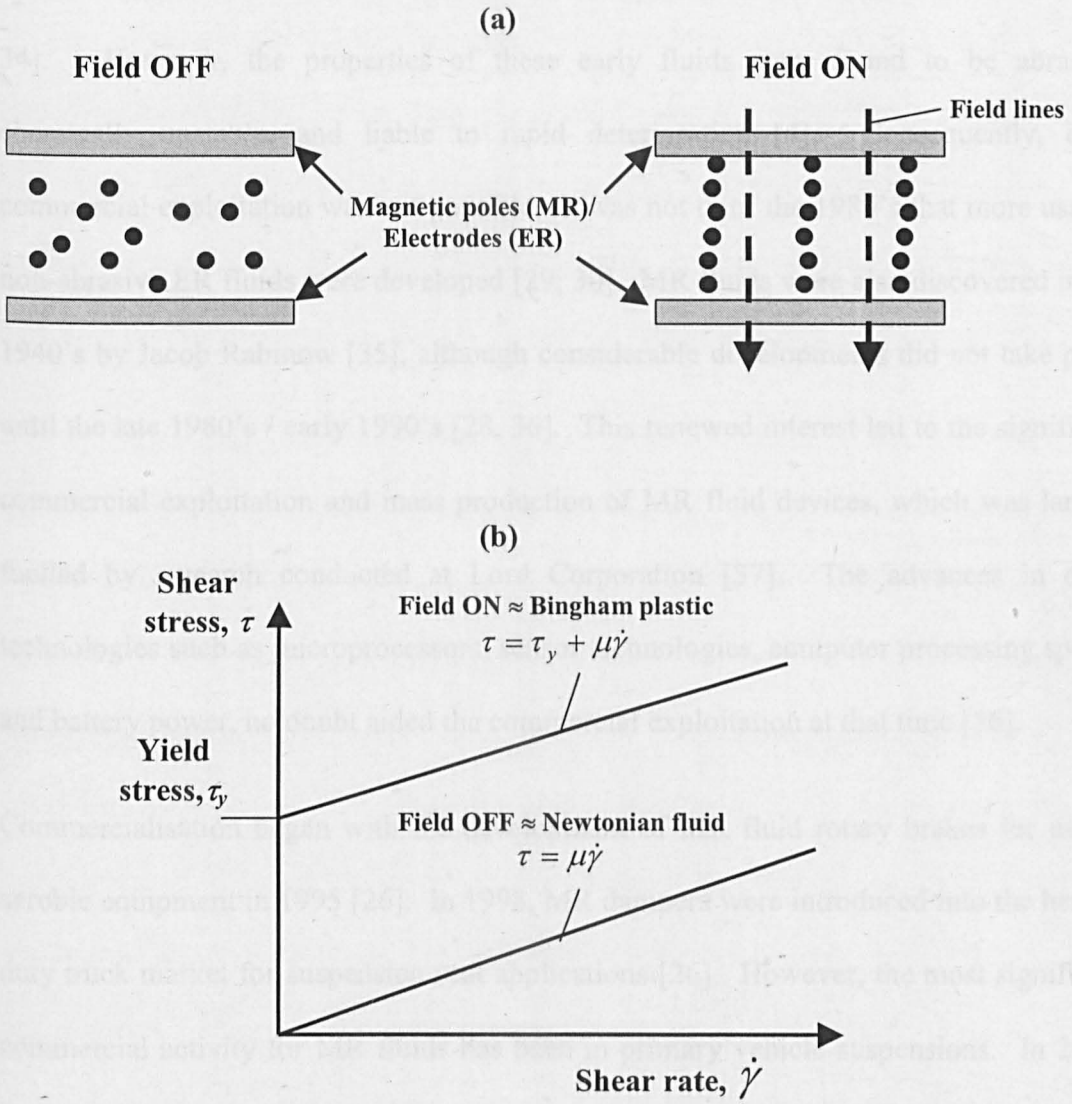

Figure 1-6: Smart fluids. (a) Formation of particle chains in smart fluids, and (b) the resulting shear stress/shear rate response

CHAPTER 2. LITERATURE REVIEW

2.1 A history of smart fluids

Willis Winslow was the first to describe the formulation of ER fluids in the 1940's [33, 34]. However, the properties of these early fluids were found to be abrasive, chemically unstable, and liable to rapid deterioration [4]. Consequently, early commercial exploitation was not possible. It was not until the 1980's that more usable, non-abrasive ER fluids were developed [29, 30]. MR fluids were also discovered in the 1940's by Jacob Rabinow [35], although considerable developments did not take place until the late 1980's / early 1990's [28, 36]. This renewed interest led to the significant commercial exploitation and mass production of MR fluid devices, which was largely fuelled by research conducted at Lord Corporation [37]. The advances in other technologies such as microprocessors, sensor technologies, computer processing speeds and battery power, no doubt aided the commercial exploitation at that time [36].

Commercialisation began with the development of MR fluid rotary brakes for use in aerobic equipment in 1995 [26]. In 1998, MR dampers were introduced into the heavy-duty truck market for suspension seat applications [26]. However, the most significant commercial activity for MR fluids has been in primary vehicle suspensions. In 2002, General Motors (GM) introduced the first primary MR suspension on the Cadillac Seville STS [26]. The shock absorbers, known as MagneRide [25], are manufactured by Delphi Corporation but incorporate Lord Corporation's MR fluid [26]. Since 2002, GM have used MagneRide shock absorbers on the 2003 and 2005 Corvette, two of the 2004 Cadillacs (SRX and XLR), and three 2005 Cadillac models (STS sedan, SRX roadster, and XLR SUV) [26]. Carlson [26] also noted that MR shock absorbers would

feature on the 2006 Cadillac DTS and the 2006 Buick Lucerne. Most recently, it has been announced that Delphi's MagneRide system will also feature on the 2007 Ferrari 599 GTB Fiorano [38] and the 2007 Audi TT [39].

Various other commercial devices have been developed by Lord Corporation, which include MR rotary brakes for force-feedback elements in steer-by-wire systems, and large-scale MR dampers (up to 180kN) for civil engineering applications e.g. for earthquake protection. To accommodate this wide range of commercial devices, Lord's MR fluid production levels in 2004 were in the order of tens of thousands of litres [26].

Clearly, MR fluids have had substantial commercial success, but the first mass-produced ER device is yet to be developed. The key reasons for this can largely be explained by considering the relative merits of ER and MR fluids. Carlson, *et al.* presented a key paper that addressed this issue in 1995 at the 5th International Conference on ER fluids, MR suspensions and Associated technology [28]. After describing the relative merits of ER and MR fluids, Carlson went onto describe the first mass-produced MR devices. Sims, *et al.* [4] noted that it was only at this time that ER specialists became aware of the immense progress that had been made at Lord Corporation. The key points that Carlson addressed were as follows:

- ER fluids exhibit yield strengths in the range of 3-5kPa, whereas MR fluids are capable of delivering yield strengths of up to 100kPa. Consequently, an ER device must have an active fluid volume (i.e. the volume exposed to the electric/magnetic field) that is two to three orders of magnitude greater than an equivalent MR device.

- ER fluids have a narrower operating temperature range. Typically, ER fluids must operate within 15°C to 90°C [31], whereas MR fluids are usable over the range -40°C to 150°C [28].

- An ER device must be supplied with a very high voltage source in order to produce the necessary electric field strengths (2-5kV [40]). On the other hand, MR fluid devices require a low voltage source (12-24V [40]), which can be provided by more conventional power supplies. Note that the power requirements of ER and MR devices are similar (≈50W) due to the contrasting current requirements (1-10mA for ER, and 1-2A for MR) [40].

- Unlike MR fluids, ER fluids are highly sensitive to the presence of contaminants.

Clearly, MR fluids have a greater potential for commercial exploitation. This is particularly true for aerospace applications, where the use of ER fluids was ruled out due to a reluctance to provide the necessary voltages [4].

2.2 Smart fluid devices

Smart fluids are suited to a wide variety of applications, by using the ER/MR effect in one of three possible modes of operation:

The first mode of operation is the flow mode, which is illustrated in Figure 2-1(a). Here, the fluid is forced between two stationary electrodes (ER) or poles (MR). The resistance to flow can then be controlled via the application of an electric/magnetic field, which is perpendicular to the direction of flow. This configuration is widely used to build controllable damping devices such as that shown in Figure 2-2(a). Here, motion of the piston rod forces fluid through an annular orifice. Activation of the

ER/MR fluid enables control of the pressure drop and hence damping force due to the development of a fluid yield stress (see Figure 1-6(b)). The flow mode configuration can also be used to build hydraulic control devices, servo-valves and actuators. Kordonsky [41] demonstrated how a series of ER/MR valves could be utilised to control the motion of a hydraulic actuator. This is illustrated in Figure 2-2(b), where the flowrate through the two inlets (2 and 4) and the two outlets (1 and 3) can be readily controlled to generate the desired actuator motion.

The second mode of operation is the shear mode, which is illustrated in Figure 2-1(b). Here, relative motion between the electrodes/poles places the smart fluid in shear. This relative motion can be either translational or rotational, and activation of the fluid enables direct control of the force or torque required to cause displacement. Shear mode configurations can be utilised to build dampers [42], clutches [43], brakes [44], and structural composites [45]. Examples of rotary MR clutches are given in Figure 2-3. Such devices could replace torque converters in automatic driveline transmissions in order to provide better control during vehicle launch, and to improve high-speed efficiency (by reducing slip) [43]. Smart fluid clutches could also be utilised to provide more precise control of engine fan speed and hence temperature. General Motors have developed such a system and state an improvement in fuel economy between 1-3% [46]. With regards to shear mode dampers, Lou, *et al* [47] developed an ER device for a landing gear, which is illustrated in Figure 2-4. This uses a screw-nut mechanism to convert translational motion of the piston rod into rotational motion between shearing disks. Variation of the ER fluid yield stress thus provides controllable torque and hence axial damping force levels.

The third key mode of operation is the squeeze mode, which is illustrated in Figure 2-1(c). Here, the electrodes are free to translate in a direction parallel to the applied field, which subjects the fluid to tension, compression, and shear forces [4]. This mode is particularly suited to vibration isolation applications requiring small displacements (typically a few millimetres) and large forces [4] e.g. automotive engine mounts. Squeeze flow devices have also been developed to control the vibration of flexible rotor systems [48].

There also exist additional 'mixed' modes of operation, which use a combination of the above three. Perhaps the most commonly used mixed mode device is the shear/flow mode damper, which is illustrated in Figure 2-5(a). Here, an annular orifice is formed between the piston head and the cylinder wall. Piston motion results in the simultaneous relative motion between the valve walls (shear mode), and the flow of fluid through the annular orifice (flow mode). Berg and Wellstead [49] developed another type of mixed mode device for an aircraft landing gear. Their device, which is presented in Figure 2-5(b), combined the shear and squeeze modes of an ER fluid. Here, the relative translation of the charge plates shears the fluid, whilst simultaneously squeezing it between the opposing peaks and troughs.

The present thesis predominantly focuses on the flow mode configuration of device, which is arguably the most suited to damper design. This is particularly true where sizing constraints are a vital concern, which is often the case for aircraft landing gear.

2.3 Modelling of smart fluids

Accurate models of smart fluids are vital, as they enable the effective design and sizing of devices, and aid the development of high performance controllers. Furthermore, they permit an assessment of the feasibility/commercial viability of new applications.

There are two main classifications of model: (1) Quasi-steady models and (2) Dynamic models. Quasi-steady models predict the behaviour (e.g. pressure drop or damping force) during steady flow conditions i.e. where the fluid shear rate is constant. Such models are useful for initial device design and sizing purposes. Dynamic models account for the transient flow behaviour, which can include effects such as fluid compressibility and fluid inertia. Consequently, they are better suited to accurately predicting device performance as part of a complete vibrating structure, and thus enable the more effective development of control strategies. In what follows, a review of both quasi-steady and dynamic modelling formats is presented. Particular attention is given to smart fluid dampers, which are the key focus of this thesis.

The quasi-steady behaviour of smart fluids is commonly characterised as a Bingham plastic (see Figure 1-6(b)). Bingham fluids exhibit a yield stress phenomenon, where flow will only occur once this critical yield stress value has been exceeded. Much attention has been paid to the development and validation of quasi-steady models for Bingham plastic flow through annular ducts, which is the most common configuration for an MR damper (see Figure 2-2(a) and Figure 2-5(a)). Kamath, *et al.* [50] developed one-dimensional axisymmetric models for both flow mode and mixed mode ER dampers. A mixed mode device was fabricated and experimental results strongly supported Bingham plastic behaviour. However, the yield stress and viscosity

predictions were poor, where fluid property values had to be updated before good correlation was achieved.

To simplify the quasi-steady analysis, annular passages are commonly approximated to parallel flat plates. The constitutive equation describing Bingham plastic flow between parallel flat plates is well known and can be found documented in various textbooks [51]. Numerous investigators have shown analytically that the parallel plate approximation compares well with more complex axisymmetric models [52-54]. In general, this is valid provided that the valve gap is sufficiently small, and that the mean annular radius is sufficiently large for curvature effects to be negligible [55]. Various non-dimensional forms of the Bingham plastic equation for parallel plate flow have also been derived [55-57]. Such forms are advantageous as they enable design concepts to be tested at model-scale before full-scale prototypes are built [57].

The performance of smart fluids can deviate from idealised Bingham plastic behaviour, particularly at high velocities. With reference to Figure 2-6, smart fluids may exhibit shear thickening or shear thinning behaviour, where the apparent viscosity tends to increase or decrease with increasing shear rate. Various authors have characterised this effect using the Herschel-Bulkley model [58-60], which assumes that the shear stress is proportional to a power law of the shear rate. As a simplification to the Herschel-Bulkley model, Dimock, *et al.* proposed using a bi-linear post-yield viscosity function in the Bingham plastic equation [61]. Here, a critical shear rate was used to define a region of high shear rate flow and a corresponding reduction (shear thinning) or increase (shear thickening) in the fluid viscosity. Peel and Bullough [55] developed an alternative approach, which used empirical coefficients to modify the equation for

Bingham plastic flow between parallel flat plates. Furthermore, dimensionless variables were used, thus enabling the updated model to be effectively applied to any other geometry of device.

Whilst the above models are effective at predicting the post-yield quasi-steady response, they do not account for the significant dynamic behaviour that is observed in real devices. To give an example of this behaviour, Figure 2-7 shows the sinusoidal force/velocity response of Lord Corporation's RD-1005-3 MR damper [62]. Also shown superimposed is the quasi-steady response for Bingham plastic flow between parallel flat plates. This clearly illustrates the inadequacy of the quasi-steady model under dynamic conditions. With reference to the experimental response, the key dynamic effects are in the form of a hysteresis loop, which has been attributed to fluid compressibility [63], and the appearance of underdamped oscillations, which are associated with the fluid inertia [63]. Furthermore, the pre-yield response appears to be viscoelastic in nature. This is in direct contrast with the quasi-steady model, which assumes rigid pre-yield behaviour.

Stanway, *et al.* [64] made the first step towards the development of effective dynamic models [4]. The authors proposed a phenomenological model of an ER damper, which used the parallel arrangement of a viscous damper (to model the post-yield response) and a Coulomb friction element (to model the yield stress). The form of the model is shown in Figure 2-8(a). Gamota and Filisko [65] proposed an extension of this model in order to account for the viscoelastic pre-yield behaviour. The extended model, which is shown in Figure 2-8(b), could more effectively account for fluid compressibility effects. However, it is significantly more complex due to the increased number of

parameters and degrees of freedom. Furthermore, the governing equations are stiff and therefore numerically difficult to solve [66].

Spencer, *et al.* [66] proposed the use of a Bouc-Wen model, which can effectively capture the hysteretic behaviour, whilst being more numerically straightforward to solve. The most basic configuration is presented in Figure 2-8(c), which uses a non-parametric element in parallel with a viscous damper and a spring. This provides acceptable predictions of the experimental response, although it was shown that an additional degree of freedom is required for significant accuracy [66]. A key disadvantage of the Bouc-Wen model is that it requires the identification of a large number of parameters. Consequently, many investigators have focused on the development of effective system identification techniques [67-69].

Kamath and Wereley [70] developed another dynamic modelling approach. The authors proposed a viscoelastic-plastic model in order to enhance the predictions of the pre-yield (viscoelastic) behaviour and the transition to post-yield (plastic) flow. The form of the model is shown in Figure 2-8(d). Here, non-linear shape functions are used to determine the weighting of two linear shear flow mechanisms – one that describes the pre-yield behaviour (parallel viscous damper and linear spring) and one that describes the post-yield behaviour (viscous damper). Various other non-parametric techniques have been developed for the dynamic modelling of smart fluid dampers. For example, Gavin, *et al.* [71] fitted Chebyshev polynomials to experimental data, and Choi, *et al.* [72] fitted 6^{th} order polynomials. Chang and Roschke [73] developed a neural network of an MR damper, which was trained using a Bouc-Wen model.

Many of the above model formats are highly complex and require the identification of many parameters. Furthermore, the parameters can often lack physical significance and the models are usually developed in parallel to existing laboratory devices. Consequently, the model is likely to be well suited to a particular device, and thus cannot be used for different designs. Sims, *et al.* [74] developed a more general modelling approach that overcomes the above shortfalls. The form of the model is presented in Figure 2-8(e), and comprises a quasi-steady damping function in series with two masses and a linear spring. The linear spring accounts for the fluid compressibility, whilst the masses m_1 and m_2 represent the fluid inertia and the piston head mass respectively. Furthermore, the damping function can be derived from analytical models such as the Bingham plastic equation for flow between parallel flat plates [63]. This physical significance means that the model parameters can initially be based upon constitutive relationships using fluid properties (e.g. bulk modulus) and device geometry, rather than using observed experimental behaviour. Thus, an accurate dynamic model can be developed prior to device manufacture, which is vital for prototyping. Nonetheless, the format of the model also enables an updating or system identification procedure to be performed. An accurate representation of many real devices is therefore possible. Sims, *et al.* [74] details an effective system identification procedure, and it is shown that the resulting model is extremely efficient in reproducing an MR damper's behaviour with broadband mechanical and electrical excitation. This model is used in the present study in order to develop effective control strategies for MR mass-isolators and vehicle suspensions.

2.4 Control of smart fluid devices

There are two key objectives that must be addressed in order to design effective controllers for smart fluid based vibration systems:

1. To calculate the desired damping force that will provide the optimal performance.

2. To determine the corresponding input current/voltage that achieves this desired force.

To achieve the above, a wide variety of control strategies are in use (either experimentally or commercially) and as yet, there is no consensus on how best to perform automatic control. A key reason for this is the inherent non-linear behaviour of smart fluids, which makes the goal of tracking a prescribed force demand a challenging task. Consequently, investigators have focused on the development of relatively complex semi-active controllers, in an attempt to fully exploit their potential within automatic control systems. For example, Lyapunov stability theory and clipped optimal control strategies have been implemented in structural control with some success [75-77] and have been shown to compare well with equivalent ideal semi-active and fully active systems [78]. Neural networks have been investigated for both structural [79] and automotive [80] applications, as well as fuzzy control schemes [68, 81, 82] and H_∞ controllers [83, 84]. Investigators have also implemented sliding mode control for both automotive [85, 86] and aerospace [87] applications.

With many of the above control strategies, investigators often simplify the force tracking strategy by using on/off or bang-bang methods. Examples include the clipped-

optimal control of structures [76-78], and the skyhook control of vehicle suspensions [20, 88] and automotive engine mounts [89]. Here, the smart damper's current/voltage supply is switched to a pre-determined level when a dissipative force is required within the controllable range of the device. Sims, *et al.* [20] concluded that the on/off approach is effective under sinusoidal excitation but breaks down under more realistic random inputs. Also, Simon and Ahmadian [88] demonstrated that an on/off controller can enhance RMS vibration levels, but at the detriment of the peak value.

Alternative force tracking methodologies include the development of approximate linear relationships between the control current and the desired damping force [78]. Also, Choi, *et al.* [72] used a polynomial model of an MR damper to analytically generate the inverse damper dynamics (i.e. the required current for a given force). In a more recent study, Du, *et al* [84] used this methodology to implement H_∞ control of an MR vehicle suspension. However, the authors concluded that the desired force could not be tracked accurately due to the insufficiency of the polynomial model to describe the low velocity behaviour. More complex force tracking strategies have utilised neural networks, which are trained to predict the control current for a given force [90-93]. As an example, Kim and Roschke [90] trained a neural network using experimental MR damper data, and illustrated that the force/velocity response could be linearised. Chang and Zhou [91] used a Bouc-Wen model for training, and tracked force demands from optimal control laws for both single and multi-degree-of-freedom systems.

Many of the above control methodologies are likely to be sensitive to parameter uncertainty. This is because they are derived using specific experimental or numerical behaviour, and thus the force tracking accuracy will suffer if this behaviour changes e.g.

due variations in temperature and hence viscosity, or due to differences in fluid properties between batches. Research at the University of Sheffield has pursued an alternative approach to controller design, which helps overcome this problem. The control strategy uses force feedback to linearise the force/velocity behaviour of a smart fluid damper [94, 95]. This feedback linearisation permits accurate set-point force tracking within the control limits imposed by the fluid properties and device geometry, thus enabling various control algorithms to be implemented effectively. Moreover, as the damping force is used as an error signal, the strategy desensitises control system performance to parameter uncertainty.

In a previous numerical study based upon an ER damper [96], feedback linearisation was shown to be effective for a single-degree-of-freedom (SDOF) mass-isolator with sinusoidal excitation. A later article [20] extended this work to investigate an ER vehicle suspension, where a 32% reduction in car body acceleration was demonstrated with the linearised controller. In that study, although a broadband mechanical excitation was used, the model had not been formally validated under such circumstances, and the excitation conditions were not representative of actual roadways. One aim of the present thesis is to overcome these issues raised by the earlier work, and to illustrate the performance of the feedback linearisation strategy in comparison with on/off control schemes. Furthermore, the control methodologies will be investigated experimentally.

The experiments are performed using the hardware-in-the-loop-simulation (HILS) method, which provides an excellent means of bridging the gap between theory and practice when the behaviour of a specific component is complex. Besinger, Cebon, and Cole pioneered this technique in the 1990's, with particular emphasis on heavy road

vehicles [22, 97]. Here, a semi-active damper was physically tested, whilst the remainder of the vehicle was simulated in real time. However, this work did not consider the use of MR dampers, which pose additional problems due to their highly nonlinear behaviour [77]. More recently, researchers from the smart materials community have considered the use of HILS techniques for MR engine mounts [89] and suspension seat applications [98]. MR vehicle suspensions have also been considered [85, 99], although these contributions did not accurately model the roadway excitation conditions. This is particularly important for MR dampers as the non-linear behaviour means that the performance can be especially sensitive to the excitation.

2.5 Landing gear shock absorber design

A key focus of the present thesis is related to the design and sizing of MR landing gear shock absorbers. It is therefore appropriate to review the previous and existing designs, which is the subject of this section. This will serve to highlight the significant advantages of an MR landing gear, and will enable an enhanced understanding of the performance requirements.

A landing gear has two key tasks. First it must absorb the kinetic energy of the aircraft during initial touchdown i.e. the impact phase of landing. Secondly, it must both suspend the aircraft and provide adequate isolation from surface irregularities during taxiing. Although the tyres play a role, it is the shock absorbers that have the main responsibility for fulfilling these tasks [100].

The main types of passive aircraft shock absorber can be grouped as follows – (1) Those using a solid spring made of steel or rubber e.g. coil or leaf springs, (2) those using a fluid spring with gas or oil, and (3) those using a mixture of gas and oil, which are

generally referred to as oleopneumatic [101]. To characterise the impact performance of landing gears, the shock absorber efficiency is commonly defined as [101]:

$$Efficiency \ \ (\%) = \frac{A}{F_{\max} D_{\max}} \times 100 \tag{2-1}$$

where A is the energy absorbed by the shock absorber during its stroke (obtained from the area beneath the force/displacement curve), and F_{max} and D_{max} are the maximum force and displacement during the impact respectively. Currey [101] compared the efficiency and relative weights of the basic passive configurations, which is shown in Figure 2-9. Clearly, oleopneumatic shock absorbers provide the most superior impact performance, with an efficiency of up to 80% (Figure 2-9(a)). Furthermore, they have the lowest weight penalty compared to any other design (Figure 2-9(b)). Consequently, oleopneumatic designs are the most widely used configuration on modern aircraft, which are therefore the focus of this research. Nonetheless, some of the other configurations are still in use on lightweight aircraft, which is largely due to their simplicity, reliability, maintainability and low cost [101].

A passive oleopneumatic shock absorber is shown schematically in Figure 2-10. When the shock strut compresses, fluid is forced turbulently through the main orifice in the piston head, resulting in a quadratic damping effect, and thus absorbing energy. The fluid subsequently compresses the gas in the upper chamber, providing a non-linear stiffness effect, and therefore enabling the aircraft to support its own weight. A typical landing impact response that would be obtained from this configuration is illustrated in Figure 2-11. Here, the total shock absorber force is the sum of the damping and spring forces. With reference to Figure 2-11(a), the damping force reaches a peak during the initial stages of the impact i.e. when the piston velocity is at a maximum. The gas

spring force peaks at a later stage when the shock absorber reaches full compression. Consequently, the sum of these forces results in an oscillating response with two maxima. The corresponding total force/displacement response is shown in Figure 2-11(b). Through consideration of the shock absorber efficiency (Eq.2-1), the optimal impact performance will result in the most rectangular force/displacement response as indicated in Figure 2-11(b). This provides the lowest possible peak force, and also reduces fatigue loading due to elimination of the force fluctuations.

Several numerical studies focusing on passive oleopneumatic landing gears can be found in the literature. Milwitzky and Cook [102] described a two-degree-of-freedom (2DOF) impact model of a telescopic (or cantilever) type landing gear. The telescopic configuration, which is illustrated in Figure 2-12(a), is the most widely used due to its superior cost and weight effectiveness [103]. Milwitzky and Cook's model was comprehensive, and accounted for the hydraulic resistance of the orifice, the non-linear gas spring force (using the polytropic gas compression law), the tyre force/deflection characteristic, the internal friction, the wing lift forces, the inclination of the landing gear, and the effects of wheel spin-up loads. The model was shown to be accurate, where numerical predictions correlated well with experimental landing impact data.

Wahi [104, 105] extended certain aspects of this model in order to account for dynamic affects. In particular, fluid compressibility was included via the incorporation of a bulk modulus term. Furthermore, a variable polytropic exponent was introduced in the gas law (Milwitzky and Cook [102] assumed a constant value), which is more consistent with the heat transfer characteristics within the device [105].

Reddy, *et al.* [106] presented a 2DOF model of a levered landing gear configuration, which is illustrated in Figure 2-12(b). Such configurations incorporate additional mechanical arms and hinges, which help reduce the bending loads and hence the excessive bearing frictional forces that are induced during wheel spin-up. Yadav and Ramamoorthy [107] numerically investigated both telescopic and levered landing gear configurations within a 4DOF heave-pitch model.

In the literature, many passive solutions are described that attempt to improve the impact efficiency and enhance the impact/taxiing performance over a wide range of conditions. For example, metering pins (illustrated in Figure 2-10) are commonly used to improve the device's efficiency by changing the damping characteristics during impact. Flugge [108] presented a methodology for optimising the shape of the metering pin. However, this was based on one landing case, and the author noted that the resulting shape would not be optimal for different excitation conditions.

Taxiing performance can be improved using a double acting shock absorber, which is illustrated in Figure 2-13 [101]. The problem arises from the inherent non-linear gas spring characteristic, which results in an excessive suspension stiffness under static loads. By incorporating a low and a high pressure gas chamber in to the shock strut, a more linear stiffness results, which gives rise to a softer suspension during taxiing. Messier Dowty designed an adaptive double stage nose landing gear in the 1990's [100]. Essentially, the pilot could switch from a single stage function, which is used for the impact phase, to a double stage function during take-off and taxiing manoeuvres. Reductions in landing gear loads of 20% and 8% were achieved during taxiing over repaired and unprepared runways respectively [100].

Schnitzer [109] drew attention to another performance limitation that exists in conventional landing gears. He noted that, whilst the shock absorber may perform well over smooth runways or during low velocity impacts, excessive loads would be generated when loads are applied rapidly e.g. over rough surfaces or during heavy landings. This is a direct result of the quadratic nature of the damping force, which causes the shock absorber to behave in a rigid manner at high velocities. In another sense, Krüger [8] noted that the low damping requirement for hard landings results in a damping factor that is too small for taxiing conditions. This is exactly related to the problem that Schnitzer addressed. As a passive solution to the problem, Schnitzer proposed a rate-actuated metering pin or valve [109, 110], which provides velocity dependent damping control. A schematic diagram of such a device is presented in Figure 2-14. During low rates of compression, fluid is able to fill the restriction tube fast enough to balance the pressures and maintain the plunger in its equilibrium position. However, for high rates of compression, the fluid cannot fill the restriction tube quick enough. Consequently, the plunger is lifted, which causes an increase in the orifice size and hence a reduction in damping levels.

Many of the above passive solutions are still limited in performance, as they will be tuned to specific landing impact/runway disturbances. Consequently, to accommodate a wider range of input conditions, investigators have sought alternative solutions, for example using active landing gear.

Substantial research efforts at NASA Langley Research Center have focused on the design of active landing gears since the 1970's [111]. Three possible actuator configurations were originally considered – (1) series-pneumatic, (2) parallel-hydraulic,

and (3) series-hydraulic [111]. The series-pneumatic approach regulated the gas pressure in the upper chamber using two gas accumulators and electronically controlled valves. In the second approach, a hydraulic actuator was used in parallel to the spring and damping elements of the existing shock strut. The series-hydraulic configuration regulates the fluid pressure in the lower chamber as illustrated in Figure 2-15(a). This was found to be the most feasible active solution [111], and has been investigated in all subsequent active landing gear research at NASA.

Ross and Edson [112] presented an analytical and experimental active landing gear investigation of the series-hydraulic configuration. Results were presented for vertical drop tests (where zero horizontal velocity was assumed), and also for impact and roll conditions onto both flat and sinusoidal runway surfaces. The control strategy used energy relations to maximise the shock strut stroke for any given impact, thus minimising the force transmitted to the aircraft. Essentially, this was achieved by comparing the kinetic energy of the aircraft with the work potential of the shock strut. When the work potential exceeded the kinetic energy, the hydraulic actuator was initiated, and the present value of the wing/gear interface force was set as the desired value for the remainder of the impact. Results indicated that the reduction in peak force over a passive system was between 9-31%, depending on the aircraft sink speed and the static gas pressure. In a separate report, Ross described the controller, hardware, and sensors used to implement this active control concept in more detail [17].

Ross and Edson also demonstrated the performance of an active landing gear while rolling over repaired bomb craters [113]. During rolling, active control is initiated only when the wing/gear interface force exceeds a preset tolerance or limit about the static

value. The commanded force to the actuator is then set to this limit value until the actual force is back within range. Using dynamic simulations, the authors demonstrated that the peak wing/gear interface force could be 74% lower than with a passive system.

McGehee and Dreher [9] presented an experimental investigation of an active landing gear. The authors used a specially constructed carriage equipped with the active gear, which could be both propelled and dropped along a runway with various surface irregularities. The control methodologies for impacts and taxiing were based on those used in previous studies, as described above. For vertical impact tests, the authors demonstrated that the percentage reduction in force improved as the aircraft sink speed was increased (e.g. from 8% at a sink rate of 0.9m/s to 32% for a sink rate of 1.7m/s). However, for more realistic impacts performed with an initial forward velocity, the control effectiveness reduced with increasing horizontal speed (e.g. for a sink rate of 1.7m/s, performance improvements were 31% at 8 knots and 11% at 80 knots). This was attributed to the larger strut binding-friction forces, which the actuator cannot control. Such forces are generated as a result of the moments applied to the gear during wheel spin-up, or whilst traversing surface irregularities during rolling/taxiing. The authors also presented the taxiing performance using step bump excitations of various frequencies. It was found that the control effectiveness reduced with an increased frequency, which was due to the low bandwidth of the actuator.

In a more recent investigation, Horta presented a different configuration of the series-hydraulic landing gear, where electro-hydraulic servo-valves were connected to both the upper and lower fluid chambers [10]. Using sinusoidal runway disturbances, experimental results indicated that closed-loop control could reduce vibrations around

the natural frequency by factor of four when compared to the open-loop system. The control of impact forces was not investigated.

The above review of active landing gears has indicated that significant performance benefits are possible over conventional passive devices. However, such active systems are inherently bulky, heavy, and have relatively complex actuation devices requiring large power supplies. As a result, active systems are yet to be introduced onto production aircraft [8].

Semi-active systems represent an attractive compromise between passive and active systems, where existing solutions aim to regulate energy dissipation through semi-active damping. This type of device is illustrated in Figure 2-15(b), where damping forces can be controlled either by altering the orifice shape (e.g. using a servo-valve or piezo-valve) or by changing the fluid properties (e.g. using smart fluids). Research conducted in the 1980's at Messier Dowty investigated the use of servo-valves to control orifice diameter [100]. However, the reduction in loads during tests was found to be negligible. Ghiringhelli [23] presented a numerical and experimental study of semi-active landing gear impacts, which also used servo-valves to control the orifice shape. Energy relations were used to calculate the desired/optimal load profile according the input conditions, and numerical results indicated load reductions of up to 15%. The experimental results contained high frequency oscillations due to inadequate filtering of the sensor signals. Krüger [8] presented a numerical study of a semi-active aircraft landing with a variable orifice diameter. Input excitations representative of actual runways were used to investigate taxiing performance, and a first-order low-pass filter with a 25ms time constant was used to account for the system dynamics. Skyhook,

fuzzy-logic and state-feedback based controllers were shown to perform well, where reductions in vertical cockpit acceleration were between 25-40% depending on the aircraft mass, speed and runway conditions. The fuzzy-logic and state-feedback controllers were particularly superior at damping higher modes of vibration. Maemori, *et al.* [24] used a stepping motor to alter the flow passages during landing impacts. Optimal orifice areas were calculated for a range of aircraft masses such that the acceleration of the fuselage during impacts was minimised. Numerical results indicated that the semi-active device could handle mass variation much better than the optimum passive device.

The ADLAND project partners have developed another semi-active approach, which uses piezoelectric material to alter the orifice geometry [114]. This is known as a piezo-valve and the concept is shown schematically in Figure 2-16. Here, a stack of piezoelectric material expands and contracts under the application of a voltage. This in turn displaces a poppet, which modifies the flow geometry of the main orifice.

Considering specifically the use of smart fluids in landing gears, various shock absorber designs have been proposed in the literature. For example, Lou, *et al.* [47] presented a shear mode ER shock strut, which was described previously (see Figure 2-4). To control the impact response, the authors used kinetic energy relationships to calculate the lowest possible landing gear force that results in the most efficient or "box-like" force/displacement response (see Figure 2-11(b)). Simulated results indicated that the peak acceleration could be reduced by 23%.

Another ER landing gear was proposed by Berg and Wellstead [49]. The authors used a shear/squeeze mode device (see Figure 2-5(b)) in series with a conventional passive

shock strut. Particular attention was given to fail-safety, where the inclusion of a locking mechanism could revert performance to that of the passive device. In terms of control, the authors suggested that the ER damping coefficient should be altered according to the frequency of the input excitation, although an exact methodology was not described.

Choi and Wereley [87] investigated the use of a flow mode ER/MR landing gear shock strut for the control of impacts. The authors developed a sliding mode controller that was designed to be robust against variations in aircraft mass, lift force, viscous damping, and the gas spring stiffness. Numerical results indicated that the acceleration and displacement response of the aircraft could be significantly improved using sliding mode control.

Whilst the above ER/MR investigations have helped to demonstrate the benefits of using smart fluids to implement semi-active control in landing gear, they have often overlooked packaging requirements/constraints, and the effects of fluid compressibility in numerical models. Sizing constraints are vital for aerospace applications such as landing gear, and will be used as a key constraint in the present study. The consideration of fluid compressibility is particularly important when considering impulsive loading, as fluid compression will reduce valve flow and hence controllability. Therefore, the present thesis aims to develop a dynamic model of the MR shock strut that accounts for fluid compressibility. Wahi [105] modelled fluid compressibility in passive landing gear, however this analysis did not consider the two fluid chambers separately (one either side of the main orifice), as is the intention of this research.

2.6 Summary of Chapters 1 and 2

The first two chapters in this thesis have described the limitations of traditional passive suspensions, whilst highlighting the advantages that can be gained using semi-active devices. Moreover, magnetorheological fluid based devices were identified as a particularly superior means to provide semi-active vibration control. For example, an MR fluid based aircraft shock absorber could be utilised to enhance both the landing impact and taxiing performance, thus improving fatigue life and levels of passenger discomfort. Although this application has been considered in previous research, specific design and packaging constraints were overlooked. Furthermore, the effects of fluid compressibility were neglected in numerical models. Fluid compression degrades controllability by reducing valve flow, and this will be particularly significant in impact applications. Consequently, the above issues will be given special attention in the present work.

Chapters 1 and 2 also drew attention to the non-linear behaviour of MR dampers. This makes the objective of achieving a desired force (and hence the application of classical control techniques) very difficult. Consequently, there is no general consensus on how to best perform automatic control. Previous research at the University of Sheffield has focused on a methodology known as feedback linearisation, which simplifies this force tracking issue. However, this research did not formally validate the approach under realistic broadband excitations. Furthermore, the approach is yet to be investigated experimentally as part of a complete vibrating structure.

This discussion underpins the principal objectives of this thesis that were described in Section 1.3.

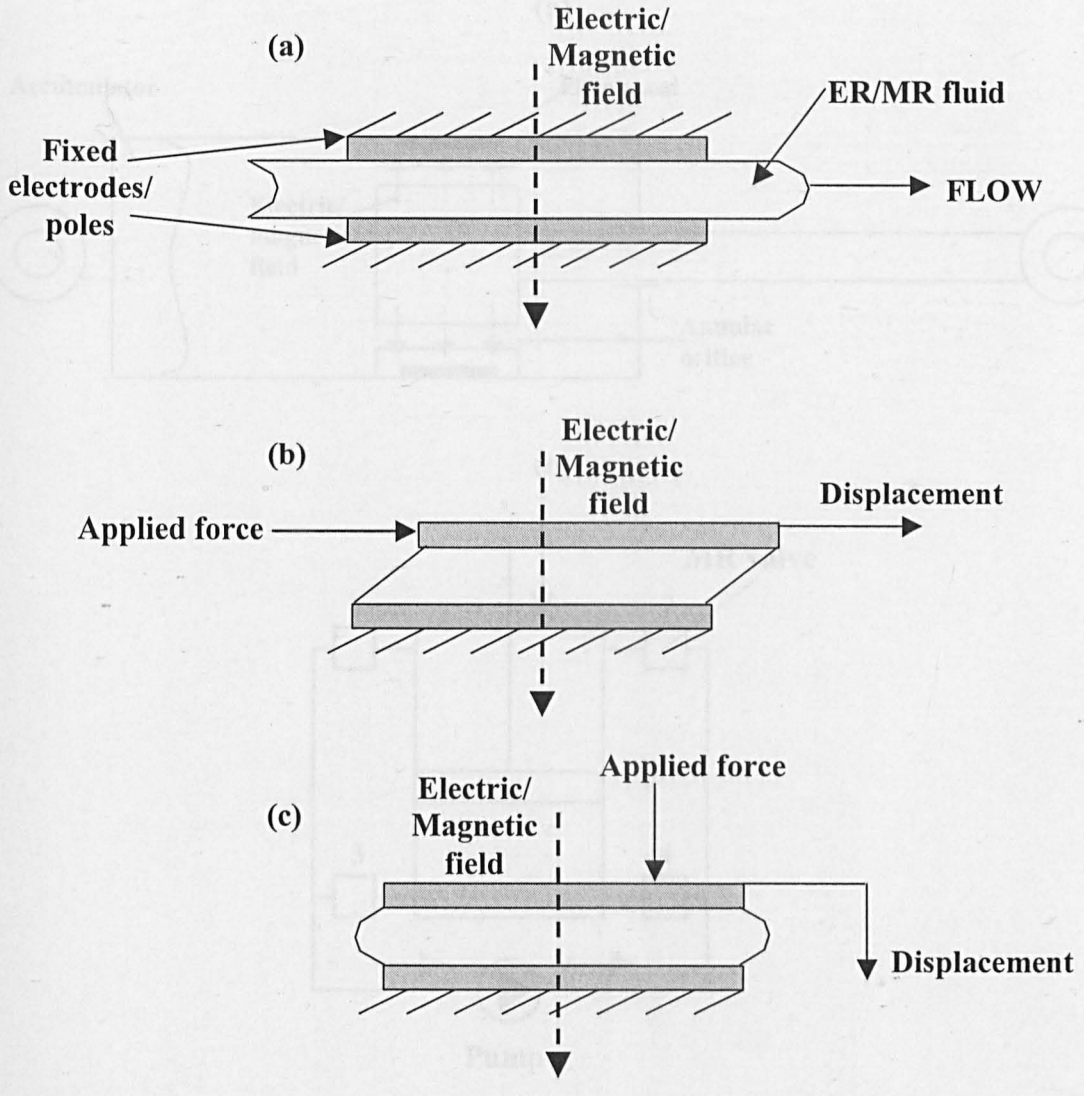

Figure 2-1: Smart fluid modes of operation. (a) Flow mode, (b) shear mode, and (c) squeeze mode.

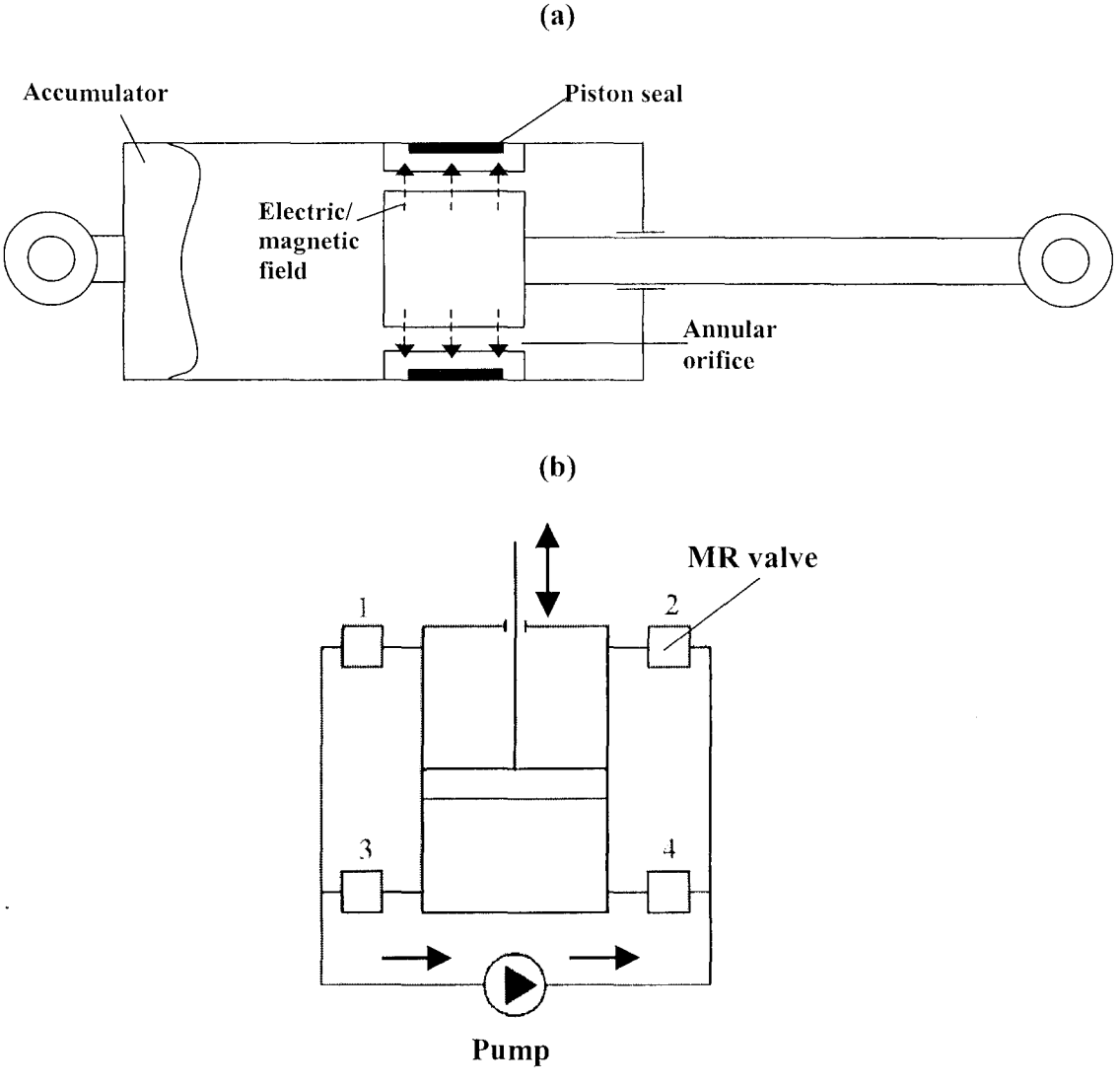

Figure 2-2: Flow mode devices. (a) Smart fluid damper, and (b) smart fluid hydraulic control system [41].

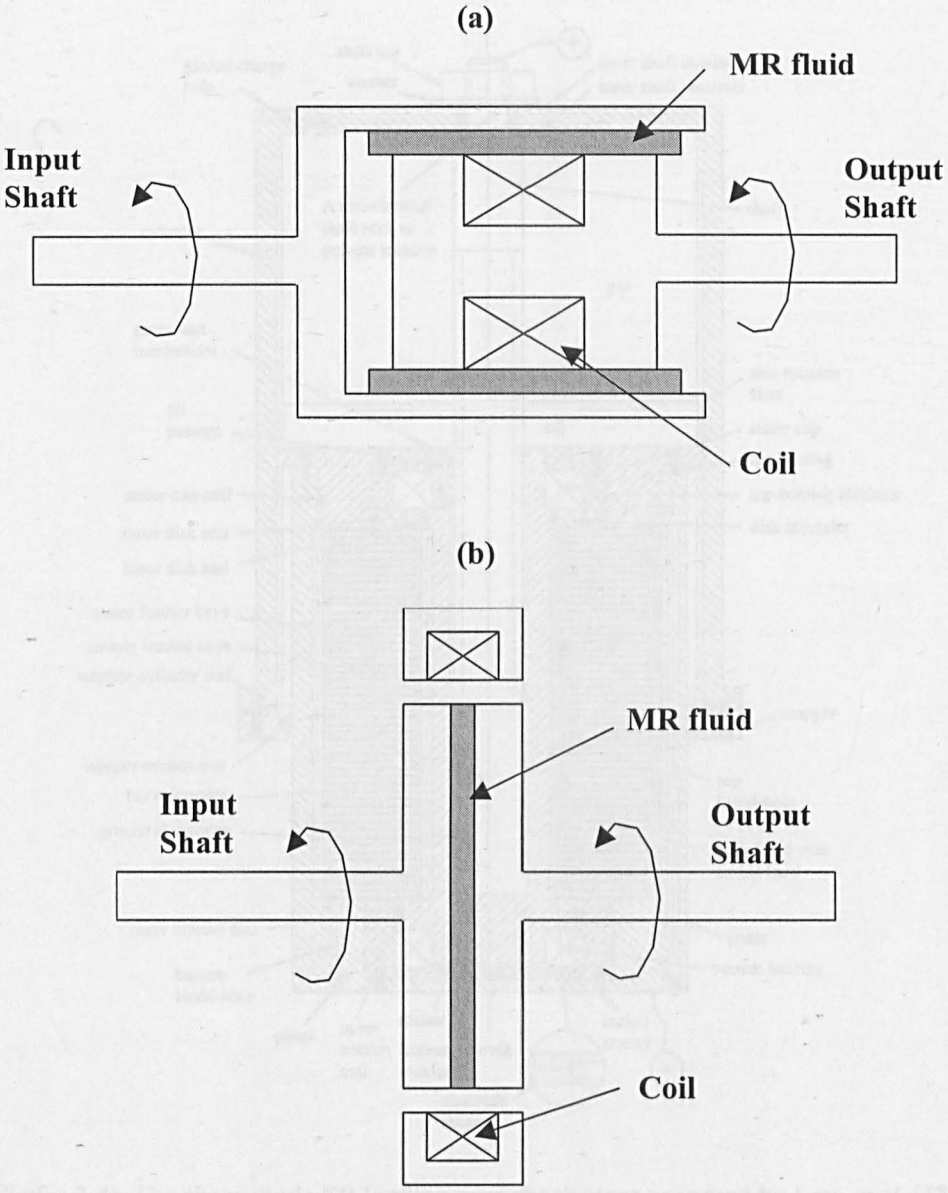

Figure 2-3: Shear mode rotary clutches [43]. (a) Cylindrical design, and (b) disk shaped design.

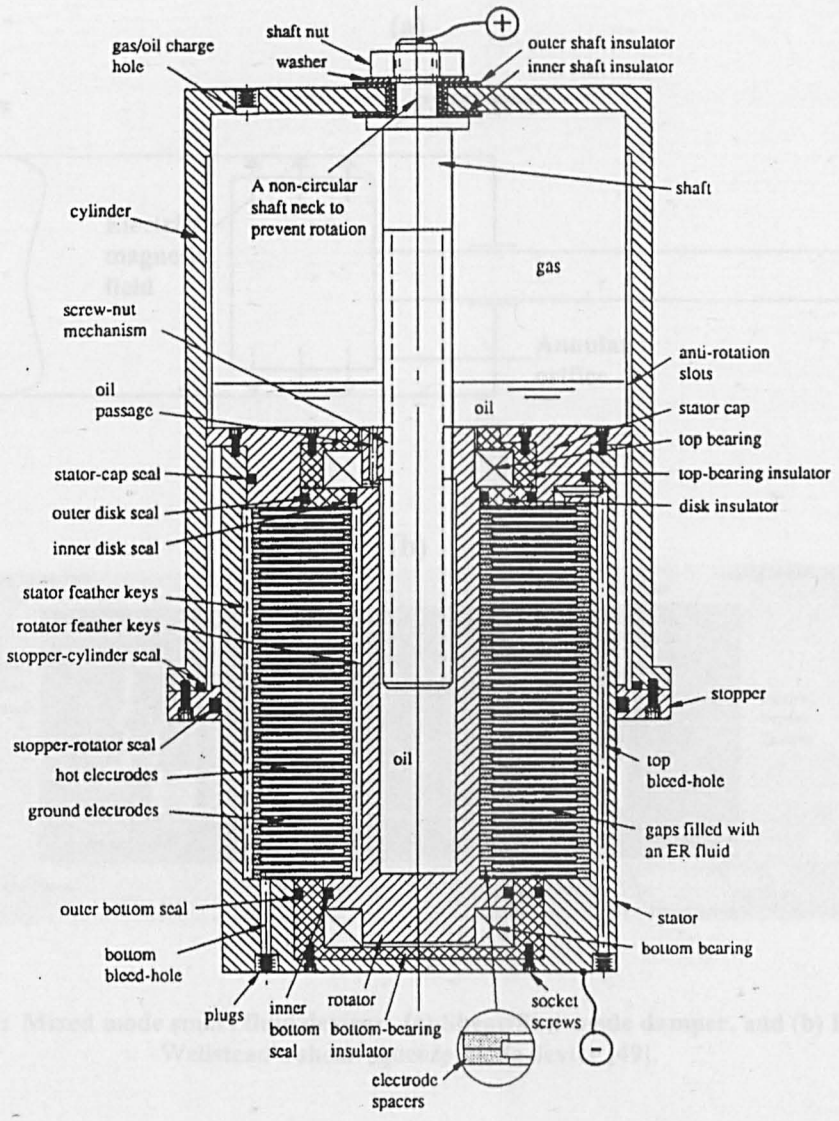

Figure 2-4: The shear mode ER landing gear shock strut proposed by Lou, *et al.* [47].

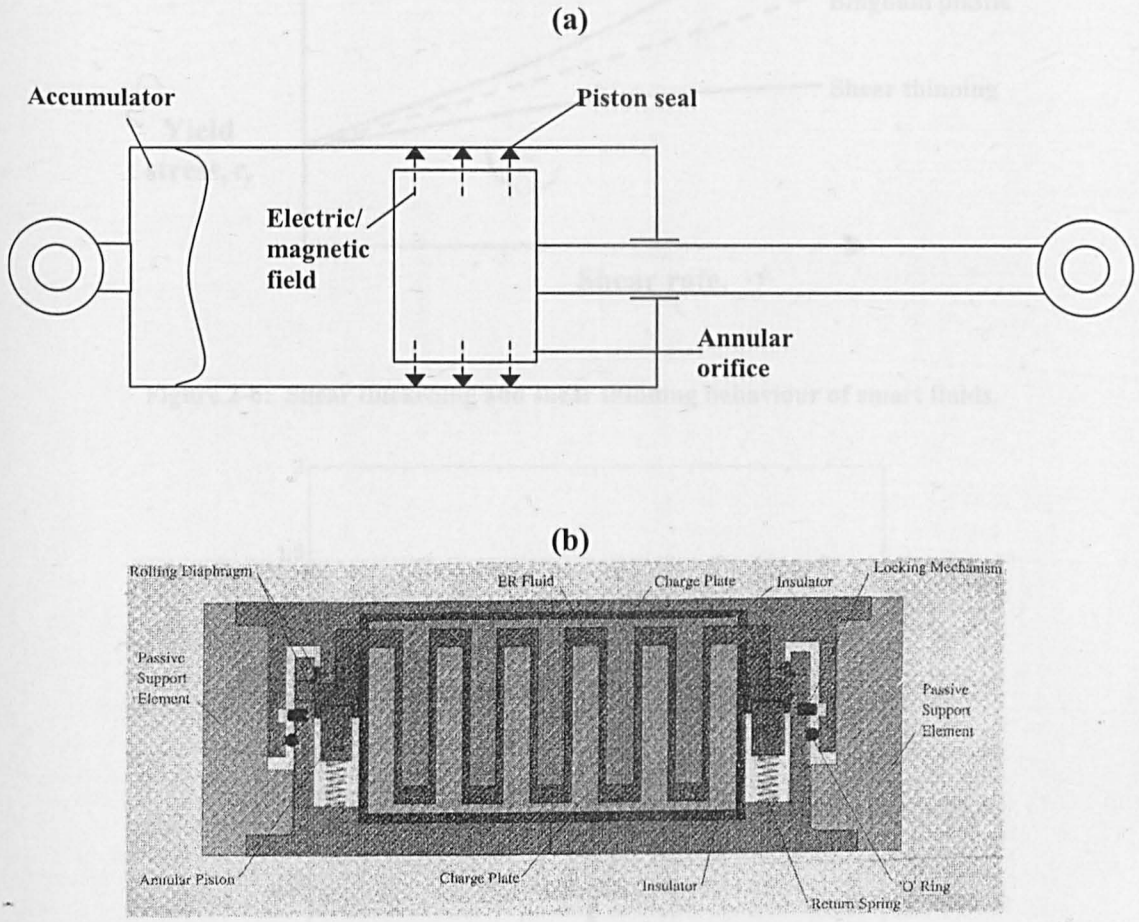

Figure 2-5: Mixed mode smart fluid devices. (a) Shear/flow mode damper, and (b) Berg and Wellstead's shear/squeeze mode device [49].

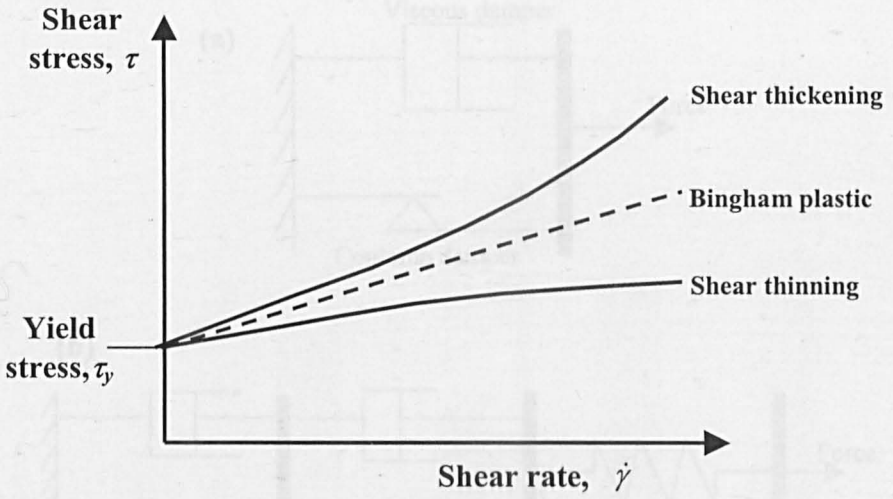

Figure 2-6: Shear thickening and shear thinning behaviour of smart fluids.

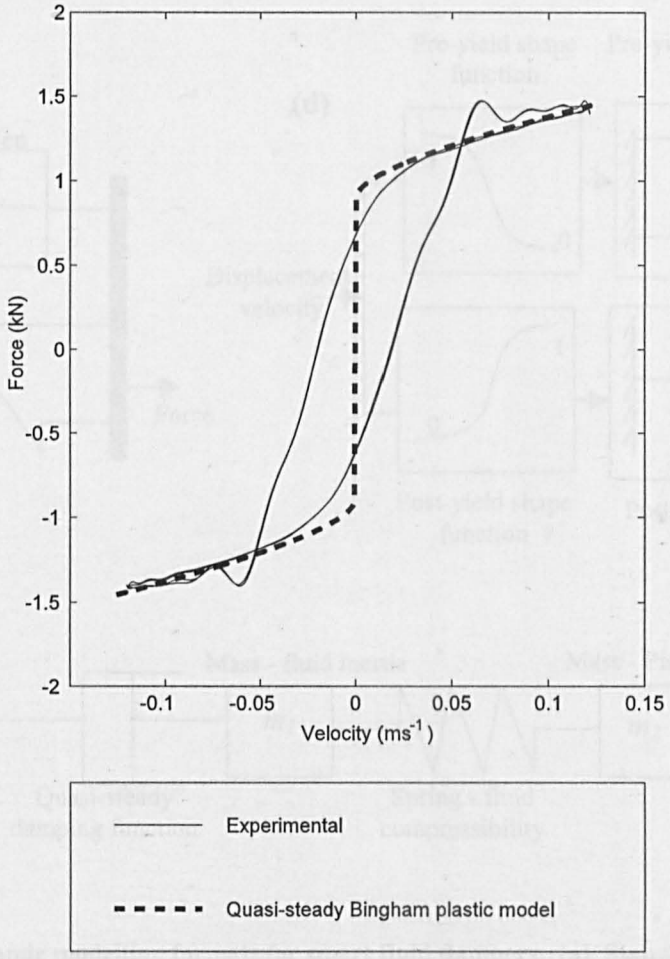

Figure 2-7: Experimental and numerical force/velocity response of Lord Corporation's RD-1005-3 MR damper. Sinusoidal excitation: Amplitude = 2mm, frequency = 10Hz.

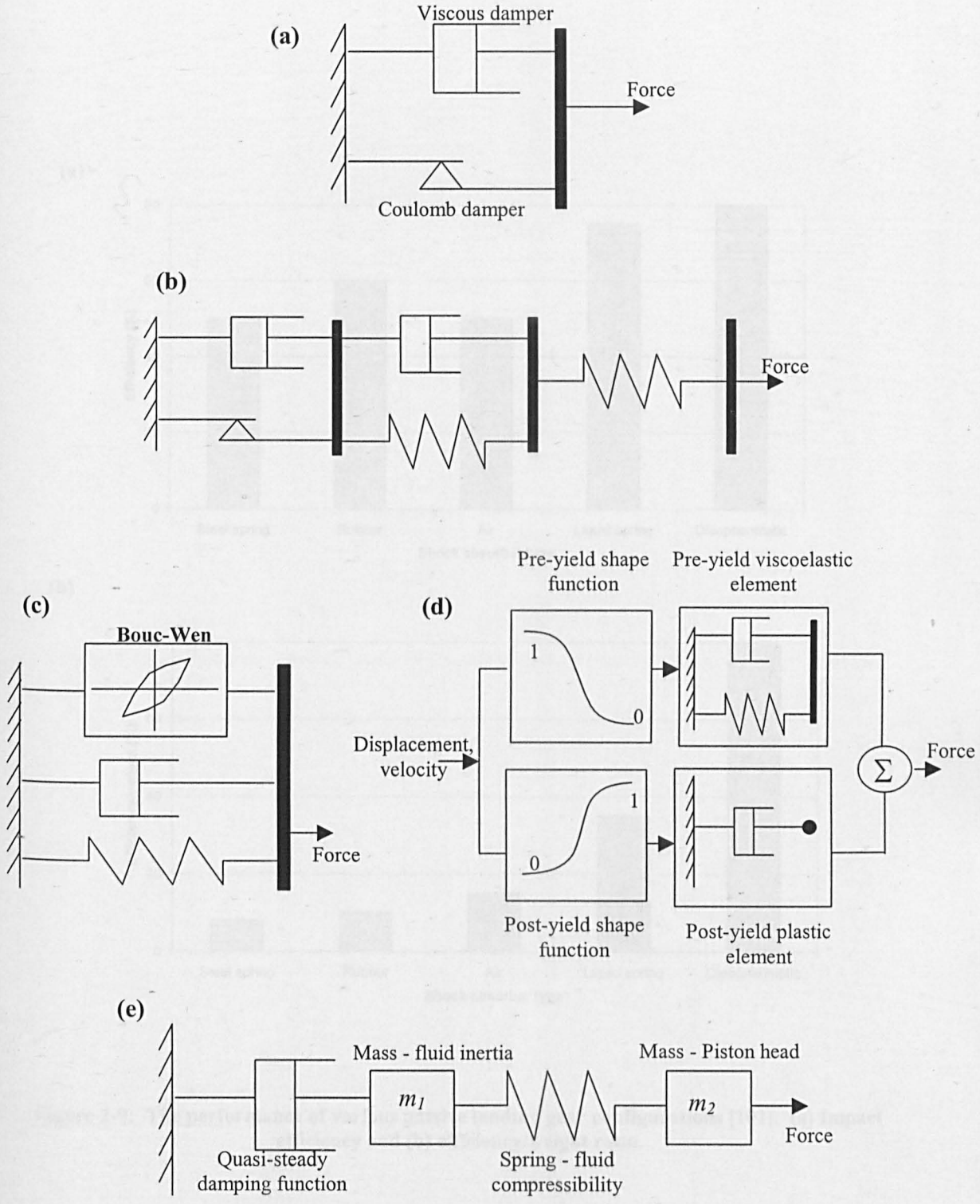

Figure 2-8: Dynamic modelling formats for smart fluid dampers. (a) Stanway, *et al.* [64], (b) Gamotoa and Filisko [65], (c) Spencer, *et al.* [66], (d) Wereley, *et al.* [115], and (e) Sims, *et al.* [74].

(a)

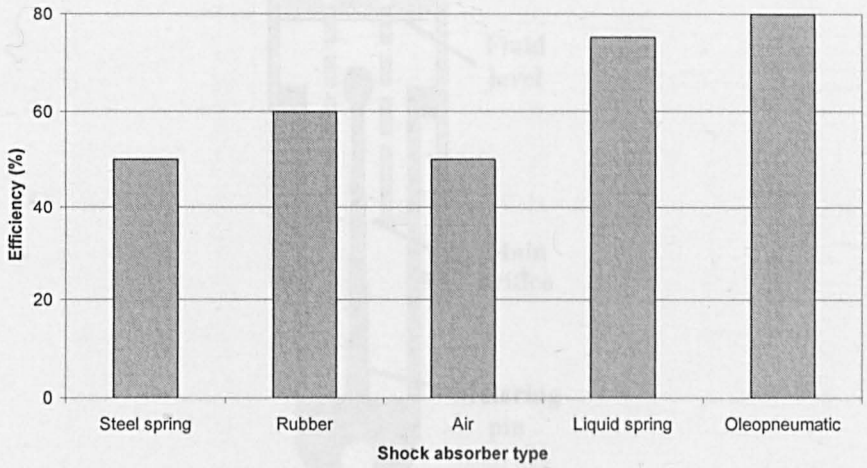

(b)

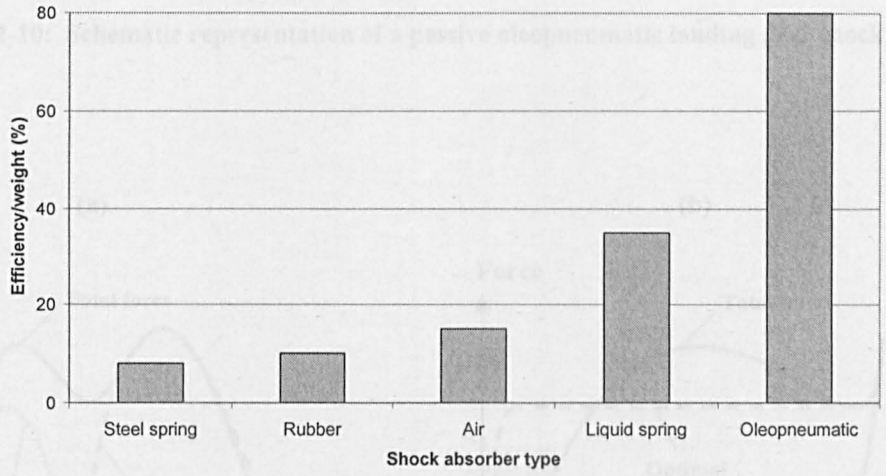

Figure 2-9: The performance of various passive landing gear configurations [101]. (a) Impact efficiency and (b) efficiency/weight ratio.

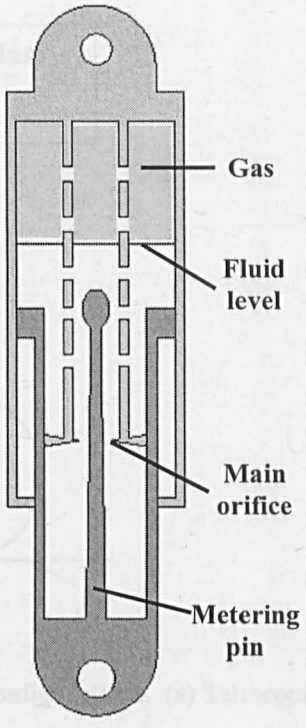

Figure 2-10: Schematic representation of a passive oleopneumatic landing gear shock strut.

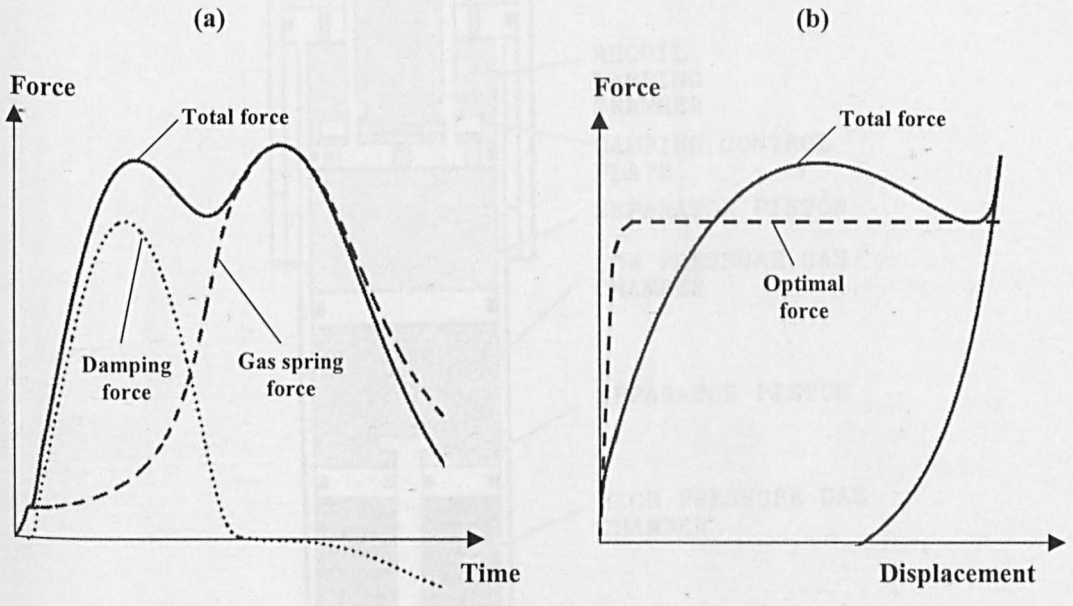

Figure 2-11: Typical landing impact responses of a passive oleopneumatic shock absorber. (a) Force/time response and (b) force/displacement response.

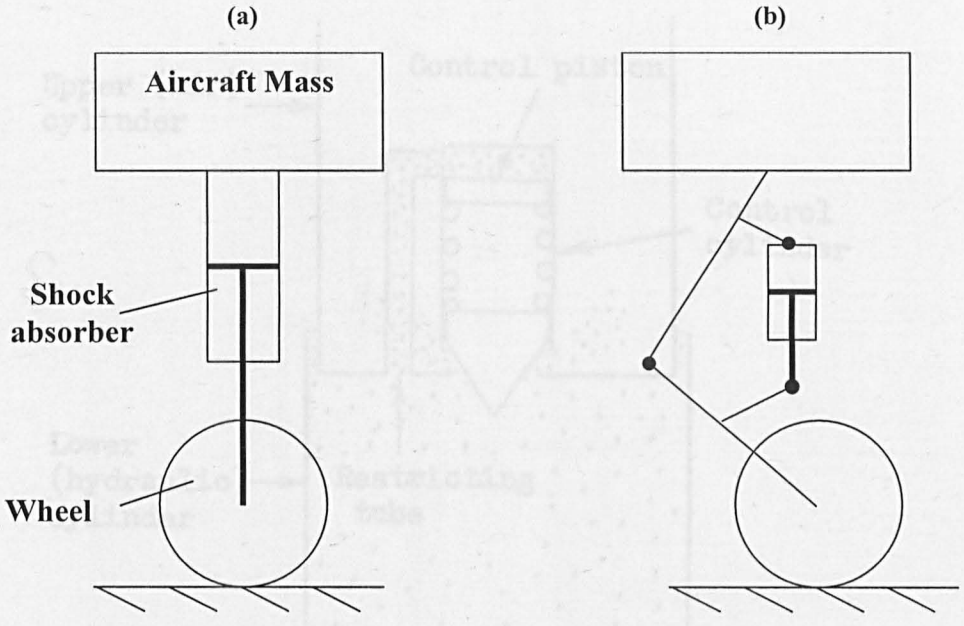

Figure 2-12: Landing gear configurations. (a) Telescopic (or cantilever) and (b) levered.

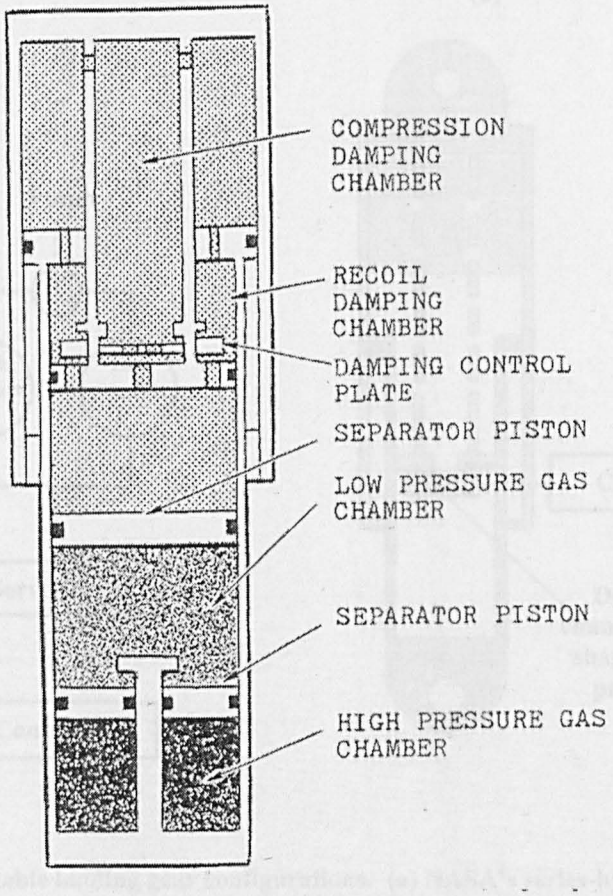

Figure 2-13: Double-acting oleopneumatic shock absorber [101].

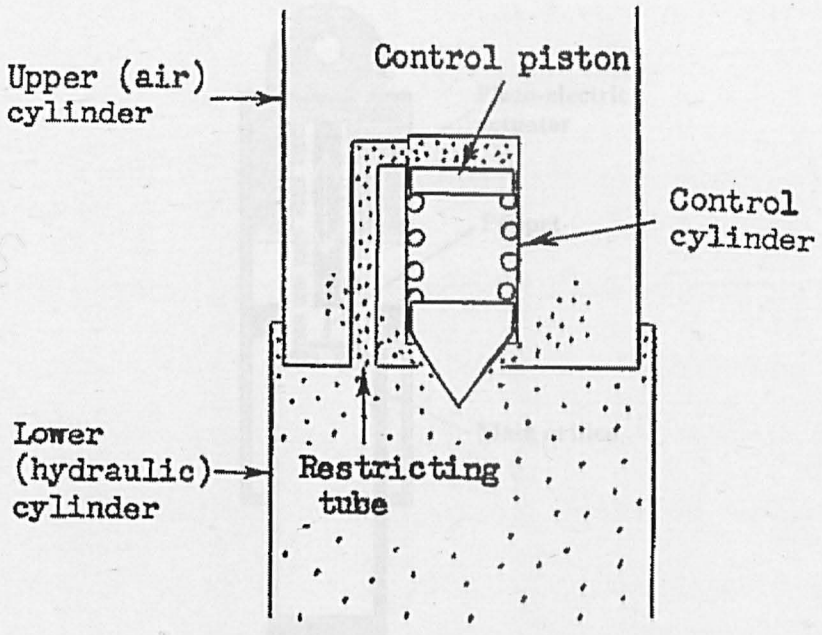

Figure 2-14: Pressure rate actuated valve [110].

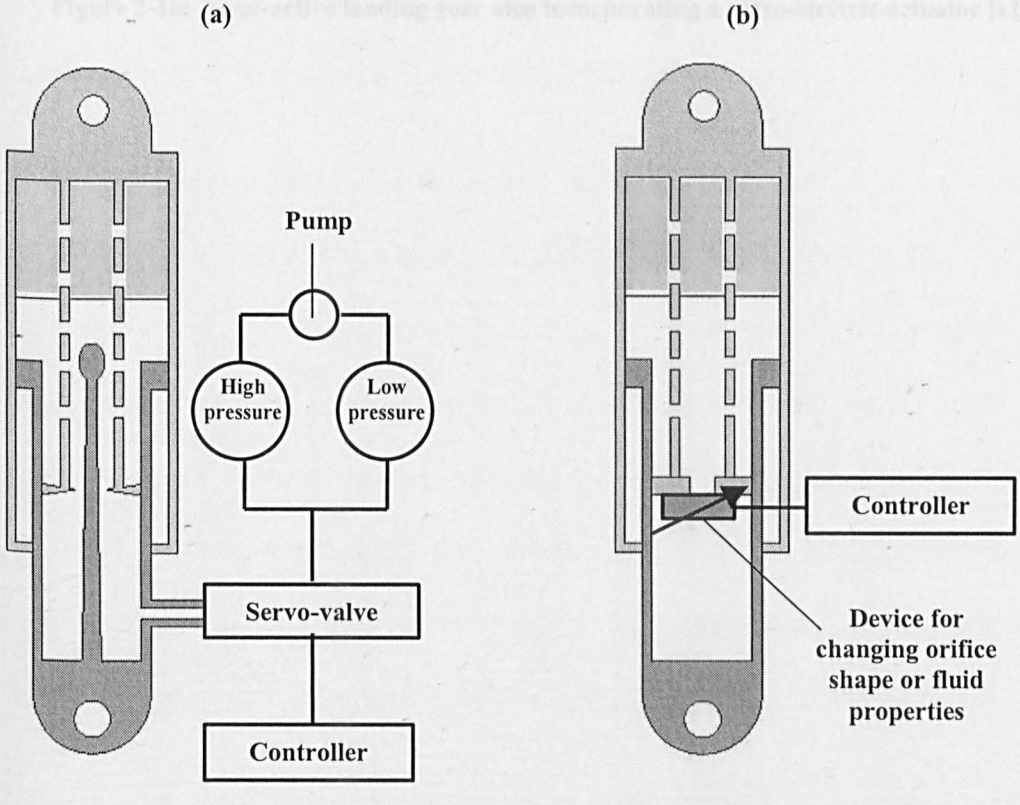

Figure 2-15: Controllable landing gear configurations. (a) NASA's series-hydraulic fully active shock absorber, and (b) the semi-active approach.

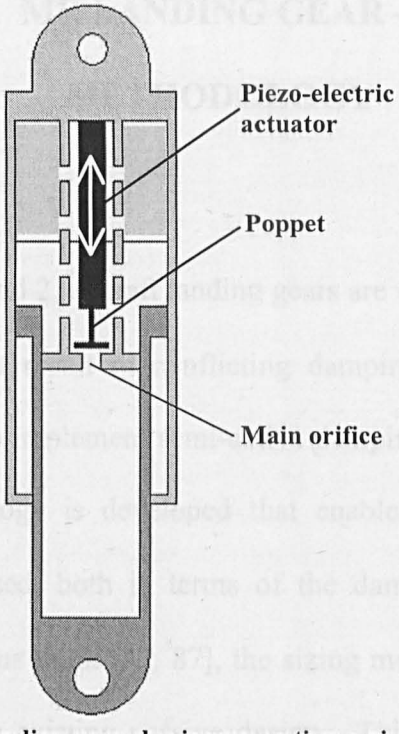

Figure 2-16: Semi-active landing gear oleo incorporating a piezo-electric actuator [114].

CHAPTER 3. MR LANDING GEAR – A DESIGN METHODOLOGY

3.1 Introduction

As discussed in Chapters 1 and 2, aircraft landing gears are subjected to a wide range of excitation conditions, which result in conflicting damping requirements. A novel solution to this problem is to implement semi-active damping using MR fluids. In this chapter, a design methodology is developed that enables the performance of MR landing gears to be optimised, both in terms of the damping and magnetic circuit performance. Unlike previous work [42, 87], the sizing methodology incorporates the packaging constraints of the existing passive design. This is an essential feasibility consideration as space and weight are vital performance indicators in landing gear.

The design approach focuses on the impact phase of an aircraft's landing, where large variations in sink speed, angle of attack, and aircraft mass makes an MR device very attractive. To implement the design procedure, two numerical tools are developed – a valve size optimisation spreadsheet, and a landing gear impact model. The landing impact model is based upon that developed by Milwitzky and Cook [102], but is extended to account for the MR flow behaviour and the fluid compressibility. This latter aspect is important in impulsive loading applications such as aircraft landing, as fluid compression will reduce valve flow and hence the controllable MR effect.

The design approach is initially demonstrated by presenting an in depth case study of the Polish Institute of Aviation's I-23. This is a lightweight aircraft for personal/business use, but to demonstrate scalability, case studies for large-scale

commercial jets are also presented. This was made possible using landing gear data provided by the ADLAND partner Messier Dowty [103].

This chapter is organised as follows. To begin, the MR landing gear design philosophy and the numerical tools required to implement it are described. These tools include a landing impact simulation, where both MR and passive shock strut models are derived. The passive simulation will serve to validate the landing impact model in general via comparisons to experimental drop test data. A valve sizing spreadsheet tool is then derived, which enables the simultaneous optimisation of the magnetic circuit and damping performance. Next, the methodology is illustrated using case studies for both lightweight and large-scale aircraft. Finally, a general discussion of the results is made and the key conclusions are drawn. The research in this chapter formed the first part of a two-part journal paper submission [116], and the abstract for this work is given in Appendix A.I. In addition, two conference papers were produced [117, 118].

3.2 The Design Methodology

In this section, an MR landing gear design methodology will be developed. The aim is to find a way of designing the device so that it can achieve an optimal performance over a range of impact scenarios. This must be achieved without exceeding the packaging constraints of an equivalent passive device. Furthermore, the magnetic design of the MR valve must be considered.

The MR valve configuration investigated in this study is shown in Figure 3-1. Here, fluid flows through an annular orifice and the magnetic flux is generated via a coil wrapped around a steel bobbin. The active section of the valve (i.e. the length exposed

to the magnetic field) is where the path of magnetic flux crosses the annular orifice. The fluid volume adjacent to the coil remains inactive.

It will be shown that the geometry of this device can be optimised from a magnetic perspective using analytical methods, and that this magnetic behaviour is relatively insensitive to the valve gap h. In contrast the damping behaviour is difficult to optimise because of the nonlinear interaction between fluid flow, tyre deflection, and shock strut gas compression. It is, however, highly sensitive to the valve gap h.

The design approach used is summarised in Figure 3-2. To begin, the MR shock absorber is sized to be that of the equivalent passive device, in terms of its length and diameter. This dictates values for the external geometry of the MR valve (length l and diameter D_p). Initial estimates for the valve's flow diameter d and active length l_a can then be determined. At this stage the precise values are not important because they will be optimised later, from a magnetic standpoint.

Landing impact simulations are then performed, using data for the actual aircraft structure, to predict behaviour. This is performed for the case where the fluid yield stress is at its maximum value $\tau_{y_{max}}$, and the impact scenario is at its most severe. Consequently, for less severe impacts with lower damping requirements, the yield stress can be controlled to give superior performance over the existing passive system. In this worst-case simulation, the valve gap h is modified to achieve desirable landing behaviour, which can be compared to experimental data from the passive device. Essentially, the aim is to achieve an equal balance between the damping and gas spring forces. From this result, the pressure drop ΔP_{max} at the maximum valve flow rate Q_{max}

is determined, and the two properties [ΔP_{max}, Q_{max}] are used to characterise the requirement of the valve.

The task now is to optimise the magnetic performance of the valve, whilst still achieving the desirable [ΔP_{max}, Q_{max}] characteristic. Furthermore, the aim is to maximise the controllability of the valve, thus maximising the range of impact conditions that can be optimally damped. This involves revising the valve's mean radius and active length, choosing the electric circuit configuration, and finally modifying the valve gap so as to maintain the [ΔP_{max}, Q_{max}] characteristic. Because the magnetic behaviour is relatively insensitive to the valve gap, it is not normally necessary to repeat the magnetic optimisation once the valve gap h has been finally chosen.

With the optimal valve geometry, the landing impact simulations can be repeated to check that the performance is close to that found for the preliminary design. Because the [ΔP_{max}, Q_{max}] characteristic is unchanged, the damping performance will not differ greatly between the magnetically optimised design and the preliminary design.

The design approach requires two modelling approaches: a time-domain landing simulation including MR damping, and an analytical approach for optimising the magnetic design of the valve. These numerical tools are derived in the following sections.

3.3 Oleopneumatic shock strut modelling

3.3.1 MR shock strut model

A schematic diagram of an MR oleopneumatic shock strut is shown in Figure 3-3. This is similar to a typical passive device (see Figure 2-10), except that an MR valve replaces the conventional circular orifice and the metering pin. The key equations used to formulate the dynamic model are also shown in Figure 3-3, which are described as follows.

Neglecting internal friction, the shock strut force F_s is readily derived using the following pressure-area balance:

$$F_s = (P_2 - P_1)a_{2i} + P_1 a_{2o} = F_h + F_g \tag{3-1}$$

where P_1 and P_2 are the pressures in chambers '1 ' and '2', a_{2i} and a_{2o} are the inner and outer cross-sectional areas of the cylinder that seals against the piston head, F_h is the hydraulic damping force and F_g is the gas force. The present study has assumed that the pressure in chamber '1 ' is equal to the gas pressure in chamber 'a'. This is valid when the fluid inertia is negligible and if the mass of the dividing piston is small. For the shock struts considered in this study, the fluid and gas volumes are mixed (i.e dividing piston mass = 0kg) and fluid inertia has been neglected for simplification purposes.

The gas pressure P_a (and hence chamber '1' fluid pressure) is determined from the polytropic law for the compression of gases:

$$P_a (= P_1) = P_{a0} \left(\frac{v_{a0}}{v_a} \right)^m \tag{3-2}$$

where P_{a0} is the initial gas inflation pressure, v_{a0} is the initial gas volume, v_a is the current gas volume, and m is the polytropic exponent. For passive landing gears, m is often assumed as 1.1, which has been shown to correlate well with observed behaviour when the fluid and gas volumes are mixed [101].

Dynamic effects are incorporated in the form of fluid compressibility using a bulk modulus term. This is a vital consideration for shock absorber modelling, especially for impact scenarios. Assuming constant density, it can be shown that the general mass flow continuity equation accounting for the fluid compressibility of a control volume is (see Appendix B):

$$\frac{dv}{dt} + \frac{v}{\beta} \frac{dP}{dt} = Q_i - Q_o \tag{3-3}$$

where v is the control volume (which changes according to piston position and/or fluid compression), β is the bulk modulus, P is the pressure, and Q_i and Q_o are the volume flow rates into and out of the control volume respectively.

With reference to Figure 3-3, Eq.3-3 is applied to each fluid chamber, which introduces non-linear stiffness terms into the model. During compression, $Q_{i2} = Q_{o1} = 0$, where subscripts '*1*' and '*2*' denote chambers *1* and *2*, respectively. Also, assuming there is no compression in the valve, then $Q_{o2} = Q_{i1} = Q$. Finally, assuming a constant bulk modulus, the mass flow continuity equation for each chamber is:

$$Q = \frac{dv_1}{dt} + \frac{v_1}{\beta}\frac{dP_1}{dt} \tag{3-4}$$

$$-Q = \frac{dv_2}{dt} + \frac{v_2}{\beta}\frac{dP_2}{dt} \tag{3-5}$$

Here, $v_1 = v_{10} + v_{a0} - (a_{2o} - a_{2i})x - v_a$ and $v_2 = v_{20} - a_{2i}x$, where x denotes the piston displacement, and the subscript '0' represents the initial conditions. Equations 3-1 to 3-5 were formulated in Simulink and the corresponding block diagram is shown in Figure 3-4. Here, Eq.3-4 is solved for v_1, whilst Eq.3-5 is solved for P_2. The gas volume v_a is then deduced by geometry, which in turn gives $P_a = P_1$ (Eq.3-2). This model formulation is necessary as it avoids the presence of an algebraic loop.

Finally, in order to model the MR effect, a look-up table containing the pressure-flowrate (ΔP-Q) characteristics of the MR valve as a function of yield stress is generated. The term ΔP is calculated by summing the individual pressure drops across the active and inactive regions of the valve. The active pressure drop is determined by the solution of the Buckingham equation for Bingham plastic flow between parallel flat plates [55]. This has been shown to characterise smart fluids well for annular flow, where the height of the valve gap is negligible in relation to the mean valve diameter. The corresponding Buckingham equation is as follows:

$$4\left(\frac{l_a}{h\Delta P_{l_a}}\right)^3 \tau_y^3 - 3\left(\frac{l_a}{h\Delta P_{l_a}}\right)\tau_y + \left(1 - \frac{12\mu l_a Q}{bh^3 \Delta P_{l_a}}\right) = 0 \tag{3-6}$$

Here, ΔP_{l_a} is the active valve pressure drop, l_a is the active valve length (equal to $2t_b$ in Figure 3-1(b)) and b is the mean annular circumference of the valve (equal to πd in Figure 3-1(b)). The two key unknowns in Eq.3-6 are the Bingham plastic yield stress τ_y

and the viscosity μ, which can be estimated from the MR fluid manufacturer's data. The inactive pressure drop is readily determined using the equation for Newtonian flow between parallel flat plates, i.e. Eq.3-6 with $\tau_y = 0$.

By specifying the valve geometry, fluid yield stress and volume flow rate, Eq.3-6 can be solved for ΔP. There is only one physically meaningful root to this equation, which is obtained using Newton's method. It can be shown that the first guess of ΔP given by Eq.3-7 will have converged on the desired root by ten iterations [119].

$$\Delta P^{(1)} = \frac{3l\tau_y}{h} + \frac{12\mu lQ}{bh^3} \tag{3-7}$$

This initial guess ensures that the most positive root of Eq.3-6 is converged upon, which represents the only root where the maximum shear stress in the fluid is greater than the Bingham plastic yield stress, hence representing fluid flow. Equation 3-6 was solved in Matlab for a range of yield stress and volume flow rate values, which results in a look up table with flow rate and yield stress as the input and pressure as the output. However, from Figure 3-4 it can be observed how the inverse of this is required to solve the dynamic model i.e. pressure is required as the input and flow rate is required as the output. This was achieved using interpolation by sampling the previously generated pressure/flow rate curves at equally spaced pressures, and then repeating the procedure at equally spaced yield stresses.

A final important point is that the pressures in the dynamic shock strut model were found to drift when subject to several excitation cycles. The author believes that this is due to a lack of mass continuity in the model as a result of the constant density assumption in Eq.3-3. Nonetheless, the model was considered to be accurate over a

single cycle, particularly during the compression phase, which is the most important for landing impacts. For longer simulations, the pressure drift problem can be overcome by linearising the stiffness term in Eq.3-3 i.e. the ratio v/β becomes a constant. It should also be noted that the derivation of Eq.3-3 has some similarities to the wave equation used in acoustics [120]. As further work, it would therefore be interesting to use the theory of acoustics to derive the model without the assumption of constant density.

3.3.2 Passive shock strut model

It is desirable to model the landing impact response of the existing passive shock strut. This enables the complete landing impact model to be validated before performing equivalent simulations of the MR device. The passive shock strut model is readily derived via substitution of Eq.3-6 with the well-known equation describing the discharge through an orifice, that is:

$$Q = C_d a_o \sqrt{\frac{2}{\rho}(P_1 - P_2)} \tag{3-8}$$

where Q is the volumetric flow rate, C_d is the coefficient of discharge, a_o is the cross-sectional area of the orifice and ρ is the density of hydraulic oil (872.6 kgm^{-3} for Aeroshell 41 which is a standard oil used in landing gear shock absorbers [121]). An uncertainty arises here regarding the value to be taken for the coefficient of discharge. The nominal value for a sharp edged orifice is 0.6 [122], although there is evidence of appreciable variation in the discharge coefficient with Reynolds number during an impact [102]. Nonetheless, this value serves as an intuitive first guess.

3.4 The landing impact model

In this section, a two-degree-of-freedom (2DOF) landing impact model is derived. For simplification purposes, wheel spin-up forces have been neglected.

A free-body diagram of the 2DOF impact model is shown in Figure 3-5. This corresponds to a telescopic type of landing gear, which is consistent with the majority of aircraft considered in this thesis. Here, the relative displacement between the airframe and wheel assembly corresponds to the displacement of the shock strut. The equations of motion for the system are as follows:

$$m_p \ddot{z}_p = m_p g - L - F_s \tag{3-9}$$

$$m_w \ddot{z}_w = m_w g - F_t + F_s \tag{3-10}$$

where m_p is the distributed aircraft mass i.e. the effective aircraft mass that acts over a single shock absorber, m_w is the mass of the wheel/tyre assembly, z_p and z_w are the displacements of the drop mass and the wheel/tyre assembly, L is the aerodynamic lift force from the wings, F_s is the shock strut force (Eq.3-1) and F_t is the tyre force. The aircraft lift maintains a constant value equal to a percentage of the aircraft's weight W. Normally, $L = 0.67W$ for lightweight utility aircraft and $L = W$ for larger transport aircraft [101]. The tyre force F_t was approximated using the following power law, which was shown by other investigators [102] to correlate well with observed behaviour:

$$F_t = c z_w^r \tag{3-11}$$

Here c and r are empirical constants. For simplification purposes, tyre hysteresis was neglected.

An added complexity in the model arises due to the initial shock strut inflation pressure P_{a0}, which generates an extension force. Assuming that the shock strut is rigid in compression and bending, the wheel and drop mass effectively remain locked until this initial force is overcome, i.e. the system behaves as a single-degree-of-freedom (SDOF) system [102]. Therefore two separate models are required with the SDOF model triggering the 2DOF model at the instant this initial force is exceeded. The equation of motion for the SDOF system is:

$$(m_p + m_w)\ddot{z} = (m_p + m_w) - L - F_t \tag{3-12}$$

where $z = z_p = z_w$. The initial condition for this SDOF model is set in terms of the sink velocity, V_{sink} $(= \dot{z}(0))$. At the instant $t = t_d$ when the shock strut begins to deflect, $F_s = P_{a0}a_{2o}$ (see Eq.3-1 and note that P_2=P_1=P_{a0}). Substituting this expression into Eq.3-9 and noting from above that $\ddot{z}_p = \ddot{z}$ gives:

$$\ddot{z}_{t_d} = \frac{m_p g - L - P_{a0}a_{2o}}{m_p} \tag{3-13}$$

Eq.3-13 represents the critical acceleration to be exceeded to cause shock strut deflection and Eq.3-12 is solved until this value is reached. The 2DOF system is then triggered with the resulting initial conditions from the SDOF system at time $t = t_d$.

3.5 MR Valve geometry optimisation

The complete MR landing impact model has now been derived, and what remains is to determine the optimal MR valve geometry. In this section, a methodology for optimising the performance of MR valves subject to sizing constraints is presented.

With reference to Figure 3-1, it is desirable to achieve large magnetic fields in the fluid (hence a large MR fluid yield stress), passing through a large active length. Also, to minimise the power requirements for a given fluid yield stress, a large number of coil turns are required. However, due to packaging constraints on valve diameter and length, this will reduce the active length. Furthermore, a larger coil will reduce the cross-sectional areas of the magnetic circuit, which may cause saturation of the valve material. This demonstrates the balance that is required between power and active length in order to optimise a geometrically constrained valve. A sizing methodology that addresses this balance will now be derived in terms of the valve geometry and valve performance.

3.5.1 Geometry formulation

Rosenfeld and Wereley [123] developed a set of analytical rules to describe an optimal geometry of an MR valve. The geometry was optimal in the sense that saturation of the magnetic circuit is avoided as far as possible. For completeness, the approach is briefly summarised below.

Three critical valve areas of the MR valve shown in Figure 3-1 are first defined, and it is important that the material in these areas does not reach magnetic saturation. The areas are the circular cross-section of the bobbin core A_1, the annular cross-section of the flux return A_2 and the cylindrical area at the interior of the bobbin flanges A_3 [123]. The valve geometry that best prevents magnetic saturation is achieved when these critical areas are equal. This helps maintain a constant flux density throughout the magnetic circuit so that a particular region does not saturate prematurely. With reference to Figure 3-1(b), these critical areas can be described by the following equations:

$$A_1 = \pi t_a^2 \tag{3-14}$$

$$A_2 = \pi\left(0.25D_p^2 - (t_a + w_c + h)^2\right) \tag{3-15}$$

$$A_3 = 2\pi t_a t_b \tag{3-16}$$

where t_a is the bobbin core radius, D_p is the constrained MR valve diameter (which corresponds to a_{2i} in Figure 3-3), w_c is the coil width, and t_b is the bobbin flange height. Setting Eq.3-14 equal to Eq.3-15 results in a quadratic equation in t_a for which the meaningful positive solution is:

$$t_a = 0.5\left(-(w_c + h) + \sqrt{0.5D_p^2 - (w_c + h)^2}\right) \tag{3-17}$$

With D_p constant, Eq.3-17 is solved for a variety of coil widths w_c and for a constant valve gap h. The term w_c was calculated as the multiple of the coil diameter for 24-gauge copper wire (diameter = 0.516mm) with the number of coil wraps. Thus a '10 wrap' coil corresponds to a width of 10×0.516mm. Setting Eq.3-14 equal to Eq.3-16 gives the bobbin flange height t_b as follows:

$$t_b = 0.5t_a \tag{3-18}$$

From Figure 3-1(b), it can be seen that the active valve length l_a is thus:

$$l_a = 2t_b = t_a \tag{3-19}$$

An ideal valve would have a fully active length thus it becomes useful to define a dimensionless valve length δ:

$$\delta = l_a/l \ (0 < \delta < 1) \tag{3-20}$$

where l is the total length of the valve (which is constrained to a fixed value), and $\delta = 1$ represents the ideal case. Finally the coil height h_c is given by:

$$h_c = l - l_a \tag{3-21}$$

To calculate the number of turns N, the value of h_c was rounded down to the nearest multiple of the coil diameter. This height in coil diameters was then multiplied by the wrap number to give an approximate value for N.

Through inspection of Eq.3-17, it can be observed how the bobbin core radius, and hence the active valve length (Eq.3-19), are independent of the total valve length. Thus for a fixed valve length, the packaging constraint on diameter may result in low dimensionless valve lengths, and hence performance could suffer. One method to overcome this constraint is to size a valve with a reduced length and then to stack identical valves together such that the total length remains unchanged. The geometry of an individual valve is then formulated for a valve of length:

$$l = l_t/n \tag{3-22}$$

where l_t is the constrained total length of the stacked valve and n is the number of individual valves (or stage number). This is shown schematically in Figure 3-6 for n = 1 to n = 2. Note that the wire in each adjacent coil must be wound in opposite directions to ensure the correct direction of magnetic flux.

3.5.2 Performance

An efficient MR valve will be able to achieve the maximum fluid yield stress without saturation of the magnetic circuit and without exceeding the maximum operating current of the solenoid wire. To assess the above requirements, an analytical methodology is developed, which proves to be relatively straightforward due to the equal critical areas of the valve. This method allows the optimal valve geometry to be rapidly and efficiently determined in a spreadsheet. This approach differed from that used by

Rosenfeld and Wereley [123], who resorted to a more complex and time-consuming finite element analysis (FEA). In the present study, FEA will be used to later validate the analytical approach. The analytical methodology mentioned above, and some important performance indicators are now derived.

First, the magnetic flux density B_f and the magnetic field strength H_f are specified according to the maximum fluid yield stress $\tau_{y_{max}}$. This information is obtained from the MR fluid manufacturer's data sheets. Next, the required magnetic flux in the fluid ϕ_f was calculated as:

$$\phi_f = B_f A_f \tag{3-23}$$

where $A_f (= \pi d t_b)$ is the pole area of the fluid. Using the principal of continuity of flux, the flux density in the valve material B_s was determined as:

$$B_s = \frac{\phi_s}{A_s} = \frac{\phi_f}{A_s} = \frac{B_f A_f}{A_1} \tag{3-24}$$

where ϕ_s and A_s are the flux and pole area of the valve carrier material respectively. Also, A_1 is the bobbin core cross-sectional area (Eq.3-14), which is equal to A_2 and A_3 (Equations 3-15 and 3-16). The carrier material was assumed to be mild steel due to its high magnetic permeability and good saturation properties. The magnetic circuit can be considered capable of achieving the maximum fluid yield stress if $B_s < 1.3$T, which approximately corresponds to the saturation level of the steel. Next, the current I required to generate the magnetic field is determined using Kirchhoff's law. This should not exceed 2.5A, which is a reasonable maximum current for 24-gauge copper wire [123] and is given by:

$$I = (H_s L_s + H_f 2h)/N \tag{3-25}$$

where N is the number of turns (as calculated in Section 3.5.1), H_s is the magnetic field strength in the steel, and L_s and $2h$ are the length of the flux path in the steel and fluid respectively. The term H_s was readily determined using a B-H curve for 1018 steel. The parameter L_s is not as straightforward to calculate and was approximated as the distance around the centre of each steel section.

Another important performance indicator is the power p required to generate the maximum fluid yield stress, which was determined as follows:

$$p = nI^2 R_c = \frac{nI^2 \sigma l_c}{A_c} \tag{3-26}$$

where R_c is the resistance of the coil, σ is the resistivity of copper (1.72×10^{-8} Ωm), l_c is the total length of wire (estimated by summing the circumferential length for each turn), and A_c is the cross-sectional area of the wire. Also, it is noteworthy that for a multi-stage design (n >1), Eq.3-26 holds regardless of whether the valve windings are arranged in series or in parallel.

The time constant was calculated using the analogy of a resistance and inductance in series:

$$\tau = \frac{L_c}{R_c} = \frac{N\phi}{IR_c} = \frac{N\phi A_c}{I\sigma l_c} \tag{3-27}$$

where L_c is the circuit inductance and ϕ ($=\phi_s=\phi_f$) is the magnetic flux.

Valve controllability was characterised in terms of a control ratio λ, which is defined as follows:

$$\lambda = \frac{\Delta P_{max}}{\Delta P_0} \quad (\lambda > 1) \tag{3-28}$$

Here, ΔP_{max} is the maximum-field pressure drop (at $\tau_{y_{max}}$), and ΔP_0 is the zero-field pressure drop i.e. where the entire valve length is inactive. The term ΔP_{max} was calculated using Eq.3-6 by summing the pressures across the active and inactive (τ_y = 0kPa) regions of the valve.

Reynolds number *Re* was also used as a performance indicator. This is important as the MR effect is strongly dependent on laminar flow, and previous research has suggested that turbulent flow regimes could reduce device performance [124]. For an MR landing gear, the onset of turbulence is more probable due to the associated higher velocities during impacts. Valve Reynolds number was therefore calculated using the parallel plate approximation as follows:

$$Re = \frac{\rho_{MR} Q}{\mu b} \tag{3-29}$$

where ρ_{MR} is the density of MR fluid, and b ($=\pi d$) is mean annular circumference. For flow to remain laminar, *Re* must remain below the critical value Re_c. However, an uncertainly arises as MR fluids are non-Newtonian and Re_c for such fluids is unknown. As an approximate benchmark, the critical value for Newtonian flow between parallel flat plates was assumed. By using the hydraulic mean diameter and by assuming a critical value of 2000 for pipe flow, this can be approximated as $Re_c = 1000$.

3.6 MR landing gears for lightweight aircraft

In what follows, the design methodology outlined in Figure 3-2 is applied to a real aircraft using the numerical tools described in Sections 3.3-3.5. Here, the aim is to size

an MR nose landing gear for the Polish Institute of Aviation's I-23, which is a lightweight personal/business aircraft. With reference to Figure 3-2, the results in this section are organised as follows. First, the landing gear system is defined, along with the corresponding parameter values required by the numerical tools. To validate this system, simulations of the existing passive landing gear are performed and compared to experimental drop test results. Next, a preliminary design study is presented in order to calculate the desirable MR valve performance [ΔP_{max}, Q_{max}]. This desirable performance is then used to calculate the 'optimal' valve size, which fully considers the constraints of the magnetic circuit. FEA is also used to validate the magnetically optimised design and hence the sizing methodology. Finally, the impact performance of the optimal design is investigated.

3.6.1 Parameter definition and validation

To begin the design process, experimental drop test data from a worst-case impact on the I-23 landing gear was provided by the Polish Institute of Aviation [125]. The Institute's test facility is shown in Figure 3-7, which has the capability of simulating aircraft lift forces using pneumatic actuators as well as wheel acceleration forces by applying an initial wheel angular velocity. However, experiments were performed without initial wheel spin-up in order to permit direct comparisons with the model. To generate the worst-case impact, a drop mass corresponding to maximum payload, and the worst-case sink velocity was used. An equivalent model of this drop test was then developed using the numerical approach described in Sections 3.3 and 3.4.

Table 3-1 lists the parameters used to construct the equivalent model. With reference to Figure 3-8, the shock strut model parameters P_{a0}, v_{a0}, v_{10}, v_{20}, a_{2i}, and a_{2o} correspond to

the actual I-23 nose gear values. The gas constant m was estimated as 1.1, which is a good approximation when the fluid and gas volumes are mixed [101]. With regards to the impact model (Figure 3-5), the parameters m_p, m_w, L, and V_{sink} correspond to the experimental drop test conditions. The tyre law constants c and r (Eq.3-11) were determined by curve fitting to the compression phase of the tyre response from an impact test. This is illustrated in Figure 3-9, where the displacement of the dropped mass has been subtracted from the shock strut deflection and plotted against the measured tyre force. As shown, acceptable correlation is achieved during compression of the tyre.

In order to validate the landing impact model, a passive simulation was performed (by replacing Eq.3-6 with Eq.3-8) and compared to the worst-case experimental drop test data. The result is presented in Figure 3-10, which shows the force/time and force/displacement responses for two values of discharge coefficient. For $C_d = 0.52$ the model accounts well for observed behaviour, particularly in terms of impact duration and maximum deflection. The simulated peak force is overestimated, although this could be due to errors and/or a variation in the lift force during the experiment. Furthermore, the discharge coefficient is lower than the nominal value of 0.6 for a sharp edged orifice, although this could be explained by the larger pressure loss due to friction in the 5mm long valve (see Figure 3-8). In other words, the "sharp edged" orifice assumption is not valid. A variable discharge coefficient may also contribute to this inaccuracy. It can also be observed that the reduction in force with displacement during the rebound phase does not correlate well with the experimental data. This is because the model does not account for the effect of the recoil orifices (shown schematically in Figure 3-8), which is a secondary issue at this stage of the design and is outside the

scope of the present study. A final point from Figure 3-10 is that the point where the shock force becomes negative represents the tyre leaving the ground. Beyond this point, the model is invalid. In conclusion, the overall correlation shown in Figure 3-10 is good and the landing impact model was considered to be of sufficient accuracy during the compression phase to be used as a tool for investigating the performance of the MR device.

Before presenting the MR landing impact and sizing results, the MR fluid properties must be defined. Experimental validation of these properties is dealt with in Chapter 4. In the present chapter, properties for Fraunhofer's AD57 MR fluid were assumed [126], and of key importance are the bulk modulus, yield stress, and viscosity. The bulk modulus of MR fluid is unknown, but the base value for a standard hydraulic oil (β = 1.7GPa [127]) serves as a reasonable approximation. The viscosity and yield stress were calculated from the fluid manufacturer's data, which is shown in Figure 3-11. With reference to Figure 3-11(a), the viscosity was estimated as 0.1Pas. This is an extrapolated value as the shear rates in a flow mode device may be two to three orders of magnitude greater than that shown in Figure 3-11(a). In terms of Reynolds number, this is a conservative estimate (Reynolds number is inversely proportional to the viscosity). From Figure 3-11(b), the maximum fluid yield stress $\tau_{y_{max}}$ was taken as 55kPa, which is generated at a flux density of 0.7T and at a magnetic field strength of 236kA/m (Figure 3-11(c)). The above properties are summarised in Table 3-2. The MR fluid's density ρ_{MR} is also given, which was used to calculate the Reynolds number (Eq.3-29) and the mass of the fluid.

3.6.2 Preliminary MR design

As shown in Figure 3-2, the first stage of the design process is to determine a desirable valve performance (Steps 'A' to 'E'). This is achieved by calculating the MR valve geometry without a detailed consideration of the magnetic circuit. The MR shock strut design considered in this study is that shown in Figure 3-3, where the existing passive orifice (Figure 3-8) has been replaced with an MR valve. With reference to Figure 3-1(b), the total length l_t and diameter D_p of the MR valve are 45mm and 36mm respectively, which correspond to the geometrical constraints of the existing passive device. The mean valve diameter d and the dimensionless valve length δ were chosen intuitively as 10mm and 0.5 respectively, giving an active valve length l_a equal to 22.5mm. The valve gap h is then determined using an iterative process by performing a worst-case landing impact simulation to achieve the desired performance at the maximum fluid yield stress ($\tau_{y_{max}} = 55$kPa).

Figure 3-12 presents the corresponding results, which shows the shock strut's force/time and force/displacement responses for a range of valve gap sizes. The worst-case experimental drop test data are also shown superimposed, which provides a useful performance benchmark. Clearly, $h = 0.5$mm results in large damping forces during the initial stage of the impact. For $h = 0.65$mm, damping levels are insufficient, and this results in large forces at the end of the impact due to excessive gas compression. The optimum response that provides the lowest peak force occurs when $h = 0.57$mm. Furthermore, it could be argued that this MR response is inherently superior to the passive system. For example, the fluctuation in force is less severe and maintains a more constant value throughout the impact. In other words, the MR response has a superior impact efficiency (Eq.2-1), which would provide an enhanced fatigue life for

the aircraft. This is a direct result of the Coulomb-viscous nature of the MR damping function, which provides large forces at low velocities. In contrast, the passive system has a quadratic damping function (Eq.3-8), which results in larger fluctuations in the overall shock strut force.

Referring to the design flowchart (Figure 3-2), the desirable valve performance was then determined as ΔP_{max} = 12.2MPa, which occurred at $Q_{max} = 2\times10^{-3}$ m^{3}s^{-1} during the optimum impact response (h = 0.57mm).

3.6.3 Optimal MR design

In what follows, a sizing study is presented that uses the magnetic circuit theory presented in Section 3.5 to optimise the internal valve geometry (Steps 'F' to 'I' in Figure 3-2). The key aims are as follows:

- To achieve the desirable valve performance [ΔP_{max}, Q_{max}] at the maximum yield stress.
- To achieve the maximum yield stress without saturation of the steel, and without exceeding the maximum current rating of the copper wire.
- To maximise the control ratio, and hence the range of impacts that can be optimally damped.

Figure 3-13 presents the performance results of each valve for wrap numbers between 4-16 and for stage numbers equal to 1 and 3. Where applicable, the results were calculated with the maximum flow rate from the preliminary design ($Q_{max} = 2\times10^{-3}$ m^{3}s^{-1}), and at the maximum yield stress $\tau_{y_{max}}$ = 55kPa. Furthermore, the

results are shown for two valve gap sizes - the preliminary valve gap size (h = 0.57mm), and h = 0.59mm, which transpires to be the optimal design, as will be illustrated in the following analysis.

First, Figure 3-13(a) plots the magnetic flux density that will result in the steel in order to generate maximum yield stress in the fluid. This is shown as a function of wrap number and since the critical area is independent of the total valve length (Equations 3-14 to 3-16), the results are independent of the stage number. The observed increase in magnetic flux density with wrap number is a direct result of the reduced steel cross-sections due to a larger coil. The saturation limit of the steel (1.3T) is also shown and is exceeded for valve geometries with a wrap number greater than 12. These geometries were therefore eliminated from the design process, as magnetic saturation could prevent the maximum fluid yield stress from being generated. Also, it is important to note how the magnetic flux density is independent of the valve gap size.

Figure 3-13(b) shows the control ratio for each valve configuration. Due to a larger coil size, and hence a smaller active valve length, the control ratio reduces with increasing wrap number. This result illustrates the key advantage of stacking geometrically similar valves together, where superior performance is achieved with increasing stage number. It can also be observed how the effect of the valve gap size h on the control ratio is fairly significant. This is because of the cubic influence of h on the pressure drop in the Buckingham equation (Eq.3-6).

The above results suggest that the optimum valve design must have a low wrap number and a high stage number. However, they fail to recognise the implications that such valve configurations have on the required current, which is now addressed in Figure

3-13(c). As shown, higher currents are associated with a decreasing wrap number and an increasing stage number, which is a result of the lower magneto-motive force that a smaller coil generates. As 2.5A was considered as the maximum safe operating current for the copper wire, this eliminated a 4-stage valve design (not shown in Figure 3-13(c)). The 3-stage-12-wrap design appears to provide the optimal configuration where superior control ratios are achieved with acceptable current levels. Furthermore, note how the valve gap size has no significant impact on the required current, and hence the optimal wrap and stage number.

A further advantage of a multi-valve configuration is a reduced time constant, which is observed in Figure 3-13(d) for increasing stage number and decreasing wrap number. Note that the reduction in time constant for large wrap numbers is due to saturation of the steel. Again, as with the previous performance indicators (except control ratio), the time constant is largely independent of the valve gap size.

Next, the Reynolds number (which is independent of stage number) is investigated in Figure 3-13(e). Clearly, the Reynolds number remains below the critical value at the maximum anticipated flow rate during the impact. This is a promising result and suggests that valve performance should not be inhibited by turbulent flow. Also, the valve gap size has a negligible influence on performance.

Using the above results, it can be deduced that a 3-stage-12-wrap valve provides the optimal configuration. However, obtaining the desired maximum field performance (ΔP_{max} = 12.2MPa) has so far been neglected, which is now addressed in Figure 3-13(f). As illustrated in the above results, the valve gap size h has no significant effect on the optimum wrap and stage number. Therefore, it is straightforward to tune h as a final

step in order to achieve the desired pressure drop. This is shown in Figure 3-13(f), where it can be observed that the optimum 3-stage-12-wrap valve correlates well with the desired performance when h is equal to 0.59mm.

The key geometrical parameters and performance indicators of the optimal 3-stage-12-wrap valve design are given in Table 3-3. In summary, this design maximises the dimensionless valve length (δ = 59%) and hence control ratio (λ = 2.26), without magnetic saturation ($B_s < 1.3T$), and without significantly exceeding the 2.5A rating of the copper wire. For example, the maximum yield stress is achieved at 2.6A, which could be sustained for short periods of time. Furthermore, this was found to require just 16.5W of power, and could be supplied by a low voltage source of 2.1V, or 6.3V, depending on whether the individual stages are wound in parallel or series. Also, the optimal design has a time constant of 19ms. In practice, if a current driver is used (the definition of time constant in Eq.3-27 assumes constant voltage) and the coils are arranged in parallel, the time constant will be lower than this [53]. Finally, Table 3-3 presents figures regarding the extra mass of the device. As the MR fluid is approximately four times denser than conventional hydraulic oil, the fluid is 0.8kg heavier. The mass of the MR valve is 0.4kg, which is not likely to be significantly heavier than the existing passive valve. Therefore, the additional mass of a single shock strut should not exceed one kilogram, which is approximately 0.2% of the distributed aircraft mass m_p (see Table 3-1)

To further clarify the performance of this optimised geometry, Figure 3-14 compares its quasi-steady pressure/flowrate characteristic with the preliminary valve design. Good correlation is observed, which suggests that the desired impact performance will be

achieved. Furthermore, it can be observed that the optimal valve has a slightly superior control ratio. This is a result of the conservative estimate of dimensionless valve length ($\delta = 50\%$) that was assumed in the preliminary sizing analysis.

3.6.4 FEA of the magnetic circuit

In order to validate the sizing methodology, an axisymmetric FEA of the optimal valve geometry (see Table 3-3) was performed. This was investigated using the software package FEMM [128], and in order to model the magnetic characteristics of the MR fluid, the fluid manufacturer's B_f/H_f data (Figure 3-11(c)) was used in the simulation.

Figure 3-15(a) shows the flux density contour plot from this analysis. This corresponds to a current of 2.6A (as determined in Section 3.6.3), where the aim is to achieve a fluid flux density of 0.7T across the active valve gap (therefore achieving the maximum fluid yield stress). The distribution of flux density is highly uniform within the critical valve areas, and the circuit remains unsaturated as expected.

Figure 3-15(b) plots the variation of the fluid flux density normal to the valve gap, as a function of the distance 'X' along the mean valve diameter (as indicated on Figure 3-15(a)). As shown, the flux density across the active valve gap adjacent to the MR fluid is approximately 0.65T, which is 7% lower than the desired value. This is due to flux leakage into the bulk of the MR fluid at the valve entry/exit, which is observed in Figure 3-15(a). In contrast, the flux density in the active lengths constructed from two adjacent valves is observed to be 0.7T as desired (Figure 3-15(b)).

The above finite element analysis validates the analytical magnetic circuit analysis presented in Section 3.6.3. Ideally, the analytical approach should be updated to

account for flux leakage, but this is likely to have no significant influence on the optimised geometry and performance, especially for a multiple-stage design.

3.6.5 MR landing gear impact performance

In the following discussion, the optimal valve geometry is investigated within the aircraft landing gear impact simulation. It is assumed that the full MR fluid yield stress range can be generated, which is a valid assumption after consideration of the FEA results in the previous section.

First, Figure 3-16 presents the worst-case landing impact results, which is compared to the experimental (passive) data, and to the preliminary valve's performance. As shown, the desired performance is still maintained, and no further refinements to the valve design are necessary. This demonstrates the robustness of the proposed design methodology.

Next, the effect of fluid compressibility on the MR landing impact response is investigated in Figure 3-17. Here, the worst case landing impact response is shown for a range of bulk moduli, which represent different amounts of entrapped air within the fluid. As seen, the effect of reducing the bulk modulus is to reduce the damping force and increase the maximum deflection. This is because fluid compression prevents valve flow, and such effects are likely to be of particular importance when investigating control. For example, Figure 3-17(a) illustrates a slight change in the rate of increase in force with reduced bulk modulus. This effect could contribute significantly to the total device time constant where fluid compression is preventing valve flow and hence controllability. Experimental validation is required to get a better indication of typical bulk modulus values, which is dealt with in Chapter 4.

Finally, to illustrate the controllability of the optimised design, Figure 3-18 presents the impact responses of the shock strut with less severe input conditions. The results are shown in open-loop control i.e. where the yield stress is maintained constant throughout the impact. In Figure 3-18, results for two different input excitations are shown. The 'soft impact' uses the original drop mass (see Table 3-1), but lowers the sink velocity to the minimum anticipated value: V_{sink} = 1m/s. The 'very soft impact' also has a sink velocity of 1m/s, but simulates a drop mass of just 284kg, which is 60% of the original (maximum) value.

For the soft impact, it can be observed that lowering the yield stress from 55kPa (the maximum value) to 6kPa, best minimises the force during the impact. Furthermore, the maximum yield stress response is a good indicator of the wide range of controllable force that is available. As before, the MR impact response is inherently efficient without the need for closed-loop control.

For the very soft impact, the control limits of the design can be observed. For example, it could be argued that the damping provided by the base viscosity of the fluid (τ_y = 0kPa), results in damping forces that are slightly high during the initial stages of the impact. This is best observed in Figure 3-18(b), where it can be observed that the forces at the end of the impact are lower. Nonetheless, the impact efficiency is still good.

To summarise, the feasibility of incorporating MR landing gears onto lightweight aircraft has been demonstrated. For example, highly controllable and reasonably lightweight devices can be designed that accommodate a wide range of landing impacts. The next step is to investigate the scalability of MR landing gears by performing similar sizing studies for large-scale aircraft.

3.7 MR landing gears for large-scale aircraft

The following case studies focus on two different landing gear shock struts produced by Messier Dowty. The first sizes an MR device for a telescopic landing gear, where the shock strut displacement is equal to the relative displacement between the airframe and wheel (Figure 2-12(a)). In the second case study, the design of an MR shock strut for a levered configuration is investigated. Here, the relative displacement between the airframe and wheel is greater than the shock strut displacement (Figure 2-12 (b)).

3.7.1 Large-scale telescopic (LST) landing gear

The aim of this study is to size and optimise the performance of an MR valve for a large-scale telescopic or LST landing gear. To recap, the sizing approach (Figure 3-2) aims to achieve an acceptable worst-case landing impact performance in the maximum fluid yield stress condition. Consequently, lower damping levels are available for less severe impacts. Furthermore, by maximising the device control ratio i.e. the ratio of pressures between the maximum-field and zero-field conditions, the range of impacts that could be optimally damped is maximised.

An existing LST landing gear and an equivalent MR shock strut are shown schematically in Figure 3-19. Here, the MR valve is constrained to the existing internal diameter of the passive device (D_p = 111mm), and a constraint of 100mm was placed on the valve length l_t. Furthermore, extra fluid passages must be included to prevent the formation of a vacuum between the piston rod and the outer cylinder.

To aid formulation of a realistic landing impact model, actual aircraft data was provided by Messier-Dowty [103]. The model parameters used in the analysis are given in Table 3-4. Here, the aircraft lift force was assumed to be equal to the aircraft weight, which is

normal for large-scale aircraft [101]. Values were also assumed for the wheel mass, and the parameters used in the tyre deflection law. For the shock strut model, the gas law parameters were chosen to give an equivalent spring force F_g to the existing passive strut. The corresponding gas law is shown in Figure 3-20. Note that the modelling complexities associated with the existing orifices and metering pin (see Figure 3-19(a)) meant that a passive shock strut model was not developed for this study.

After using the landing impact model to calculate the desirable MR valve performance (steps A-E in Figure 3-2), the magnetic circuit design and device controllability were optimised (steps F-G). The corresponding geometry and performance of the optimised designs are given in Table 3-5. Here, two different MR fluids were used to optimise the valve (Fraunhofer's AD57 and AD275 [126]), and the reasons for this will become clear in the following discussion.

The optimal configuration with AD57 MR fluid has a single valve stage, and a good control ratio (λ = 2.05 at $\tau_{y_{max}}$, Q_{max}). Furthermore, the maximum yield stress can be achieved without saturation of the steel (B_s = 0.81T < 1.3T), and without exceeding the maximum current of the copper wire (I = 2.28A < 2.5A). Vitally, the desirable MR valve performance is close to being achieved, thus an acceptable worst-case impact performance should result. However, the maximum Reynolds number is about 3.6 times greater than the critical value, which could cause performance to suffer. An effective way to overcome this is to use an MR fluid with a higher off-state viscosity. However, this higher viscosity may cause the control ratio to suffer due to the larger off-state force.

Fraunhofer's AD275 is an MR fluid with a larger viscosity. This is illustrated in Figure 3-21(a), and can partly be explained by the slightly higher volume fraction of iron particles (AD57 = 35% and AD275 = 36%). As a consequence of this larger iron content, AD275 also has a higher maximum fluid yield stress equal to 65kPa (Figure 3-21(b)). This larger viscosity and yield stress is an effective combination as it permits a new MR valve to be sized with a lower Reynolds number (due to the larger viscosity), but without significantly affecting the control ratio (due to the larger yield stress). This result is illustrated in Table 3-5, which also presents the optimal valve configuration with AD275 MR fluid. Here, a viscosity of 0.2Pas was assumed, which is an extrapolated estimate from the viscosity/shear stress response in Figure 3-21(a). Also a slightly higher fluid density of 3570kgm^{-3} was used due to the higher iron content. As shown, the maximum Reynolds number has been reduced by a factor of 1.9, whilst the control ratio is only 4% lower than the design with AD57 fluid. Although the Reynolds number is still nearly twice the critical value, this serves as a useful example to illustrate how higher viscosity/higher yield stress fluids could be exploited in devices to maintain the Reynolds number within laminar values.

The other important performance indicators are the maximum power, time constant and the increased mass, which are fairly similar for both designs. Focusing on the AD275 design, the maximum power requirement is 56W, which could be supplied by a voltage source of 15V, or 30V, depending on whether the individual stages are wound in parallel or series. The time constant of the magnetic circuit is quite large (74ms), but the use of a current driver would improve this. The extra mass of fluid Δm_f (compared to the passive device) is approximately 16.7kg. When combined with the mass of the valve, the total extra mass of a single shock strut will be around 22kg, which includes a

2kg deduction for the mass of the existing passive valve and metering pin. Although this is just 0.2% of the distributed mass, this is a notable increase that could render the solution as unviable. However, it is feasible that an enhanced fatigue life will result in weight savings for other aircraft components. Furthermore, it is possible that the overall diameter of the shock strut could be reduced, thus lowering the extra fluid mass. This design would also benefit from a lower maximum Reynolds number due to a smaller piston area. However, the pressure drop required to produce an equivalent damping force F_h would be increased, which could result in a larger wall thickness and hence additional mass. Fluid compressibility effects would also be amplified, and the sealing efficiency could be degraded. A more detailed analysis of this kind of device is outside the scope of the present study, and requires further investigation.

To better illustrate the performance of the optimised design, the worst-case landing impact response for the valve designed with AD275 MR fluid is shown in Figure 3-22. Here, the sink velocity was set to 3.66m/s, and the yield stress is at its maximum level (τ_y = 65kPa). Furthermore, Figure 3-22(b) presents the corresponding experimental force/displacement response. As expected, the performance of the optimised MR shock struts is good i.e. the peak force is minimised, and thus the impact efficiency is maximised. In comparison with the experimental data, the impact efficiency is superior for the MR design, in spite of the use of a metering pin in the passive device (see Figure 3-19(a)). This inherent open-loop efficiency of the MR design could be particularly beneficial for large-scale devices, which have larger time constants. For example, closed-loop control may not be required and thus the magnitude of the time constant is less crucial.

Figure 3-23 presents the numerical landing impact performances with less severe input conditions. Here, V_{sink} = 2ms^{-1}, and the aim is to lower the MR fluid yield stress such that the peak force is minimised. As shown, an efficient impact response is provided when τ_y = 3kPa, which provides further scope to optimise even less severe landings.

3.7.2 Large-scale levered (LSL) landing gear

The following investigation represents an interesting addition to the previous case study, as the levered configuration will provide lower piston velocities. The existing shock strut design and an equivalent MR device is illustrated in Figure 3-24. As shown, the diametrical constraint on the MR valve was 133mm, and the constraint on piston length was 50mm.

Again, the aim of this study is to maximise the device control ratio whilst generating a desirable pressure drop ΔP_{max} at $Q_{max}, \tau_{y_{max}}$. However, the available landing gear data did not permit determination of the desirable performance in the usual manner i.e. using impact simulations. Instead, information about the maximum permissible shock strut forces was used to size the device as follows.

First, the maximum piston velocity V_{max} (and hence Q_{max}) was calculated using experimental data from a worst-case impact on the LSL landing gear. With reference to Figure 3-25(a), which illustrates a typical velocity/displacement response, this was determined as 1.26ms^{-1} for a sink velocity of 3ms^{-1}. Next, data describing the maximum permissible shock strut forces was used to calculate the damping requirement $F_{h_{max}}$ at this velocity. This is illustrated in Figure 3-25(b), which shows the maximum permissible shock strut force as a function of displacement. As the forces due to

friction and gas compression are also superimposed, the maximum damping force can be determined. With reference to Figure 3-25(a), the maximum piston velocity occurs at the displacement $D_{v_{max}}$ = 30mm. Thus from Figure 3-25(b), the maximum damping requirement $F_{h_{max}}$ was determined as 300kN.

The next step is to determine the maximum pressure drop ΔP_{max} that corresponds to $F_{h_{max}}$. This was readily calculated as 21.6MPa using a pressure/area balance on the shock strut. Finally, the magnetic circuit sizing methodology (Section 3.5) was used to determine the optimal valve geometry that generates this desired performance at Q_{max}, $\tau_{y_{max}}$. In this study, properties for AD275 MR fluid were used ($\tau_{y_{max}}$ = 65kPa, μ = 0.2Pas), as they were previously shown to provide a superior Reynolds number performance without significant detriment to the control ratio.

Note that the above methodology will not be as accurate as that used in the previous I-23 and LST case studies, where preliminary impact simulations were used to determine the desired performance. This is because it does not fully consider the non-linear interaction between fluid compressibility, tyre deflection and the shock strut's gas compression. Furthermore, due to the inherent differences in damping behaviour between the passive and MR landing gear, the maximum piston velocity in the MR device is likely to differ from that in Figure 3-25. Nonetheless, the above methodology will provide good ballpark results, and will enable a useful assessment of feasibility.

The geometry and performance of the optimised MR valve is given in Table 3-5. As shown, this is a single stage design, and the maximum fluid yield stress can be achieved without exceeding the current rating of the wire, and without magnetic saturation.

Furthermore, the maximum power requirement (25W) could be readily supplied from a 10V source. With $h = 0.82$mm, the desired valve pressure drop of 21.6MPa is achieved, thus an acceptable worst-case landing impact performance should result. Furthermore, the control ratio is reasonably high ($\lambda = 1.81$), thus accommodating a large range of impacts.

The most significant difference with the previous LST design is the maximum Reynolds number, which remains sub-critical. This is a result of the lower piston velocities associated with the levered design, which outweigh the increase in piston diameter (and hence force) that is required to absorb an equivalent amount of energy. Thus it could be argued that MR landing gears for large-scale aircraft are particularly suited to levered configurations.

3.8 Summary of Chapter 3

In this chapter, a sizing methodology was developed for MR landing gear shock struts. Using packaging requirements as a key constraint, the sizing methodology maximised the device's control ratio, whilst accommodating for a worst-case impact. Consequently, the semi-active landing gear can produce desirable behaviour for a wide range of impact conditions, unlike a passive device.

A 2DOF landing impact model, and a valve size optimisation tool were developed to implement the design methodology. The impact model was designed to be equivalent to existing landing gear drop tests, which permitted accurate design assessments. Furthermore, the model accounted for fluid compressibility. This is important when considering device control, especially under impulsive loading. The valve sizing methodology included an analytical assessment of the magnetic circuit, which was

formulated in a spreadsheet. This permitted the fast and efficient determination of the optimised geometry, which was validated using a finite element analysis.

To illustrate the proposed design methodology, three case studies were presented – one for lightweight aircraft and two for large-scale aircraft with different landing gear configurations (one telescopic and one levered). The methodology proved to be very robust, where the desired worst-case impact performance of the magnetically optimised valves was accurately achieved. Moreover, widely adjustable valve control ratios resulted in damping levels that could accommodate a large range of impact conditions. Therefore, when combined with an appropriate control strategy, the optimised designs should demonstrate significant advantages over passive systems. Even in open-loop control (i.e. constant yield stress), it was shown that the MR effect provides an inherently superior damping performance over conventional passive orifices. For example, the impact efficiency, and hence the severity of fatigue loading was significantly improved. This could be particularly beneficial for large-scale landing gears, which suffer from larger time constants.

A key issue that arose for large-scale telescopic landing gears was the excessive valve Reynolds number, which could cause performance to suffer. To overcome this, it was shown how MR fluids with larger viscosities and yield strengths could be used to lower the Reynolds number, without significant detriment to the control ratio. Furthermore, it was shown that levered configurations are particularly advantageous, where the lower piston velocities provide an inherently low Reynolds number. Smaller piston areas could also be used, although the effect of this on the structural integrity, sealing efficiency, and fluid compressibility would require investigation.

MR landing gears will inevitably weigh more than their passive counterparts because of the high fluid density. For example, for both small and large-scale aircraft, the extra mass of an MR shock strut was approximately 0.2% of the distributed mass. However, an enhanced fatigue life should provide weight savings for other aircraft components.

Feasibility will also be dependent on fail-safety, which was not directly considered in this study i.e. in the event of a power failure, and the subsequent loss of the MR effect, the landing gear must provide acceptable damping performance during a worst-case landing. A novel solution might incorporate a permanent magnet within the MR valve [129], which could be designed by updating the numerical sizing tools presented in this chapter.

In conclusion, this chapter has made an important first step to help demonstrate the feasibility of MR landing gears for small and large-scale aircraft. However, the results were based on a time-domain model that has assumed values for certain parameters. Consequently, the model needs validating, and this will be addressed in Chapter 4.

	Parameter	Symbol/unit	Value
Shock strut	Initial gas pressure	P_{a0} /bar	9.5
	Initial gas volume	v_{a0} /cm^3	170
	Initial fluid volume of chamber 1	v_{10} /cm^3	201
	Initial fluid volume of chamber 2	v_{20} /cm^3	132
	Inner area of the inner cylinder	a_{2i}/cm^2	10.18
	Outer area of the inner cylinder	a_{2o}/cm^2	13.85
	Diameter of the existing main orifice	d_p/mm	4.8
	Length of the existing main orifice	l_p/mm	5
	Gas constant	m/-	1.1
Impact	Distributed aircraft mass	m_p/kg	473
	Mass of wheel/tyre assembly	m_w/kg	4.7
	Lift force	L/N	3120
	Sink velocity	V_{sink}/ ms^{-1}	2.43
	Tyre constant	c/-	8×10^6
	Tyre exponent	r/-	2.26

Table 3-1: Landing impact model parameters for the I-23 nose gear.

Parameter	Symbol/unit	Value
Maximum yield stress	$\tau_{y_{max}}$ /kPa	55
Flux density at $\tau_{y_{max}}$	B_f/T	0.7
Magnetic field strength at $\tau_{y_{max}}$	H_f/kAm^{-1}	236
Bulk modulus	β/GPa	1.7
Viscosity	μ/Pas	0.1
Density	ρ_{MR}/kgm^{-3}	3290

Table 3-2: Properties for AD57 MR fluid [126].

	Parameter	Symbol/unit	Value
Geometry	Total constrained length of valve stack	l_t /mm	45
	Constrained valve diameter	D_p /mm	36
	Stage number	n/-	3
	Coil width	w_c/mm	6.19
	Valve gap height	h /mm	0.59
	Bobbin core radius	t_a /mm	8.88
	Flange height	t_b /mm	4.44
	Mean valve diameter	d /mm	30.72
	Dimensionless valve length	δ/-	0.59
	Number of turns of gauge-24 wire	N/-	132
Performance	Flux density in the steel at $\tau_{y_{max}}$	B_S /T	1.2
	Current to achieve $\tau_{y_{max}}$	I /A	2.6
	Power to achieve $\tau_{y_{max}}$	P/W	16.5
	Desired MR valve pressure drop	ΔP_{max}/MPa	12.2
	Maximum pressure drop at $\tau_{y_{max}}$, Q_{max}	ΔP /MPa	12.3
	Control ratio at $\tau_{y_{max}}$, Q_{max}	λ/-	2.26
	Reynolds number at Q_{max}	Re/-	680
	Time constant	τ /ms	19
	Mass of valve	m_v /kg	0.4
	Extra mass of fluid	Δm_f/kg	0.8

Table 3-3: Geometry and key performance indicators of the optimised I-23 valve

	Parameter	Symbol/Unit	Value
Impact	Distributed aircraft mass	m_p/kg	12790
	Mass of wheel and tyre assembly	m_w/kg	30
	Lift force	L/kN	125.8
	Tyre constant	c/-	16×10^6
	Tyre exponent	r/-	2.26
Shock strut	Initial gas pressure	P_{a0} /bar	19
	Initial gas volume	v_{a0} /cm^3	3494
	Piston rod area/reference area	a_{1o}/cm^2	77.24
	Piston head area	a_{2i}/cm^2	96.77
	Polytropic exponent	m/-	1.2

Table 3-4: Parameters used in the LST landing gear impact model.

	Parameter	Symbol/unit	LANDING GEAR/FLUID LST/ AD57	LST/ AD275	LSL/ AD275
Geometry	Total constrained length of valve stack	l_t /mm	100	100	50
	Constrained valve diameter	D_p /mm	111	111	133
	Stage number	n/-	2	2	1
	Coil width	w_c/mm	5.16	6.19	8.26
	Valve gap height	h /mm	1.12	1.38	0.82
	Bobbin core radius	t_a /mm	35.97	35.26	42.27
	Flange height	t_b /mm	17.98	17.63	21.13
	Mean valve diameter	d /mm	83.38	84.3	101.86
	Dimensionless valve length	δ/-	0.72	0.71	0.85
	Number of turns of gauge-24 wire	N/-	270	336	224
Performance	Flux density in the steel at $\tau_{y_{max}}$	B_S /T	0.81	0.84	0.84
	Current to achieve $\tau_{y_{max}}$	I /A	2.28	2.21	2.16
	Power to achieve $\tau_{y_{max}}$	P/W	56	65	25
	Maximum flowrate	Q_{max}/ m^3s^{-1}	0.0291	0.0291	-
	Desired MR valve pressure drop	ΔP_{max}/MPa	19.3	19.3	21.6
	Maximum pressure drop at $\tau_{y_{max}}$, Q_{max}	ΔP /MPa	19.4	19.4	21.6
	Control ratio at $\tau_{y_{max}}$, Q_{max}	λ/-	2.05	1.94	1.81
	Reynolds number at Q_{max}	Re/-	3644	1955	976
	Time constant	τ/ms	72	74	91
	Mass of valve	m_v /kg	7.7	7.7	5.5
	Extra mass of fluid	Δm_f/kg	15	16.7	unspecified

Table 3-5: Geometry and performance of the optimised large-scale landing gear designs.

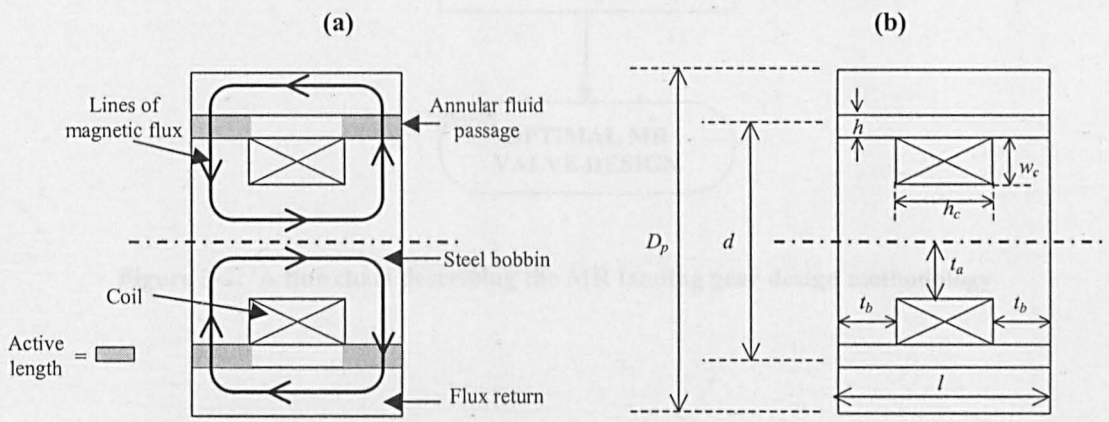

Figure 3-1: A flow mode MR valve. (a) Valve configuration and (b) valve nomenclature.

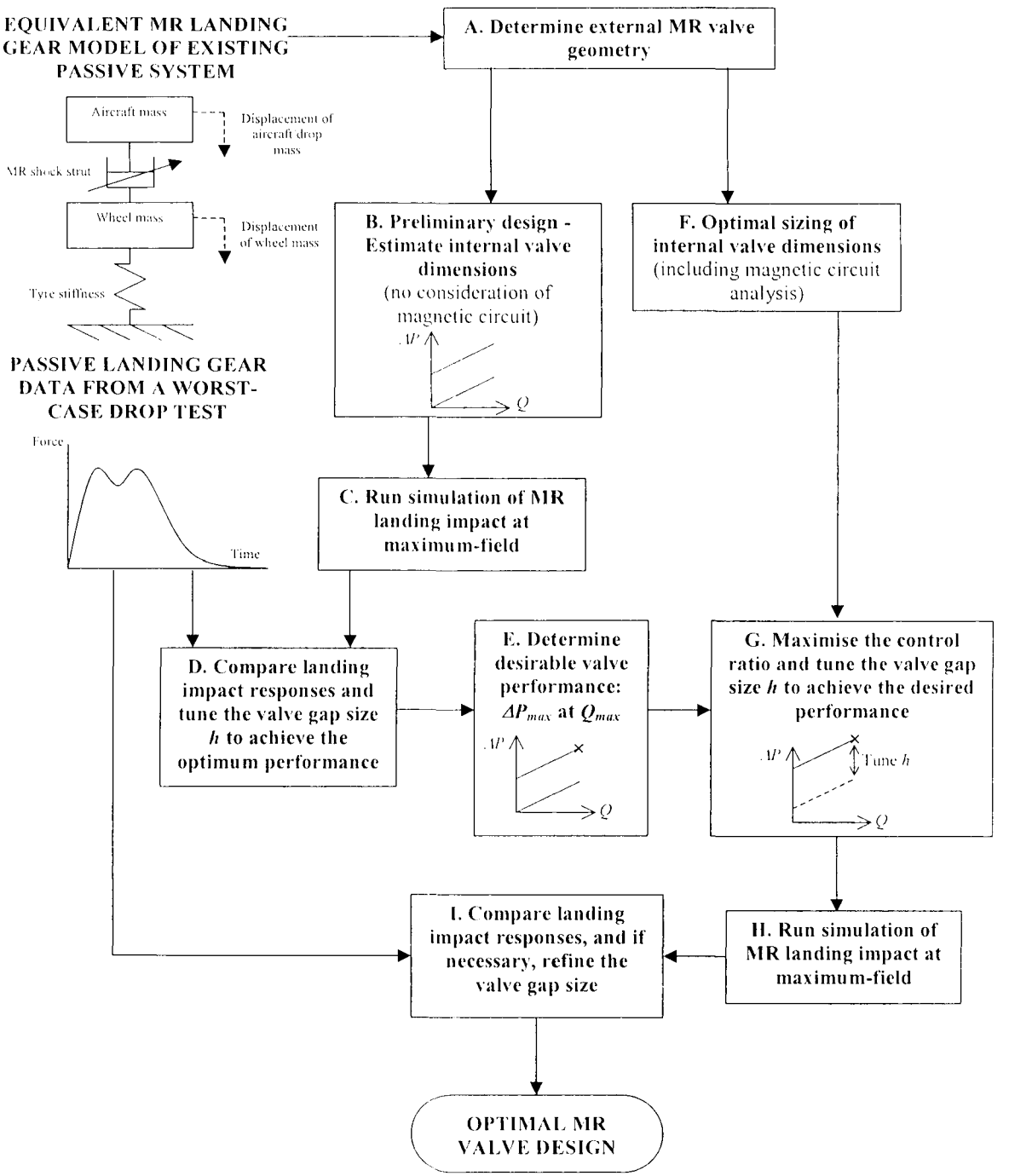

Figure 3-2: A flowchart describing the MR landing gear design methodology

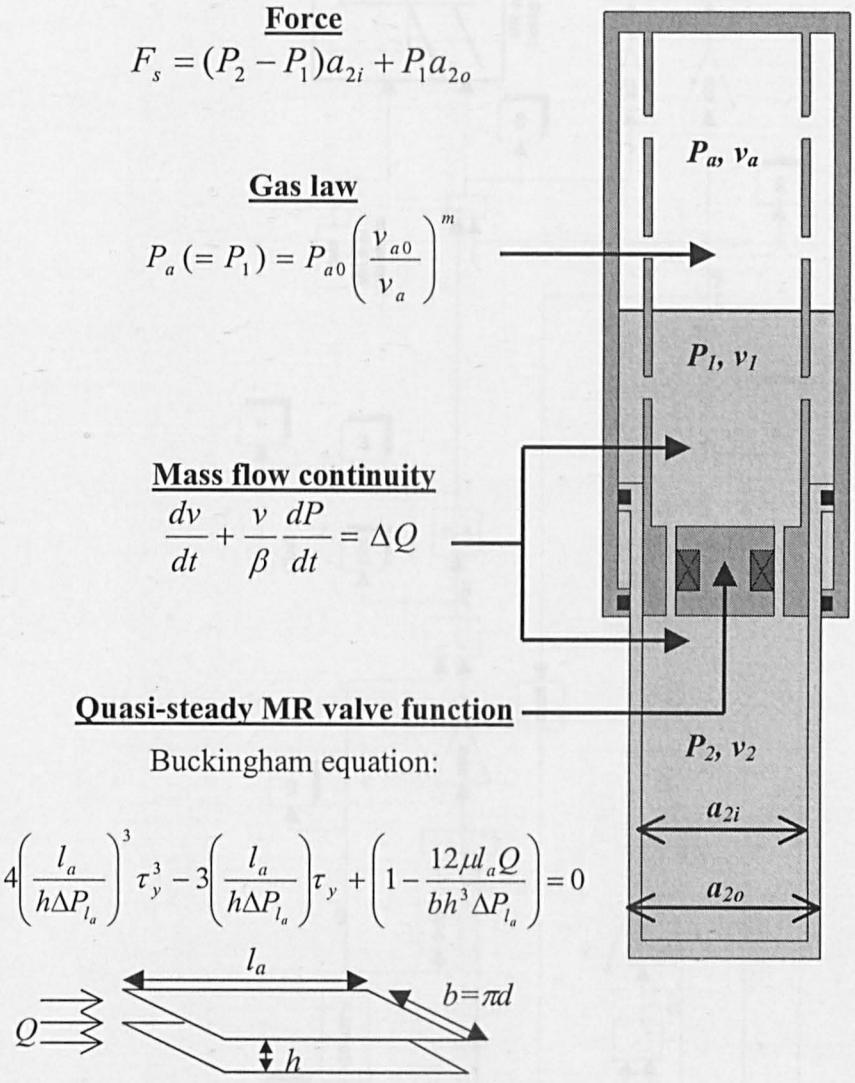

Figure 3-3: Summary of the dynamic MR shock strut model

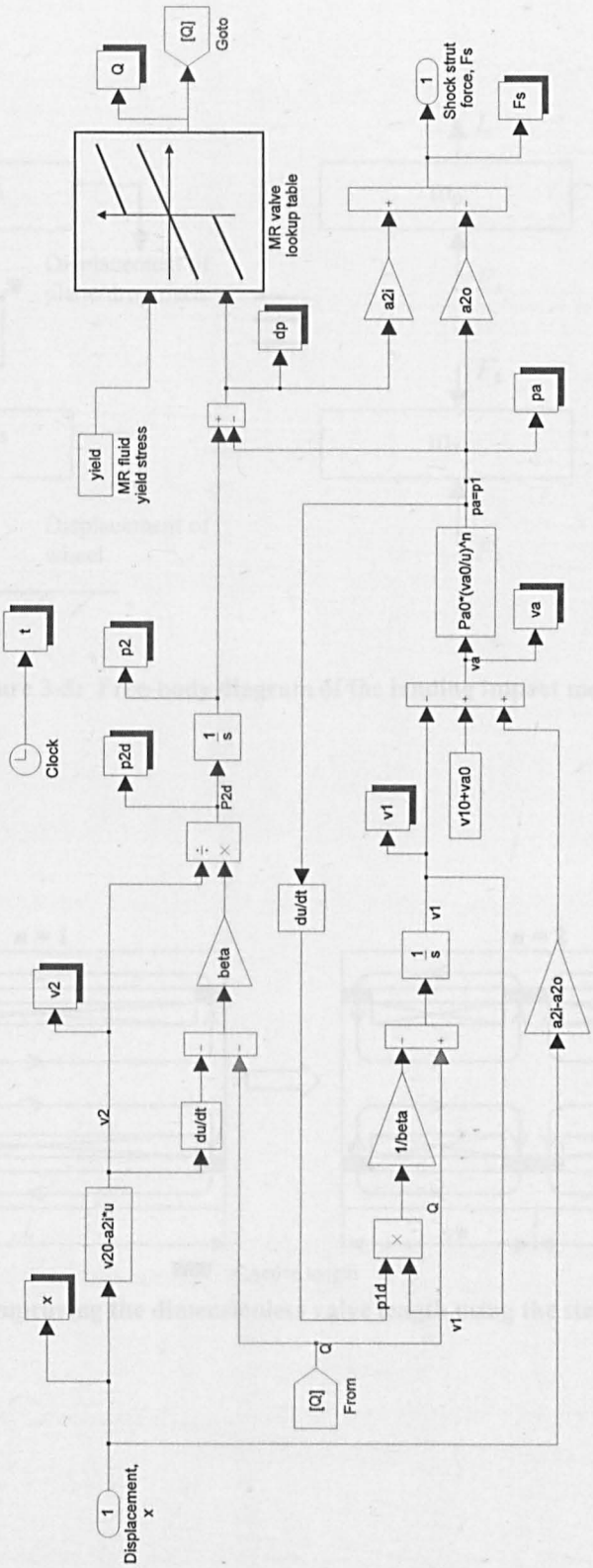

Figure 3-4: Simulink block diagram of the dynamic MR shock strut model.

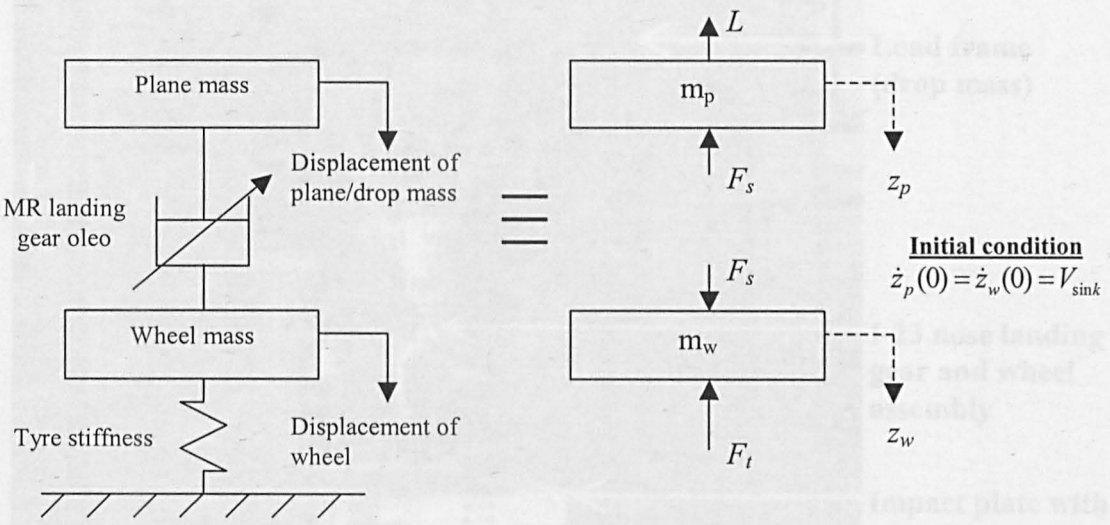

Figure 3-5: Free-body diagram of the landing impact model.

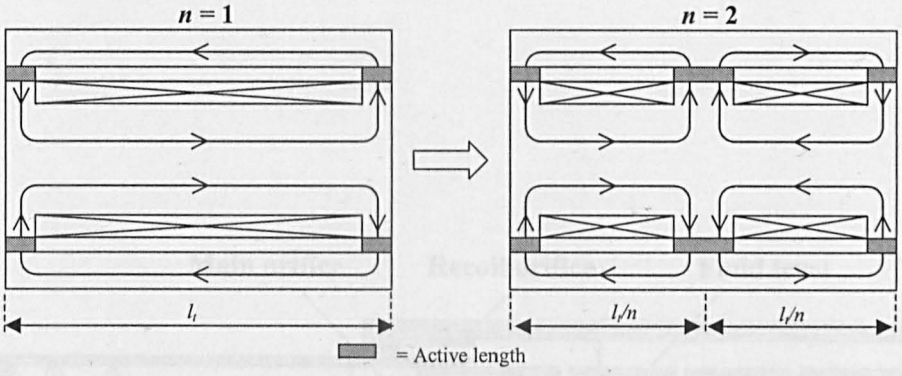

Figure 3-6: Improving the dimensionless valve length using the stacking method.

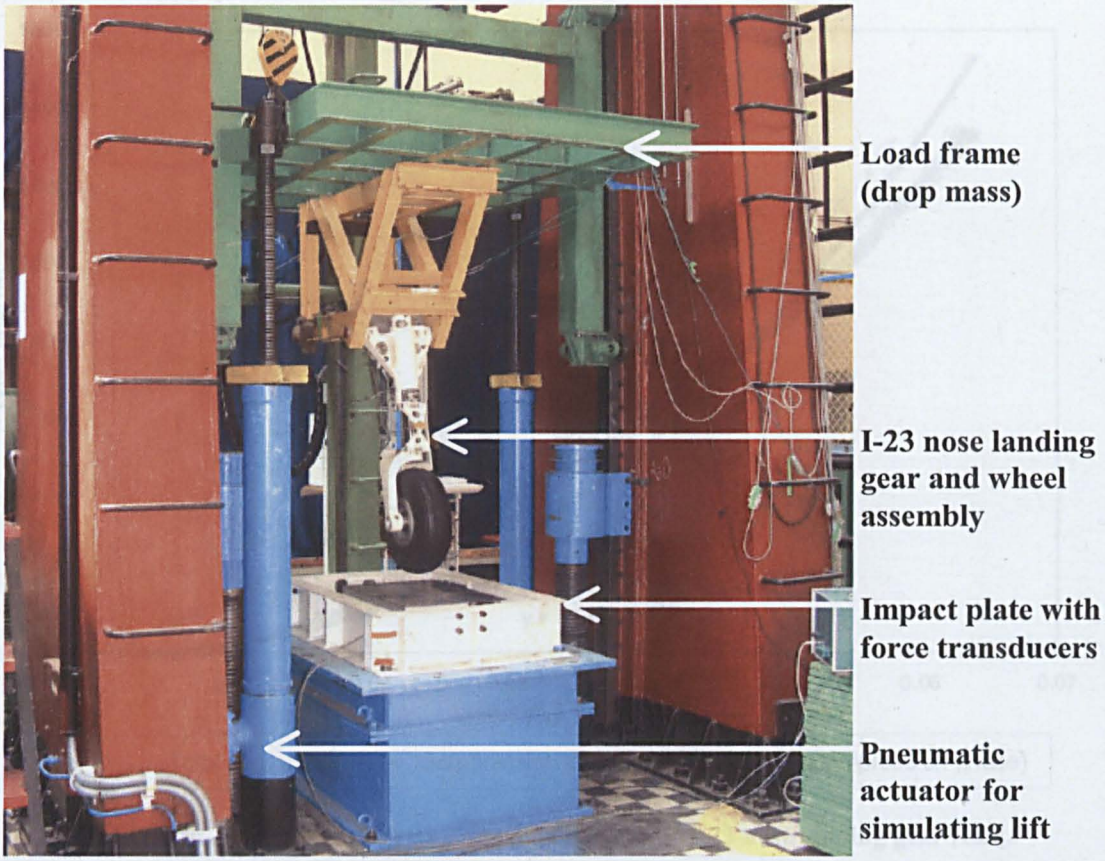

Figure 3-7: The Polish Institute of Aviation's landing gear drop test facility [125].

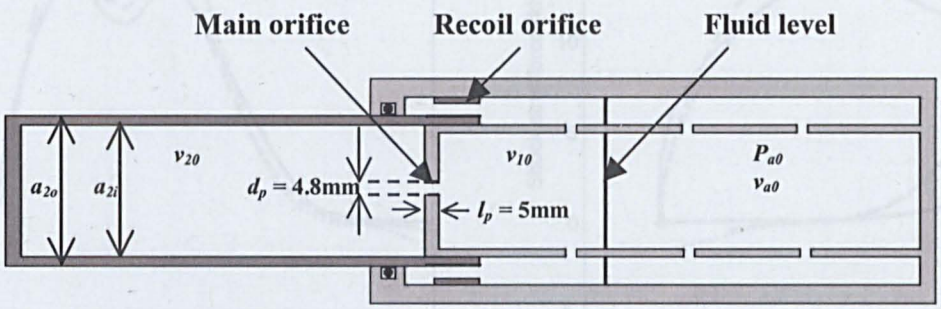

Figure 3-8: Schematic diagram of the existing I-23 nose gear.

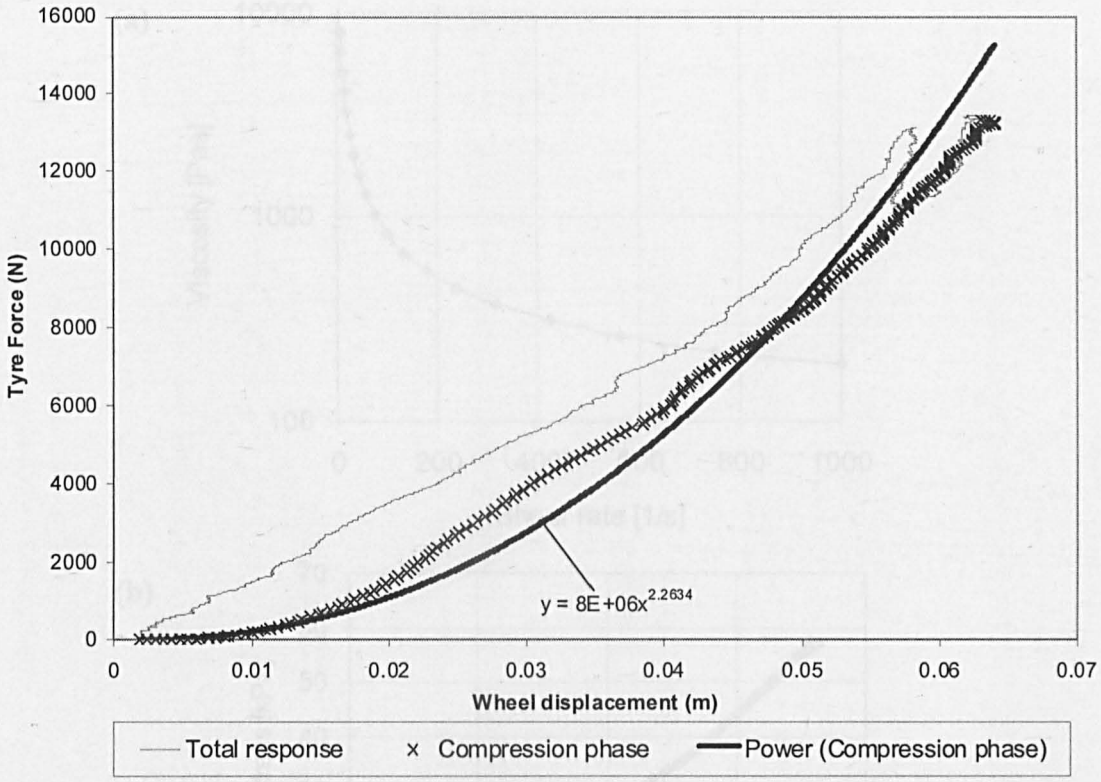

Figure 3-9: Tyre response from an impact test on the I-23 nose landing gear [125].

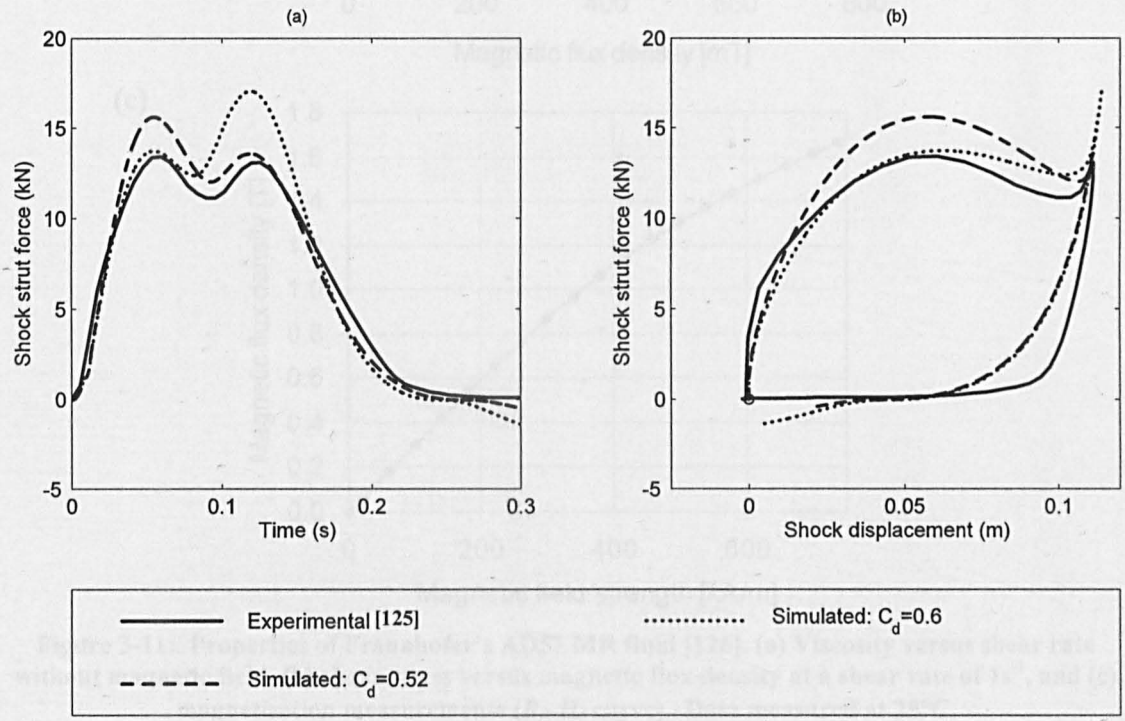

Figure 3-10: Experimental and simulated passive landing impact responses for a range of discharge coefficients C_d.

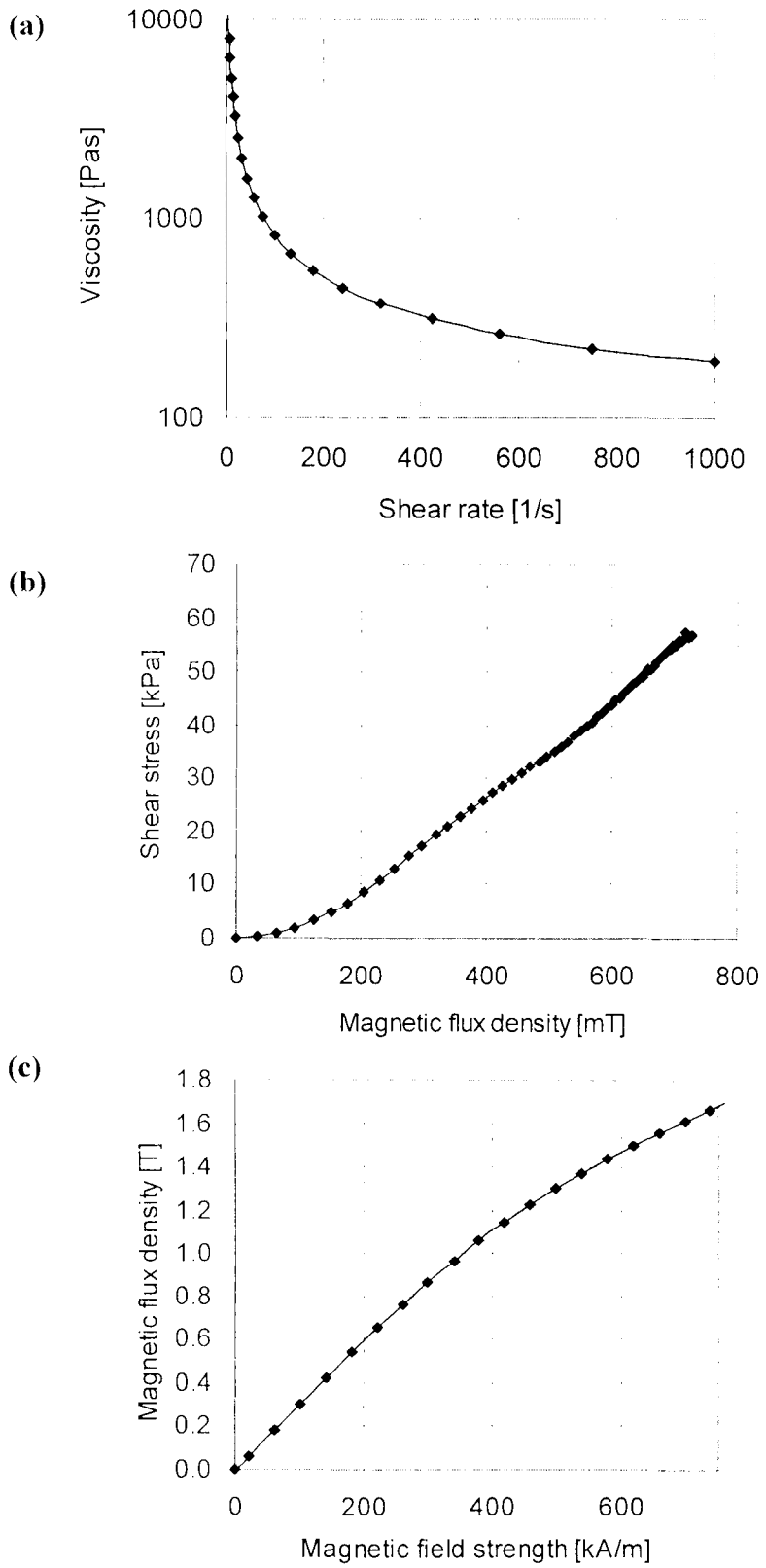

Figure 3-11: Properties of Fraunhofer's AD57 MR fluid [126]. (a) Viscosity versus shear rate without magnetic field, (b) shear stress versus magnetic flux density at a shear rate of $1s^{-1}$, and (c) magnetisation measurements (B_f–H_f curve). Data measured at 25°C.

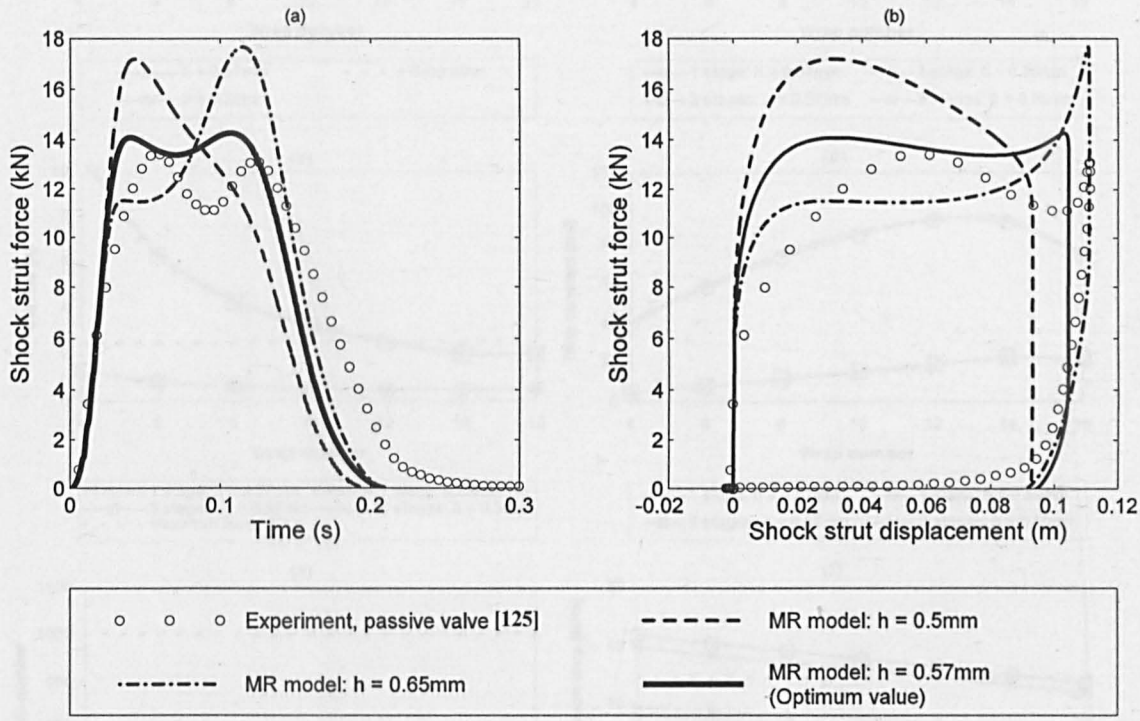

Figure 3-12: Tuning the valve gap size to achieve the desired worst-case landing impact performance. τ_y = 55kPa.

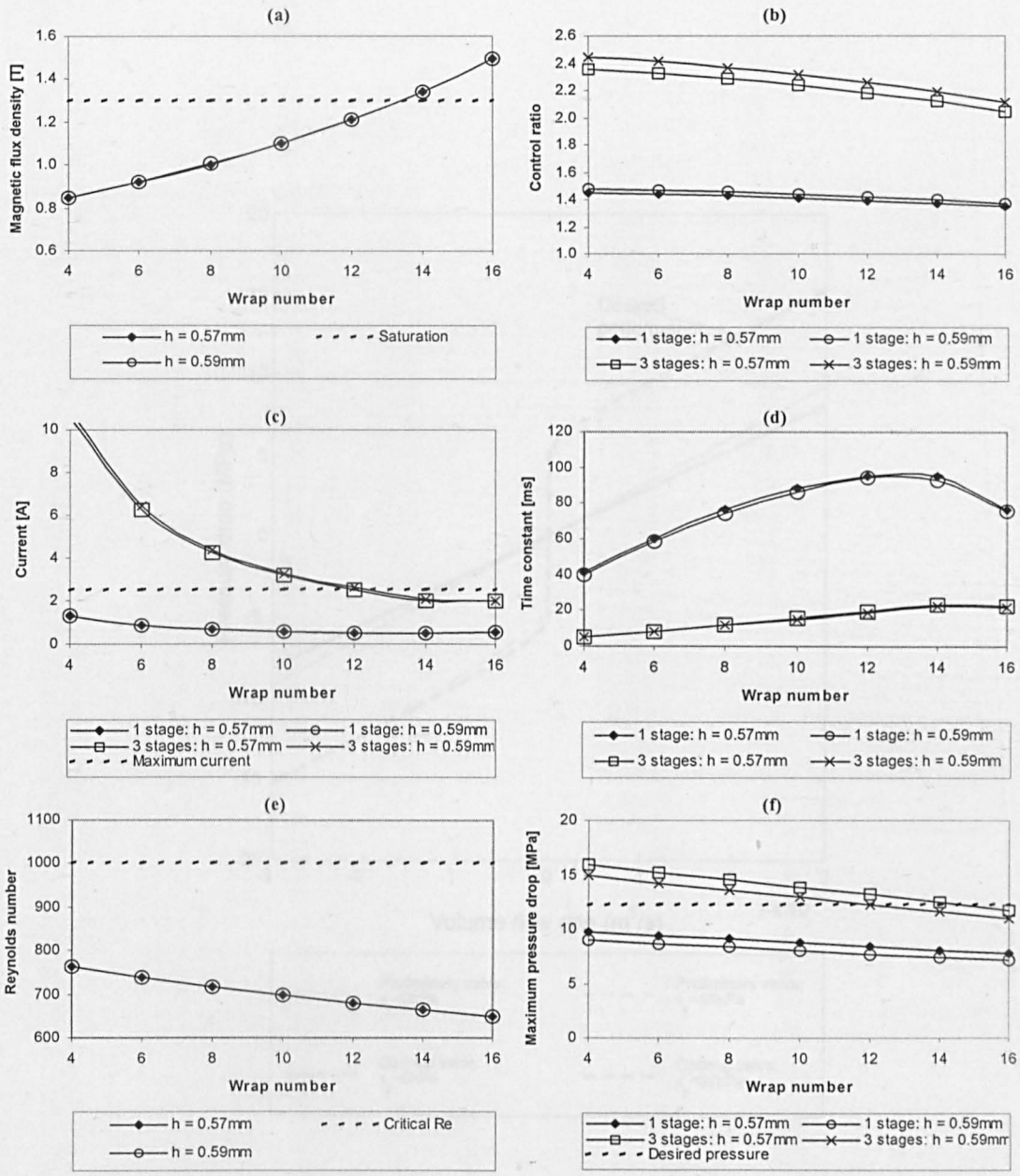

Figure 3-13: MR valve sizing results for the I-23 landing gear. (a) Magnetic flux density B_s (b) control ratio λ, (c) current I, (d) time constant τ, (e) Reynolds number Re, and (f) maximum pressure drop ΔP_{max}. $Q = 2\times10^{-3}$ m^{3}s^{-1}, $\tau_y = 55$kPa.

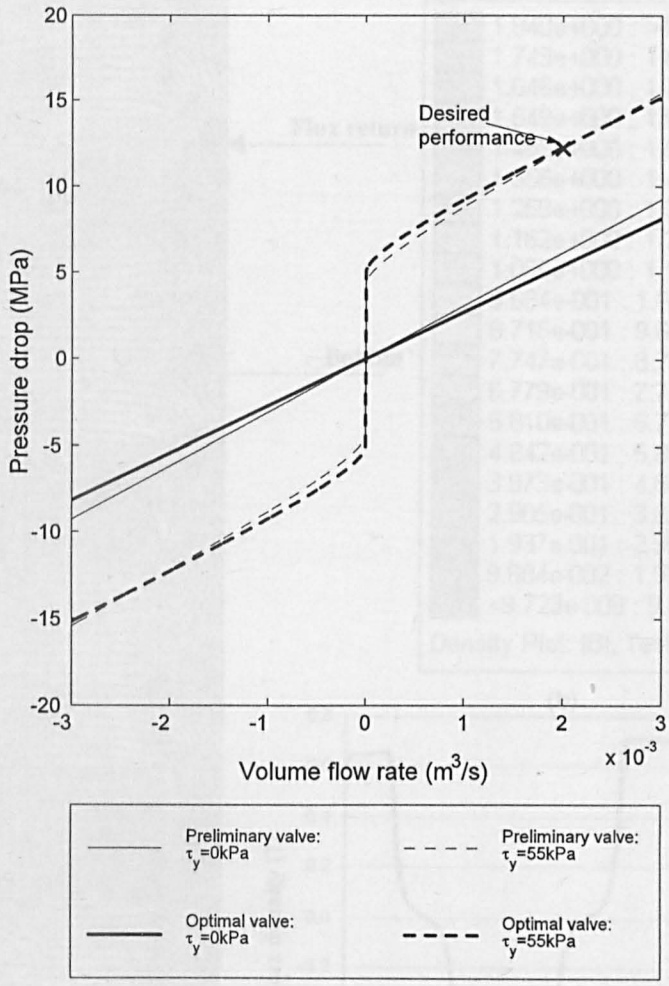

Figure 3-14: Quasi-steady pressure/flowrate characteristics of the preliminary and optimal I-23 valve designs.

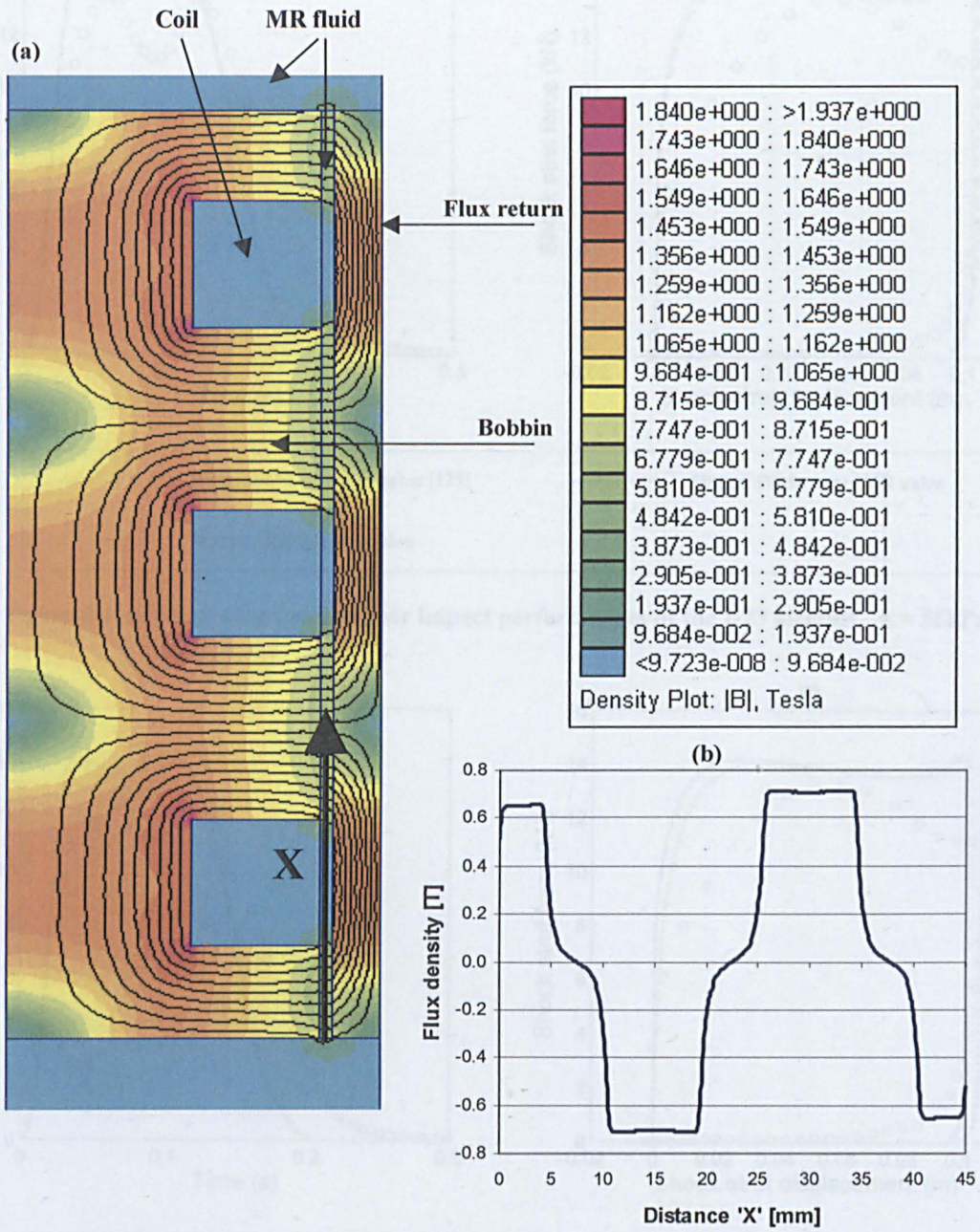

Figure 3-15: Axi-symmetric FEA analysis of the optimised valve geometry. (a) Flux density contour plot and (b) the normal flux density within the fluid along the mean valve diameter. *I* = *2.6A*.

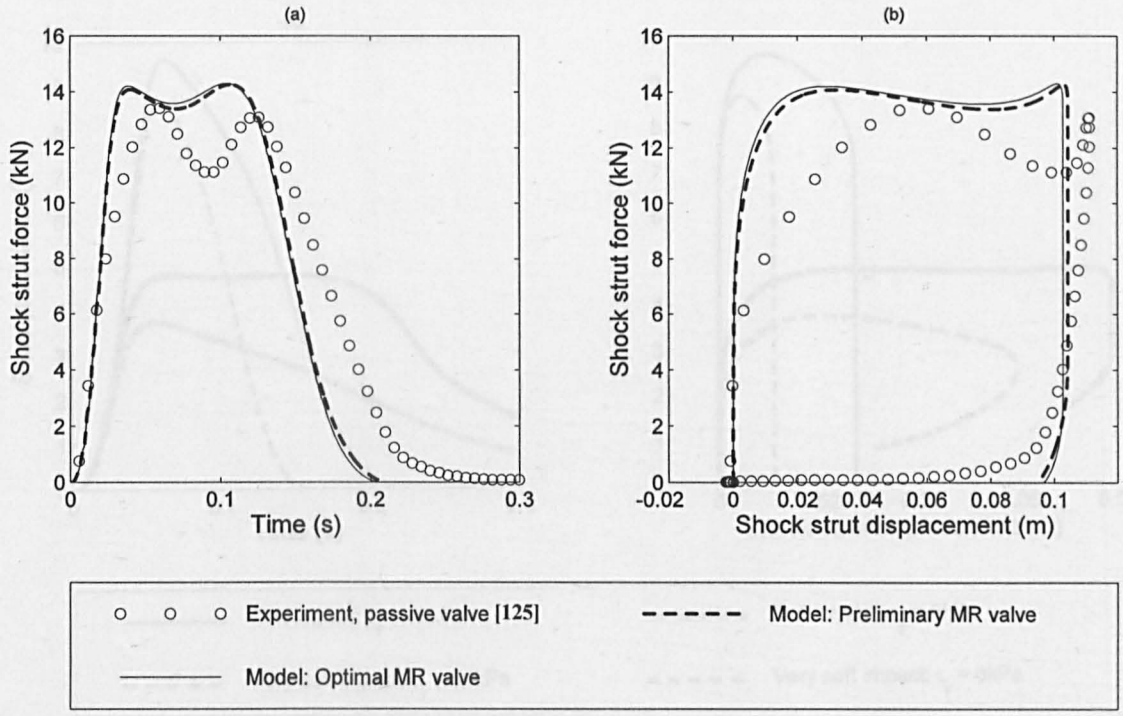

Figure 3-16: Worst case landing gear impact performances of the I-23 aircraft. τ_y = 55kPa.

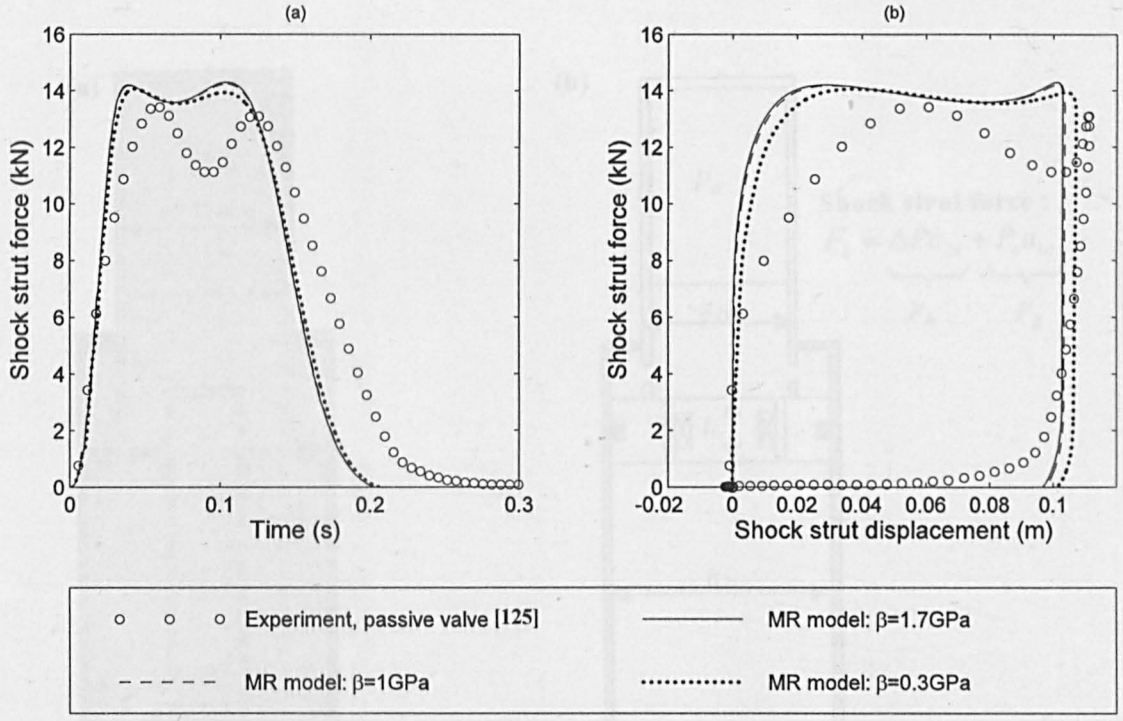

Figure 3-17: The effect of fluid compressibility on the I-23 landing impact response. Worst case impact: τ_y = 55kPa.

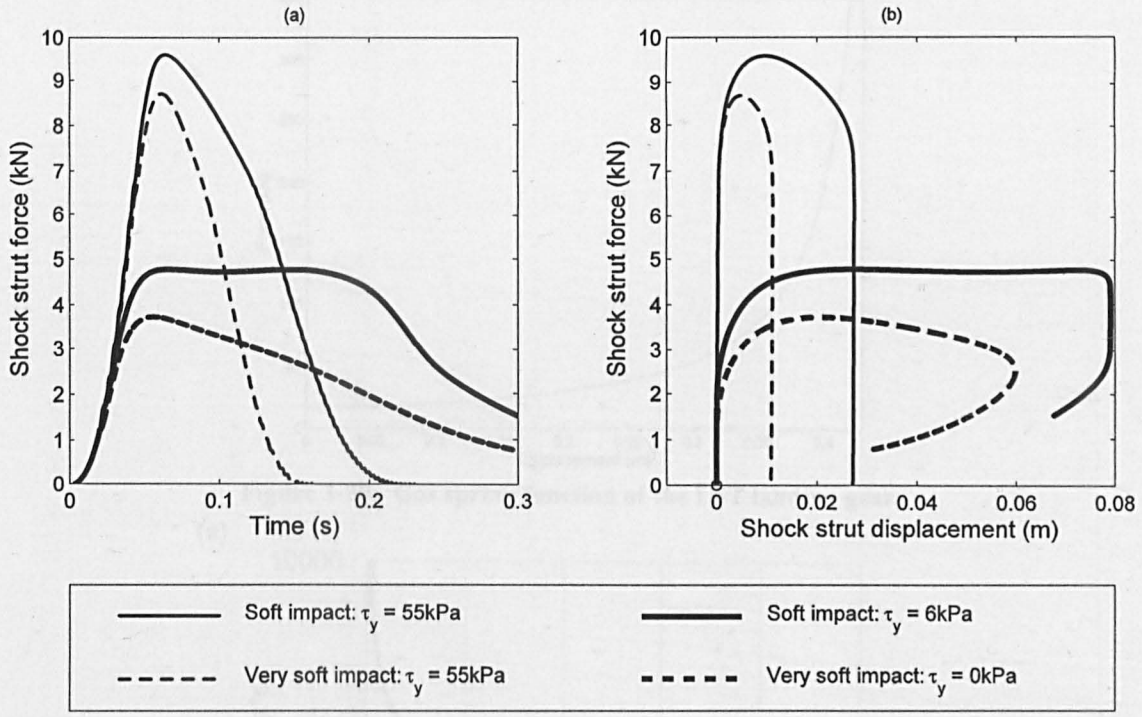

Figure 3-18: Landing gear impact performances of the I-23 with less severe input conditions. Soft impact: m_p = 473kg and V_{sink} = 1m/s. Very soft impact: m_p = 284kg and V_{sink} = 1m/s. β = 1.7GPa.

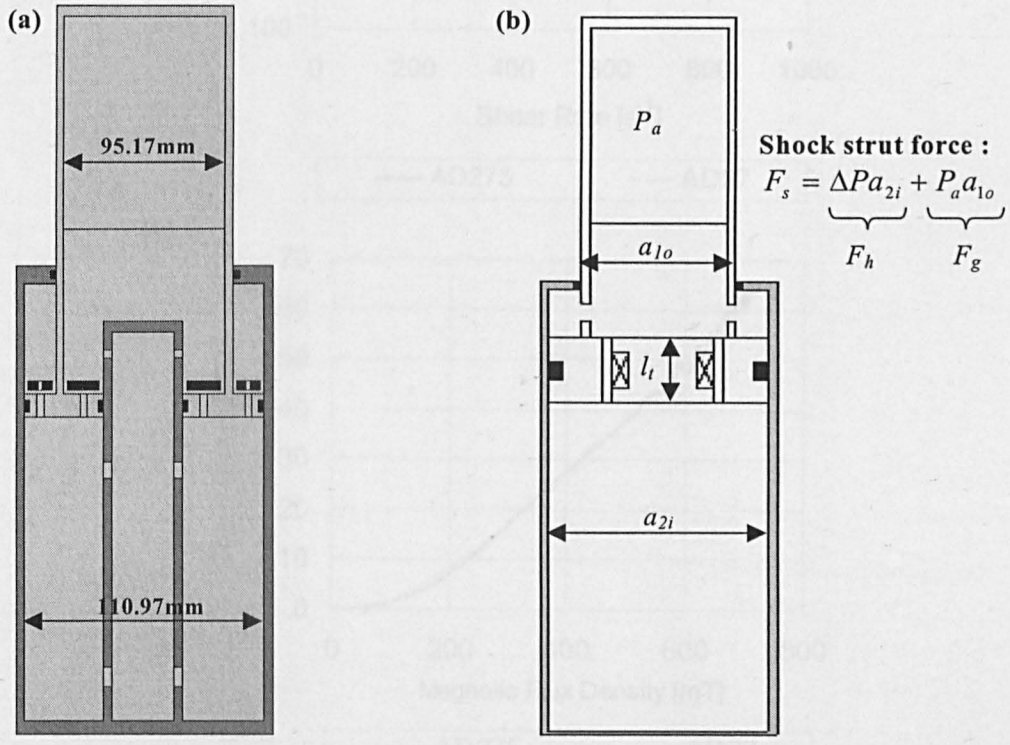

Figure 3-19: Shock strut designs for the LST landing gear. (a) Existing (passive) design [103], and (b) equivalent MR design.

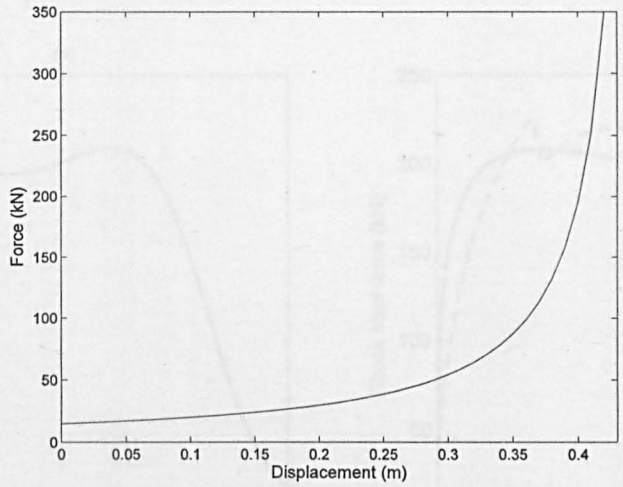

Figure 3-20: Gas spring function of the LST landing gear.

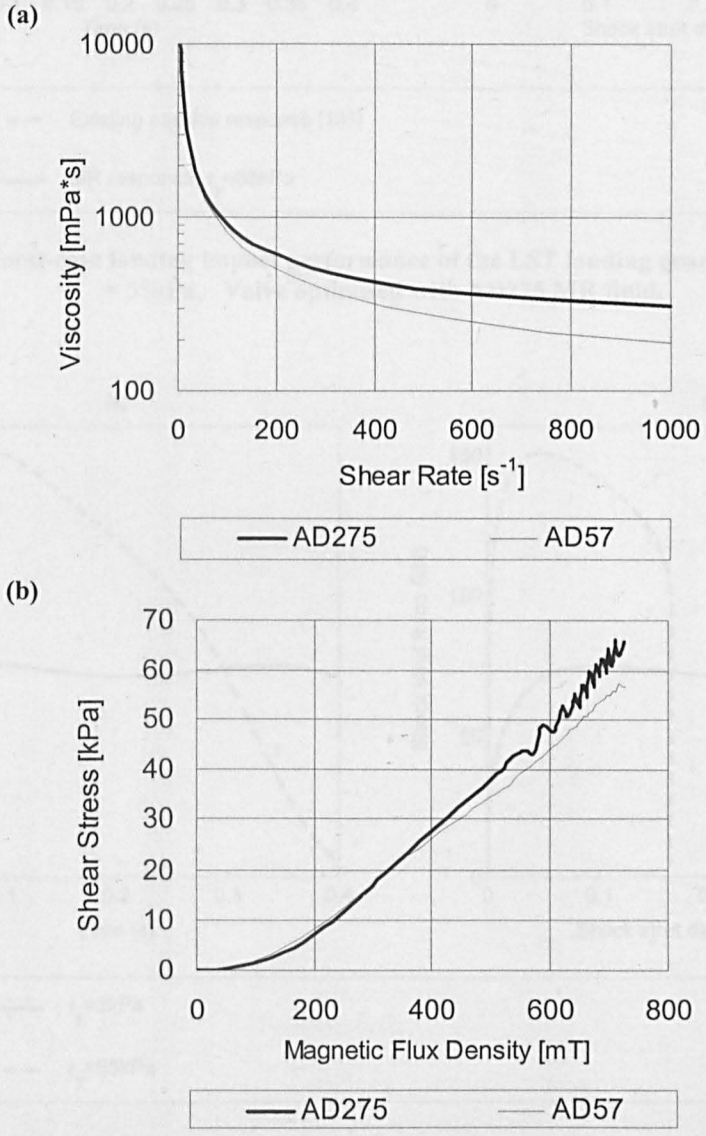

Figure 3-21: Comparison of the properties between AD57 and AD275 MR fluid. (a) Viscosity versus shear rate and (b) shear stress versus magnetic flux density [126].

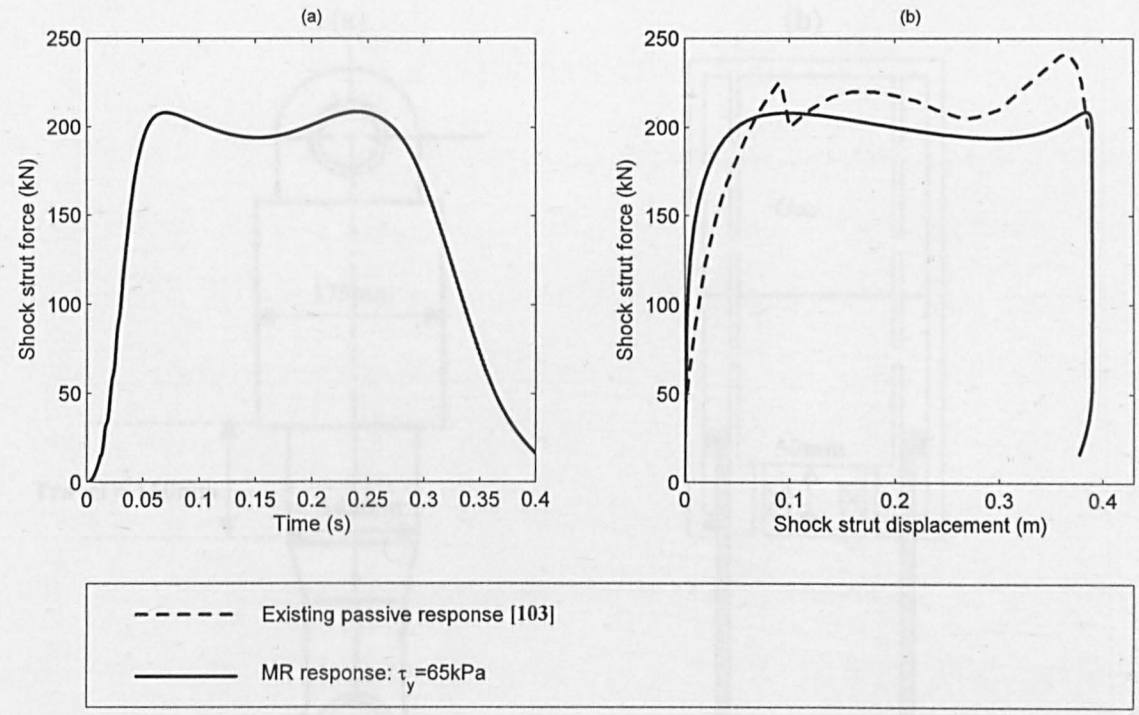

Figure 3-22: Worst-case landing impact performance of the LST landing gear. V_{sink} = 3.66ms^{-1}, τ_y = 55kPa. Valve optimised with AD275 MR fluid.

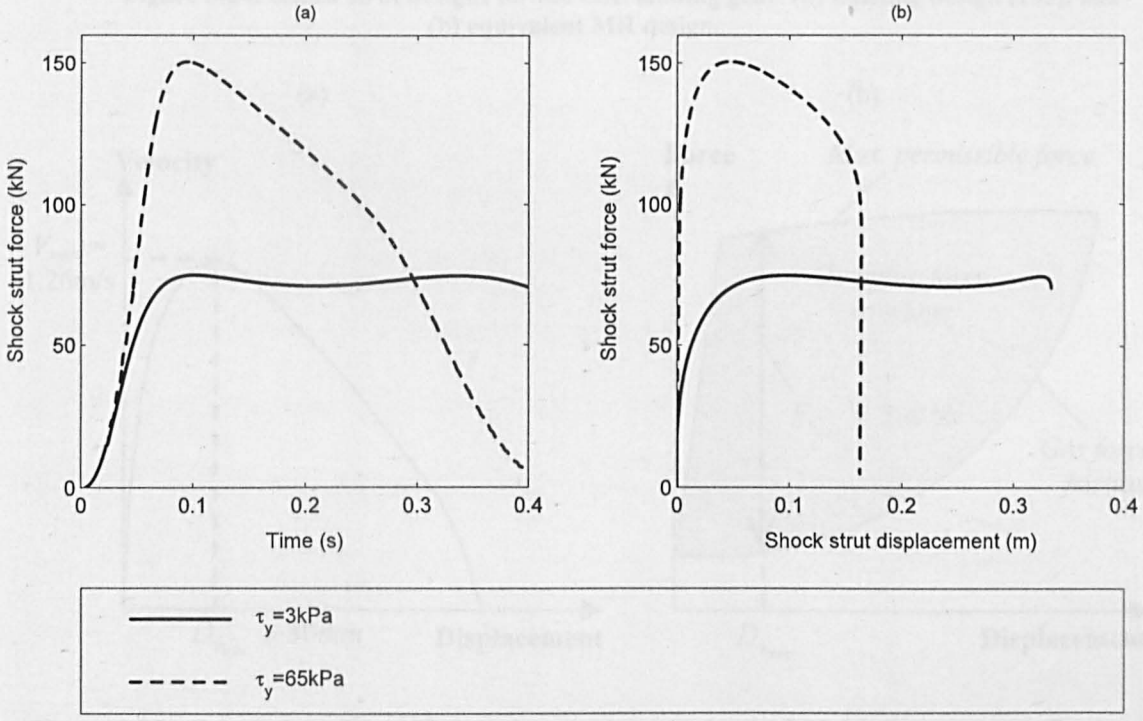

Figure 3-23: MR impact performance of the LST device with less severe input conditions. V_{sink} = 2ms^{-1}. Valve optimised with AD275 MR fluid.

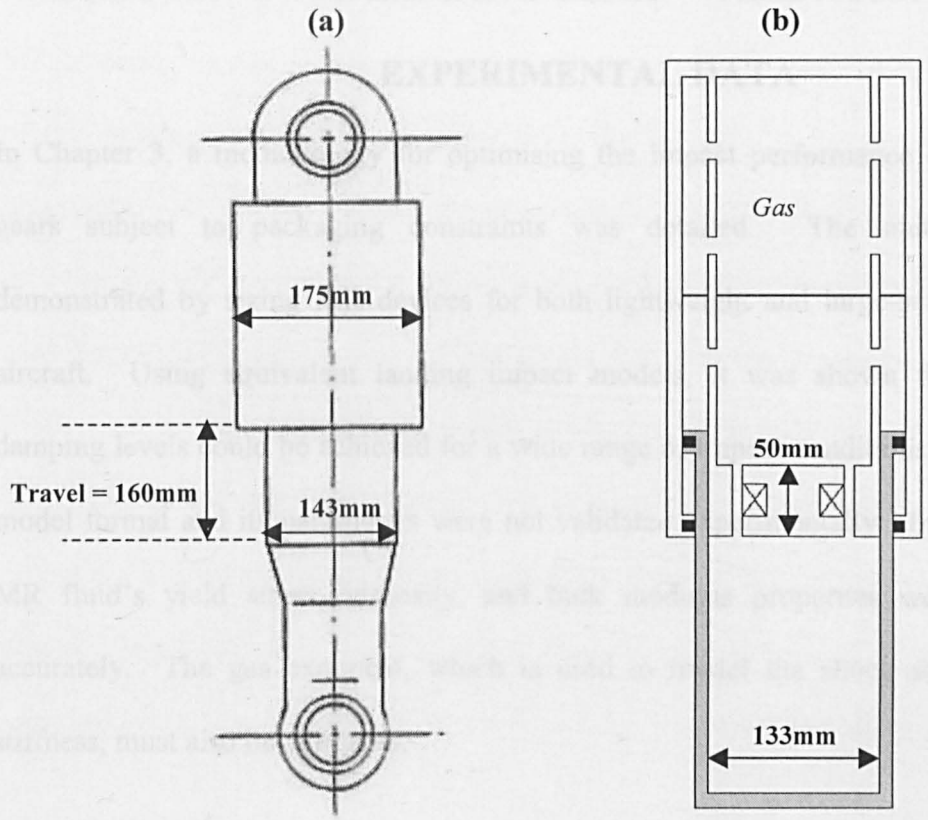

Figure 3-24: Shock strut designs for the LSL landing gear. (a) Existing design [103], and (b) equivalent MR design.

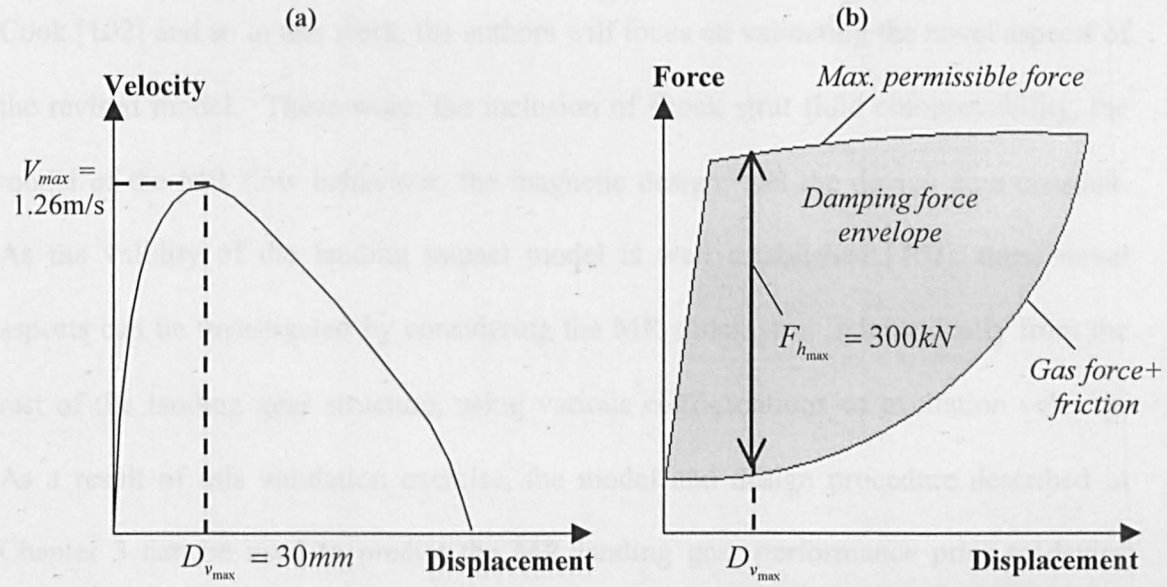

Figure 3-25: Calculation of the MR damping requirement for the LSL landing gear. (a) Shock strut velocity/displacement response during worst-case impact and (b) maximum permissible shock strut forces [103].

CHAPTER 4. MR LANDING GEAR – VALIDATION USING EXPERIMENTAL DATA

In Chapter 3, a methodology for optimising the impact performance of MR landing gears subject to packaging constraints was detailed. The methodology was demonstrated by sizing MR devices for both lightweight and large-scale commercial aircraft. Using equivalent landing impact models, it was shown that appropriate damping levels could be achieved for a wide range of impact conditions. However, the model format and its parameters were not validated experimentally. In particular, the MR fluid's yield stress, viscosity, and bulk modulus properties were not known accurately. The gas exponent, which is used to model the shock struts non-linear stiffness, must also be validated.

The aim of the present chapter is to experimentally validate the MR landing gear model developed in Chapter 3. This model was based upon that developed by Milwitzky and Cook [102] and so in this work, the authors will focus on validating the novel aspects of the revised model. These were: the inclusion of shock strut fluid compressibility, the model of the MR flow behaviour, the magnetic design, and the device time constant. As the validity of the landing impact model is well established [102], these novel aspects can be investigated by considering the MR shock strut independently from the rest of the landing gear structure, using various configurations of excitation velocity. As a result of this validation exercise, the model and design procedure described in Chapter 3 can be used to predict the MR landing gear performance prior to device manufacture.

The present chapter is organised as follows. First, the design and manufacture of the MR landing gear shock strut is described along with the corresponding dynamic model of the device. After describing the experimental facility, an investigation is then presented which aims to validate the quasi-steady performance of the MR valve. Here, the accuracy of the yield stress and viscosity predictions is tested. After validating the MR fluid's bulk modulus and the gas spring function, the sinusoidal response of the shock strut is then compared to model predictions. Furthermore, an analysis of the device's time constant is given, which is a vital performance indicator when considering potential control strategies. After a discussion of the results, the main conclusions are drawn. The research in this Chapter formed the second part of the two-part journal submission [130], and the abstract for this work is given in Appendix A.II.

4.1 Design and manufacture of the MR shock strut

In order to fabricate an MR landing gear shock strut for this investigation, it was decided to retrofit an MR valve to an existing passive device. The passive shock strut was acquired from a RALLYE, which is a lightweight trainer/tourer aircraft built by the Socata Aircraft company some years ago [131]. A schematic drawing of this shock strut is shown in Figure 4-1(a).

In order to retrofit an MR valve, some design modifications were necessary and these are illustrated in Figure 4-1(b). The MR valve is incorporated within the inner cylinder, and the gas transfer tube has been removed, as this posed significant restrictions on the magnetic circuit. The MR valve is secured into place by the piston head, which completely seals against the outer cylinder. Therefore to prevent the formation of a vacuum, four fluid transfer orifices were included within the piston rod, which were

sufficiently large so that the pressure drop across them was negligible. To accurately characterise the performance of the MR valve, two static pressure transducers [132] were incorporated (one on either side of the piston). These were rated at 0-207bar gauge (0-3000 psig), and measured the fluid pressure on the 'non-gas side' of the piston, and the gas pressure on the 'gas side' (see Figure 4-1(b)). The shock strut was filled with AD57 MR fluid [133], and charged with Nitrogen gas to a pressure of 7.5bar (at full extension of the shock strut). By comparing the volume of MR fluid (≈173ml) with the internal volume of the shock strut, the initial gas volume v_{a0} was calculated as $60cm^3$.

The geometry of the MR valve was determined using the magnetic circuit sizing methodology developed in Chapter 3. Here, the valve gap size was fixed at 0.6mm, and the optimum valve configuration was determined. This provided the greatest control ratio, and could achieve the maximum fluid yield stress without magnetic saturation, and without exceeding the maximum current rating of the copper wire. With reference to Figure 3-1(b), the resulting valve geometry is given in Table 4-1. The method of assembly and manufacture of this valve is illustrated in Figure 4-2. The annular valve gap was accurately maintained using two valve-gap support spiders. These spiders were manufactured from titanium, whose non-magnetic properties direct the magnetic flux into the active region of the valve. The flux return and valve core were manufactured from a low-carbon mild steel due to its high magnetic permeability. Also, the coil was surrounded with a wear resistant resin that was machined to the same diameter as the bobbin flange. This protected the coil from the abrasion of iron particles and furthermore, provided a smooth surface to encourage laminar valve flow.

4.2 Dynamic model of the MR shock strut

In what follows, a summary of the dynamic MR shock model is provided. In this discussion, attention will be drawn to the parameters that were assumed in Chapter 3, and which therefore require validation. For a more detailed description of the modelling format, the reader is referred to Section 3.3.

A schematic diagram of the MR shock strut and the key equations used to formulate the corresponding model are presented in Figure 4-3. As shown, the shock absorber force F_s is readily derived using a pressure/area balance. This is slightly different to that used in Chapter 3, due to the difference in the configuration of device. The gas pressure was determined using the polytropic law for the compression of gases, where the key unknown is the gas exponent m. In Chapter 3, this was assumed to be 1.1, which is known to correlate well when the fluid and gas volumes are mixed [101]. Fluid compressibility was modelled using the mass flow continuity equation. Here, the bulk modulus β is unknown, and the base value for a standard hydraulic oil (1.7GPa) was assumed as a reasonable approximation. Finally, the MR effect was characterised using the Buckingham equation for Bingham plastic flow between parallel flat plates [55]. In order to formulate the quasi-steady valve function, the Buckingham equation is solved in terms of the active pressure drop ΔP_{l_a}, for a range of flow rates Q and MR fluid yield stress values τ_y. Each ΔP_{l_a} term is then summed with the inactive pressure drop ΔP_{l_i}, which is calculated using the Buckingham equation for τ_y = 0kPa. Once arranged as a 3-D look-up table, the quasi-steady valve function can be used within the dynamic model. The two key unknowns in the Buckingham equation are the MR fluid viscosity μ, and the relationship between the MR fluid's yield stress and the applied magnetic

field/current. As described in Chapter 3, the viscosity was assumed as 0.1Pas for AD57 MR fluid. This is an extrapolated value taken from the manufacturer's MR fluid property data at 25°C (Figure 3-11). Calculation of the yield stress/current relationship is dealt with in Section 4.4.

4.3 Description of the test facility

A photograph of the damper test facility is shown in Figure 4-4. A corresponding schematic diagram is also provided in Figure 4-5, which illustrates the interaction between the various hardware and software components. The setup comprised an Instron PLL25K servo-hydraulic actuator [134], which was controlled by two high response Moog servo-valves [135] and an Instron 8400 digital controller [134]. This enabled accurate displacement feedback control, and the system could deliver ±25kN force, ±50mm displacement and velocities of up to $\pm 1 ms^{-1}$. A Kepco BOP amplifier [136] also provided high bandwidth dynamic current control for the MR valve.

The MR shock strut's displacement and current were controlled externally using real-time control software. Here, a host PC running xPC target [137] was used to develop the excitation signals and test automation scripts. This was coded in Simulink, compiled as a C-programme, and subsequently downloaded onto a target PC, which performed the real-time control of the actuator. The target PC comprised a 1.3GHz AMD Athlon processor with 128Mb of RAM, which was booted from a floppy disk containing the xPC operating kernel.

Data logging was achieved via a National Instruments PCI-MIO-16XE-10 data acquisition card [138]. This was capable of sample rates up to 100kHz and supported an interface board with eight 16-bit analogue differential input channels (A/D

conversion) and two 16-bit analogue output channels (D/A conversion). Once a test had completed, the measurement data stored on the target PC's RAM was uploaded to the host PC ready for post-processing. This measurement data was acquired from an inductive displacement transducer, which was also used for position feedback control of the actuator, two static pressure transducers (as described in Section 4.1), and an Instron ±25kN dynamic load cell (IST Dynacell [134]).

Finally, to permit continuous testing without overheating of the shock strut, copper tubing was coiled around the shock strut body and fed with mains water.

4.4 Quasi-steady analysis

In this section, an analysis is presented that aims to validate the quasi-steady pressure/flowrate function of the MR valve i.e the Buckingham equation (see Figure 4-3 or Eq.3-6). The validated function can then be used as a look-up table within the shock strut model to predict the dynamic behaviour.

The experimental quasi-steady behaviour was determined using a constant velocity excitation, where the aim was to achieve a steady-state pressure drop. This was applied in the compression phase of the shock strut's stroke only. The extension phase was not considered as the initial shock strut pressure was not high enough to prevent cavitation of the fluid. The valve pressure drop was then calculated by subtracting the static pressure sensor readings. Here, it is assumed that the gas pressure is equal to the fluid pressure in the piston rod, which is a valid assumption as there is no dividing piston.

A typical result from this test is shown in Figure 4-6. This is shown for a step-velocity excitation from $0ms^{-1}$ to $0.1ms^{-1}$ at time 7s, and for a range of input currents between

0A and 2A. Clearly, steady-state conditions are soon achieved after the step velocity change is applied. The quasi-steady pressure drop can therefore be determined, which was calculated as the mean value over the second half of the response. This was repeated for velocity excitations between $0.01ms^{-1}$ and $0.4ms^{-1}$ in order to form the quasi-steady valve function.

Before the numerical model can be correlated with experimental data, the yield stress/current relationship of the MR valve must be determined. This was calculated by performing a 2-D axisymmetric finite element analysis (FEA) of the MR valve, which was carried out using FEMM software [128]. FEA was used instead of the more straightforward analytical analysis presented in Part 1, as it permitted the effects of flux leakage to be more accurately accounted for. In this analysis, the mean flux density across the active valve length was calculated for each current magnitude. The yield stress corresponding to this mean applied field was then determined using the fluid manufacturer's data (Figure 3-11(b)). Consequently, the Buckingham equation can be formulated and compared to the experimental quasi-steady valve performance.

The corresponding results are shown in Figure 4-7 for the 0A and 1A responses. In the initial model, a viscosity equal to 0.1Pas was assumed (as described in Section 3). Also, the initial yield stress for the 1A response (16kPa) was calculated using Fraunhofer's B_f-H_f data for AD57 MR fluid. Clearly, the numerical results do not correlate well with the experimental behaviour, since the viscosity and yield stress predictions are too low.

To improve correlation, these parameters were updated, and the corresponding results are also shown in Figure 4-7. Here, the viscosity was increased to 0.14Pas, and the yield stress for the 1A response was increased to 43kPa. The higher than predicted

viscosity may partly be due to temperature effects. For example, the fluid manufacturer's viscosity information was measured at 25°C, but the actual fluid temperature was likely to be lower than this due to the presence of the cooling circuit.

As shown in Figure 4-7, the updated parameters significantly improve the model's prediction of the low velocity behaviour, particularly for the 1A response. However, correlation deteriorates at high velocities, where a larger resistance to flow is observed in the experimental data. This could be attributed to a shear-thickening phenomenon, where the apparent viscosity increases with increasing shear rate. The Buckingham equation, which uses the Bingham plastic relationship between shear stress and shear rate (see Figure 1-6(b)), does not account for such behaviour. Another reason might be due to the valve gap support spiders (see Figure 4-2), which obstruct flow. The quadratic nature of the quasi-steady response could be a result of turbulence caused by this obstruction.

To summarise the yield stress results, Figure 4-8 compares the FEA predictions with the updated experimental values between 0A and 2A. The error between the predicted and observed yield stress values is clearly very large when Fraunhofer's (FhG-ISC) B_f-H_f data are used in the FEA analysis. This error is partly due to repeatability problems, which is indicated in Figure 4-8 by the triangular markers. Here, the quasi-steady test was repeated for certain current values, which has resulted in a reduced yield stress. This could be due to increased amounts of entrained air as a result of mixing with the gas. Another reason might be due to a better homogeneity of iron particles, which has developed during the final higher velocity tests. This is fairly probable because the AD57 MR fluid was found to suffer significantly from sedimentation problems.

Nonetheless, the error between the repeated experimental results and the numerical predictions with FhG-ISC's data is still very large. It was originally thought that this was due to a poor tolerance on the valve gap, although this was found to be insignificant. Another reason might be due to a variation in the fluid properties between batches. However, B_f-H_f measurements that were later provided by a different ADLAND partner (Cedrat [139]) indicated that the error was most likely caused by inaccurate B_f-H_f data. This result is also illustrated in Figure 4-8, where the FEA analysis was repeated with Cedrat's B_f-H_f data in order to predict the yield stress. Clearly, the accuracy of the yield stress predictions is significantly improved, particularly when correlated with the repeated test results.

Further credence to the above result is given by considering David Carlson's empirical equation [26], which is known to provide a useful prediction of the B_f-H_f response for virtually any MR fluid:

$$B_f = 1.91\Phi^{1.133}\left[1-\exp(-10.97\mu_0 H_f)\right]+\mu_0 H_f \qquad (4\text{-}1)$$

Here, Φ is the volume fraction of iron particles and μ_0 is the magnetic constant ($4\pi\times10^{-7}$H/m). As shown in Figure 4-9, Carlson's equation correlates very well with Cedrat's B_f-H_f measurements, but the correlation with Fraunhofer's data is poor. This further suggests that Fraunhofer's B_f-H_f data are inaccurate, thus giving rise to the poor yield stress predictions shown in Figure 4-8.

4.5 Dynamic analysis

In the following analysis, the aim is to accurately predict the dynamic response of the MR shock strut. First, the bulk modulus of the MR fluid, and the shock strut's gas spring function are validated. The validated parameters and the updated quasi-steady

valve function (from Section 4.4) are then used to predict the sinusoidal response of the shock strut. Finally, an investigation is presented to identify the time constant, which is an important performance indicator when considering potential control strategies.

4.5.1 Fluid compressibility

The compressibility of a fluid directly determines the rate of change in fluid pressure. An effective way to investigate this, and hence validate the associated bulk modulus β, is to analyse the pressure transients in a step-velocity test. Here, an incompressible fluid would correspond to an instantaneous development of the quasi-steady valve pressure drop.

The results from this analysis are shown in Figure 4-10 for a step velocity input between $0ms^{-1}$ and $0.1ms^{-1}$, and for current excitations of 0.5A and 1A. The updated quasi-steady valve function has been included in the model, which is accurate for the chosen input conditions (see Figure 4-7). As indicated by the steep pressure gradients, the numerical response with β = 1.7GPa is too 'stiff'. By updating the bulk modulus to 0.3GPa, i.e. to a more compressible (or less stiff) value, the correlation in slope with the experiment is improved. However, the model does not account for the higher order dynamics observed in the experiment. For example, the rate of change in pressure in the experiment is more gradual at the beginning than at the end of the response. Furthermore, the experimental response has an 'underdamped' nature. This could be attributed to fluid inertia, which is not accounted for in the model. Nonetheless, the general slope of the experimental response correlates well with the model, and therefore serves as a useful methodology to approximate the bulk modulus of the MR fluid. The

lower observed value of 0.3GPa is probably due to entrapped air, which may have been introduced during mixing of the fluid prior to filling.

4.5.2 Gas model

Before the dynamic response of the shock strut model can be investigated, the gas law (see Figure 4-3 or Eq.3-2) must first be validated. The key parameters that require validation are the initial gas volume v_{a0} and the gas exponent m.

As mentioned in Section 4.1, the initial gas volume was calcuated to be 60cm^3. However, due to filling difficulties, a degree of error was probable in this calculation. Consequently, v_{a0} must be validated, and this was effectively achieved using the following isothermal analysis. In the experiment, pressure measurements were taken in 2mm increments across the full stroke of the shock strut. Between each measurement, enough time was allowed to ensure that the pressure had reached a steady isothermal value. The experimental results are shown in Figure 4-11(a) as the 'stationary measurements'. The results are then compared to a simulation of the gas pressure in the dynamic model with m = 1 i.e. an isothermal compression, and with β = 0.3GPa (the updated value). Also, the initial gas pressure (P_{a0}) was determined according to the experimental reading. As shown in Figure 4-11(a), by updating the initial gas volume from 60cm^3 to 66cm^3, excellent correlation in the isothermal gas pressure is achieved.

Identification of the gas exponent is addressed in Figure 4-11(b). Here, the numerical and experimental gas pressure responses are compared using sinusoidal excitations. As shown, by updating the gas exponent from m = 1 to m = 1.33, good correlation is achieved. This suggests that the gas compression is more adiabatic than expected, where m = 1.1 was originally assumed (Section 4.2). The reason for this could be

explained by considering the difference in flow regimes between passive and MR shock struts. For example, the assumed value was based on typical behaviour from conventional passive shock struts [101], which rely upon turbulent flow. In contrast, MR damping is based upon laminar flow. Therefore, in the passive shock strut, more energy is likely to be transferred away from the gas as a result of the more vigorous/turbulent mixing with the fluid. Consequently, the gas exponent will be more isothermal in nature. Further credence is given to this point by considering a passive device that uses a floating piston to separate the fluid and gas. Currey [101] suggests that the more adiabatic value of $m = 1.35$ should be used, which correlates well with the observed MR behaviour.

A final point is how the model does not account for the observed hysteresis in the experimental response. This is attributed to the heat transfer processes within the shock strut, which is associated with a variable gas exponent m. Wahi [105] described how this variation could be modelled in landing gear. However, for the purpose of the present study, the accuracy obtained with the existing model was considered as acceptable (Figure 4-11(b)).

4.5.3 Prediction of the sinusoidal response

In this section, the updated quasi-steady valve function (Section 4.4), bulk modulus (Section 4.5.1), and gas law (Section 4.5.2) are used to validate the dynamic behaviour of the shock strut model. This is investigated using two types of sinusoidal excitation. First, complete cycles were used to validate the low velocity behaviour. Here, the velocity and current was limited in order to prevent fluid cavitation during the extension phase of the stroke. Therefore, to investigate higher velocity/higher current behaviour,

half cycles were applied in the compression phase only. In the analysis, shock strut pressures are modelled rather than forces. This enables the effects of friction to be eliminated, which were found to be fairly significant. For example, Figure 4-12 shows the friction force response as a function of displacement (Figure 4-12(a)) and velocity (Figure 4-12(b)) for various sinusoidal excitations. The responses were estimated by subtracting the pressure/area balance (using the pressure transducer readings) from the measured force. Clearly, the friction force tends to decrease with increasing velocity. This could be attributed to fluid escaping under the seals, or even an increase in seal temperature. The friction is also higher towards maximum compression, which is due to the more significant compression of the rod seals under higher gas pressures (see Figure 4-1(b)). Furthermore, friction slightly increases with the current magnitude. This could be due to compression of the piston head seal under the higher pressures on the non-gas side. In conclusion, the behaviour of the seals is highly complex and thus difficult to analytically model. An empirical model could be developed, but this would be very device specific. Furthermore, it is likely that the device/seal design could be altered in order to make the frictional forces less significant. For the purpose of the present study, it is therefore appropriate to neglect friction and to concentrate on modelling the fluid pressure.

Figure 4-13 compares the fluid pressure predictions with the experiment, for a full sinusoidal excitation with amplitude a = 25mm, and frequency f = 0.5Hz. Here, the fluid pressure on the non-gas side of the piston (P_2 in Figure 4-3) is shown as a function of displacement. Displacement is used because it provides a better insight into the gas spring effect, which contributes significantly to the response (due to the large stroke). Furthermore, the updated yield stress values in the model correspond to those from the

initial quasi-steady experiments (see Figure 4-8). This is because the full sinusoidal tests were performed before the quasi-steady experiments, thus the fluid behaviour should more accurately correspond to the *initial* test. Clearly, the correlation between model and experiment in Figure 4-13 is excellent throughout the range of excitation currents.

As a further example, Figure 4-14 presents the results for a full sinusoidal excitation with a = 10mm, and f = 0.5Hz. This time, the fluid pressure is shown as a function of velocity, which is more appropriate as the damping effect dominates the response. Again, excellent correlation is observed, particularly in the post-yield behaviour. The fluid compressibility effect can be observed through the hysteresis in the pre-yield behaviour. The observed inaccuracies in this region may be attributed to the un-modelled higher order dynamics (see Figure 4-10). Nonetheless, correlation is still good.

The higher velocity response is presented in Figure 4-15, where a half cycle excitation with a = 25mm, and f = 3Hz was used. This result is effectively represented in terms of the pressure drop as a function of velocity. Also, note that the updated yield stress values correspond to those from the repeated quasi-steady experiments (see Figure 4-8). This is because the half-sine tests were performed after the quasi-steady experiments. As expected, Figure 4-15 illustrates good prediction of low velocity response, but the model breaks down at higher velocities due to the quadratic damping behaviour.

4.5.4 Device time constant

The time constant is a vital performance indicator and will have a large influence on potential control strategies. The power supply, the magnetic circuit design, and the

smart fluid rheology all contribute to the time constant associated with a change in the excitation current. Furthermore, fluid compressibility will have an affect, and this must be isolated from the other contributors.

In the present study, the time constant was investigated by applying a step change in current, from I_1 to I_2, during a constant velocity excitation. The corresponding yield-stress response in the dynamic shock strut model was then simulated using the following transfer function $G(s)$ [74, 94].

$$G(s) = \frac{1}{\tau s + 1} \tag{4-2}$$

Here, τ is the time constant, and s is the Laplace operator. To identify the time constant, the transient behaviour between the steady-state pressure levels can be correlated. The numerical and experimental step responses are shown in Figure 4-16 for I_2 = 1A and I_2 = 2A. The initial current for both cases corresponds to I_1 = 0.5A. Also, the numerical yield stress values correspond to those updated inline with the *repeated* quasi-steady test. This is because the time constant analysis was performed *after* the quasi-steady experiment.

With reference to Figure 4-16, the 'ideal response' assumes that the step change in yield stress is generated instantaneously. This represents the effects of fluid compressibility only. Therefore, the observed error between the ideal case and the experiment corresponds to the time response of the power supply, magnetic circuit, and fluid rheology. As shown in Figure 4-16, the time constant associated with these factors was identified as τ = 1.8ms, where excellent correlation with the experiment is observed. Due to the use of a current driver in the experiment, this is approximately 80% lower

than predicted in the sizing analysis, where a constant voltage source was assumed (Eq.3-27). This rapid response suggests that the landing gear shock strut would be highly suited to feedback control strategies (and the use of a constant current source).

The time constant of the complete experimental response (i.e. including fluid compressibility effects) was also calculated to be 2.5ms, which is the time taken for the pressure to reach 63% of its final value. Therefore, the overall time constant is increased by 28% due to compression of the fluid. This is likely to become even more significant at higher velocities, but could be improved via the removal of entrapped air prior to filling e.g. using a vacuum pump.

4.6 Discussion

In the present study, it has been shown that an accurate model of the MR valve's quasi-steady performance will result in good predictions of the shock strut's dynamic behaviour. However, using the existing Buckingham equation for Bingham plastic flow, only the low velocity behaviour produced good agreement due to a quadratic damping effect.

The Bingham plastic model could be modified to better characterise the MR fluid's high velocity behaviour. For example, Peel and Bullough [55] adopted a dimensionless form of the Buckingham equation, and demonstrated how empirical relationships could be defined to describe shear thinning behaviour. This method could be adopted to further update the model and hence enhance predictions of the high velocity response. Moreover, due to the dimensionless form of Peel and Bullough's approach, the updated model would not be device specific, thus enabling new valve geometries to be accurately characterised prior to manufacture. However, this approach is only valid if

the quadratic damping behaviour is a property of the fluid e.g. shear thickening. If the valve gap support spiders affected the response, then the quadratic behaviour would be a property of the device. To determine this, higher velocity shear stress/shear rate characteristics of the MR fluid is required. For example, fluid data for AD57 MR fluid is available at shear rates up to $1000s^{-1}$ [126], but in the flow mode shock strut, shear rates were found to be two orders of magnitude greater than this.

In Chapter 3, it was suggested that turbulence could hinder device performance as a result of the large impact velocities associated with landing gear. However, the test facility was limited to operating at relatively low/sub-critical Reynolds numbers. Nonetheless, there is the possibility that turbulence has occurred unintentionally, due to the obstructions to flow in the valve design. This may have led to the quadratic damping effect that is observed in Figure 4-7 and Figure 4-15. Here, it can be seen how a deteriorating control ratio with increasing velocity is exacerbated by the more substantial quadratic damping in the zero-field condition. However, if this phenomenon is a result of shear thickening rather than turbulence, then it is possible that the control ratio might be so low at high Reynolds numbers that the effects of turbulence are insignificant. Again, fluid property data at significantly higher shear rates is required in order determine the cause of this quadratic damping phenomenon.

4.7 Summary of Chapter 4

In this chapter, the manufacture and testing of an MR oleopneumatic landing gear shock strut was described. This was sized and modelled using the numerical approach described in Chapter 3, where the aim was to validate the MR landing gear design methodology.

In a quasi-steady analysis, it was found that the initial analytical predictions of yield stress and viscosity were poor. The error in the yield stress results was largely due to the use of inaccurate magnetic fluid property data (the B_f-H_f curve). Here, correlation between model and experiment was significantly improved using a new B_f-H_f curve, which was later validated. Using updated viscosity and yield stress values, the prediction of the low velocity behaviour was significantly improved, but correlation at higher velocities deteriorated due to a quadratic damping effect.

In a dynamic analysis, the bulk modulus of the MR fluid was identified as 0.3GPa. In general, this resulted in a good prediction of the pressure transients, but the model failed to account for higher order dynamics, and fluid inertia. The gas exponent was identified as 1.33, which is higher than the value commonly used for an equivalent passive shock strut. It was thought that this could be attributed to the differing valve flow regimes, and hence heat transfer characteristics between passive and MR devices. After formulating the dynamic shock strut model with the updated parameters, excellent correlation with the experimental behaviour was demonstrated using low velocity sinusoidal excitations. Therefore, if an accurate model of the quasi-steady behaviour can be developed, a good prediction of the dynamic shock strut performance will result.

However, in order to validate the landing gear design methodology, the quasi-steady MR valve function must be analytically formulated throughout the velocity range of the device. The dimensionless model updating approach described by Peel and Bullough could be adopted to achieve this [55], but only if the observed quadratic behaviour is a property of the fluid and not the device - behaviour such as shear thickening. This will

be dependent on acquiring more detailed fluid property information at significantly higher shear rates.

The lack of repeatability in the experimental results presented a further problem. It was found that the yield stress tended to decrease after many tests. This could be attributed to mixing of the fluid with the gas, or even a lack of homogeneity between the iron particles and the base fluid i.e. sedimentation. This could prove a significant problem in landing gears, which are only in use for a fraction of an aircrafts flight. Large degrees of sedimentation will inevitability cause excessive damping forces during impact. Consequently, there is a strong requirement for sedimentation resistance in MR fluids for landing gear applications.

Parameter	Symbol/Unit	Value
Valve length	l /mm	14
Valve gap height	h /mm	0.6
Bobbin core radius	t_a /mm	5.79
Flange height	t_b /mm	2.89
Mean valve diameter	d /mm	20.42
Outside diameter	D_p /mm	28
No. of turns of copper wire (Diameter = 0.45mm)	N/-	136

Table 4-1: The optimised valve geometry.

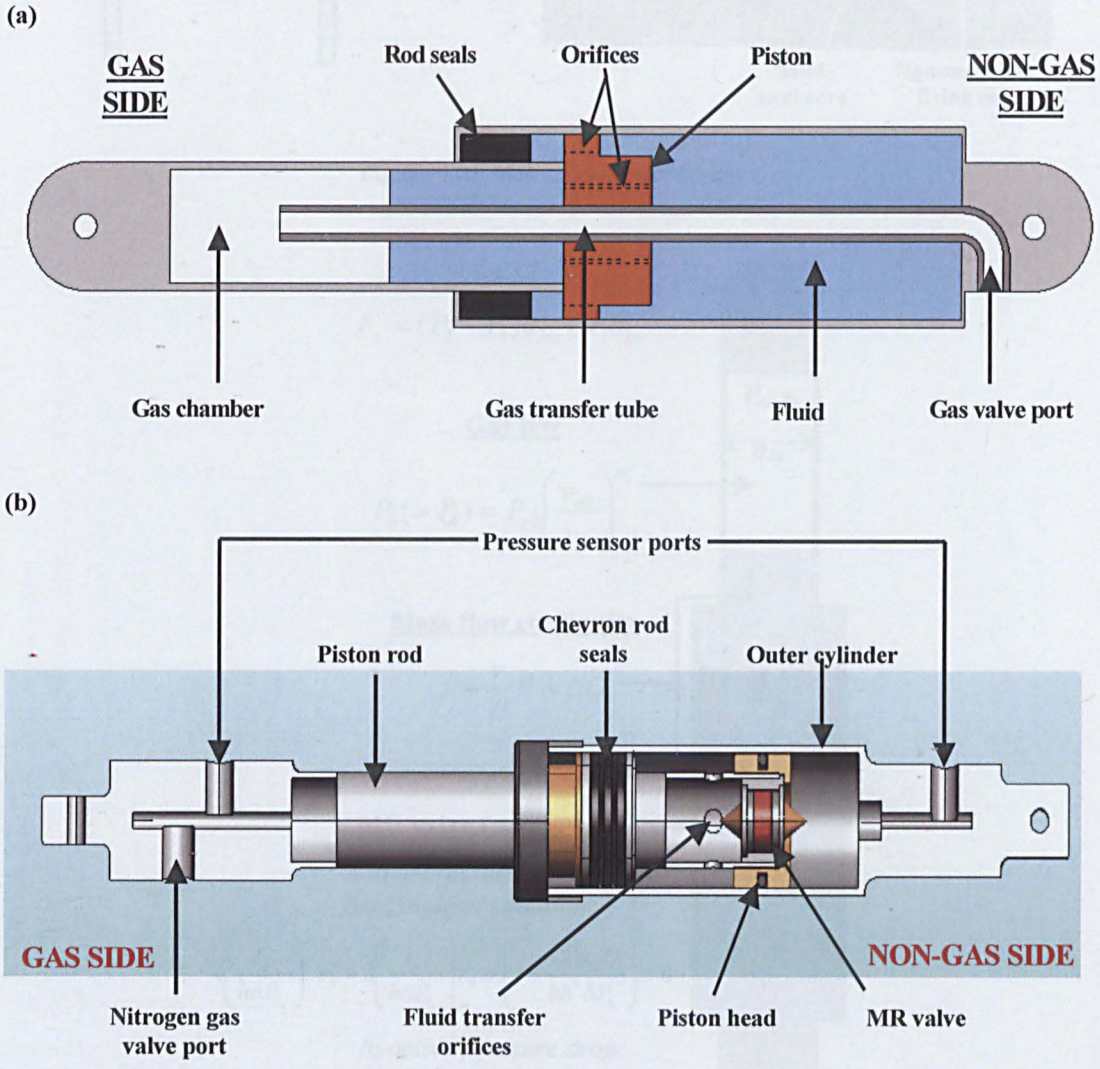

Figure 4-1: Schematic diagrams of the oleopneumatic shock struts. (a) Commercial passive shock strut taken from a RALLYE aircraft and (b) modified shock strut with MR valve.

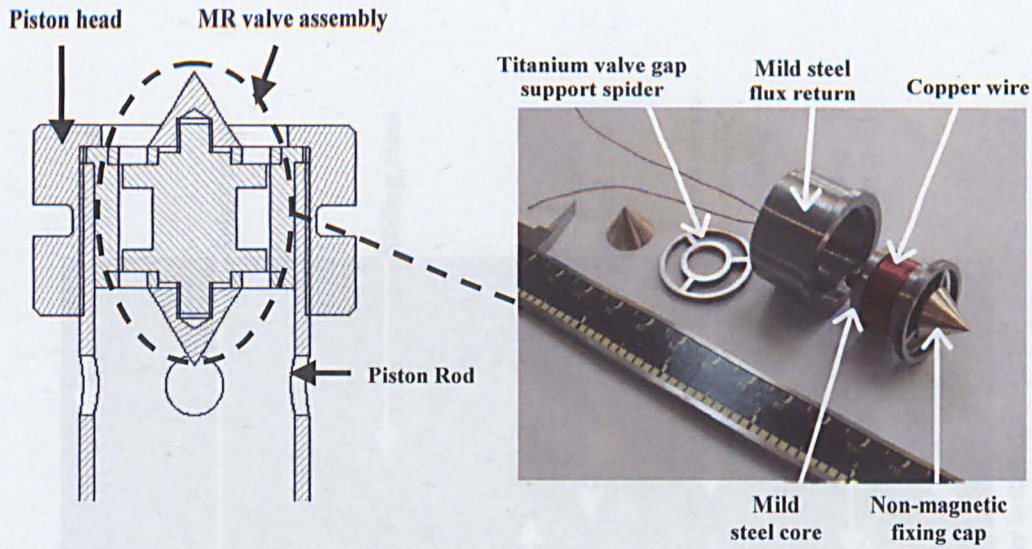

Figure 4-2: MR piston head design

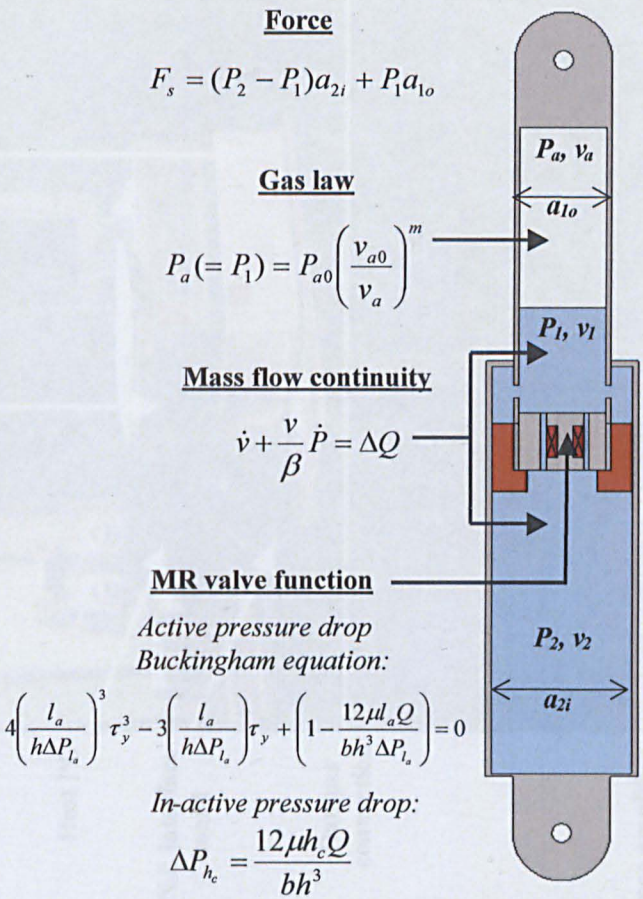

Figure 4-3: Summary of the dynamic MR shock strut model.

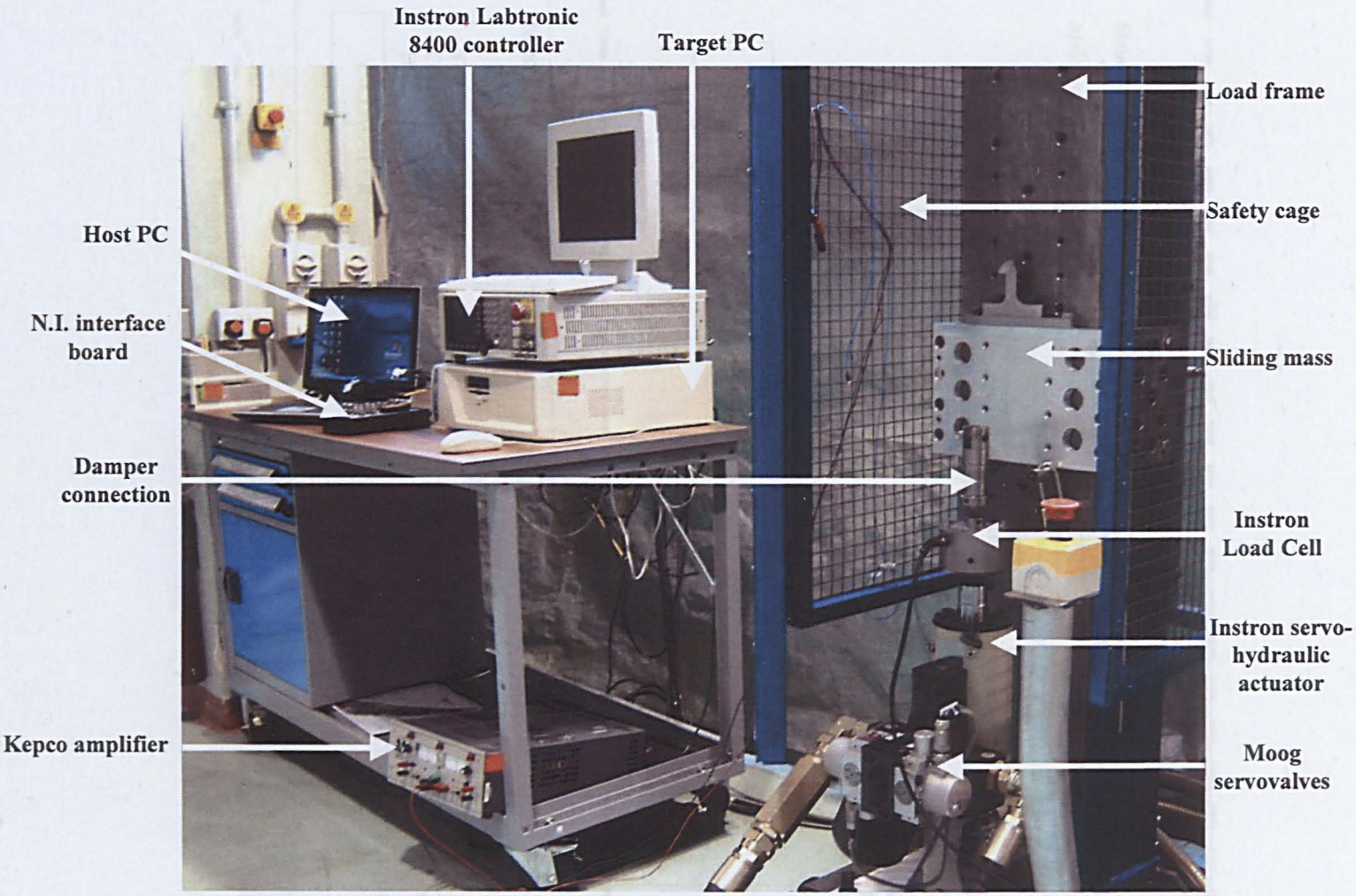

Figure 4-4: Photograph of the experimental facility (without damper installed).

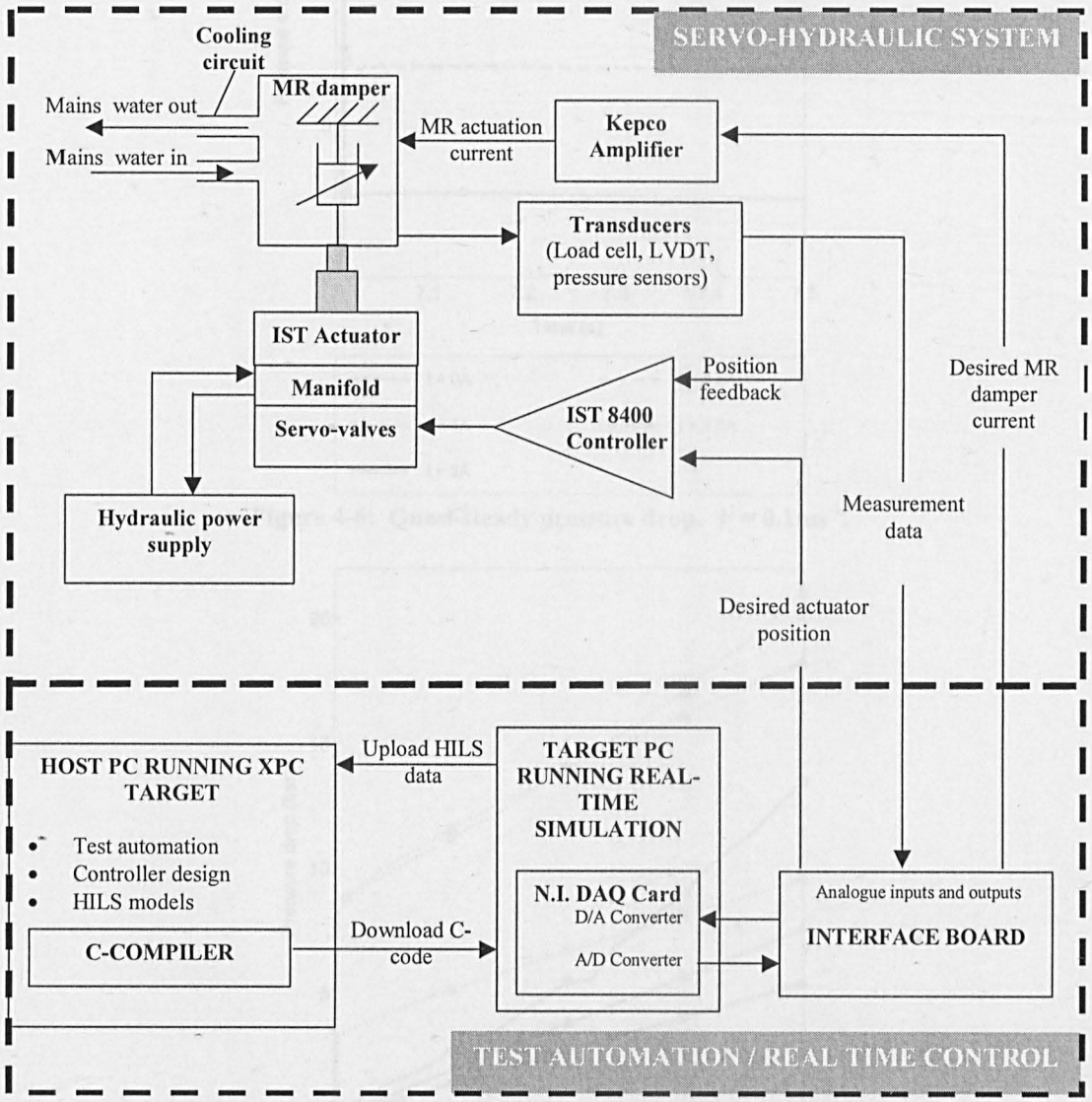

Figure 4-5: Schematic diagram of the experimental facility.

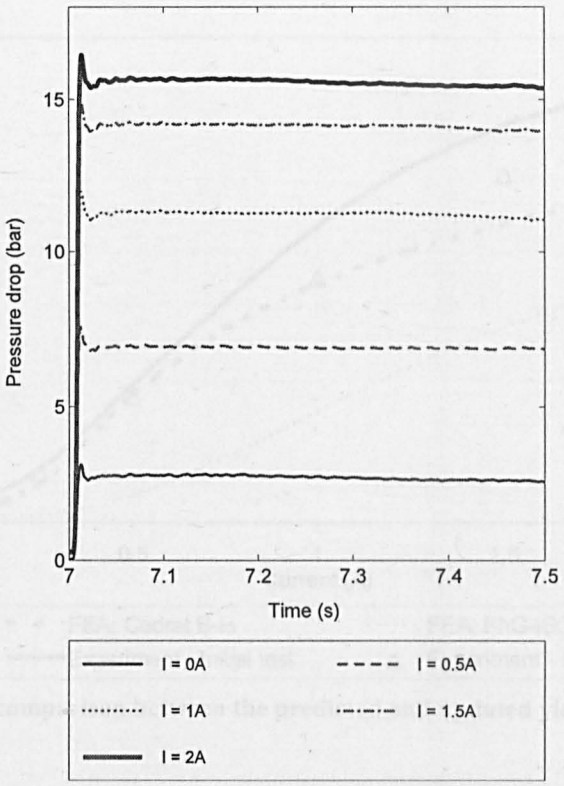

Figure 4-6: Quasi-steady pressure drop. $V = 0.1\text{ms}^{-1}$.

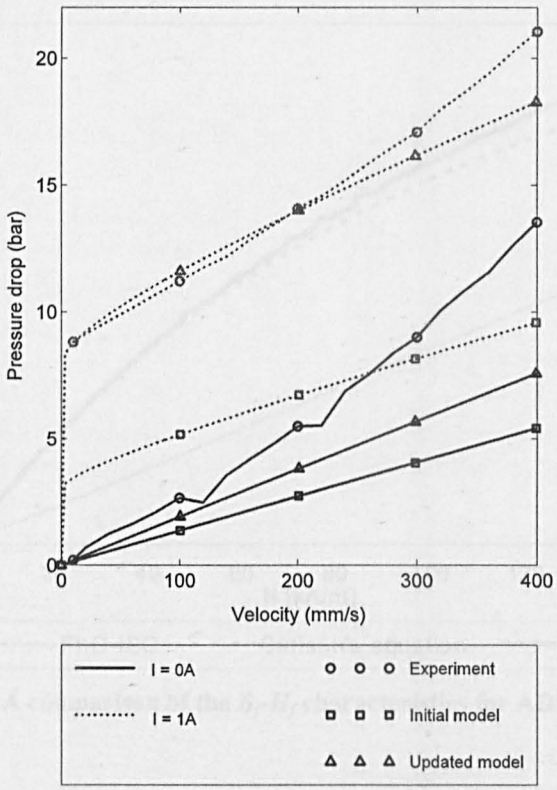

Figure 4-7: A comparison between the modelled and experimental quasi-steady pressure/velocity characteristics.

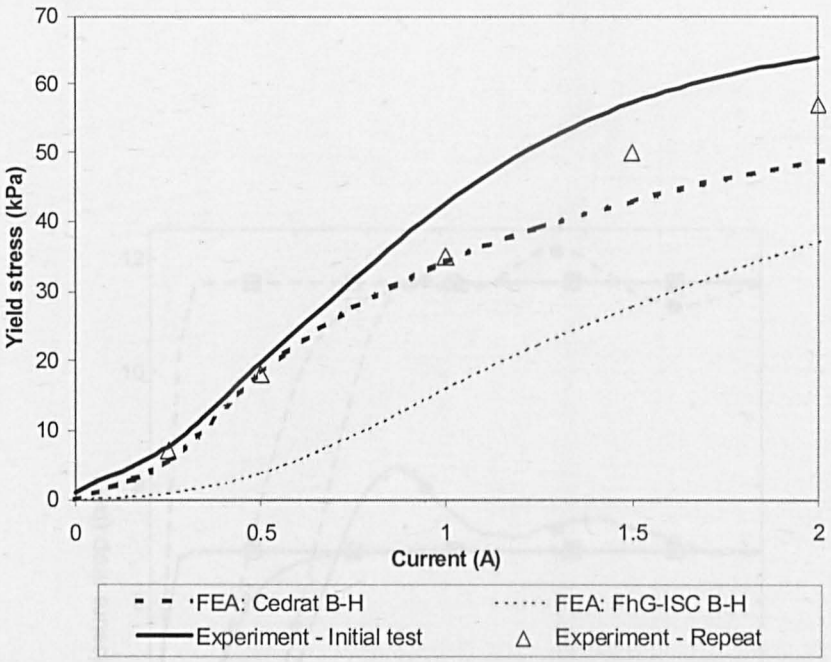

Figure 4-8: A comparison between the predicted and updated yield stress values.

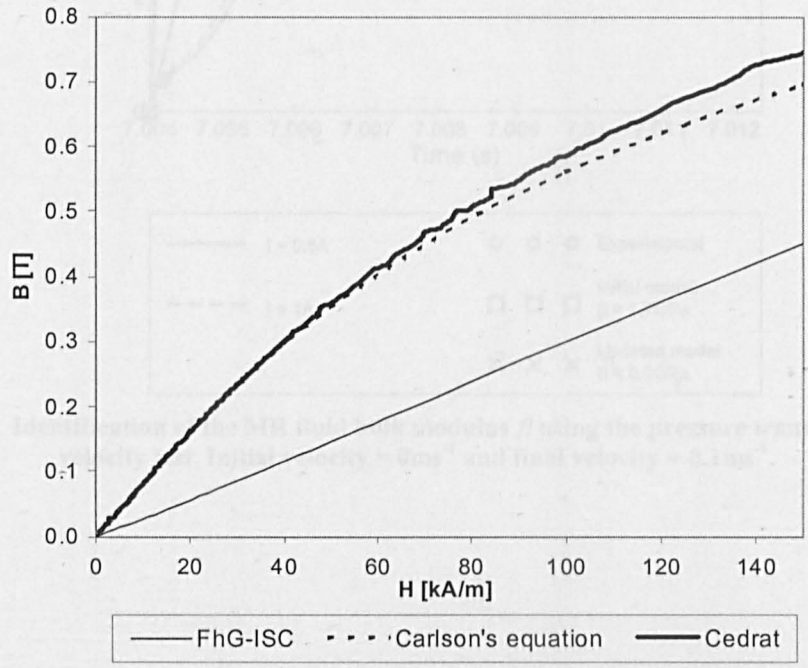

Figure 4-9: A comparison of the B_f-H_f characteristics for AD57 MR fluid.

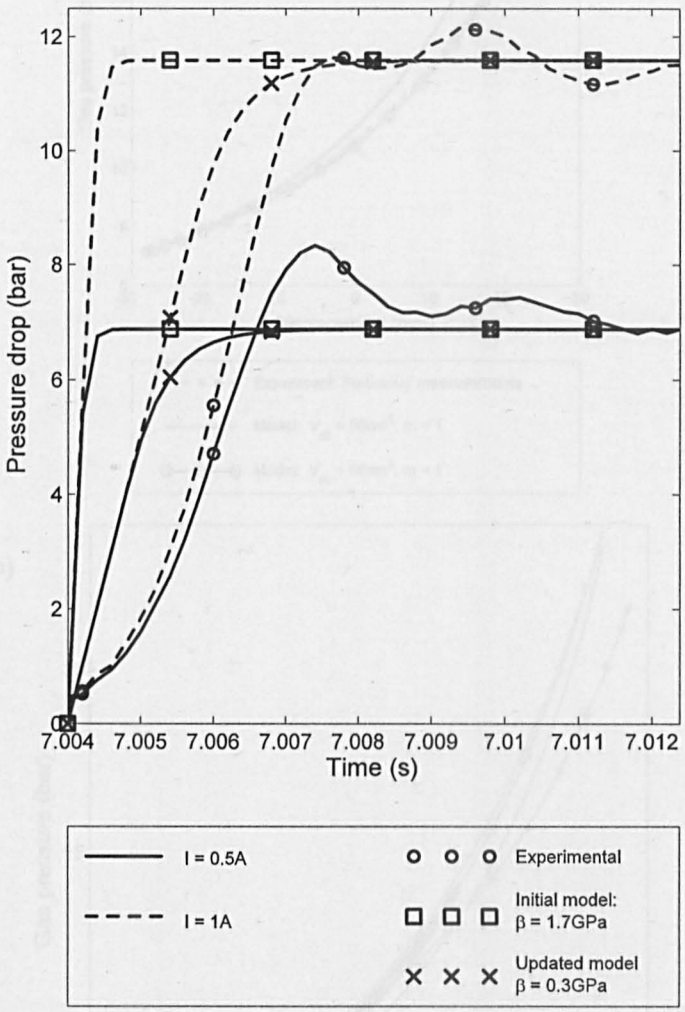

Figure 4-10: Identification of the MR fluid bulk modulus β using the pressure transients in a step-velocity test. Initial velocity = 0ms^{-1} and final velocity = 0.1ms^{-1}.

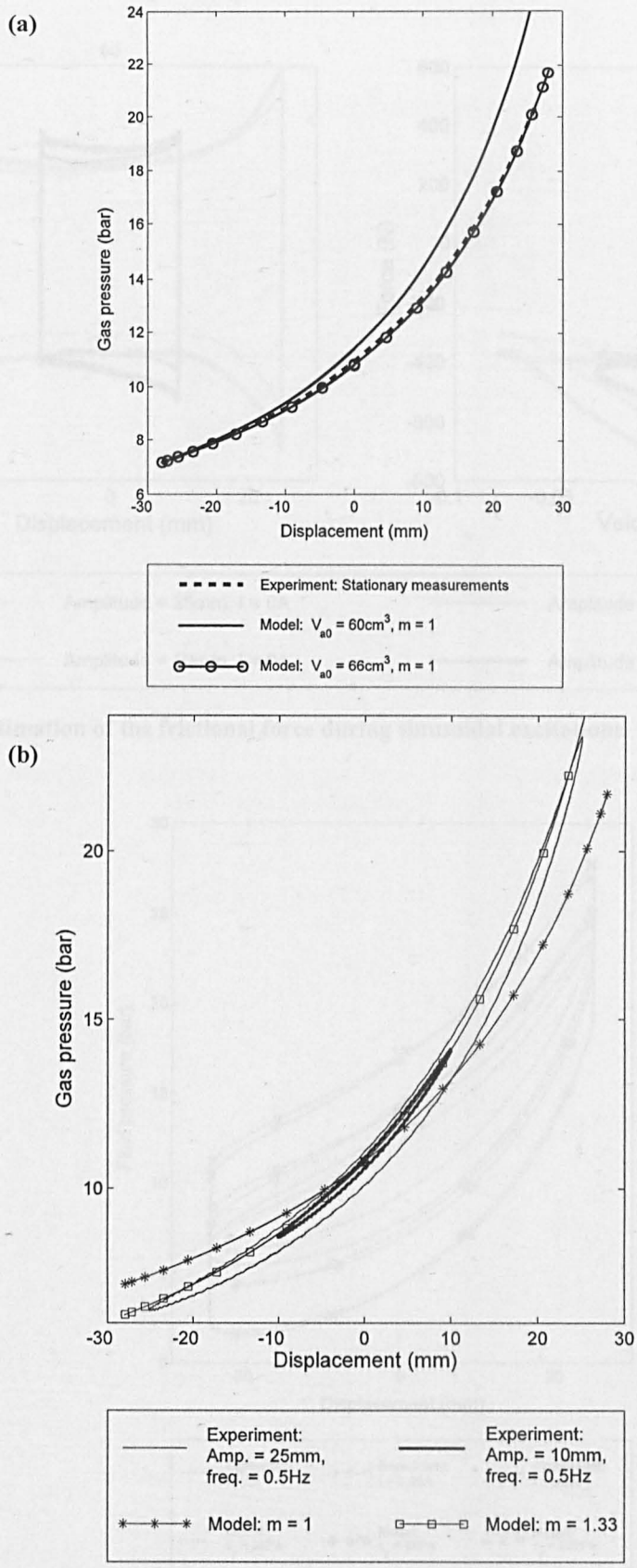

Figure 4-11: Identification of the gas model parameters. (a) Initial gas volume v_{a0} and (b) gas exponent m. β = 0.3GPa.

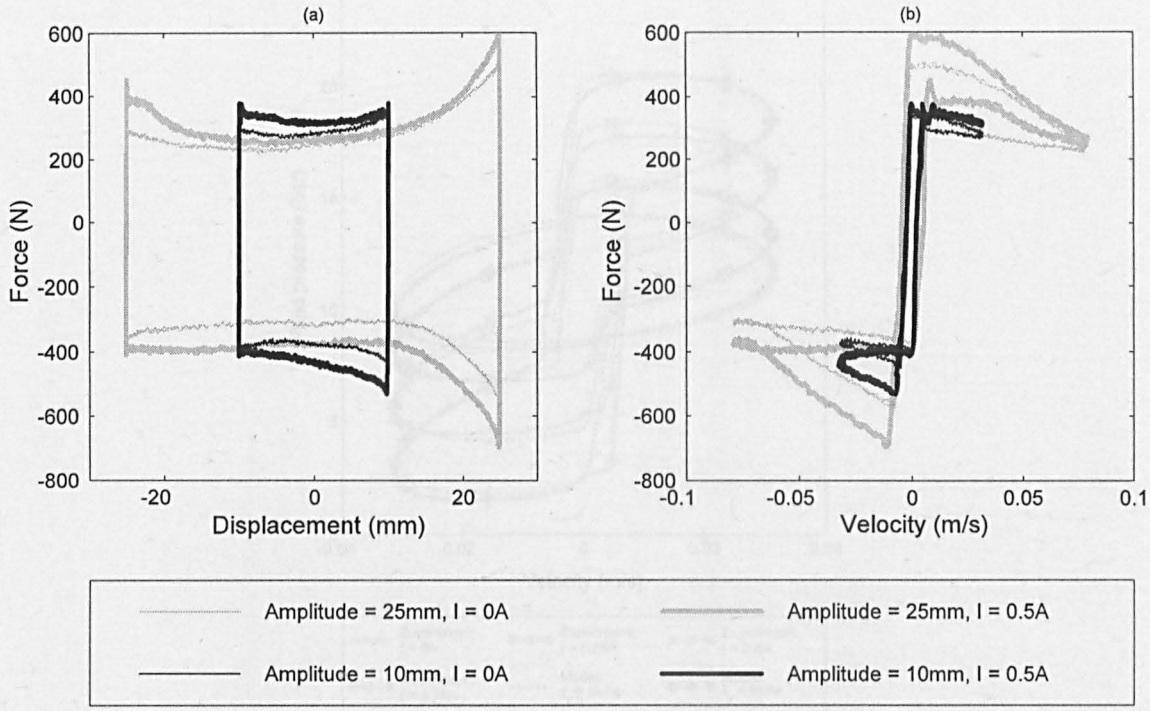

Figure 4-12: Estimation of the frictional force during sinusoidal excitations. Frequency = 0.5Hz.

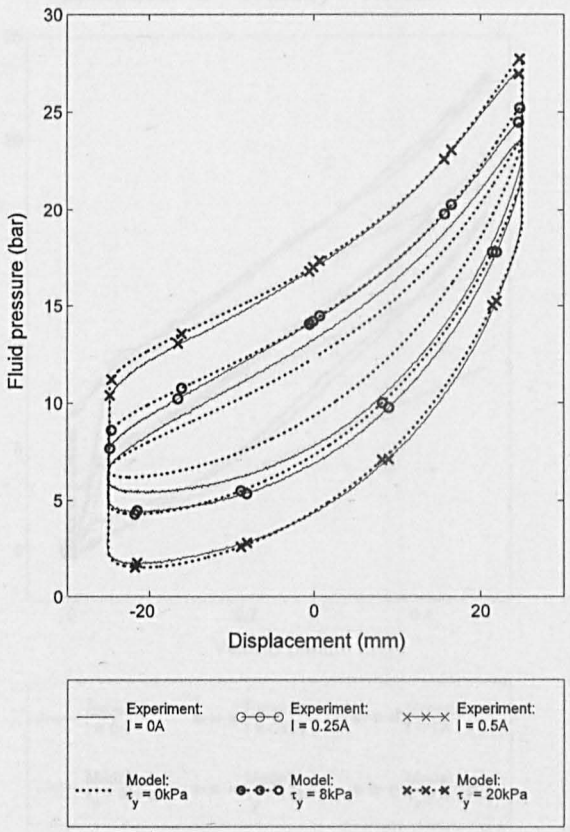

Figure 4-13: Simulated and experimental pressure (non-gas side)/displacement response for a sinusoidal excitation. a = 25mm, f = 0.5Hz.

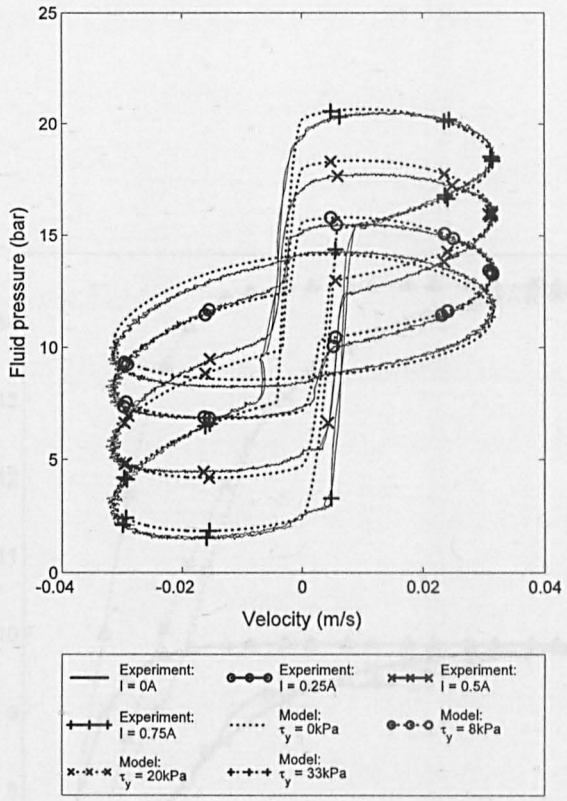

Figure 4-14: Simulated and experimental pressure (non-gas side)/velocity response for a sinusoidal excitation. $a = 10\text{mm}, f = 0.5\text{Hz}$.

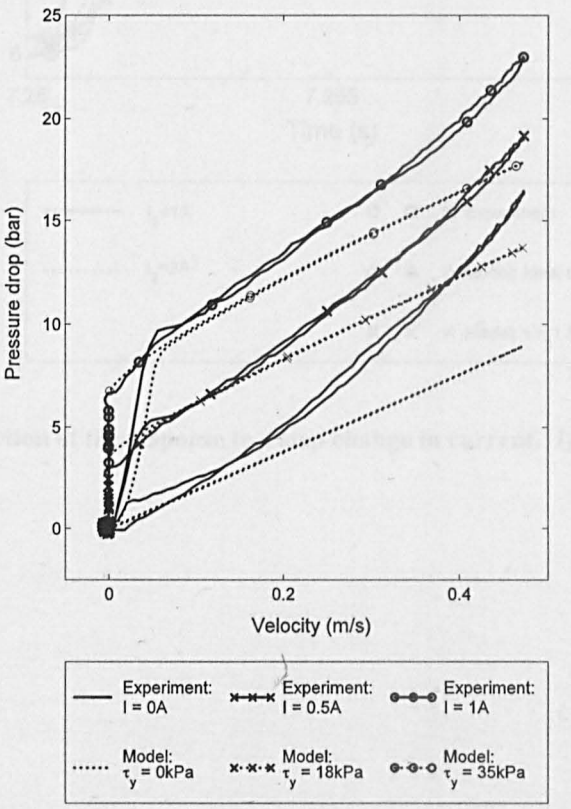

Figure 4-15: Simulated and experimental valve pressure drops during a half-sine test. $a = 25\text{mm}$, $f = 3\text{Hz}$.

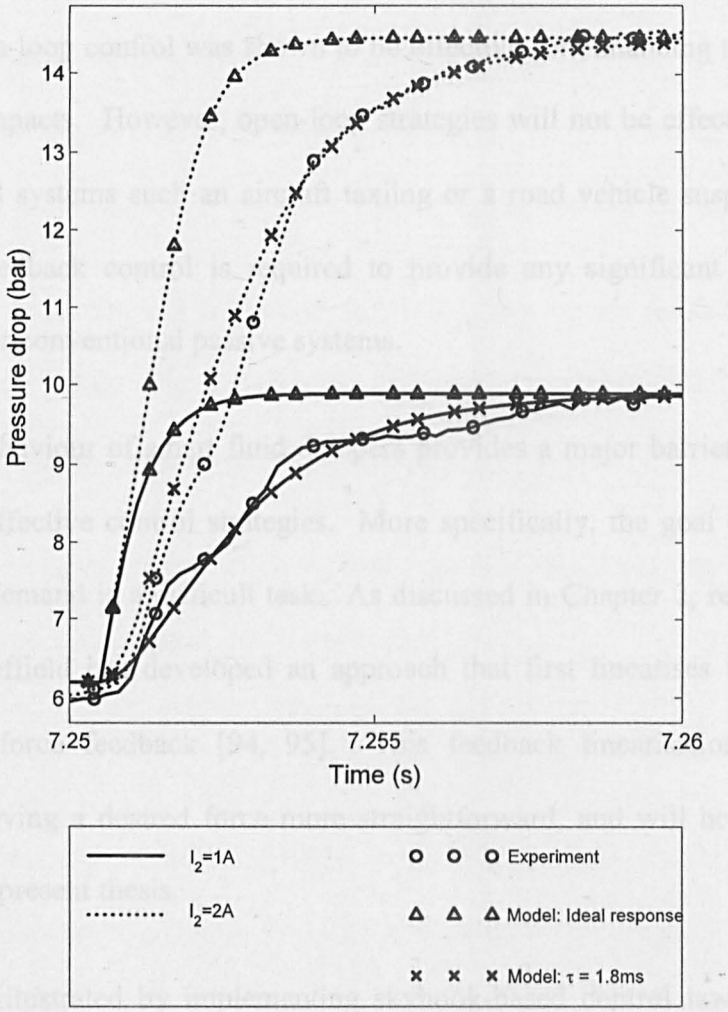

Figure 4-16: Prediction of the response to a step change in current. $I_1 = 0.5$A, $V = 0.1$m/s.

CHAPTER 5. CONTROL OF MR DAMPERS – A NUMERICAL INVESTIGATION

5.1 Introduction

In Chapter 3, open-loop control was shown to be effective for enhancing the efficiency of landing gear impacts. However, open-loop strategies will not be effective for other broadband excited systems such an aircraft taxiing or a road vehicle suspension. For these systems, feedback control is required to provide any significant performance enhancements over conventional passive systems.

The non-linear behaviour of smart fluid dampers provides a major barrier towards the development of effective control strategies. More specifically, the goal of tracking a prescribed force demand is a difficult task. As discussed in Chapter 2, research at the University of Sheffield has developed an approach that first linearises the damper's behaviour using force feedback [94, 95]. This feedback linearisation makes the objective of achieving a desired force more straightforward, and will be investigated extensively in the present thesis.

The approach is illustrated by implementing skyhook-based control laws for single-degree-of-freedom (SDOF) and two-degree-of-freedom (2DOF) vibration systems subject to realistic broadband excitations. Furthermore, the linearised systems are benchmarked against more simplistic on/off control schemes, as well as idealised passive, semi-active and fully active dampers. This is important, as previous studies have not always compared the performance to equivalent passive systems, alternative control designs, or idealised active systems. As a result, it is often difficult to compare the performance of different smart damper control strategies.

The present study is based upon the MR damper model developed by Sims, *et al.* [74], which was briefly described in Section 2.3. New experimental results are used to validate the model under closed-loop conditions with broadband mechanical excitations. Two numerical case studies are then investigated: an SDOF mass-isolator with a variety of broadband excitation signals, and a 2DOF system excited by realistic road profiles [140, 141]. The 2DOF model is configured to represent a vehicle suspension, although the results from the study should be equally applicable to an aircraft taxiing.

At this stage, it is worth pausing to consider the motivation for this generic approach to the control problem, rather than focusing on the specific problem of aircraft taxiing. The key reasons for this generic approach are as follows:

- Vehicle dampers are commercially available. In fact, this study begins by testing Lord Corporation's automotive seat damper [62].

- Roadway models are clearly defined and so excitations can be realistic.

- Hardware-in-the-loop-simulation (HILS) testing (Chapter 6) can be achieved on full-scale vehicle dampers, but not on large-scale aircraft landing gear.

- The control principles are relevant to SDOF systems and vehicles, as well as aircraft.

The present chapter is organised as follows. First, the modelling strategy for the MR damper is described. Next, the theory of feedback linearisation is summarised and experimental results are compared to model predictions. After that, the SDOF control systems are described before presenting the corresponding results, and the 2DOF investigation is then presented in a similar manner. Finally some general issues are

discussed and conclusions are drawn. The research described in this chapter was published in reference [142], and the abstract for this work is given in Appendix A.III. Also, much of the SDOF study was presented at the 11th SPIE International Symposium on Smart Structures and Materials, San Diego, USA [143].

5.2 MR damper model

In earlier work [74, 144] a general modelling approach was described that can be applied to a variety of smart fluid devices, and enables a model updating or system identification procedure to be performed so that the model can be adjusted in line with observed behaviour. In the present study, the model developed by Sims *et al.* [74] will be used, and this model is summarised here for the sake of completeness.

The model is based on Lord Corporation's RD-1005-3 MR damper [37] and a schematic drawing of this device is shown in Figure 5-1(a). This is a flow mode device (see Figure 2-1(a)) where movement of the piston rod forces fluid through an annular orifice. An accumulator is also incorporated to accommodate for the change in the working volume caused by the presence of the piston rod. This introduces an element of stiffness to the damper response, however this was found to be insignificant when compared to the suspension stiffness terms in the SDOF and 2DOF models. Consequently, the effect of the accumulator has been neglected in the development of the MR damper model.

The form of the model is a bi-viscous damper in series with a mass and a linear spring, as shown in Figure 5-1(b), and can be strongly linked to the constitutive behaviour of the device. For example, the valve flow (which is assumed to be quasi-steady) is represented by the non-linear function χ and is a function of the quasi-steady velocity

$\dot{x}_1$ and the control signal I to the smart damper. The spring element of stiffness k is incorporated to account for fluid compressibility and the lumped mass m_1 represents fluid inertia. The co-ordinate x_2 corresponds to the displacement of the damper piston.

The resulting physical significance means that parameters can initially be chosen based on constitutive relationships using fluid properties such as bulk modulus, viscosity and yield stress [63]. However, in practice, fluid properties may vary between devices, for example due to environmental effects or manufacturing tolerances. Consequently, a model updating procedure is desirable so that the model accurately predicts observed behaviour. This procedure has been adopted to form an accurate model of the commercial MR damper used in this study. A description of this model updating procedure is detailed by Sims et al. [74].

Figure 5-2 compares a typical set of predictions from the updated model with the corresponding test data for a range of sinusoidal excitation conditions. The model results agree very well with observed behaviour. The previous study [74] also validated the model under non-sinusoidal test conditions, making the model an appropriate tool for the present investigation. Furthermore it was demonstrated that the dynamics of the electro-magnetic circuit and smart fluid rheology could be modelled using a first order lag term, where a time constant between 3-5ms was shown to be adequate. Throughout this study, a 3ms device time constant has been used as part of the controlled MR systems.

5.3 Feedback linearisation

The non-linear behaviour of smart fluid dampers makes the objective of achieving a desired force very difficult. Researchers at The University of Sheffield have developed

one solution to this problem using feedback linearisation, which is briefly summarised below.

The control strategy is shown in block diagram form in Figure 5-3(a). Here, feedback control is being used to implement a semi-active force generator. Through appropriate selection of the feedforward gain G, and the feedback gain B, it can be shown how the actual damping force F becomes equal to the desired set-point damping force F_d [94]. If the set-point force is proportional to the piston velocity then the force/velocity response is linearised. The values of G and B were previously determined through extensive experimental testing on the MR damper, which led to G = 0.0015 and B = 0.6. For a detailed description of the methodology that was used to arrive at these values, the reader is referred to Sims, *et al.* [94, 95].

Figure 5-3(b) shows schematically how feedback linearisation can be integrated within a vibrating structure such as a mass-isolator or vehicle suspension. Here, the linearised damper is able to track a force demand derived from a separate controller, for example a skyhook or optimal controller. However, the desired force will only be met if it lies within the control limits imposed by the device geometry and MR fluid properties. This is better described with the help of Figure 5-4, which illustrates the control envelope of the MR damper. If the desired force lies within this envelope, then feedback linearisation can accurately achieve that force. However if an energy input is required i.e. the desired force lies within quadrants 2 and 4, or if a dissipative force requirement (within quadrants 1 and 3) is lower than that governed by the base viscosity of the fluid (I=0A), then this force cannot be achieved. In this scenario, the MR damper will remain in its 'off' state to minimise the energy dissipated. Alternatively, if the desired force is

a dissipative one and exceeds the upper boundary of the control envelope (I=2A), then the damper current will saturate at its maximum level to maximise the energy dissipated.

5.4 Validation

In previous work, the proposed linearisation technique was shown to be effective for an ER damper under sinusoidal mechanical excitation [94, 95]. However, the present study was based upon a model of a commercially available MR damper and the simulated mechanical excitation was non-sinusoidal. Consequently it was necessary to validate this model under closed-loop conditions with a broadband mechanical excitation.

To achieve this, the MR damper was mounted in the servohydraulic test machine described in Section 4.3, and excited with a broadband command signal. This was generated by filtering a white noise signal to reduce its high frequency content (i.e. above 25Hz) to within the duty of the MR damper. Meanwhile, the xPC real-time digital signal processing system (see Figures 4-4 and 4-5) was used to implement the feedback linearisation strategy. With reference to Figure 5-3(a), the set-point F_d was made proportional to the mechanical excitation velocity:

$$F_d = DV \tag{5-1}$$

Here, V is the damper excitation velocity (equivalent to $\dot{x}_2$ for the model shown in Figure 5-1) and D is a controller set-point gain. The feedback strategy should result in viscous damping behaviour with an effective damping rate equal in value to the controller gain D.

Figure 5-5 shows a sample of the input displacement signal and Figure 5-6(a) shows the resulting experimental force/velocity responses for a range of set-point gains between D = 2kNs/m and D = 20kNs/m. Shown superimposed are straight lines of slope D, which represent the idealised responses. Very good linearisation is demonstrated for values of D between 2 and 10kNs/m thus validating the controller's behaviour under broadband excitation. For the set-point D = 20kNs/m, the control limits of the MR damper can be observed. For example, the force beyond ± 0.08m/s is less than the ideal viscous force, resulting in a non-linear response (owing to saturation).

To validate the model under closed-loop conditions, Figure 5-6(b) shows the simulated linearised responses under identical excitation and controller conditions as for the experiment. Again, highly linear characteristics can be observed with the actual responses closely matching the ideal responses. Moreover, the simulated results correlate very well with the experiment and the onset of saturation in the response (D=20kNs/m) is predicted accurately.

5.5 SDOF study

Having demonstrated the experimental and simulated performance of the feedback linearisation strategy under broadband excitation, the approach will now be used as part of a simulated mass-isolator vibration problem. The performance will be benchmarked against a range of idealised systems and an on/off control strategy. For each system, the input excitations and, where applicable, the MR damper model were identical in order to permit a direct comparison between them. The mass-isolator and damper control configurations are now described, before presenting the simulated results.

5.5.1 Mass-isolator configurations

The basic parameters for the mass-isolator were chosen to give a system natural frequency of 5Hz and a damping ratio of 0.1 when the MR damper was in its 'off' state. This frequency is well within the range of frequencies validated experimentally and resulted in a mass M of 115kg and a spring stiffness K_{iso} of 113.5kN/m. Three different broadband displacement inputs were investigated for each system. The first input was generated with a constant velocity amplitude (i.e. white noise) over the frequency range 0-100Hz. The second and third inputs were generated by passing this signal through a finite impulse response filter, designed with a least-squares method to produce cut-off frequencies at 25Hz and 10Hz respectively.

Five damper configurations were investigated and these are described below.

- **Passive system**

Previous studies have not always compared the performance of MR systems to equivalent passive systems. For example, investigators commonly use the MR damper in its 'on' or 'off' state to represent a passive suspension [85]. In the 'off' state, the damping is likely to be less than that of a well-damped passive device, whereas in the 'on' state the damping will be higher than a well-damped passive device. A more realistic passive benchmark was used in the present study where the damping force was generated by a viscous damper with damping coefficient C_p as shown in Figure 5-7(a). C_p was varied to optimise the passive system response to enable a true performance comparison with the MR systems.

- **MR linearised skyhook control**

As described in Chapter 1, skyhook control is where the damping force is proportional to the *absolute* velocity of the isolated mass (see Figure 1-2). This is optimal for an SDOF system and enables the resonant vibrations to be suppressed without degradation of the higher frequency response (see Figure 1-3(b)). Under certain conditions skyhook control requires an energy input, but feedback linearisation can be utilised to accurately achieve the skyhook force within the semi-active limits of the MR damper (see Figure 5-4). With reference to Figure 5-7(b), the set-point force is given by:

$$F_d = D_{MR}\dot{x}_m \tag{5-2}$$

The controller subsystem of Figure 5-7(b) corresponds to that shown in Figure 5-3(a).

- **On/off skyhook control**

In semi-active vibration control, on/off skyhook control strategies are commonly investigated [22, 88]. The strategy involves switching the input current to a predetermined and constant level when the force required by the skyhook control law is a dissipative one:

$$I = I_{\max} : \dot{x}_m(\dot{x}_m - \dot{x}_b) > 0 \text{ - Energy dissipation required} \tag{5-3}$$

$$I = 0 : \dot{x}_m(\dot{x}_m - \dot{x}_b) \le 0 \text{ - Energy input required} \tag{5-4}$$

The controller gain I_{max} dictates the current applied in the 'damper on' condition. Since no force feedback is required, the need to measure or estimate the damping force is eliminated. On/off skyhook control therefore represents a major simplification over the linearised skyhook controller. However, the performance may suffer, and by studying

the behaviour of the two controllers under identical circumstances, a fair comparison can be made.

- **Fully active skyhook control**

In this system, the desired skyhook force was assumed to be produced by an ideal force actuator capable of instantaneously supplying and dissipating energy. This represents the ideal skyhook system and will act as an upper boundary of performance for the MR damper systems. The fully active system is shown in Figure 5-7(c), where the force F is given by:

$$F = D_{IS}\dot{x}_m \tag{5-5}$$

- **Ideal semi-active skyhook control**

In this system the desired skyhook force is achieved only if the force is a dissipative one, otherwise zero damping force is transmitted i.e:

$$F = D_{SAS}\dot{x}_m \quad \dot{x}_m(\dot{x}_m - \dot{x}_b) > 0 \tag{5-6}$$

$$F = 0 \quad : \dot{x}_m(\dot{x}_m - \dot{x}_b) \leq 0 \tag{5-7}$$

This will act as a more realistic upper performance boundary for the MR based systems.

5.5.2 SDOF Results

First, the MR linearised skyhook system is compared with the fully active skyhook system. Figure 5-8(a) shows the transmissibility curves, obtained using Welch's numerical method [145], for the displacement input filtered to 25Hz. The passive response for C_p = 2kNs/m is also shown since, of all the passive damping rates for this particular input, it had the lowest root-mean-square (RMS) acceleration, which is an

important performance indicator. As expected, the fully active system improves both the low and high frequency response with increasing controller gain D_{IS}. This is superior to the MR system where a slight degradation in the high frequency response is observed with increased controller gain D_{MR}. Nonetheless, there is a significant improvement over the passive system.

Figure 5-8(b) compares the transmissibility curves, again for the displacement input filtered to 25Hz, between the linearised MR skyhook system and the idealised semi-active skyhook system, which represents a more realistic performance benchmark. For skyhook gains of 3kNs/m, it can be seen how the frequency response of the MR system around the natural frequency is better than the ideal semi-active system, but worse at higher frequencies. For skyhook gains of 6kNs/m, the semi-active system is superior throughout the frequency range.

Figure 5-8(c) compares the transmissibility curves between the linearised MR skyhook and the on/off MR skyhook systems. Much like a passive system, there is a clear compromise between the low and high frequency performance of the on/off system with increasing controller gain I_{max}. For example, the low frequency response is superior to the MR system for large gains, but this is at the expense of a poorer high frequency response compared to both MR and passive systems.

It is difficult to get a clear indication of the relative performance between the above systems using transmissibility plots alone. For example, a trade-off has been demonstrated between the low and high frequency responses when the controller gain is increased and thus it becomes difficult to determine an optimum value. Direct comparison is made more straightforward when a conflict diagram is used. This is

where the RMS value of one performance indicator is plotted against that for another, as a controller gain is varied. This not only helps to optimise the control systems but also gives clarity on the inevitable trade-offs between the performance indicators themselves. Suitable performance indicators are the RMS acceleration, which represents the severity of the vibration of the mass, and the RMS working space, which is a common design constraint. The conflict diagram has also been used as a means to compare the three different displacement inputs. Figure 5-9 presents the conflict diagrams for each of the input excitations.

In the case of the input signals filtered to 10Hz (Figure 5-9(a)) and 25Hz (Figure 5-9(b)), feedback linearisation is seen to enhance RMS acceleration compared to the on/off control strategy. For the unfiltered input signal containing frequencies up to 100Hz (Figure 5-9(c)), there appears to be no significant advantage gained by implementing feedback linearisation, where RMS acceleration levels are similar to the on/off system.

With regards to the benchmark systems, Figure 5-9 demonstrates how the ideal semi-active and fully active skyhook systems are superior in terms of acceleration, but this is at the expense of larger working spaces. Furthermore, the performance benefits of a fully active system are substantially better than the ideal semi-active system if larger working spaces can be tolerated.

To better illustrate the relative performance between systems, optimum controller gains (i.e. D_{MR}, D_{IS}, D_{SAS}, I_{max} and C_p) were chosen for the input signal filtered to 10Hz such that RMS acceleration was minimised. These gains, which are shown in Table 5-1, were then maintained for all three excitation conditions and the resulting performance is

indicated on Figure 5-9. Figure 5-10 then compares the percentage performance improvements of the controlled systems over the optimised passive system at the chosen operating points. For the signal filtered to 10Hz, this resulted in a 25% reduction in RMS acceleration for the linearised system compared to a 15% reduction for the on/off system. The optimised on/off system performs quite well, but when analysing the position of the operating points on Figures 5-9(b) and 5-9(c), a key advantage of feedback linearisation becomes apparent. From Figure 5-10, it can be observed how RMS acceleration for the linearised system remains consistently low regardless of the input conditions. By comparing Figures 5-9(a) and 5-9(b), this arises because the shape of the conflict curve, and thus the optimum controller gain D_{MR}, remains unchanged. On the other hand, the on/off system is very sensitive to the input conditions and RMS acceleration levels are degraded as frequency content increases. This occurs because of the change in shape of the conflict curve between Figures 5-9(a) and 5-9(b), which also explains the improved working space levels. Therefore the 'straightforward' on/off system may in fact need a rather more complex control strategy to alter the controller gain according to input excitation. This would be necessary to ensure that its implementation is justifiable against its passive counterpart.

For the linearised system subject to the unfiltered signal (Figure 5-9(c)), there is a change in shape of the conflict curve compared to Figures 5-9(a) and 5-9(b). However performance does not suffer due to its shallow gradient. It should be noted that the accuracy of the results presented in Figure 5-9(c) and Figure 5-10(c) is less certain, because the MR damper model does not take into account high frequency behaviour, and has not been validated above 25Hz. At high frequencies, seal friction effects and device joints may have an important role. Also, the attenuation of high frequency

vibrations is likely to be outside the duty of the isolator, due to the compliance of the mechanical connections and bushings.

To illustrate performance of the benchmark systems, Figure 5-10(a) demonstrates a 64% improvement in acceleration for the fully active system compared to 36% for the ideal semi-active system. This is clearly superior to the MR systems, however the corresponding working spaces are 58% and 18% worse than the passive system respectively. This is a consistent result across the range of excitation conditions.

5.6 2DOF Study

The results presented so far have demonstrated the relative performance of two MR damper control strategies, compared to ideal passive, semi-active and fully active dampers. In this section, the analysis is repeated using a two-degree-of-freedom system that is representative of a vehicle suspension problem. As before, the same input excitations and MR damper model (where applicable) were used for each control system in order to permit a direct comparison between the control strategies.

It should be mentioned that the MR damper under investigation was not specifically designed for use in a primary vehicle suspension. However, the intention here is not to fine-tune the actual device for a specific vehicle but rather to demonstrate the performance potential of linearising an MR damper to implement semi-active vehicle control strategies. For this purpose, a simplified vehicle model serves as a useful case study. The vehicle model is first described before presenting the simulated results.

5.6.1 Quarter car model

In the design of suspension for passenger vehicles, it is desirable to achieve low levels of car body acceleration, thus ensuring passenger comfort, and adequate control of dynamic tyre loads, thus ensuring vehicle safety and stability. The dynamic tyre load is associated with the reduction in a tyre's ability to generate shear forces if the load on it is fluctuating substantially about the mean value. A relatively low value of dynamic tyre load implies relatively little impairment of shear force generation and hence good vehicle manoeuvrability due to road roughness [7]. This must be designed within a finite amount of space, which acts as a constraint to the designer. The three main criteria often used to assess vehicle performance are therefore:

- RMS vehicle body acceleration,
- RMS dynamic wheel contact force,
- RMS suspension working space.

It transpires that these fundamental features of suspension design are effectively captured in the quarter car model [15] which has therefore been used in this study. Figure 5-11(a) shows a schematic quarter car model with an idealised passive suspension. Parameters were chosen so as to represent a typical family saloon car and are shown in Table 5-2. To characterise performance, the above three performance indicators were calculated, where lower values correspond to superior performance levels.

5.6.2 *Quarter car configurations*

Five configurations of suspension damper were investigated and these configurations are described below.

- **Passive**

As for the SDOF study, the passive quarter car model (shown in Figure 5-11(a)) was investigated to provide a useful performance benchmark to assess the MR systems. The damping coefficient C_p was varied between 1kNs/m and 5kNs/m, which approximately corresponds to sprung mass damping ratios between 0.2 and 1.

- **MR linearised modified skyhook control**

For 2DOF systems such as the quarter car, it is well known that skyhook control attenuates vibration at the natural frequency of the sprung mass but has an adverse effect at the natural frequency of the wheel mass (wheel hop frequency) [3, 146, 147]. This has led to an alternative strategy known as modified skyhook control, which combines the concept of skyhook damping with passive damping in an attempt to gain the advantages of both [22]. This is particularly advantageous for a semi-active device since the introduction of passive damping means that the control law will dissipate power more frequently. Consequently, the semi-active damper will approach more closely the behaviour of an ideal actuator [3]. With reference to Figure 5-11(b) and Figure 5-3(a), the set-point control force F_d is given by:

$$F_d = D_{MRm}(\alpha(\dot{x}_c - \dot{x}_w) + (1-\alpha)\dot{x}_c) \tag{5-8}$$

Here, α is a weighting parameter between 0 and 1. $\alpha = 1$ corresponds to a viscous set-point damping force thus emulating the passive system and $\alpha = 0$ corresponds to a pure

skyhook set-point force. As before, the desired force will only be achieved accurately if it is within the control limits of the MR damper (see Figure 5-4).

- **On/off modified skyhook control**

The input current for the on/off controller is given by:

$$I = I_{max}: \ (\alpha(\dot{x}_c - \dot{x}_w) + (1-\alpha)\dot{x}_c)(\dot{x}_c - \dot{x}_w) > 0 \ \text{- Energy dissipation required} \tag{5-9}$$

$$I = (\alpha(\dot{x}_c - \dot{x}_w) + (1-\alpha)\dot{x}_c)(\dot{x}_c - \dot{x}_w) \le 0 \ \text{- Energy input required} \tag{5-10}$$

- **Fully active modified skyhook control**

With reference to Figure 5-11(c), the ideal damping force F is given by:

$$F = D_{ISm}(\alpha(\dot{x}_c - \dot{x}_w) + (1-\alpha)\dot{x}_c) \tag{5-11}$$

- **Ideal semi-active modified skyhook control**

Again referring to Figure 5-11(c), the ideal semi-active damping force is given by:

$$F = D_{SASm}(\alpha(\dot{x}_c - \dot{x}_w) + (1-\alpha)\dot{x}_c): \ \dot{x}_c(\dot{x}_c - \dot{x}_w) > 0 \tag{5-12}$$

$$F = 0 \ : \ \dot{x}_c(\dot{x}_c - \dot{x}_w) \le 0 \tag{5-13}$$

5.6.3 Real road disturbance

In order to realistically assess the capability of the MR damper as part of a vehicle suspension, a broadband random signal, representative of a typical road profile was generated to provide an input to the quarter car model. The profile of a single track along the length of a road surface can be approximately described by a displacement power spectral density function (PSD) $S(\psi)$ at wave-number ψ (cycles/m) as follows [140]:

$$S(\psi) = C\psi^{-w}\left(\frac{m^2}{cycle/m}\right) \tag{5-14}$$

Here, C and w are fitting constants describing the severity of road roughness. The wave-number ψ is given by f/V_c, where f is the vibration frequency and V_c is the vehicle speed. Consequently, for a given vehicle speed, the inverse fast Fourier transform can be used to determine the road surface heights in the time domain [141]. Motorway, principal and minor road excitations were generated with frequency content between 0 to 15Hz. Table 5-3 shows the corresponding values of C, w and V_c and Figure 5-12 shows a typical motorway excitation in the time and frequency domain.

5.6.4 2DOF Results

To begin, Figure 5-13(a) shows the PSD of wheel contact force for the MR linearised modified skyhook system. The responses shown are for the motorway excitation and are compared to the passive system with C_p = 2kNs/m, which corresponds to a damping ratio of 0.4. For the MR system, responses are shown for a range of α with controller gain D_{MRm} = 3kNs/m. In the pure skyhook case (α = 0), the vibration at the sprung mass natural frequency has been significantly reduced but, as expected, an adverse effect at the wheel hop frequency is observed. It can be seen how increasing α, and thus augmenting the system with passive damping, improves this by allowing the magnitudes of the two resonant peaks to be compromised against one another. Through appropriate parameter selection, the MR system is clearly superior to the passive system.

Similarly, Figures 5-13(b) and 5-13(c) compare the motorway PSD plots of the passive system with the fully active and ideal semi-active modified skyhook systems

respectively. Skyhook gains equal to 3kNs/m have been used in both cases. A key difference between the fully active/ideal semi-active systems and the MR linearised system is in the mid frequency range (3-9Hz), where the fully active/ideal semi-active systems achieve much lower vibration levels. Reducing the damping rate at 0A, for example by changing vehicle parameters or fluid properties, should improve the MR system in this range and push the performance levels nearer to the ideal semi-active system. It can also be observed how the performance levels of fully active and ideal semi-active systems are similar for values of α which give acceptable levels of wheel hop vibration.

Next, the on/off modified skyhook system is investigated. Figure 5-13(d) shows the PSD of wheel contact force for the controller gain I_{max} = 0.06A. Again, the motorway excitation has been used as an example. The vibration at the sprung mass natural frequency is clearly lower than the passive system, however the wheel hop response is very poor with no significant gain in performance when α is increased. A pure skyhook strategy ($\alpha = 0$) is therefore optimal for the on/off control strategy.

As with the SDOF system, the conflict diagram can be used to optimise and compare each control strategy. For the quarter car model, these have been constructed by plotting RMS car body acceleration and RMS wheel contact force versus the RMS suspension working space for each road excitation. Figure 5-14 shows the resulting conflict curve comparing each vehicle configuration subject to the motorway excitation. The modified skyhook systems have already been optimised in terms of the controller gain (D_{MRm} = 3kNs/m, D_{ISm} = 3kNs/m and D_{SASm} = 3kNs/m) where that value which best minimised car body acceleration was chosen. With the exception of on/off control

(where it has already been established that skyhook control is optimal), each curve shown corresponds to the range α = 0-1. The on/off conflict curve corresponds to a range of controller gains I_{max} for α = 0 and the passive response corresponds to the range C_p = 1-5kNs/m.

As shown in the SDOF study, the MR linearised modified skyhook system is superior to the on/off controller. Nonetheless, the on/off controller does perform well, outperforming the passive system. The superiority of the linearised system is more obvious in terms of wheel contact force because, unlike the on/off controller, MR linearised modified skyhook control is able to suppress the wheel hop vibrations. However, RMS wheel contact force for the linearised system is still on a par with the passive system. This is partly due to the way in which the controller gains were optimised in terms of car body acceleration as outlined previously. It is well known that ride comfort will be traded off against vehicle handling and optimising the controller gain in terms of wheel contact force should improve this result.

To investigate the effect of the operating conditions on performance, a specific operating point (α or I_{max}) has been chosen and maintained for the three excitation conditions (motorway, principal and minor road). The performance of each controlled system has then been rated as a percentage improvement over the passive system with C_p=2kNs/m (which corresponds to a damping ratio of 0.4). The operating points were chosen, using the motorway conflict diagram (Figure 5-14), so as to minimise car body acceleration whilst maintaining adequate wheel contact force and suspension working space levels that are similar to the passive system. The corresponding operating points are indicated on Figure 5-14 and are tabulated in Table 5-4, and Figure 5-15 shows the

results in graphical form. By first taking the motorway excitation as an example, the linearised system demonstrates a 10% improvement in RMS acceleration whilst maintaining similar wheel contact force levels to the passive system, whereas the on/off system results in a 3% reduction in RMS acceleration but RMS wheel contact force is 4% worse than the passive system. There is a 9% and 13% improvement in RMS suspension working space for the linearised and on/off system respectively. By analysing the full excitation range, the results re-iterate the key advantage in using feedback linearisation, which was demonstrated for the SDOF system. From Figure 5-15, it can be observed how the MR linearised operating point is insensitive to changes in the input conditions. This is seen through the steady performance levels, which are consistently superior to the passive system across the full excitation range. Furthermore, the car body acceleration is similar to the fully active and ideal semi-active systems. In contrast to the linearised system, the optimum controller gain for the on/off controller is highly dependent on the input conditions. This is seen through the progressive deterioration of suspension working space as the harshness of the road surface worsens.

For some performance criteria, the MR systems can be observed to outperform the fully active and ideal semi-active systems. For example, the RMS suspension working space of the on/off system is superior for the motorway excitation (Figure 5-15(a)), and the car body acceleration of the linearised system is slightly superior for the principal road excitation (Figure 5-15(b)). However the fully active/ideal semi-active systems always outperform the MR systems in two out of the three performance indicators.

5.7 Discussion

Using skyhook-derived control laws, this chapter has demonstrated for both SDOF and 2DOF systems, how feedback linearisation can better harness the controllability of a smart fluid damper when compared to more straightforward on/off control strategies.

In the SDOF study, the fully active and ideal semi-active systems demonstrate superior acceleration levels when compared to the MR systems but this is at the expense of poorer suspension working space levels. Fully active control is particularly superior if these larger working spaces can be tolerated. However, the 2DOF study did not demonstrate such advantages with the ideal semi-active system closely approaching the fully active system. This suggests that dissipative energy is required for most of the time. Furthermore, the similarity between the MR and ideal semi-active system suggests that the MR performance could be further enhanced by designing the system with a lower 'off-state' damping rate.

A key advantage of feedback linearisation is how the damping behaviour becomes less sensitive to external changes. For example, environmental effects and manufacturing tolerances, which would result in varying fluid properties, should have no major effect on performance. On the other hand, it is probable that degradation in the performance of an on/off system, and a shift in the optimum controller gain would be observed when such effects play a role. When this effect is coupled with the changing optimum controller gain due to variations in the input conditions, performance could seriously suffer.

5.8 Summary of Chapter 5

In this chapter, the author numerically investigated the feedback control of vibration isolation systems using MR dampers. The vibrating systems were investigated using broadband mechanical excitations, and the results have been benchmarked against ideal passive, semi-active, and fully active systems.

Two control strategies have been studied: feedback linearisation, and on/off control. New experimental results have demonstrated that feedback linearisation is effective under broadband mechanical excitation, and that the proposed MR damper model remains valid under these conditions.

An SDOF mass-isolator problem was investigated, and MR linearised skyhook control was shown to be superior to on/off skyhook control, demonstrating a 25% reduction in acceleration over an optimised passive system compared to 15% for the on/off strategy. The ideal semi-active and fully active systems outperformed both of the MR damper systems in terms of acceleration, but this was at the expense of larger working spaces.

A 2DOF system representing a vehicle was then investigated numerically. The MR linearised controller, in conjunction with a modified skyhook strategy, was able to outperform the passive system by 10% in terms of car body acceleration and suspension working space, whilst also maintaining slightly superior wheel contact force levels. In contrast, the on/off control strategy provided just a 3% reduction in car body acceleration, whilst wheel contact force levels were degraded. This is because an on/off controller is unable to suppress wheel hop vibrations, where it was shown that a pure skyhook strategy is the most optimal. The fully active and ideal semi-active systems were generally superior to the MR systems, where performance was better in at least

two of the three performance indicators investigated. Nonetheless, car body acceleration levels for the MR linearised system were comparable to the fully active/ideal semi-active systems.

For both of the isolation systems, the feedback linearisation strategy was shown to be relatively insensitive to changes in the input excitation conditions. On the other hand, the on/off strategy was highly sensitive to the input excitation. In the next chapter of this thesis, the behaviour will be investigated experimentally using the HILS approach.

Control strategy	Controller gain
Passive	C_p = 3kNs/m
MR linearised skyhook	D_{MR} = 4kNs/m
On/off skyhook	I_{max} = 0.5A
Fully active skyhook	D_{IS} = 7kNs/m
Ideal semi-active skyhook	D_{SAS} = 6kNs/m

Table 5-1: Controller parameters for the optimised mass-isolator systems.

Parameter	Symbol/unit	Value
Mass of car body	M_c / kg	300
Mass of wheel assembly	M_w / kg	35
Suspension stiffness	K / Nm^{-1}	20000
Tyre stiffness	K_w / Nm^{-1}	200000
Passive damping rate	C_p / Nsm^{-1}	1000-5000
Tyre damping rate	C_w / Nsm^{-1}	80

Table 5-2: Quarter car suspension parameters.

Profile	C	w	V_c (miles/hr)
Motorway	7×10^{-8}	2.5	70
Principal road	50×10^{-8}	2.5	60
Minor road	500×10^{-8}	2.5	30

Table 5-3: Road profile parameters.

Control strategy	Controller gain	α
Passive	C_p = 2kNs/m	-
MR linearised modified skyhook	D_{MRm} = 3kNs/m	0.25
On/off skyhook	I_{max} = 0.08A	0
Fully active modified skyhook	D_{ISm} = 3kNs/m	0.6
Ideal semi-active modified skyhook	D_{SASm} = 3kNs/m	0.6

Table 5-4: Controller parameters for the optimised vehicle suspension systems.

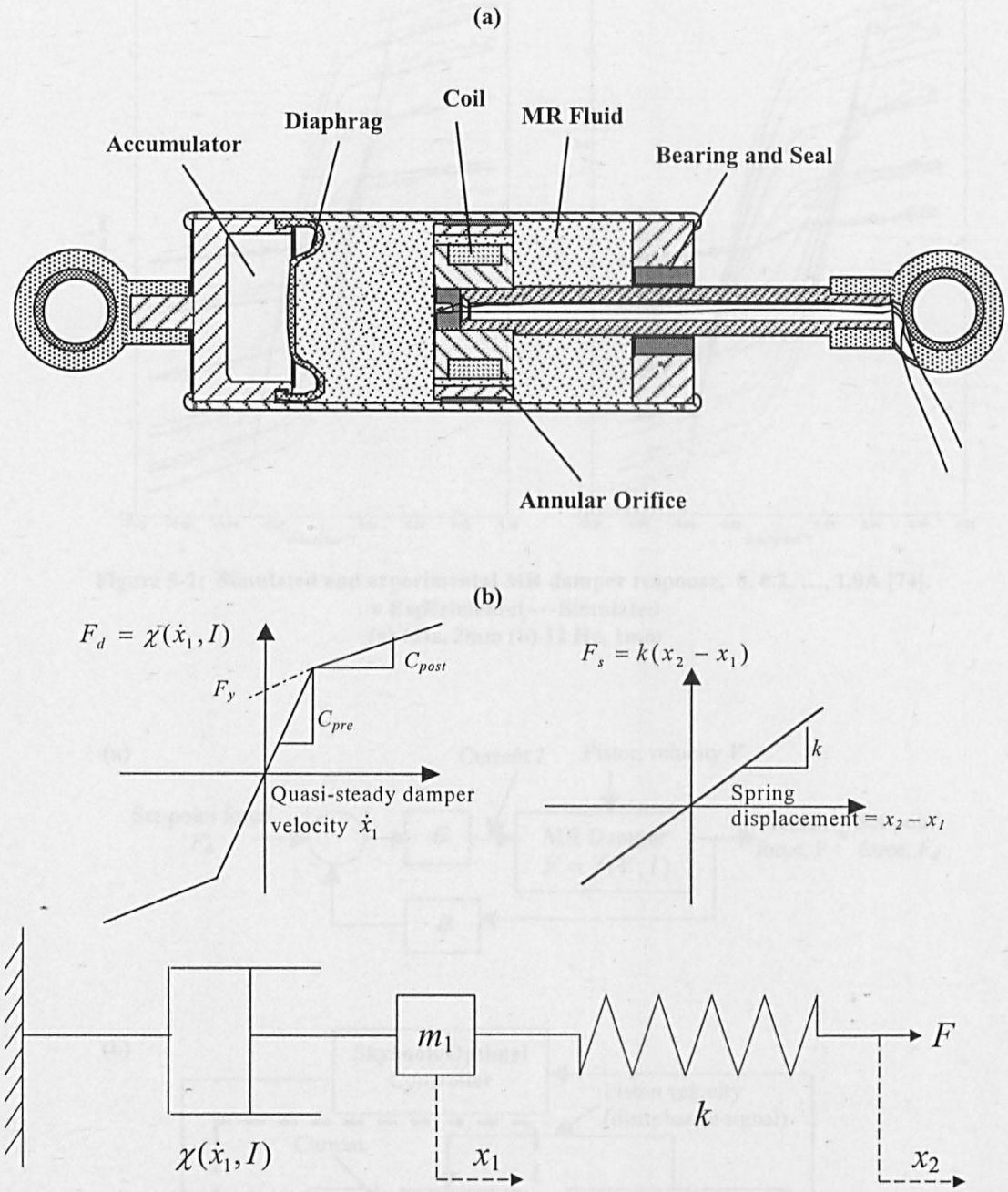

Figure 5-1: (a) Schematic diagram of the Lord Corporations RD-1005-3 MR damper [148] and (b) the lumped parameter model [74].

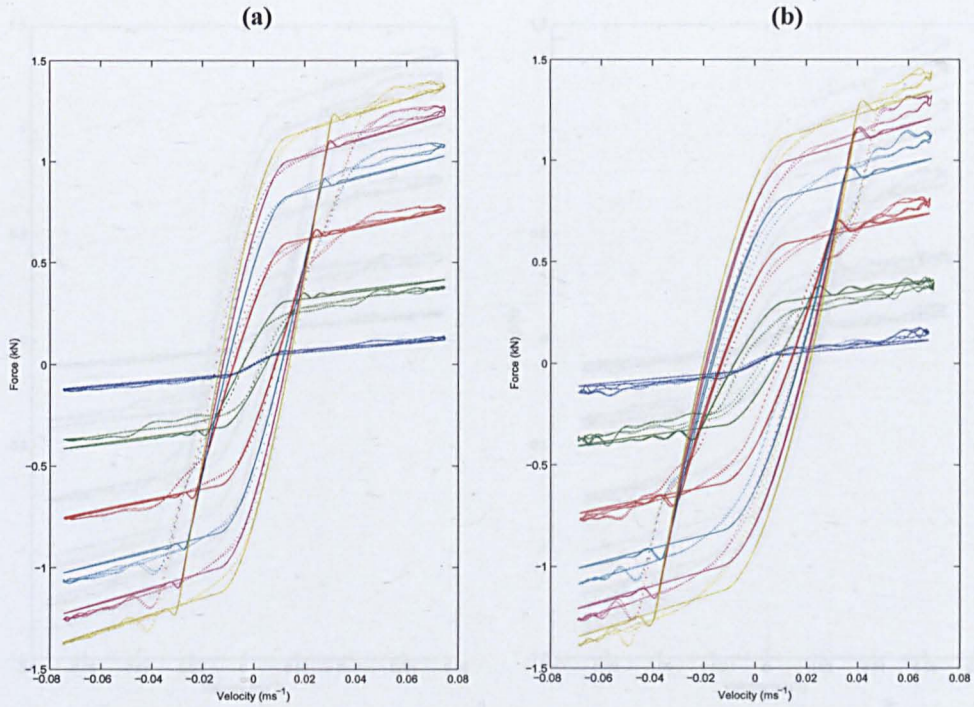

Figure 5-2: Simulated and experimental MR damper response. 0, 0.2, …, 1.0A [74].
• Experimental — Simulated
(a) 6Hz, 2mm (b) 12 Hz, 1mm

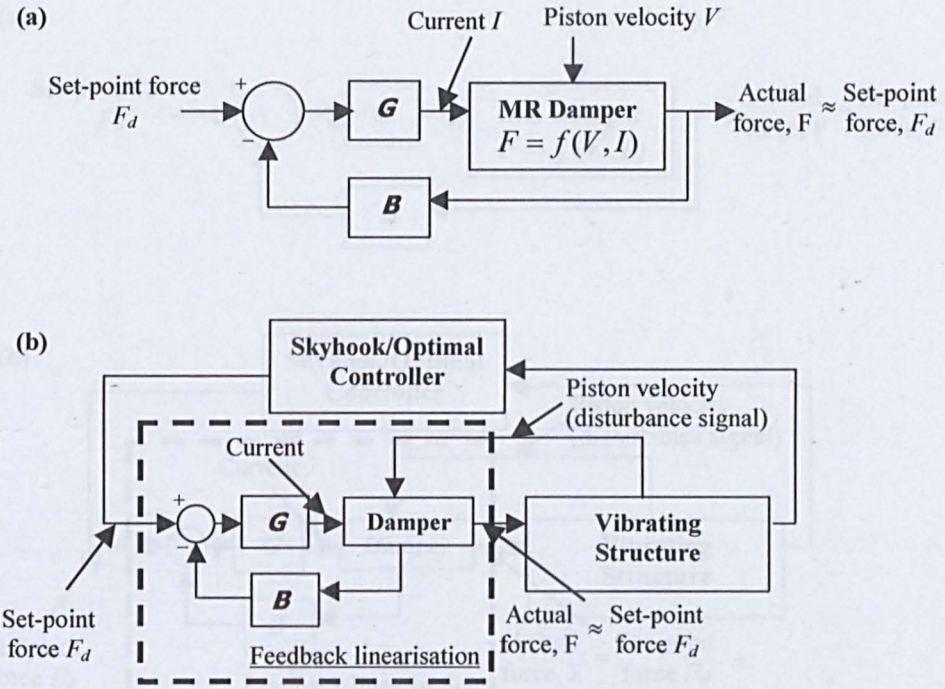

Figure 5-3: Semi-active force generator. (a) Controller block diagram and (b) implementation within a controlled vibration system.

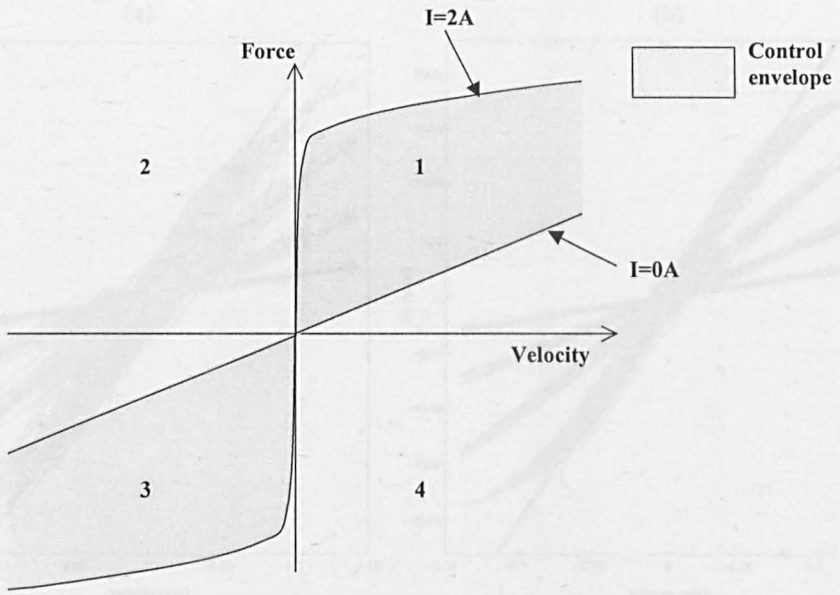

Figure 5-4: Control envelope of the MR damper.

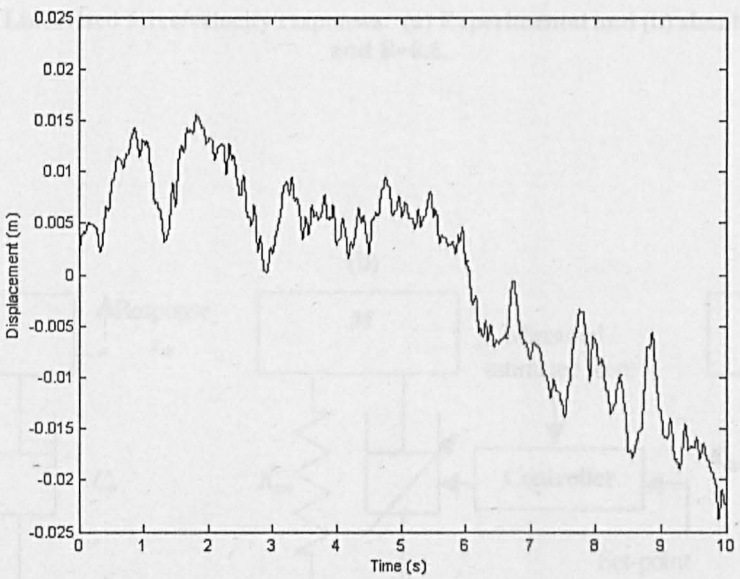

Figure 5-5: Broadband input excitation used for experimental validation of feedback linearisation.

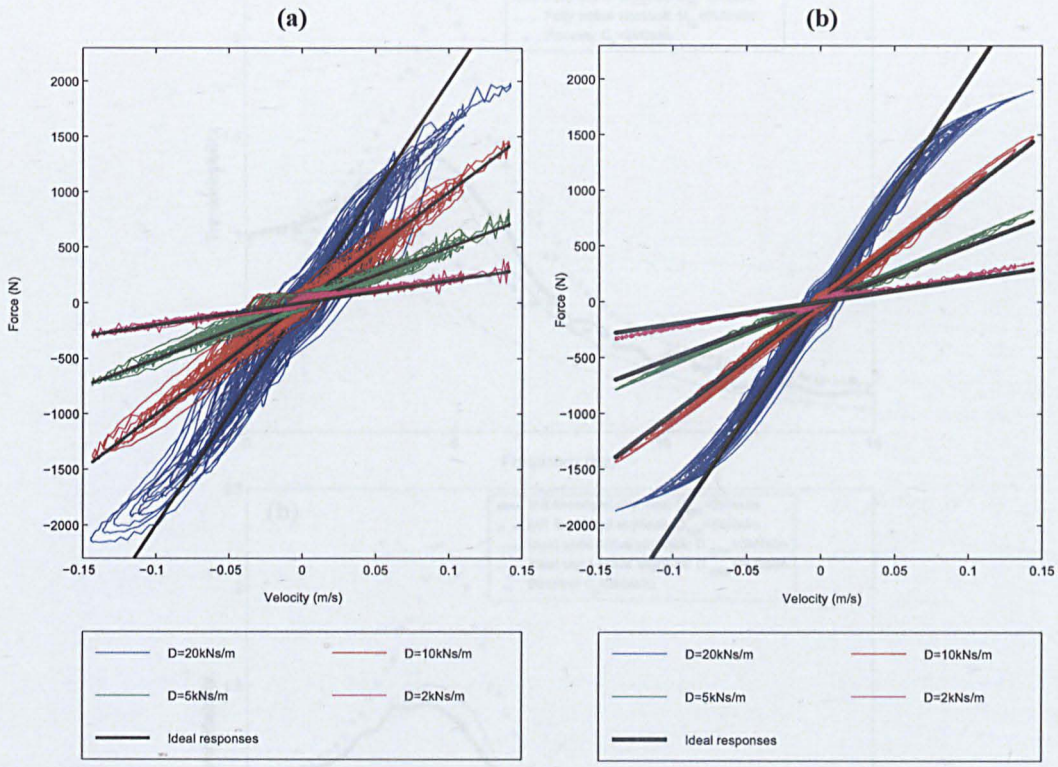

Figure 5-6: Linearised force/velocity responses. (a) Experimental and (b) simulated. G=0.0015 and B=0.6.

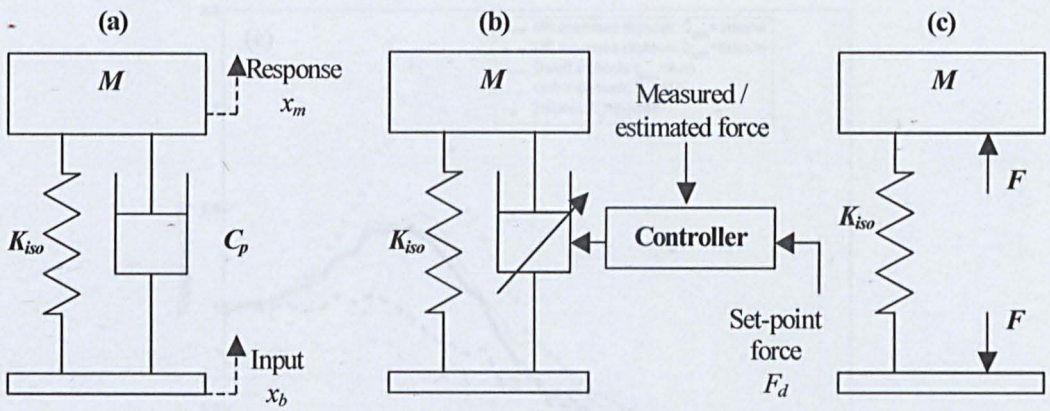

Figure 5-7: Mass-isolator models. (a) Passive system, (b) MR linearised system and (c) ideal system.

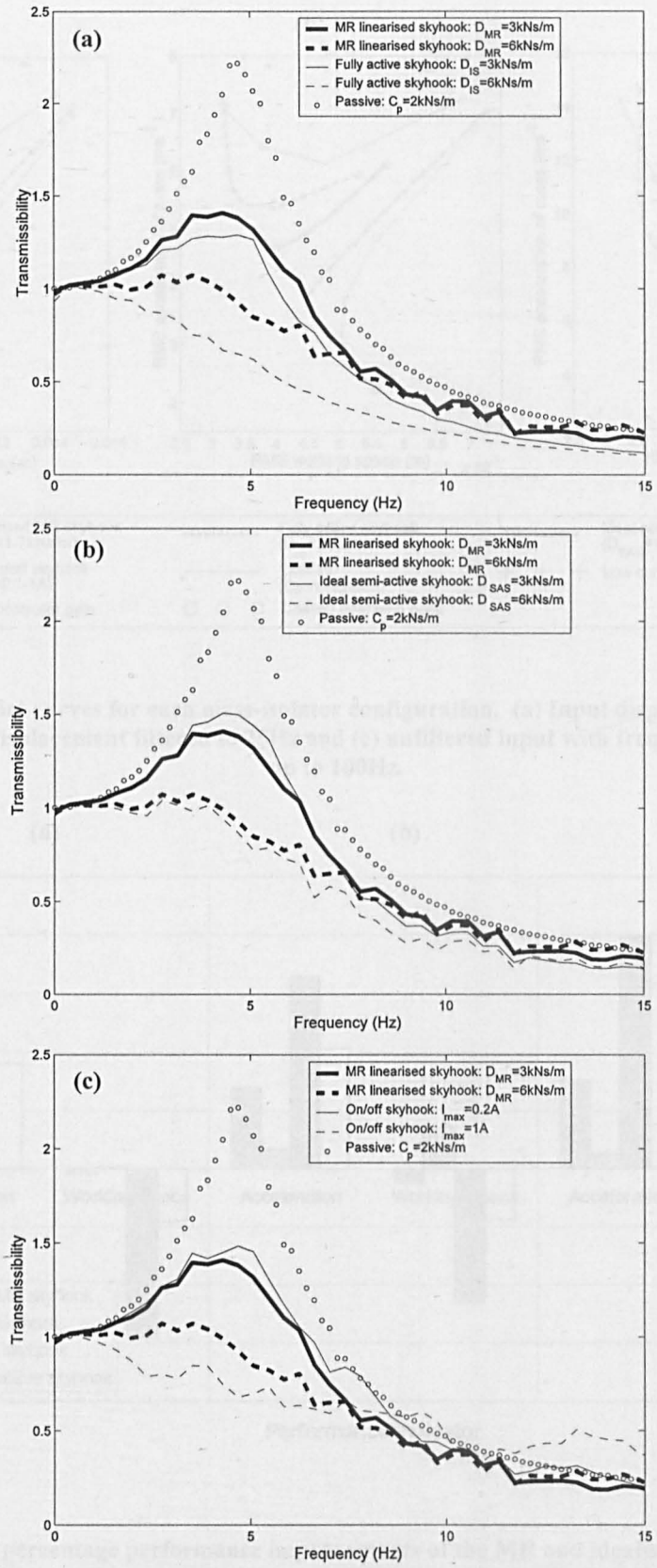

Figure 5-8: Transmissibility comparisons between (a) linearised MR skyhook and fully active skyhook systems, (b) linearised MR skyhook and idealised semi-active skyhook systems and (c) linearised MR skyhook and on/off MR skyhook systems. Input signal with cut-off frequency at 25Hz.

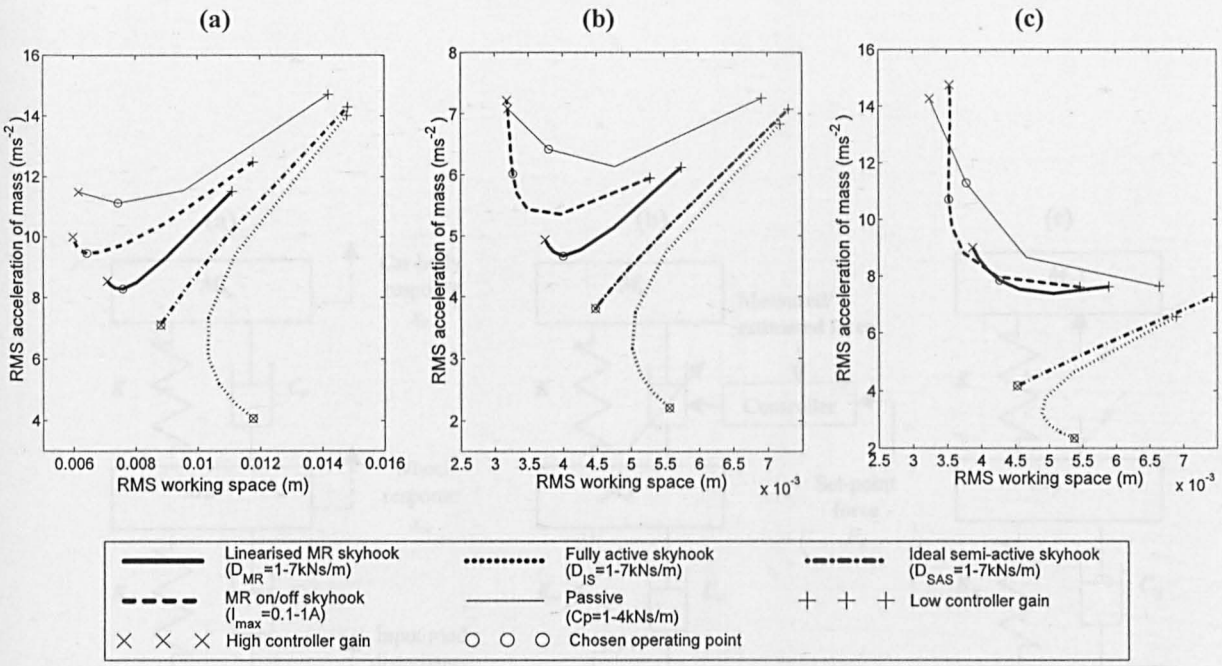

Figure 5-9: Conflict curves for each mass-isolator configuration. (a) Input displacement filtered to 10Hz, (b) input displacement filtered to 25Hz and (c) unfiltered input with frequency components up to 100Hz.

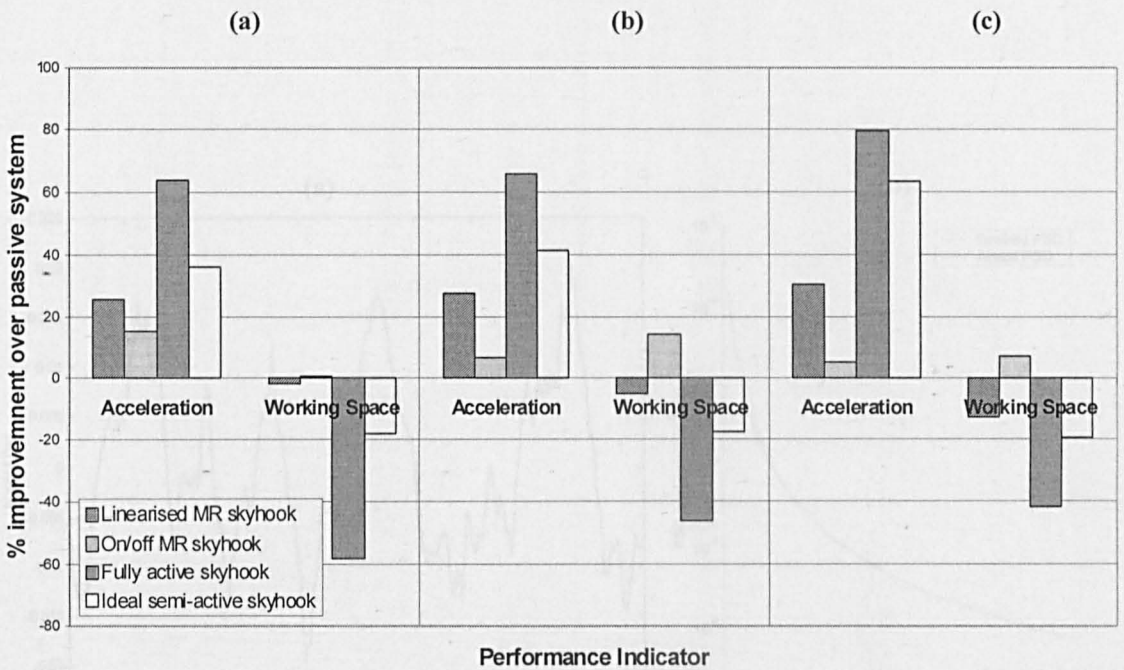

Figure 5-10: The percentage performance improvements of the MR and idealised systems over the passive system. (a) Input displacement filtered to 10Hz, (b) input displacement filtered to 25Hz and (c) unfiltered input with frequency components up to 100Hz. Controller parameters correspond to those given in Table 5-1.

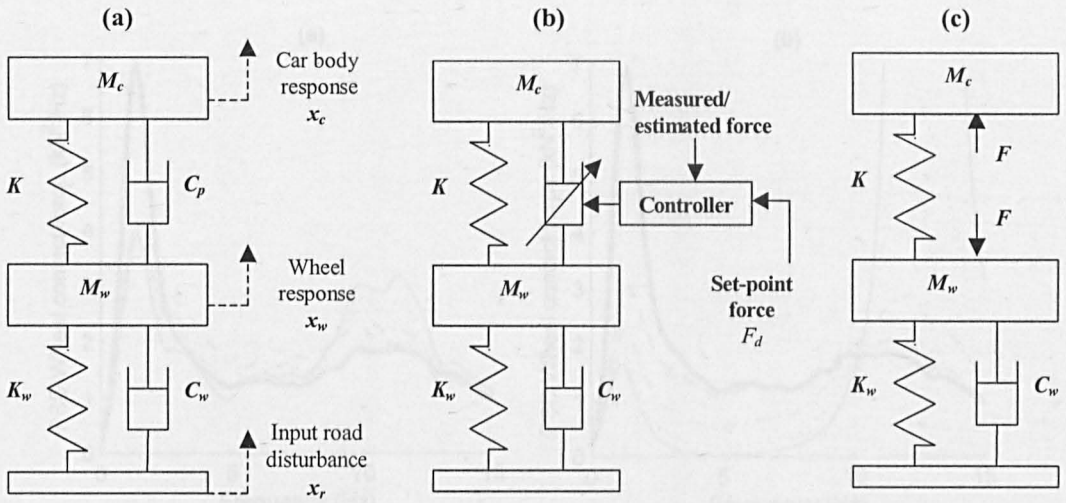

Figure 5-11: Quarter car models. (a) Passive system, (b) MR linearised system and (c) ideal system.

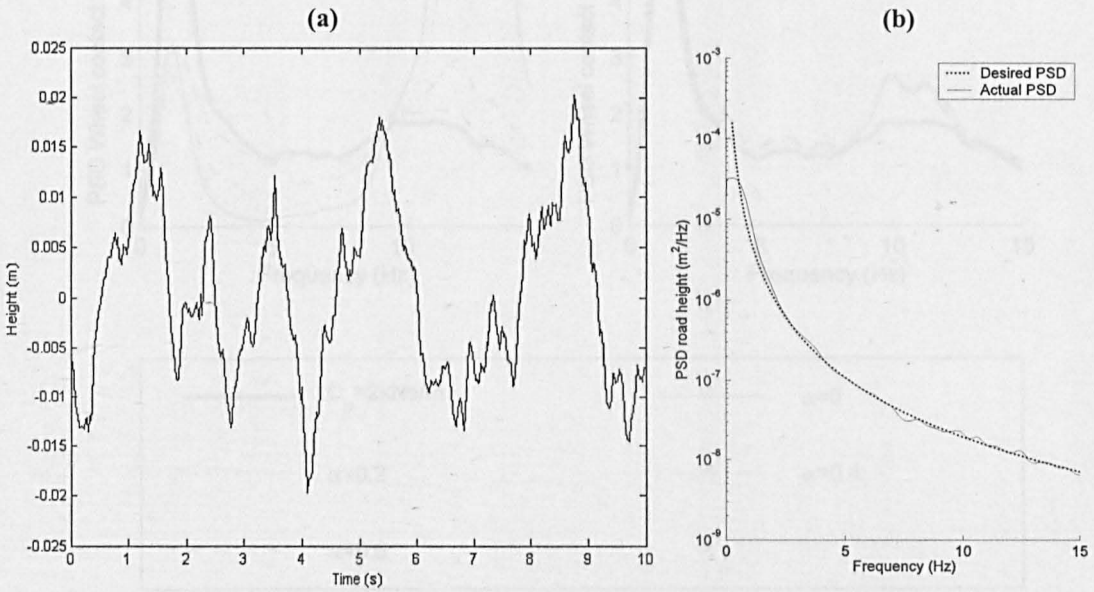

Figure 5-12: Motorway excitation. (a) Time history and (b) a comparison between the desired and actual power spectral density.

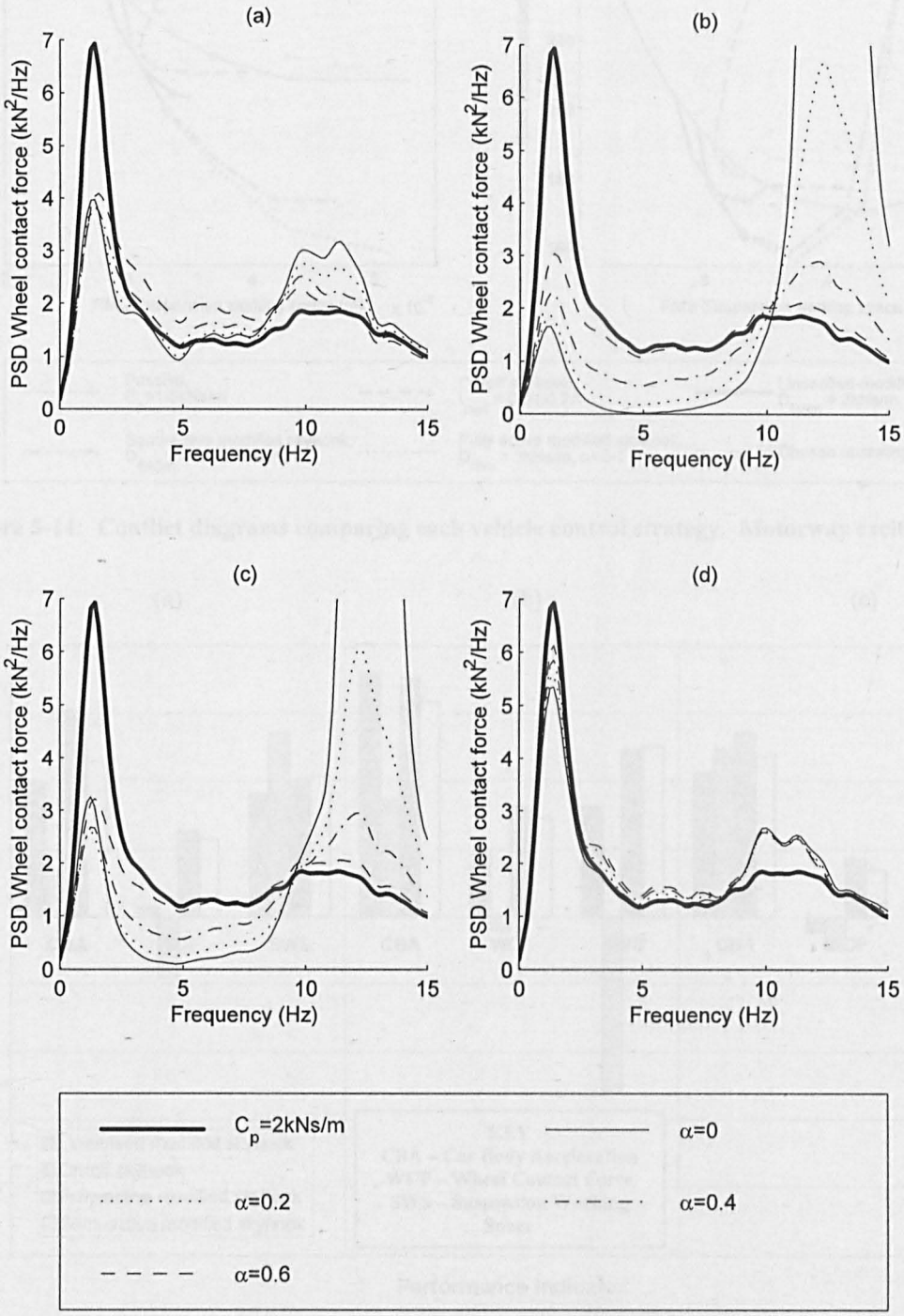

Figure 5-13: Frequency response to the motorway excitation. (a) MR linearised modified skyhook system - D_{MRm} = 3kNs/m, (b) fully active modified skyhook system - D_{ISm} = 3kNs/m, (c) ideal semi-active modified skyhook system - D_{SASm} = 3kNs/m and (d) MR on/off modified skyhook system -I_{max} = 0.06A.

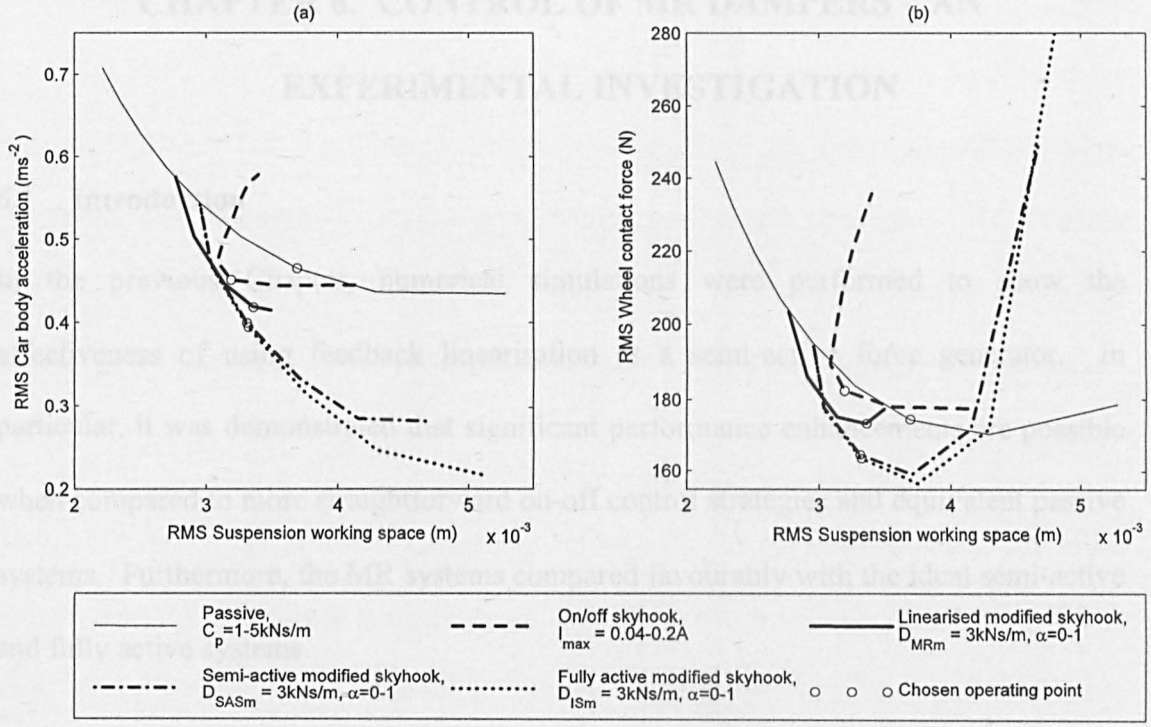

Figure 5-14: Conflict diagrams comparing each vehicle control strategy. Motorway excitation.

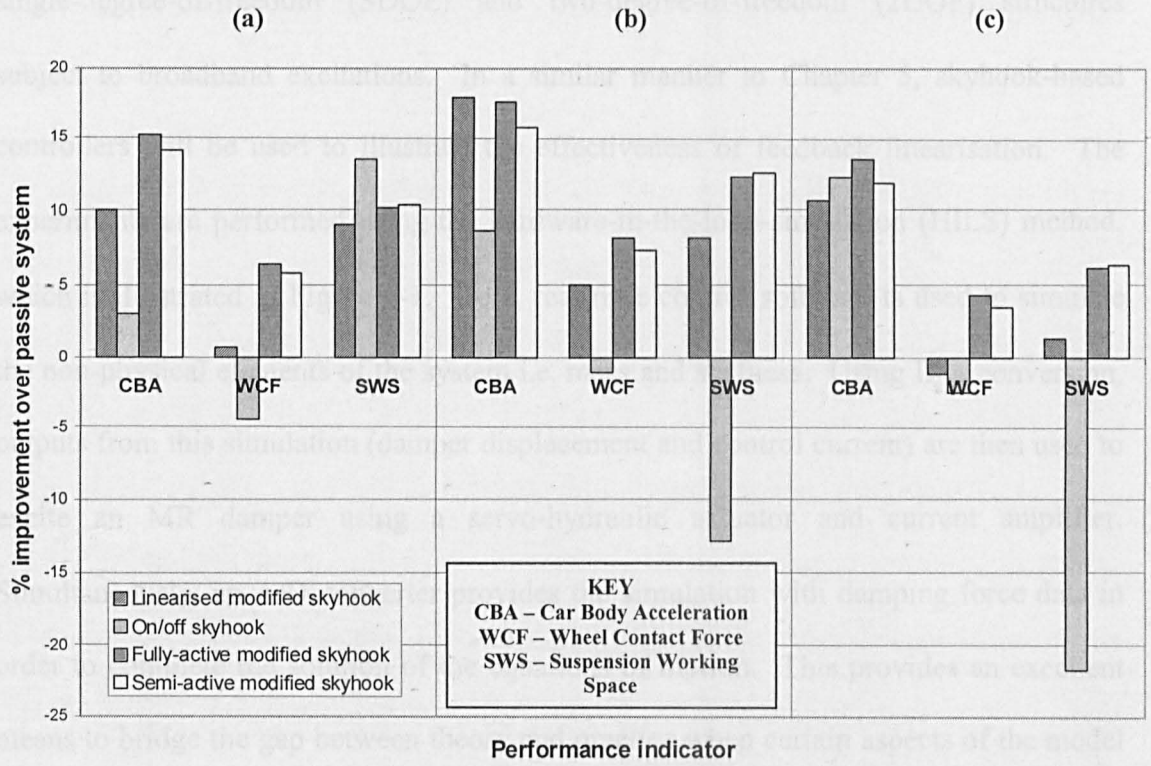

Figure 5-15: The percentage performance improvements of the MR and idealised systems over the passive system. (a) Motorway excitation, (b) principal road excitation and (c) minor road excitation. Controller parameters correspond to those given in Table 5-4

CHAPTER 6. CONTROL OF MR DAMPERS – AN EXPERIMENTAL INVESTIGATION

6.1 Introduction

In the previous Chapter, numerical simulations were performed to show the effectiveness of using feedback linearisation as a semi-active force generator. In particular, it was demonstrated that significant performance enhancements are possible when compared to more straightforward on-off control strategies and equivalent passive systems. Furthermore, the MR systems compared favourably with the ideal semi-active and fully active systems.

The present chapter aims to build upon this work by performing experiments of both single-degree-of-freedom (SDOF) and two-degree-of-freedom (2DOF) structures subject to broadband excitations. In a similar manner to Chapter 5, skyhook-based controllers will be used to illustrate the effectiveness of feedback linearisation. The experiments are performed using the hardware-in-the-loop-simulation (HILS) method, which is illustrated in Figure 6-1. Here, real-time control software is used to simulate the non-physical elements of the system i.e. mass and stiffness. Using D/A conversion, outputs from this simulation (damper displacement and control current) are then used to excite an MR damper using a servo-hydraulic actuator and current amplifier. Simultaneously, an A/D converter provides the simulation with damping force data in order to complete the solution of the equations of motion. This provides an excellent means to bridge the gap between theory and practice when certain aspects of the model have complex behaviour i.e. the MR damper. However, due to the additional dynamics that are introduced by the servo-hydraulic actuator, the HILS method must be validated.

In the SDOF study, Lord Corporation's RD-1005-3 MR damper [62] is used to perform the HILS tests. By comparing the HILS results to numerical simulations, both with and without hydraulic actuator dynamics, the aim is to validate the use of the HILS method to predict the relative performance of MR vibration control strategies. This is made possible using the previously validated model of the MR damper (Section 5.2) along with a servo-hydraulic system model that was provided by the equipment manufacturer [149].

In the 2DOF study, Carrera's Magneshock [150] MR damper is used to perform HILS experiments. This damper is made specifically for primary vehicle applications, and is therefore a more appropriate device for quarter-car HILS tests. A model of this device was not developed. Nonetheless, due to the large similarities between the SDOF and 2DOF vibration systems, the SDOF investigation will help to validate the HILS method in general.

The present chapter is organised as follows. First, the experimental HILS test facility is outlined before presenting the SDOF investigation. In the SDOF study, a numerical model of this HILS system is described, which includes a validated model of both the hydraulic actuator and MR damper. Comparisons are then made between the HILS experiments and the numerical simulations with and without actuator dynamics. Next, the 2DOF study is presented, which compares HILS experimental results for a variety of controllers. Finally, a general discussion is made and the key conclusions are drawn. The research in this chapter has been accepted for publication [151], and the abstract for this work is given in Appendix A.IV. The SDOF study was also presented at the II ECCOMAS conference on Smart Structures and Materials, Lisbon, Portugal [152].

6.2 The HILS test facility

With reference to Figures 4-4 and 4-5, the damper test facility (Section 4.3) was configured for HILS testing as follows. First, Simulink was used to develop the controllers and to model the non-physical system parameters on the host PC. These models were then downloaded onto the target PC, which performed the real-time simulation by transferring data to and from the hardware via the data acquisition card. Here, the simulated damper displacement was sent to the Instron controller via the D/A converter. Simultaneously, the damping force data (measured by the load cell) was sent via the A/D converter to the target PC, thus permitting the real-time solution of the equations of motion.

At this stage, it is worth drawing attention to the test facility's performance specifications that are most relevant to the HILS method. To perform HILS tests effectively, the servo-hydraulic system must have an excellent magnitude and phase response. In particular, the phase delay (i.e. the time difference between the desired and actual actuator displacement) must be minimised as large values can lead to system instability [153]. To maximise control system performance, the MR damper's power supply must also be dynamically responsive in order to minimise the time constant associated with the MR effect. The specifications of the test facility that are most relevant to these factors are as follows:

- The bandwidth of the servo-hydraulic actuator was rated at 40Hz. This is more than adequate for HILS testing, where frequencies above 20Hz are outside the duty of shock absorbers [7].

- To regulate oil flow to and from the actuator, two 38l/min Moog D765 electronic feedback valves were used [135]. These are two-stage servo-valves that incorporate a position transducer (LVDT) and integrated electronics to control the main spool and hence oil flow. The frequency response curves of this servo-valve are provided in Figure 6-2, where excellent magnitude and phase response characteristics can be observed. Also, the step response of the spool was rated at 2ms [135], which is far superior to conventional mechanical feedback valves.

- To power the MR damper, a high specification Kepco BOP amplifier [136] was used. This had a maximum DC output range of ±36V and ±6A. Furthermore, in current control mode, the amplifier had a bandwidth of 13kHz and a rise / fall time of 27μs between 10%-90%. Therefore, the effect of the power supply on the response time of the MR effect was negligible.

In summary, the dynamic characteristics of the servo-hydraulic system and the MR damper's power supply are more than adequate. Consequently, the stability and accuracy of the HILS tests, and the control system performance will be maximised.

6.3 SDOF study

The parameters used for the SDOF system are defined in Figure 6-3(a). The mass (M=80kg) and stiffness (K_{iso}=78.5kN/m) were chosen to give a system natural frequency equal to 5Hz, with a damping ratio of 0.2 when the MR damper is in the 'off' state. Each system was excited by the same broadband displacement excitation. This was generated by passing white noise (with a constant velocity amplitude) through a 2nd order low-pass Butterworth filter, which was designed with a cut-off frequency at 25Hz.

6.3.1 Numerical modelling

In this section, a numerical model of the experimental HILS system will be presented. This will be referred to as a "HILS simulation", and the development of this model will help validate the effect of the actuator dynamics on the performance of the controlled SDOF systems. Consequently, by removing the actuator dynamics in the numerical model (giving an "idealised simulation"), the accuracy of using the HILS method to evaluate controller performance can be determined.

Figure 6-4 shows a schematic representation of the numerical model. In accordance with Chapter 5, the dynamics of the electro-magnetic circuit and smart fluid rheology are modelled using a first order lag term with a time constant equal to 3ms. In the HILS simulation, the actual displacement across the MR damper model, which was described and validated in Section 5.2, differs in magnitude and phase to the desired displacement due to the dynamics of the servo-hydraulic system. This was accounted for using numerical models of the servo-hydraulic actuator, servo-valves, and controller, which were provided by the equipment manufacturer [149].

To validate the accuracy of the servo-hydraulic system model, a frequency response analysis was performed. Here, the actuator was excited with a broadband displacement signal that was passed though a low-pass Butterworth filter with a cut-off frequency of 50Hz. This cut-off frequency was chosen so as to just exceed the bandwidth of the test facility, which is rated at 40Hz. The frequency response between the demanded input and the actual displacement was then calculated and compared to a corresponding simulation of the test. The results are presented in Figure 6-5, where it can be observed that the servo-hydraulic system model predicts both the magnitude and phase response

well. The magnitude of the actuator displacement remains largely unaffected in the frequency range of interest, and it is the phase φ that is likely to have the most significant effect on the HILS system performance. With reference to Figure 6-5(b), it can be readily shown that a time delay Δt of approximately 6ms exists throughout the frequency range ($\Delta t = {}^{-\varphi}/_{360f}$, where the units of φ and f are measured in degrees and hertz respectively).

6.3.2 Control

Three SDOF control strategies were investigated, which are summarised below. For more detailed descriptions, the reader is referred to Section 5.5.1.

- **Linearised system**

Here, feedback linearisation is utilised such that the MR damper emulates a passive damper with a linear damping rate i.e. the set-point force to the semi-active force generator (Figure 5-3(a)) is proportional to the relative velocity between the vibrating mass and the base of the SDOF isolator. This system provides a useful performance benchmark.

- **Linearised skyhook control**

For this system, the semi-active force generator (Figure 5-3 (a)) is used to track the skyhook damping force (Eq.5-2). However, when implementing feedback control within a HILS experiment or HILS simulation, a complication arises due to the phase delay between the desired and actual MR damper displacements. This complication is shown in Figure 6-6, which illustrates the implementation of linearised skyhook control

within an SDOF HILS system. Here, the phase delay means that the 'simulated' velocity of the mass, which is used to compute desired force (and hence control current), does not coincide with the actual force and displacement that is being measured. In order to correct for this, an additional 6ms time delay is applied to the velocity of the mass (as shown in Figure 6-6), thus bringing the set-point and measured forces back in phase. This is essentially a 'virtual' velocity sensor, and the above delay helps it to function as similar as possible to the sensor that would be on a real system incorporating a physical mass, spring and MR damper. Without this additional delay, the controller would be able to pre-empt the displacement of the MR damper, which is not physically realisable. Note that the value of 6ms corresponds to the time delay associated with the phase response in Figure 6-5(b).

- **On/off skyhook control**

On/off control skyhook control represents a major simplification to the linearised controller as it eliminates the need to measure/estimate the damping force. With reference to Equations 5-3 and 5-4, the current supplied to the MR damper is switched to a constant value when the force required by the skyhook law is a dissipative one.

For the reasons described above, a 6ms time delay was applied to the demanded control current within the HILS experiments and HILS simulations. This ensures that the timing of the demanded current corresponds to the actual actuator displacement (or velocity) that was used in the simulation to determine when to switch the damper current on. Thus the controller will function as similar as possible to a real system where all isolator components are physical.

6.3.3 SDOF Results

For each control strategy, the following three SDOF mass-isolator investigations were performed:

1. HILS experimental investigation (as described in Section 6.2).

2. Numerical study incorporating actuator dynamics i.e. the HILS simulation (as described in Section 6.3.1).

3. Numerical study without actuator dynamics i.e. the idealised simulation. Here, the servo-hydraulic system model has been switched out (see Figure 6-4) such that the MR damper displacement has exactly the same magnitude and phase as the spring displacement. This represents a simulation of the real system incorporating physical mass, spring and damper components. The additional 6ms time delays that were incorporated into the controllers described in Section 6.3.2 were obviously removed in these systems.

Comparisons between the results of the above investigations are presented below.

HILS experiment versus HILS simulation

Figure 6-7(a) compares the frequency responses of the HILS experiment with the HILS simulation for the linearised skyhook system. The responses shown are transmissibility estimates, which were obtained using Welch's method [145]. Clearly, there exists good correlation between the HILS experiment and HILS simulation, and this holds throughout the range of set-point gains D_{MR} = 1-5kNs/m.

In a similar fashion, Figure 6-7(b) presents the results for the on/off skyhook system. The correlation between the HILS experiment and HILS simulation is good for the case

I_{max} = 0.1A, but accuracy deteriorates as I_{max} is increased. More specifically, the HILS simulation contains greater damping levels than observed in the HILS experiment, where the transmissibility is underestimated around the natural frequency and overestimated at higher frequencies. This discrepancy is largely due to the inaccuracy of the MR damper model i.e. it is likely that the fluid properties have altered since the model was first developed. Moreover, this inaccuracy is not observed in the linearised skyhook system results (Figure 6-7(a)), which serves to illustrate a key advantage of feedback linearisation – it desensitises the skyhook controller to parameter uncertainty. Device performance will therefore be insensitive to fluid property variations that may occur between batches, during long-term use, or due to environmental effects e.g. temperature.

The relative performance between the linearised and on/off skyhook strategies can be determined by comparing Figure 6-7(a) with Figure 6-7(b). Clearly, the linearised skyhook system can be tuned to outperform the on/off system throughout the frequency range. In particular, the linearised skyhook system is superior at substantially reducing the transmissibility around the natural frequency without significant degradation in performance at higher frequencies. Furthermore, the frequency when the transmissibility is amplified rather than suppressed with increasing set-point gain, is superior for the linearised skyhook system. This will be referred to as the crossover frequency and, with reference to Figure 6-7, this occurs at approximately 10 Hz for the linearised skyhook system and 8 Hz for the on/off skyhook system.

To further illustrate the above points, the performance of the various HILS experiments and HILS simulations are compared using the conflict diagram. This is shown in

Figure 6-8, where the RMS acceleration is plotted against the RMS working space as function of the control parameter. For each of the three controllers, the HILS experiments correlate well with the HILS simulations, thus validating the numerical model. Furthermore, the conflict diagram effectively highlights the significant advantages of using feedback linearisation to implement control, where much lower acceleration levels are achieved for a similar working space. For example, for an RMS working space of 3.6mm, the RMS acceleration of the linearised skyhook controller is 17.5% lower than the on/off skyhook controller, and 36% lower than the linearised system. However, the effect of the actuator dynamics on the above results must be validated.

HILS simulation versus ideal simulation

The results presented above validate the HILS simulation, where good correlation with the experimental results has been demonstrated. This was particularly the case with the linearised skyhook controller, and it was shown that the poor correlation associated with the on/off controller was due to a slightly inaccurate MR damper model. Therefore, by removing the actuator dynamics from the HILS simulation (giving the idealised simulation), a good indication of the performance of the real system will result. Moreover, the effect that the servo-hydraulic system dynamics has on the performance of the control systems will be evident.

Figure 6-9 compares the transmissibility estimates between the HILS simulation and the idealised simulation. In general, for both linearised (Figure 6-9(a)) and on/off (Figure 6-9(b)) skyhook systems, the main effect of the actuator dynamics is to shift the transmissibility curves to larger values, and to reduce the crossover frequency.

Furthermore, by observing the responses with the lowest set-point gains (D_{MR} and I_{max}), it can be seen how the actuator dynamics have slightly increased the damped natural frequency. The performance of the control systems has therefore been reduced due to the incorporation of the servo-hydraulic system dynamics in a HILS test. Nonetheless, the relative performance between the linearised and on/off skyhook systems remains largely unchanged, which validates the use of the HILS method to predict the performance of controllers in MR vibration systems.

To further illustrate this point, Figure 6-10 compares the conflict curves between the idealised and HILS simulations. As shown, the key effect of the actuator dynamics is to degrade the RMS acceleration of the mass, but the relative performance of the controllers remains largely unaffected. The shapes of the conflict curves are also unchanged, which indicates that the optimum controller parameter determined from a HILS test will remain optimal in the real system.

6.4 2DOF Study

In the previous section, it was shown that the effect of the hydraulic actuator dynamics in HILS tests is to reduce performance. However, the relative performance of the control systems, and the optimum controller gains remain largely unchanged. This result helps validate the use of the HILS method in general, which is now used to investigate a 2DOF MR vibration system.

The system parameters for the 2DOF system were chosen to represent a small sized passenger car as shown in Figure 6-11. However, the Carrera MR damper that was used in this study provided an excessive damping rate ζ in the zero-field condition.

Consequently, a scaling factor of 0.36 was applied to the measured damping force F in order to give a zero-field damping ratio $\zeta \approx 0.2$.

To excite the quarter car system, broadband random signals representative of typical roads were used. Motorway and principal road excitations were generated with frequency content between 0-20Hz. For details on how the road signals were generated, the reader is referred to Section 5.6.3.

6.4.1 Feedback linearisation

As with the previous control studies, feedback linearisation is utilised to provide effective semi-active force generation. For the Carrera damper, a new set of feedback gains must therefore be determined and validated. Sims, *et al.* [94, 95] described a formal approach to identify the optimal values, but a more ad-hoc approach was considered appropriate in the present study. Through trial and error, the feedback and feedforward gains B and G were tuned such that the MR damping force correlated well with the desired value.

In this study, values of G equal to 0.001 and B equal to 0.8 were found to provide a good response. This is illustrated in Figure 6-12, where the sinusoidal response of the MR damper has been linearised. Here, the set-point force to the controller is proportional to the piston velocity through the damping constant D. As shown, when D = 6kNs/m the response is highly linear. Moreover, the actual damping rate correlates very well with the desired value, thus validating the accuracy of the controllers force tracking capability. The responses for D = 2kNs/m and D = 10kNs/m represent the control limits of the device. When D = 2kNs/m, the set-point damping force is lower than the minimum value that is governed by the viscosity of the MR fluid.

Consequently, the current is set to 0A, and the desired force is not achieved. Note that the yield stress effect that can be observed in this response is due to seal friction. For D = 10kNs/m, the set-point force is accurately achieved between ± 0.06m/s. Beyond ± 0.06m/s, saturation occurs as the maximum yield stress in the fluid has been reached i.e. the current is at its maximum value. Consequently, the actual force falls short of the set-point value.

6.4.2 Quarter car controllers

The quarter car controllers are briefly described below, but more detailed descriptions can be found in Section 5.6.2. Where appropriate, 6ms time delays were also built into the controllers in order to account for the 6ms phase difference between the desired and actual MR damper displacement. As with the SDOF study, this ensures that the application of the desired current corresponds to the correct MR damper displacement/velocity that was used to calculate it within the controller (e.g. Figure 6-6). Thus, the control systems will behave as similarly as possible to the real structure, where all vehicle parameters are physical.

- **Open-loop**

To provide a performance benchmark for the controlled MR systems, an open-loop controller was investigated. Here, the current supplied to the MR damper was maintained at a constant level I_{OL}, where values between 0 and 0.2A were investigated.

- **Linearised**

As a more realistic benchmark, the MR damper was linearised using the semi-active force generator that was first described in Section 5.3. As shown in Figure 6-12, this

system is more representative of a conventional passive suspension with a linear viscous damper. The set-point gain D was varied between 1kNs/m and 5kNs/m, which approximately corresponds to sprung mass damping ratios between 0.2 and 1.

- **Linearised modified skyhook control**

Here, the semi-active force generator is used to achieve the modified skyhook damping force (see Eq.5-8). As shown in Figure 6-12, this set-point force will be accurately achieved within the dissipative control limits of the MR damper.

- **On/off modified skyhook control**

The on/off controller switches the input current to a predetermined and constant level I_{max} when the force required by the modified skyhook control law is a dissipative one (see Equations 5-9 and 5-10). This represents a major simplification over the linearised modified skyhook controller as force feedback is not required.

6.4.3 2DOF Results

Frequency responses for the motorway excited linearised system are first presented in Figure 6-13. The performance is illustrated in terms of the power spectral density of the car body acceleration (Figure 6-13(a)) and wheel contact force (Figure 6-13(b)). As the set-point gain D (or the effective damping constant) is increased, the resonant peaks corresponding to the sprung mass (1.6Hz) and unsprung mass (11.5Hz) natural frequencies are suppressed. For large values of D, the masses are effectively locked together and the system behaves as an SDOF system (as shown by the single resonant peak). This behaviour is typical of a linear 2DOF vibration system, and gives the first

indication that the HILS technique is providing reliable results, in spite of the servo-hydraulic actuator dynamics.

In Figure 6-14, the PSD responses of the linearised modified skyhook system are presented for the motorway excitation. Results are shown for D_{MRm} = 4kNs/m where α is varied between zero and one. Skyhook control (α = 0) is most superior in terms of passenger comfort (Figure 6-14(a)), but wheel contact force levels at the wheel hop frequency are poor (Figure 6-14(b)). Augmenting the system with viscous damping ($0<\alpha<1$) improves the unsprung mass vibrations at the expense of the sprung mass performance.

The performance of the motorway excited on/off modified skyhook system is shown in Figure 6-15 for I_{max} = 0.15A, where α is varied between zero and one. Much like the linearised modified skyhook system, pure skyhook control (α = 0) provides the most superior response in terms of passenger comfort (Figure 6-15(a)). However, the on/off controller is unable to significantly suppress the wheel contact force vibrations at the wheel hop frequency when α is increased (Figure 6-15(b)). Although a slight improvement can be observed for $\alpha > 0$, an analysis of the area under the PSD curves illustrates that there is no enhancement in the RMS value. Therefore, pure skyhook control is optimal for a 2DOF on/off system.

The results of Figures 6-14 and 6-15 are promising as they directly concur with the previous numerical findings in Chapter 5. It is therefore apparent that the HILS method provides accurate results for 2DOF MR vibration systems.

To further illustrate the effectiveness of the semi-active force generator, the time histories between the set point and actual damping forces have been compared. This is shown in Figure 6-16 for the motorway excited linearised system. Clearly, the accuracy of the semi-active force generator is excellent, where the actual damping force tracks the commanded value very closely. For the linearised modified skyhook system, the desired force is not always dissipative, so it is interesting to investigate the tracking accuracy for this controller. The force/time history for this system is shown in Figure 6-17, and the instants when an energy input is required are also indicated. During these instants, the damper can no longer achieve the set-point force, and so the accuracy of the semi-active force generator deteriorates. Nonetheless, when the required force is dissipative, the force tracking accuracy is very good as before. Furthermore, it was found that an energy input was only required for 20% of the entire HILS test. This suggests that the performance of the semi-active MR system is likely to approach that of a fully active system. In conclusion, the semi-active force generator performs extremely well in the face of broadband random excitations.

In what follows, the performance of the various quarter car control strategies are compared through an analysis of the conflict diagram, which enables an enhanced assessment of the relative controller performance. Figure 6-18 shows the conflict diagram for the motorway excitation, where the RMS car body acceleration (Figure 6-18(a)) and RMS wheel contact force (Figure 6-18(b)) are plotted against the RMS suspension working space. The variable parameter for each control system is as follows:

- Open-loop- I_{OL} is varied between 0.05-0.2A
- Linearised– D is varied between 1-5kNs/m
- Linearised modified skyhook– Curves are plotted for D_{MRm} = 3kNs/m and 4kNs/m, where α is varied between 0-1.
- On/off modified skyhook – As skyhook control is optimal for this system (see Figure 6-15), $\alpha = 0$ and I_{max} is varied between 0.05A-0.2A.

With reference to Figure 6-18, the open loop system clearly has the worst performance. This is likely due to the non-linear force/velocity characteristics, which creates a harsh response when the velocity changes direction. The linearised system, which emulates a passive device, improves on this response but it is the skyhook-based controllers that provide the best performance. Moreover, the linearised modified skyhook system is superior to the on/off skyhook system, where lower levels of car body acceleration and wheel contact force can be achieved.

In Chapter 5, it was shown how feedback linearisation tends to desensitise the controller performance to changes in the input excitation. This can also be observed in the HILS results by comparing Figure 6-18 with Figure 6-19, which shows the conflict curves for the principal road excitation. Unlike the on/off system, the shape of the linearised modified skyhook conflict curve, and hence the optimum controller gain, remains unchanged. Again, this result illustrates the efficacy of the HILS method, where identical conclusions to the previous numerical study of Chapter 5 can be drawn.

To better illustrate the sensitivity to the input excitation, an operating point for each control system was chosen such that the wheel contact force is minimised on the motorway. These operating points are highlighted on Figure 6-18 by the circular markers, and the corresponding controller values are given in Table 6-1. The performance of the same controller configurations is also highlighted on Figure 6-19 for the principal road excitation. With the exception of the linearised modified skyhook system, wheel contact force levels are no longer optimal.

This result is summarised in Figure 6-20, which shows the performance of the optimised controllers as a percentage improvement over the linearised system. Linearised modified skyhook control is clearly superior for all performance indicators and input excitations. For the motorway excitation, improvements in car body acceleration (CBA), wheel contact force (WCF), and suspension working space (SWS) are 8.3%, 4.5% and 18.7% respectively. The motorway excited on/off skyhook system also performs well where improvements are 6.2% CBA, 1.7% WCF, and 12.1% SWS. However, when the input excitation changes, the on/off system performance is degraded and no improvement in wheel contact force and suspension working space is offered. On the other hand, the linearised modified skyhook system maintains superior performance, where improvements are 10.2% CBA, 5.4% WCF and 10% SWS.

6.5 Summary of Chapter 6

This chapter has presented a HILS experimental investigation of semi-active SDOF and 2DOF mass isolation systems. Here, MR dampers excited by a high response servo-hydraulic actuator were used as the physical hardware components. Meanwhile, the non-physical system components were modelled in a real time digital simulation. For

each case study, the performance of feedback linearisation was investigated by implementing skyhook-based controllers, where comparisons were made with more simplistic on/off controllers and equivalent passive systems.

In order to validate the effect of the actuator dynamics on control system performance, experimental data was compared to a numerical simulation of the HILS SDOF system. This incorporated a previously validated model of the corresponding MR damper, and a servo-hydraulic actuator model, which was validated herein. It was shown that the main effect of the actuator dynamics was to lower performance, where a shift to higher transmissibilities and RMS accelerations was observed. Nonetheless, the relative performance and the optimum controller gain of the various control systems remained unchanged, thus validating the use of the HILS method to predict controller performance.

To give further credence to the efficacy of the HILS method, similar conclusions to the SDOF and 2DOF numerical investigations of Chapter 5 were drawn. More specifically:

- For SDOF systems, it was shown that linearised skyhook control provides far superior transmissibility and RMS acceleration levels to on/off skyhook control. Nonetheless, the on/off system performed well, outperforming the linearised "passive" configuration.

- For 2DOF systems, linearised skyhook control is optimal in terms of passenger comfort, and outperformed the equivalent passive and on/off skyhook systems. Augmenting the linearised skyhook system with viscous damping (modified skyhook control) enhanced the wheel contact force levels at the expense of car body

acceleration. On the other hand, an on/off modified skyhook controller cannot significantly enhance wheel hop vibrations i.e. the pure skyhook system is optimal.

- Feedback linearisation desensitises the controller performance to parameter uncertainty. In the SDOF study, this was indicated through the good correlation between the HILS simulation and the HILS experiment, despite a slightly inaccurate MR damper model. This slight inaccuracy could be representative of changes in the fluid properties due to temperature effects, or variations in the fluid properties due to manufacturing tolerances or long-term use e.g. in-use thickening [27]. In the 2DOF study, the performance of the linearised skyhook systems remained optimal in the face of roadway disturbance changes, unlike the on/off system.

In conclusion, feedback linearisation permits very accurate set-point force tracking in the face of broadband random excitations. Not only does this permit superior performance levels in comparison to more simplistic on/off methods, but also the sensitivity to parameter uncertainty is significantly reduced. In the previous two chapters, this was demonstrated for skyhook-based controllers, although the control concept is equally applicable to other well-established control techniques. For example, the semi-active force generator could be used to track force demands derived from sliding mode or optimal control laws.

Control strategy	Controller gain	α
Linearised	D = 2kNs/m	-
Open-loop	I = 0.075A	-
MR linearised modified skyhook	D_{MRm} = 4kNs/m	0.4
On/off modified skyhook	I_{max} = 0.125A	0

Table 6-1: Controller parameters for the optimised 2DOF control systems.

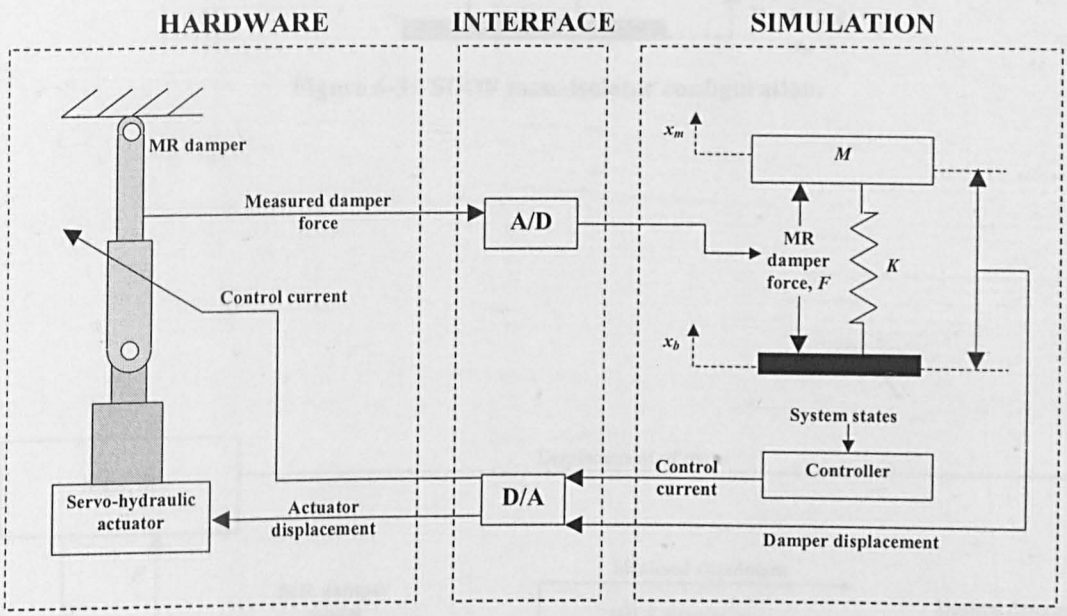

Figure 6-1: Schematic diagram of a HILS system.

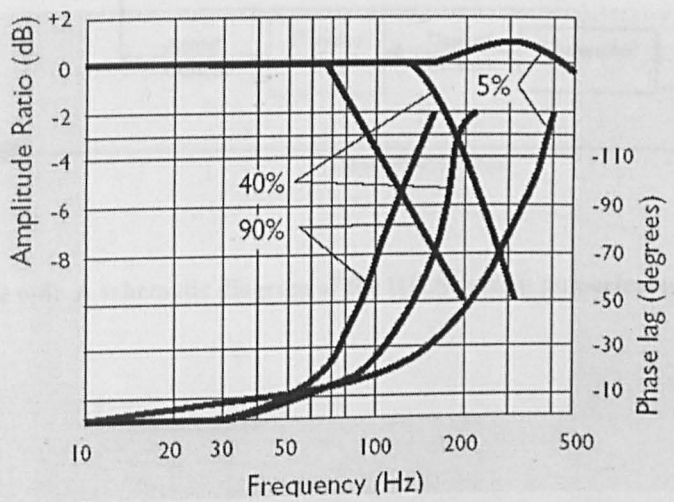

Figure 6-2: Performance curves for the 38l/min Moog D765 EFB servo-valve [135]. Curves are shown for ±5%, ±40 and ± 90% input signal. Data measured at an operating pressure of 210bar, with a fluid viscosity equal to 32mm^{2}s^{-1} and a fluid temperature equal to 40°C.

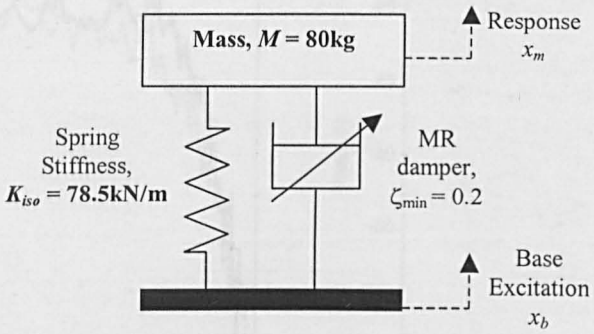

Figure 6-3: SDOF mass-isolator configuration.

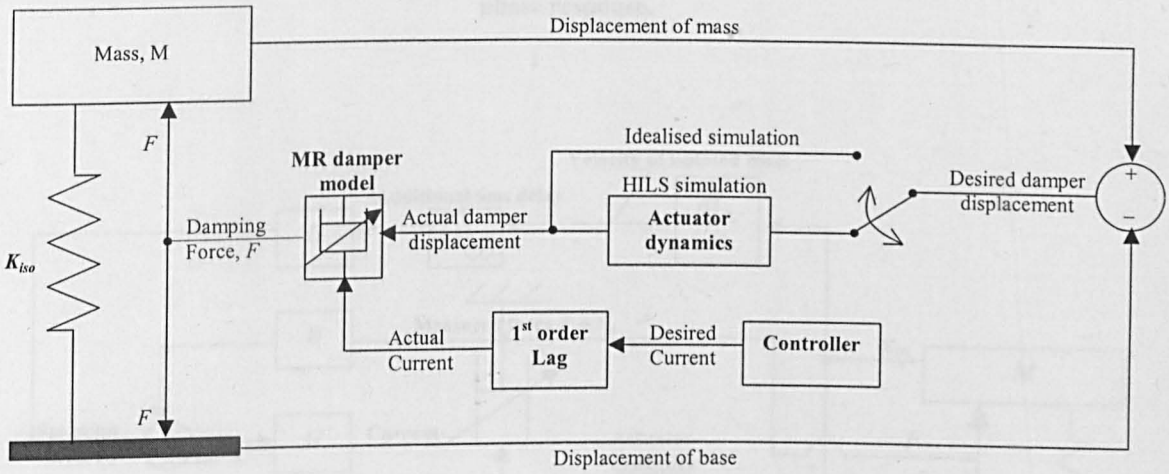

Figure 6-4: A schematic diagram of the HILS system numerical model.

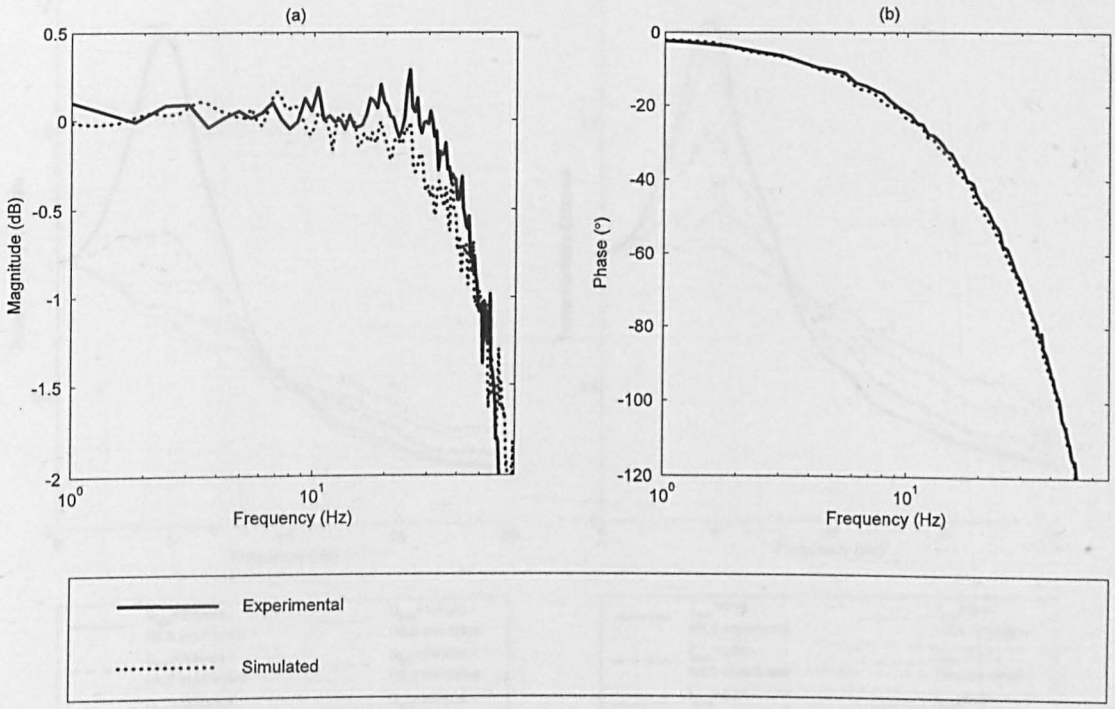

Figure 6-5: A comparison between the experimental and simulated hydraulic actuator frequency response curves (actual displacement / desired displacement). (a) Magnitude response and (b) phase response.

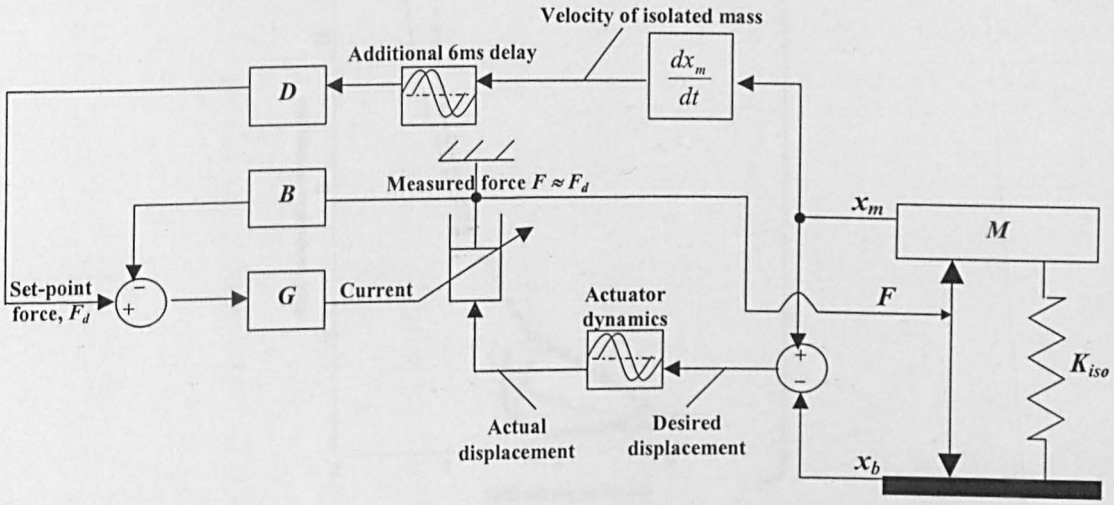

Figure 6-6: Implementation of linearised skyhook control within a HILS system

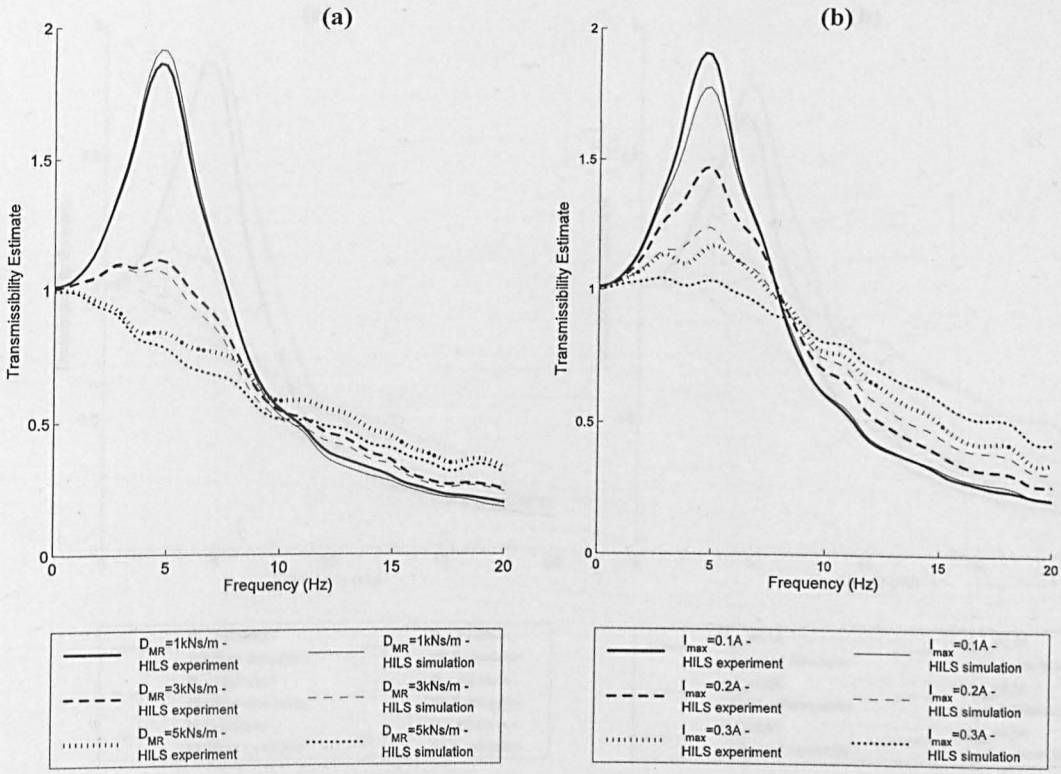

Figure 6-7: Frequency response plots comparing the HILS experiment with the HILS simulation. (a) Linearised skyhook control and (b) on/off skyhook control.

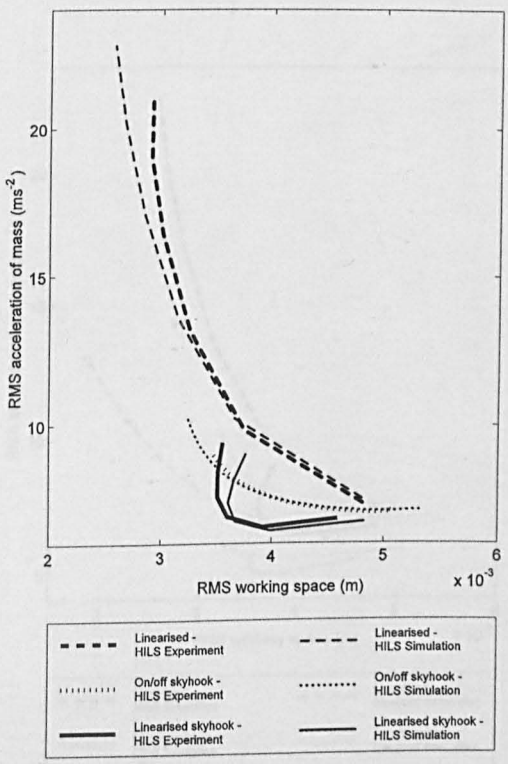

Figure 6-8: Conflict diagram comparing the HILS experiment with the HILS simulation. $D = D_{MR}$ = 1-6kNs/m. I_{max} = 0.02-0.3A.

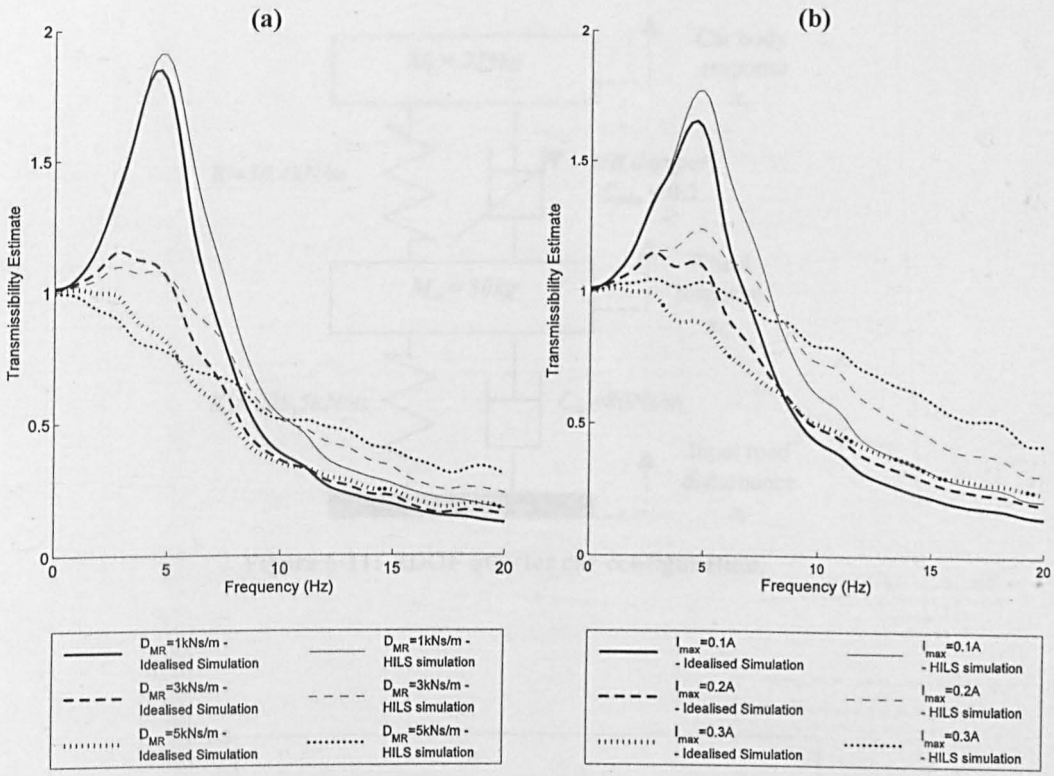

Figure 6-9: Simulated frequency response plots with (HILS simulation) and without (idealised simulation) servo-hydraulic actuator dynamics. (a) Linearised skyhook control and (b) on/off skyhook control.

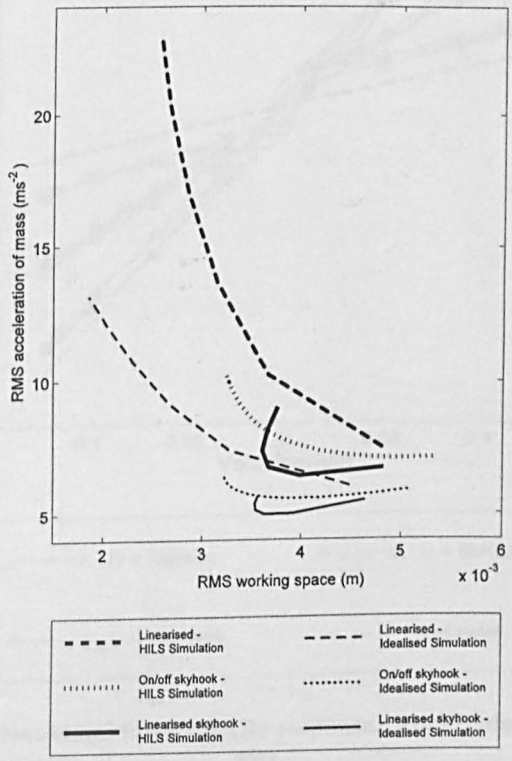

Figure 6-10: Conflict diagram comparing the HILS simulation with the idealised simulation. D = D_{MR} = 1-6kNs/m. I_{max} = 0.02-0.3A.

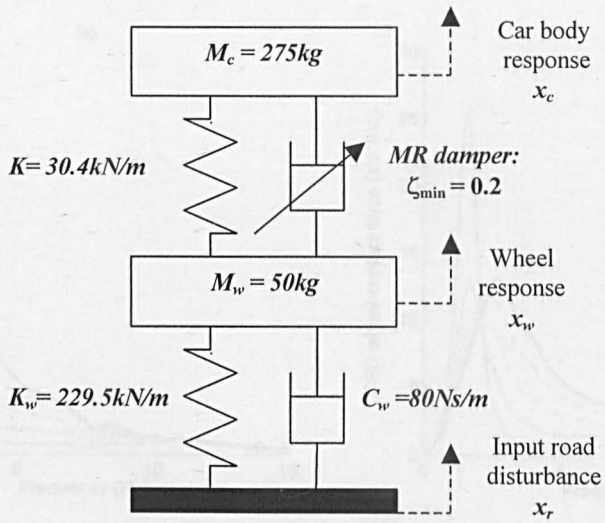

Figure 6-11: 2DOF quarter car configuration.

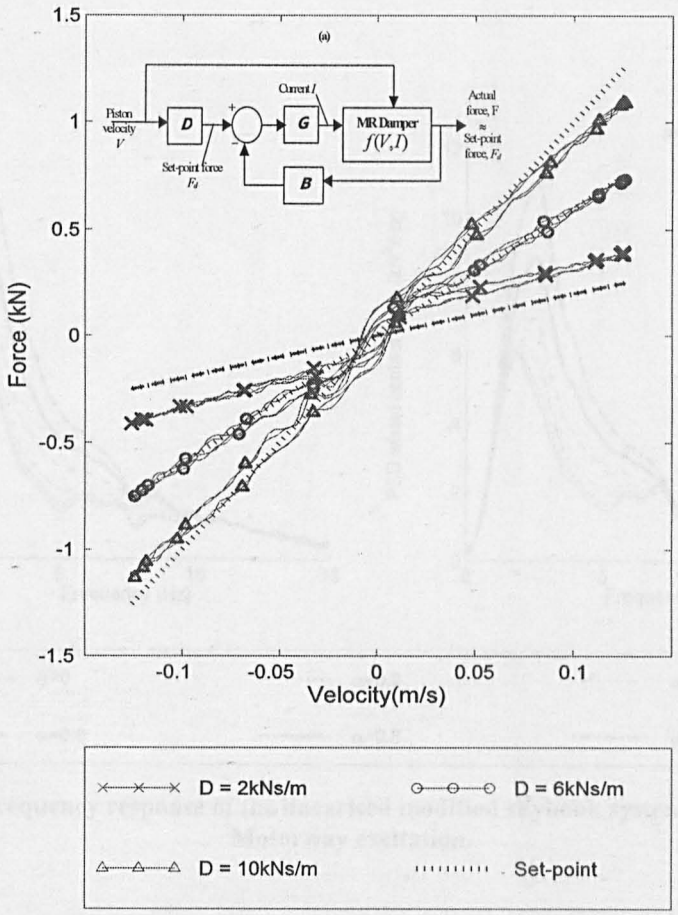

Figure 6-12: Linearised sinusoidal force/velocity response. Amplitude = 5mm, and frequency = 4Hz.

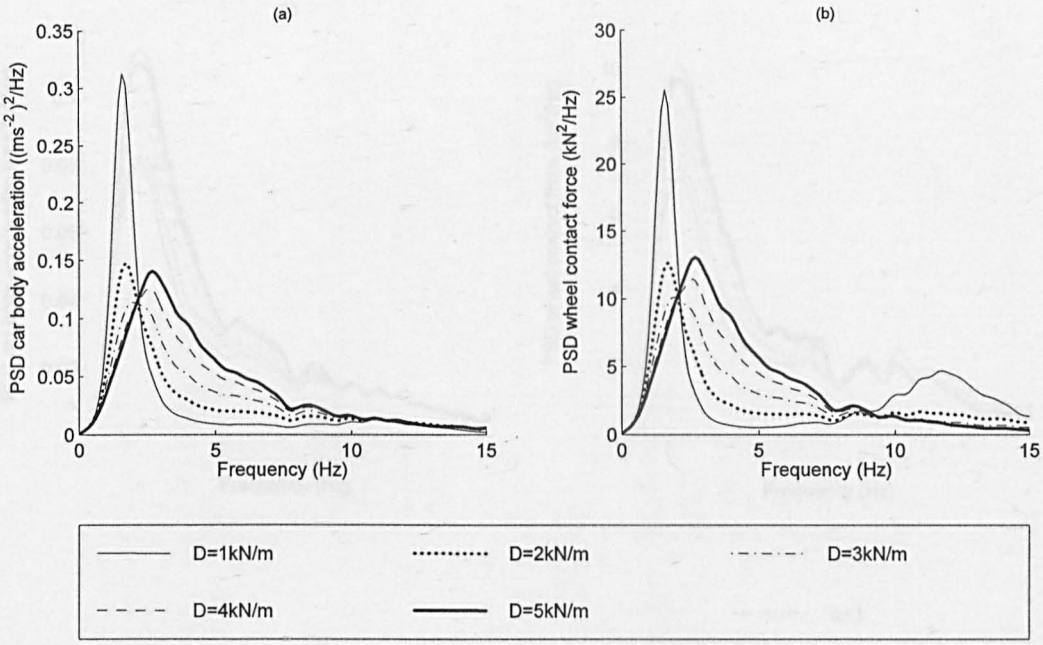

Figure 6-13: Frequency response of the linearised system. Motorway excitation.

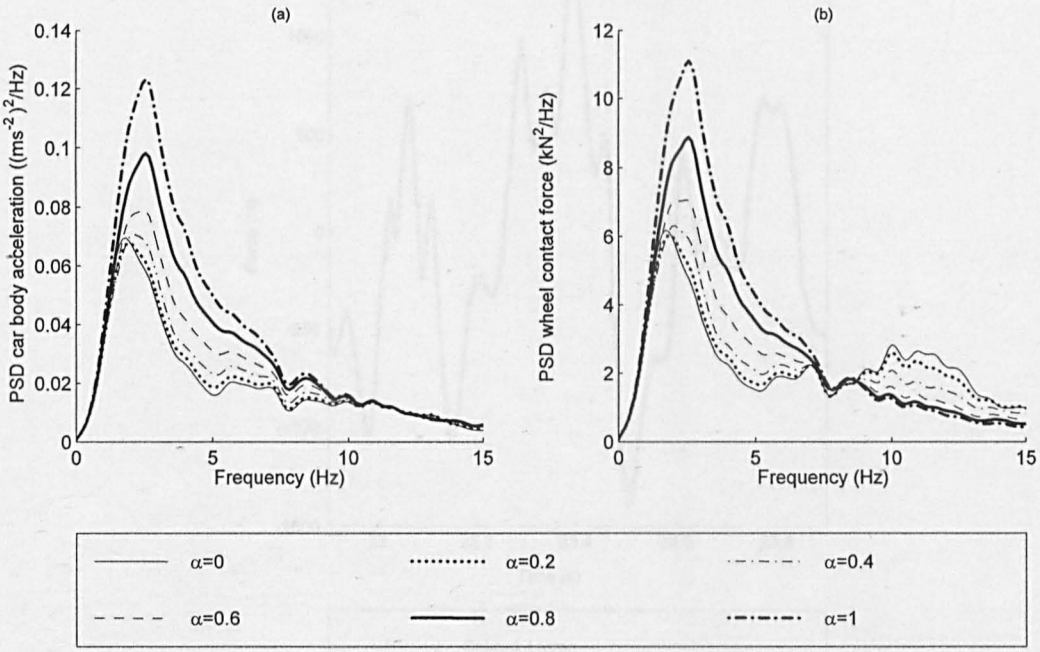

Figure 6-14: Frequency response of the linearised modified skyhook system. D_{MRm} =4kNs/m. Motorway excitation.

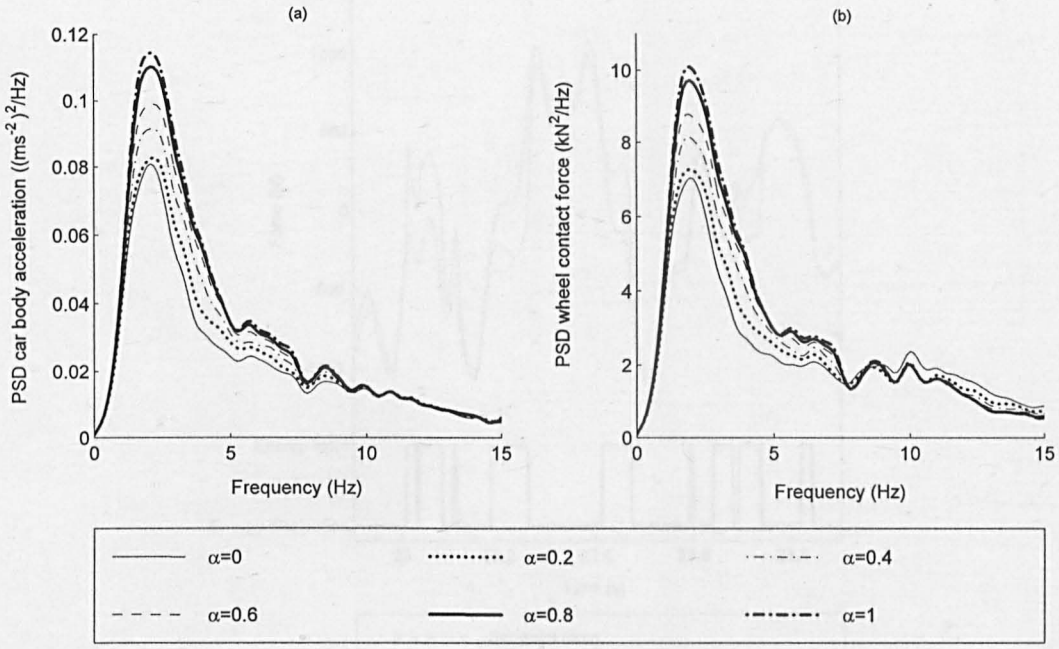

Figure 6-15: Frequency response of the on/off modified skyhook system. I_{max} = 0.15A. Motorway excitation.

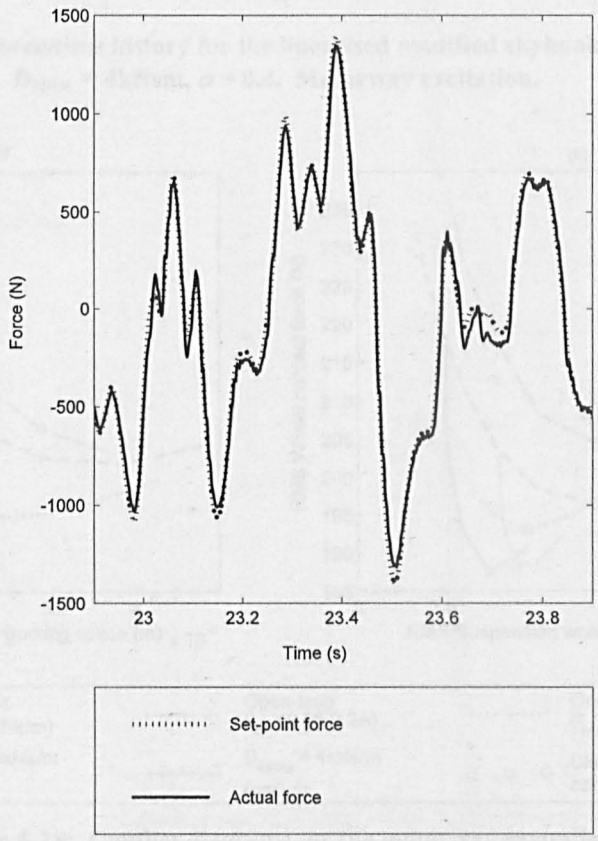

Figure 6-16: Damping force/time history for the linearised quarter car system. D = 3kNs/m. Motorway excitation.

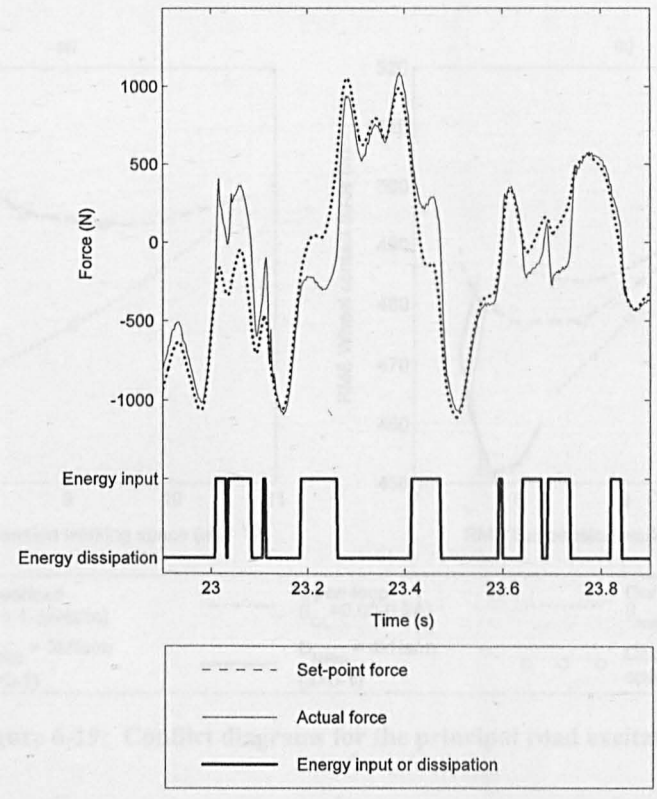

Figure 6-17: Damping force/time history for the linearised modified skyhook quarter car system. D_{MRm} = 4kNsm, α = 0.4. Motorway excitation.

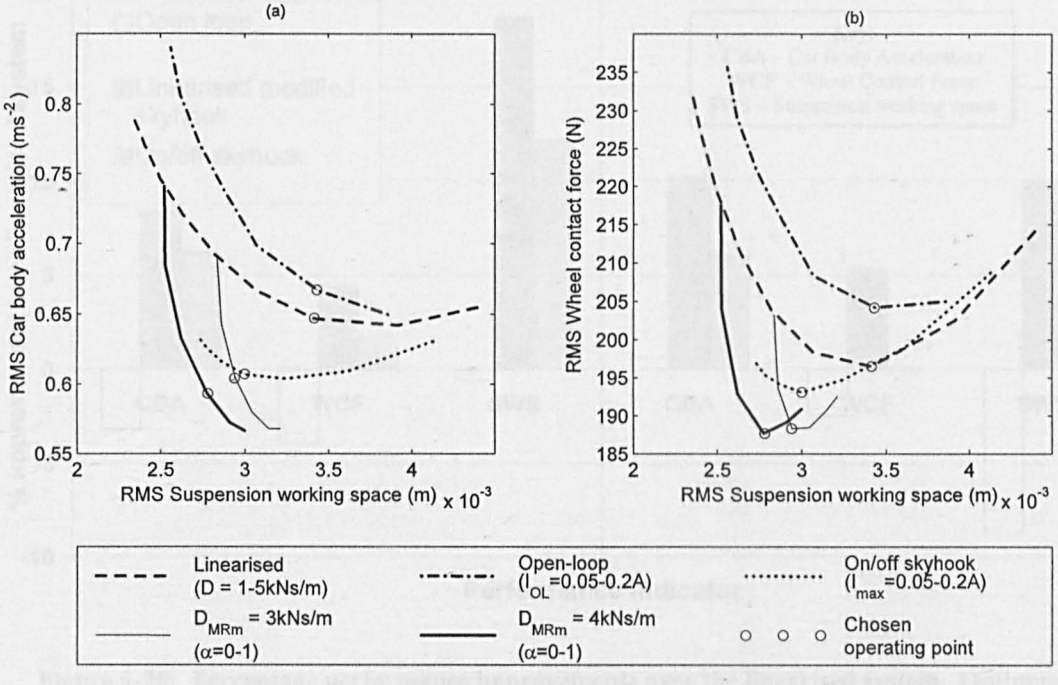

Figure 6-18: Conflict diagrams for the motorway excitation.

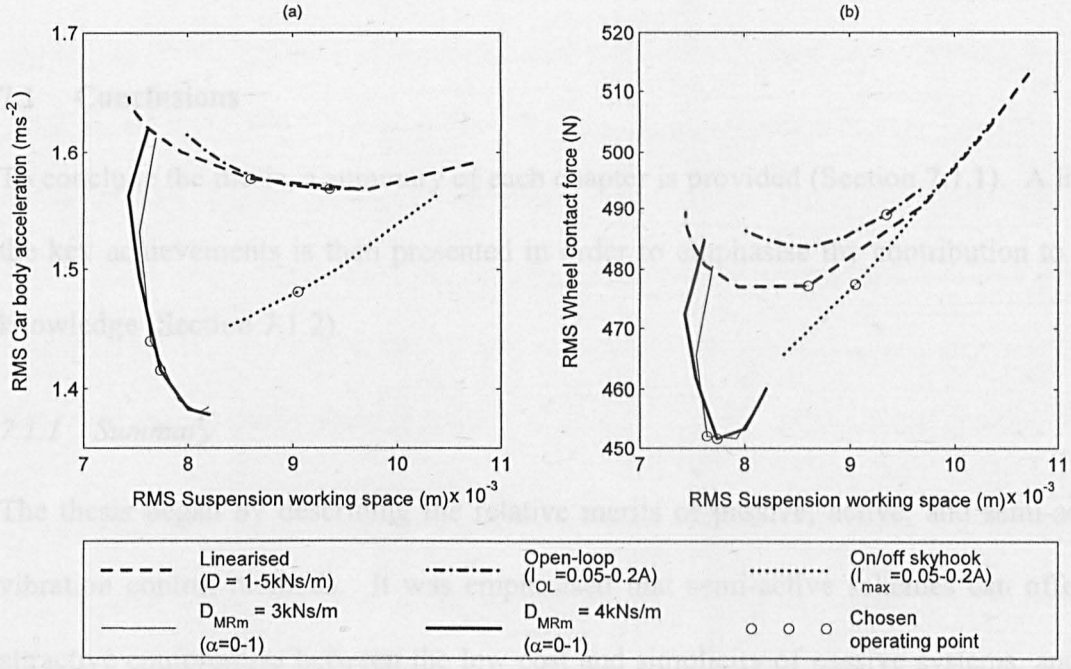

Figure 6-19: Conflict diagrams for the principal road excitation.

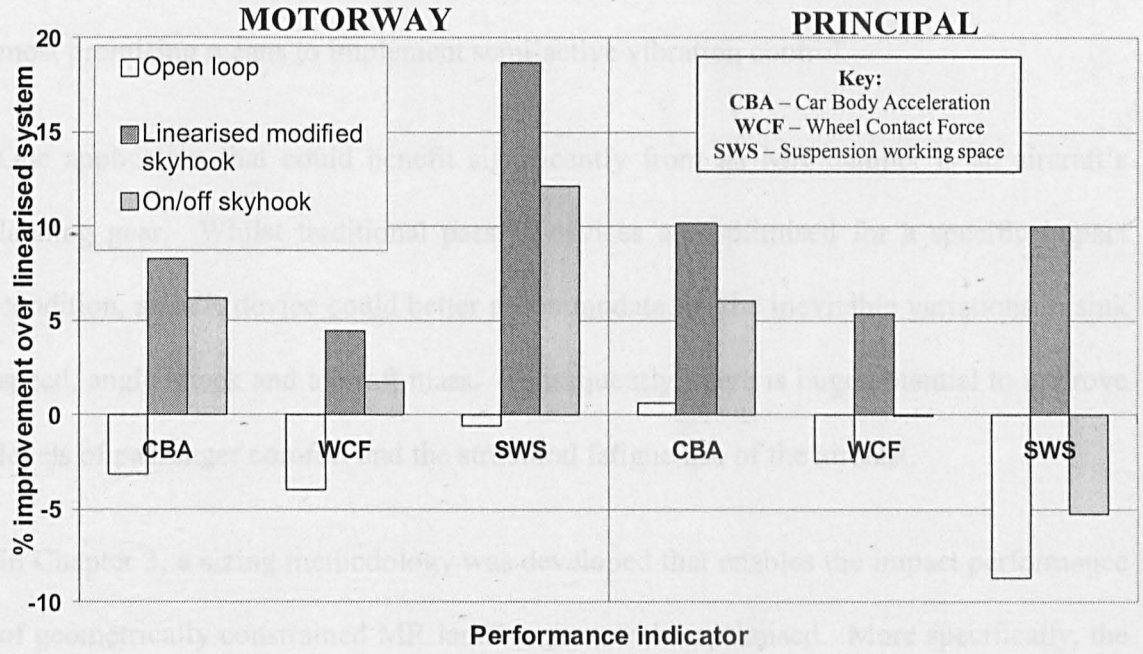

Figure 6-20: Percentage performance improvements over the linearised system. Optimum controller parameters are given in Table 6-1.

CHAPTER 7. CONCLUSIONS AND FURTHER WORK

7.1 Conclusions

To conclude the thesis, a summary of each chapter is provided (Section 7.1.1). A list of the key achievements is then presented in order to emphasise the contribution to new knowledge (Section 7.1.2).

7.1.1 Summary

The thesis began by describing the relative merits of passive, active, and semi-active vibration control methods. It was emphasised that semi-active schemes can offer an attractive compromise between the low cost and simplicity of passive systems, and the high performance of active systems, which are heavier, more complex, and have significant power requirements. In particular, MR dampers were identified as one of the most promising means to implement semi-active vibration control.

One application that could benefit significantly from an MR damper is an aircraft's landing gear. Whilst traditional passive devices are optimised for a specific impact condition, an MR device could better accommodate for the inevitable variations in sink speed, angle attack and aircraft mass. Consequently, there is huge potential to improve levels of passenger comfort and the structural fatigue life of the aircraft.

In Chapter 3, a sizing methodology was developed that enables the impact performance of geometrically constrained MR landing gears to be optimised. More specifically, the methodology permits the simultaneous optimisation of the device's control ratio and the magnetic circuit design. Consequently, the semi-active landing gear can produce desirable behaviour for a wide range of impact conditions, unlike a passive device.

Using real data provided by landing gear manufacturers, the sizing methodology was applied to both lightweight aircraft, and large-scale commercial jets in order to demonstrate scalability. For both aircraft types, results indicate that the peak force and the severity of fatigue loading can be enhanced over a wide range of impact conditions. However, it was shown that MR landing gears are invariably heavier than passive systems, which was largely due to the increased mass of the fluid. Nonetheless, an improved fatigue life is likely to provide weight savings for other aircraft components.

The landing gear sizing methodology was validated in Chapter 4, where a prototype MR landing gear shock strut was designed, fabricated and tested. Here, good correlation between the numerical predictions and the experimental behaviour was shown, particularly for low velocity excitations. At higher velocities, correlation deteriorated due to a quadratic damping effect. This may have been caused by shear thickening of the fluid or even turbulence induced by flow obstructions in the MR valve. Higher shear rate fluid property data would provide an enhanced understanding of this issue.

The complex non-linear behaviour of MR dampers has meant that the choice of an effective control strategy remains an unresolved problem. For landing gear impacts, it transpired that this behaviour could be used to an advantage, where it was shown that an inherently efficient impact response could be obtained using open-loop control i.e. with a constant magnetic field. However, this non-linear behaviour is highly undesirable for other broadband excited systems such as an aircraft taxiing or a vehicle suspension. Consequently, the aim of Chapters 5 and 6 was to investigate control strategies for broadband excited MR vibration systems. In particular, this thesis focused on a control technique known as feedback linearisation, which uses force feedback to linearise the

force/velocity response of the MR damper. This permits accurate force tracking within the semi-active limits of the device, and hence the effective application of classical control techniques.

In Chapter 5, numerical studies of both single-degree-of-freedom (SDOF) and two-degree-of-freedom (2DOF) MR vibration systems were performed. Using skyhook-based control laws, feedback linearisation was shown to outperform more simplistic on/off controllers and equivalent passive systems, whilst approaching that of ideal semi-active and fully active schemes. Furthermore, the use of feedback linearisation desensitised the controller performance to changes in the input excitation. For example, the performance of the on/off systems deteriorated under different excitation conditions, whilst the controller configuration for the linearised systems remained optimal.

The results from this numerical study were further validated in Chapter 6, which presented experimental investigations of SDOF and 2DOF MR vibration systems. Here, the hardware-in-the-loop simulation (HILS) method was adopted, which enabled the complex behaviour of the MR damper and controller to be physically tested, whilst the remainder of the system dynamics were simulated in real-time. After validating the efficacy of the HILS technique, feedback linearisation was again shown to outperform more conventional on/off systems, and to desensitise the performance to parameter uncertainty.

7.1.2 Key Contributions

The key contributions of this thesis to new knowledge are as follows:

- A design methodology has been developed that enables the impact performance of MR landing gears to be optimised. This used an efficient magnetic circuit sizing spreadsheet, which incorporated the existing packaging constraints, and a dynamic landing impact model, which accounted for the effects of fluid compressibility. This is the first time that packaging constraints and fluid compressibility issues have been considered in ER/MR landing gear research. Consequently, a unique tool for assessing the feasibility of smart fluid landing gears has been developed, which could also be applied more generally to other impact systems.

- A prototype MR landing gear was designed, fabricated and tested. In the experiments, a method was developed to accurately validate the quasi-steady model, and to measure the fluid's bulk modulus. This method utilised pressure sensor readings from a constant velocity test, which enabled the gas spring and frictional forces to be neglected. A technique for identifying the device time constant of the magnetic circuit/smart fluid rheology was also developed. Here, the validated dynamic shock strut model enabled the effects of fluid compressibility to be eliminated from the identified value.

- The numerous publications from this thesis will help to promote the feasibility of MR landing gears, and the various issues that must be addressed before the technology can be commercialised [116-118, 130].

- Feedback linearisation has been more formally investigated within SDOF and 2DOF structures, where excellent force tracking accuracy has been demonstrated in the face of realistic broadband excitation signals. This was demonstrated numerically, and validated experimentally using HILS. Furthermore, the HILS

method was validated using a numerical model of the servo-hydraulic system dynamics.

- The superiority of feedback linearisation over the more commonly used on/off methods has been clearly illustrated. Consequently, this thesis has made a significant contribution to enabling the non-linear behaviour of MR dampers to be better controlled. The control based publications from this thesis [142, 143, 151, 152, 154] should help feedback linearisation become recognised as one of the most effective means to implement classical control techniques e.g. skyhook, optimal, and sliding mode controllers.

7.2 Further work

In this section, the potential areas for further research are described under the following categories – MR landing gear design, and the control of MR dampers.

7.2.1 MR landing gear design

In the analytical sizing spreadsheet, the magnetic performance calculations could be improved by considering flux leakage effects in the fluid. This would further avoid the necessity to perform FEA. Moreover, it would enable the full yield stress range of the MR fluid to be better exploited, which would enhance controllability. Flux leakage could be accounted for by increasing the pole area of the fluid (in Eq.3-23), but the extent of this would require investigation/validation.

Another interesting topic would be to investigate the effect of eddy currents on the magnetic circuit performance. Eddy currents are induced when the solenoid current changes, and they will act to oppose the direction of the desired magnetic field.

Consequently, the eddy currents could degrade the time constant associated with the generation of the fluid yield stress. Such effects are likely to be particularly significant in larger devices, and it would be interesting to investigate whether the choice of valve material could improve performance. For example, silicon-iron alloy is known to reduce eddy current losses due to its larger resistivity [155]. These eddy current effects could be accurately investigated using a dynamic FEA software package e.g. FLUX [139]. The FEMM software used in this thesis could only perform static analyses [128].

In Chapter 3, a numerical model of the landing gear was developed that included the effects of fluid compressibility. The model was not stable over many excitation cycles, and this was thought to be due to the assumption of constant density in the mass flow continuity equation derivation (see Appendix B). To try and overcome this problem, it would be interesting to re-derive the model using a variable density. One method might be to use the acoustic wave equation, which describes the propagation of pressure waves in a compressible fluid [120]. The wave equation has some similarities to the model used in the present thesis but it does assume constant density.

To experimentally validate the sizing methodology, this thesis focused on the relatively low velocity behaviour of MR landing gear shock struts. This was due to the velocity limitations of the servo-hydraulic actuator, which was rated at $\pm 1 ms^{-1}$. To investigate higher velocity behaviour, future work should focus on the impact performance of the MR shock strut. The existing test facility, which incorporates a sliding mass (see Figure 4-4), will have the capability to perform impacts up to $7ms^{-1}$ once the drop mass hoist/release mechanism, and the impact zone have been commissioned.

Drop tests will enable an enhanced understanding of the force/velocity behaviour, the fluid compressibility effects, and the device's controllability under more realistic conditions. Fluid compressibility is likely to be particularly important at higher velocities, where in this thesis it was found that at just $0.1ms^{-1}$, the time constant was increased by 28%. Furthermore, drop tests would enable the effects of valve turbulence to be better understood, which still remains a largely unexplored research topic. In the present study, maintaining a sub-critical Reynolds number was given particular importance in the sizing analysis. This could be validated by correlating impact test results with a dynamic MR shock absorber model. Ahmadian and Norris [156] performed a similar investigation and showed that performance deteriorated beyond a certain Reynolds number. However, the Reynolds number calculations were based upon incompressible flow, which is highly unrealistic in an impact scenario.

Another issue that requires further investigation is the quadratic damping effect in the prototype shock strut's response. This effect could be a result of shear thickening of the fluid, or even turbulence caused by the flow obstructions in the valve. Fluid property data at significantly higher shear rates is required to investigate this. Such data cannot be obtained using modern rheometers, although a way forward might be to test the fluid in a bypass arrangement as shown in Figure 7-1. This would enable a parallel plate MR valve to be tested, thus eliminating any obstructions in the flow path. If the quadratic damping effect is found to be turbulence related, then an alternative method to construct the annular passage must be sought. As shown in Figure 7-2, one solution might be to use spot welds, which would provide less of an obstruction than the valve gap support spiders (see Figure 4-2). Furthermore, this method would be significantly more cost-

effective, as it would eliminate the expensive wire-cutting process required by the existing design.

A further issue that was raised in this thesis was the lack of repeatability in the experimental results. More specifically, the fluid yield stress reduced after performing higher velocity tests. It was hypothesised that this occurred either as a result of fluid mixing with the gas, or due to a reduced amount of iron particle sediment. It would therefore be interesting to re-design the MR landing gear with a floating piston, which would separate the fluid from the gas, thus eliminating the former reason. If sedimentation transpires to be the problem, then it would be interesting to investigate the use of shear-thinning gels as a base fluid. Such gels are often used to prevent sedimentation in applications that do not see regular motion e.g. seismic dampers [27]. This is likely to be an important issue for MR landing gears, where sediment may build up during flight.

This thesis has focused on the design of flow mode MR landing gears. It would also be interesting to investigate whether other modes of operation could be incorporated within the packaging constraints e.g. shear, mixed. A shear mode device could be advantageous as the working volume of fluid, and hence the fluid mass would be lower. Furthermore, a shear mode device would eliminate compression of the fluid. A device combining shear and flow modes is likely to yield similar conclusions to the present thesis.

Finally, it would be interesting to investigate the use of ER valves in landing gears. Traditionally, electrorheological (ER) fluids were ruled out from aerospace applications, owing to a reluctance to provide the necessary voltages (up to 5kV). However, with

more recent advances in aerospace technology, higher voltages are becoming more acceptable. Although conventional ER fluids have lower yield strengths, they also have a much lower mass than their MR counterparts, which could make them a strong candidate for landing gear. One means to overcome the low yield strength of ER fluids would be to consider the use of multi-duct valves [157] as shown in Figure 7-3. The ducts, which could either be arranged in series or parallel, boost controllability by enhancing the active volume of fluid.

7.2.2 Control of MR dampers

The present thesis has made a significant contribution towards the development of effective controllers for MR vibration systems. In particular, using numerical and HILS experimental methods, feedback linearisation was shown to provide superior performance over more simplistic on/off strategies. The next step should be to develop a physical MR vibration system, which incorporates real masses and springs in addition to the MR damper. In comparison to the HILS method, this would eliminate the effect of the actuator dynamics and the need to use additional time delays that emulate the real sensors (see Figure 6-6). Consequently, an enhanced understanding of the real control system performance will result. To build a physical vibration system, the existing damper test facility could be modified as shown Figure 7-4. Here, the servo-hydraulic actuator provides the base input, whilst the drop test facility is used to constrain an isolated mass in the vertical direction.

As a further extension to this thesis, it would be interesting to investigate sliding mode controllers, which are inherently robust against parameter uncertainty and external disturbances [87]. To implement this strategy, investigators commonly assume a

relationship between the smart damper's yield force and the applied field [86, 87]. It would therefore be interesting to investigate whether feedback linearisation could offer any advantages over this method. Lam and Liao [85] used feedback linearisation to track the sliding mode force for a quarter car system. However, the authors did not use realistic broadband excitations, and the method was not benchmarked against other controllers.

Another research topic would be to formally investigate the effects of temperature on control system performance. More specifically, changes in temperature will alter the MR fluid's viscosity, and will have an impact on performance. Fluid temperature is difficult to control experimentally, but analytical methods would provide an excellent means to investigate this e.g. using uncertainty propagation techniques [158]. Here, the ability of feedback linearisation to desensitise control system performance to parameter uncertainty could be formally investigated. Furthermore, it would be interesting to design a sliding mode controller that is robust against viscosity variations. To the author's knowledge, this has not been considered previously.

Finally, the stability of feedback linearisation should be formally investigated. Sims investigated the limit cycle behaviour of linearised MR dampers [159]. This work could be extended to consider the stability effects within a vibrating structure. Furthermore, the effects of parameter uncertainty on control system stability (e.g. temperature) would also form an interesting topic of research.

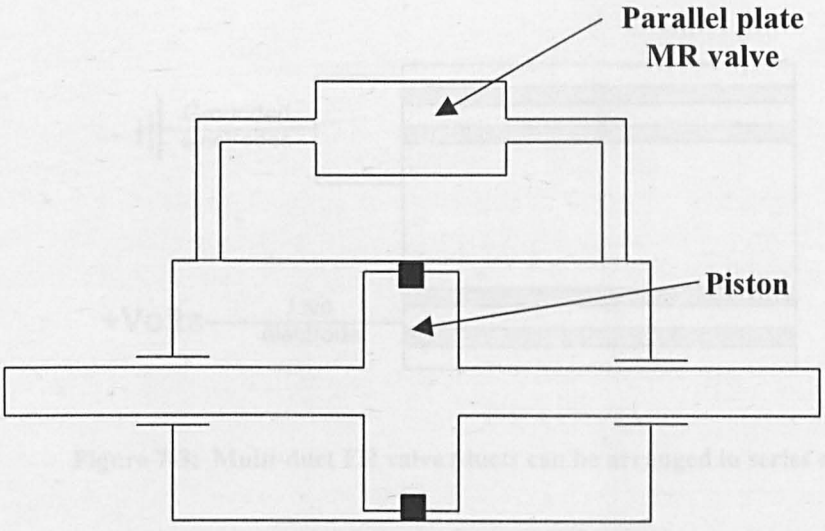

Figure 7-1: MR bypass damper.

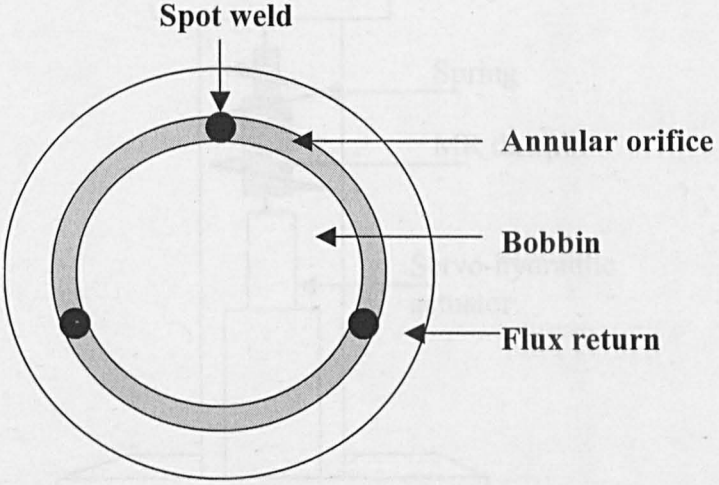

Figure 7-2: An alternative method to fabricate the annular orifice.

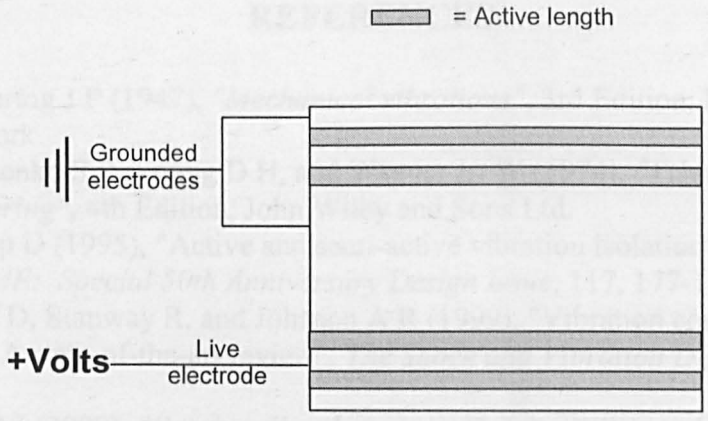

Figure 7-3: Multi-duct ER valve (ducts can be arranged in series or parallel).

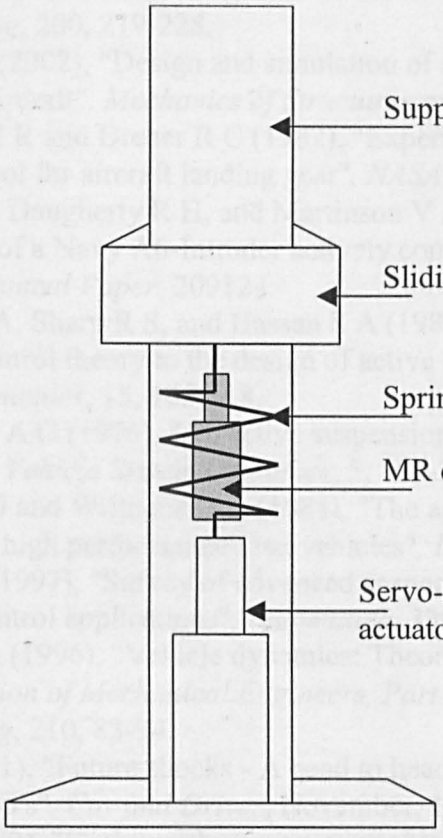

Figure 7-4: Experimental SDOF MR vibration system.

REFERENCES

[1] Den-Hartog J P (1947), *"Mechanical vibrations"*, 3rd Edition, McGraw-Hill, New York.

[2] Timoshenko S P, Young D H, and Weaver Jr. W (1974), *"Vibration problems in engineering"*, 4th Edition, John Wiley and Sons Ltd.

[3] Karnopp D (1995), "Active and semi-active vibration isolation", *Transactions of the ASME: Special 50th Anniversary Design Issue*, 117, 177-185.

[4] Sims N D, Stanway R, and Johnson A R (1999), "Vibration control using smart fluids: A state-of-the-art review", *The Shock and Vibration Digest*, 31(3), 195-203.

[5] Mead D J (2000), *"Passive vibration control"*, John Wiley and Sons Ltd.

[6] Karnopp D, Crosby M J, and Harwood R A (1974), "Vibration control using semi-active force generators." *Journal of Engineering for Industry*, 96, 619-626.

[7] Sharp R S and Hassan S A (1986), "The relative performance capabilities of passive, active and semi-active car suspension systems", *Proceedings of the Institution of Mechanical Engineers, Part D: Journal of Automobile Engineering*, 200, 219-228.

[8] Krüger W (2002), "Design and simulation of semi-active landing gears for transport aircraft", *Mechanics of Structures and Machines*, 30(4), 493-526.

[9] McGehee J R and Dreher R C (1982), "Experimental investigation of active loads control for aircraft landing gear", *NASA Technical Paper*, 2042.

[10] Horta L G, Daugherty R H, and Martinson V J (1999), "Modelling and validation of a Navy A6-Intruder actively controlled landing gear system", *NASA Technical Paper*, 209124.

[11] Wilson D A, Sharp R S, and Hassan S A (1986), "The application of linear optimal control theory to the design of active automotive suspensions", *Vehicle System Dynamics*, 15, 105-118.

[12] Thompson A G (1976), "An active suspension with optimal linear state feedback", *Vehicle System Dynamics*, 5, 187-203.

[13] Wright P G and Williams D A (1984), "The application of active suspension systems to high performance road vehicles", *IMechE C239/84*, 23-28.

[14] Hrovat D (1997), "Survey of advanced suspension developments and related optimal control applications", *Automatica*, 33(10), 1781-1817.

[15] Crolla D A (1996), "Vehicle dynamics: Theory into practice", *Proceedings of the Institution of Mechanical Engineers, Part D: Journal of automobile engineering*, 210, 83-94.

[16] Csere (1991), "Future shocks - A head to head comparison of active and passive Infinity Q45's", *Car and Driver*, November, 171-177.

[17] Ross I (1980), "Flightworthy active control landing gear system for a supersonic aircraft", *NASA Contractor Report*, 3298.

[18] Howell W E, Mcgehee J R, Daugherty R H, and Vogler W A (1990), "F-106B airplane active control landing gear drop test performance", *NASA Technical Memorandum*, 102741.

[19] McGehee J R and Morris D L (1985), "Active control landing gear for ground load alleviation", *AGARD Technical Evaluation Report on the Flight Mechanics Symposium on Active Control Systems*, 19850301.

[20] Sims N D and Stanway R (2003), "Semi-active vehicle suspension using smart fluid dampers: A modelling and control study", *International Journal of Vehicle Design*, 33(1-3), 76-102.

[21] Bender E K, Karnopp D C, and Paul I L (1967), "On the optimisation of vehicle suspensions using random process theory", *ASME Paper No. 67-Tran-12.*

[22] Cebon D, Besinger F H, and Cole D J (1996), "Control strategies for semi-active lorry suspensions", *Proceedings of the Institution of Mechanical Engineers, Part D: Journal of Automobile Engineering*, 210, 161-178.

[23] Ghiringhelli G L (2000), "Testing of semiactive landing gear control for a general aviation aircraft", *Journal of Aircraft*, 37(4), 606-616.

[24] Maemori K i, Tanigawa N, Koganei R, and Morihara T (2003), "Optimization of a semi-active shock absorber for aircraft landing gear", *2003 ASME Design Engineering Technical Conferences and Computers and Information in Engineering Conference, Sep 2-6 2003*, 2 A, Chicago, IL, United States, American Society of Mechanical Engineers, New York, NY 10016-5990, United States, 597-603.

[25] Delphi MagneRide (2006), http://delphi.com/manufacturers/auto/chsteer/ride/magneride/.

[26] Carlson J D (2005), "Magnetorheological fluids - Engineering applications today and tomorrow", *2nd ECCOMAS Thematic Conference on Smart Structures and Materials*, Lisbon, Portugal, July 18-21.

[27] Carlson J D (2003), "Critical factors for MR fluids in vehicle systems", *International Journal of Vehicle Design*, 33(1-3), 207-217.

[28] Carlson J D, Catanzarite D M, and St. Clair K A (1996), "Commercial magnetorheological fluid devices", *Proceedings of the 5th International Conference on Electrorheological Fluids, Magnetorheological Suspensions and Associated Technology*, World Scientific Publishing, Singapore, 20-28.

[29] Brookes D A (1982), "Electro-Rheological Devices", *Chartered Mechanical Engineer*, September, pp 91-93.

[30] Stangroom J E (1983), "Electro-Rheological Fluids", *Physics in Techology*, 14, 290-296.

[31] Ma Y, Zhang Y, and Lu K (1998), "Frequency and temperature dependence of complex stronium titanate electrorheological fluids under an alternating electric field", *Journal of Applied Physics*, 83, 5522-5524.

[32] ADLAND (2003-2006), "Adaptive landing gears for improved impact absorption", *Project reference number: IST-FP6-2002-Aero-1-502793-STREP*, http://smart.ippt.gov.pl/adland/.

[33] Winslow W M (1947), "Method and means for translating electrical impulses into mechanical forces", U.S. Patent No. 2,417,850.

[34] Winslow W M (1949), "Induced fibration of suspensions", *Journal of Applied Physics*, 20, 1137-1140.

[35] Rabinow J (1948), "The magnetic fluid clutch", *AIEE Transactions*, 67, 1308-1315.

[36] Lord Corporation (2004), "Lord Corporation magnetorheological fluid for automotive suspension systems", *IIR Suspension and Damping Conference*, http://www.lord.com/Portals/_default/LordDocuments/root/white_papers/2004_IIR_Suspension_and_Damping_Conference_v5.pdf.

[37] Lord Corporation, Materials Division, 406 Gregson Drive, Cary, NC 27511, USA, http://www.lord.com.

[38] Delphi Press Release (2006), "Ferrari 599 GTB driving experience boosted by Delphi Technology", http://www.delphi.com/news/pressReleases/pr72389-03012006.

[39] Delphi Press Release (2006), "Delphi's MagneRide semi-active suspension helps increase comfort and handling on the new Audi TT", http://delphi.com/news/pressReleases/pr_2006_06_01_001/.

[40] Lord MR Solutions (2002), "What is the difference between MR and ER fluid", *Presentation*, http://literature.lord.com/root/other/rheonetic/MRvsER.pdf.

[41] Kordonsky W I (1993), "Magnetorheological effect as a base of new devices and technologies", *Proceedings of the 6th International Conference on Magnetic Fluids, Jul 20-24 1992, Journal of Magnetism and Magnetic Materials*, 122(1-3), 395-398.

[42] Ervin R D, Lou Z, Filisko F E, and Winkler C B (1996), "Electrorheology for Smart Landing Gear", *NASA-CR*, 200883.

[43] Neelakantan V A and Washington G N (2005), "Modeling and reduction of centrifuging in magnetorheological (MR) transmission clutches for automotive applications", *Journal of Intelligent Material Systems and Structures*, 16(9), 703-711.

[44] Li W H and Du H (2003), "Design and experimental evaluation of a magnetorheological brake", *International Journal of Advanced Manufacturing Technology*, 21(7), 508-515.

[45] Harland N R, Mace B R, and Jones R W (2001), "Adaptive-passive control of vibration transmission in beams using electro/magnetorheological fluid filled inserts", *IEEE Transactions on Control Systems Technology*, 9(2), 209-220.

[46] Kightlinger D (2006), "Magnetizable Fluid Proves a Plus in a Clutch Situation", http://www.gm.com/company/careers/career_paths/rnd/prj_magnetorheological.html.

[47] Lou Z, Ervin R D, Filisko F E, and Winkler C B (1993), "Electrorheologically controlled landing gear", *Aerospace Engineering (Warrendale, Pennsylvania)*, 13(6), 17-22.

[48] Wang J, Meng G, Feng N, and Hahn E J (2005), "Dynamic performance and control of squeeze mode MR fluid damper-rotor system", *Smart Materials and Structures*, 14(4), 529-539.

[49] Berg C D and Wellstead P E (1998), "The application of a smart landing gear oleo incorporating electrorheological fluid", *Journal of Intelligent Material Systems and Structures*, 9(8), 592-600.

[50] Kamath G M, Hurt M K, and Wereley N M (1996), "Analysis and testing of Bingham plastic behavior in semi-active electrorheological fluid dampers", *Smart Materials and Structures*, 5(5), 576-590.

[51] Wilkinson W L (1960), *"Non-Newtonian fluids"*, Oxford: Pergamon Press.

[52] Wereley N M and Li P (1998), "Nondimensional analysis of semi-active electrorheological and magnetorheological dampers using approximate parallel plate models", *Smart Materials and Structures*, 7(5), 732-743.

[53] Yang G, Spencer Jr B F, Carlson J D, and Sain M K (2002), "Large-scale MR fluid dampers: Modelling and dynamic performance considerations", *Engineering Structures*, 24, 309-323.

[54] Gavin H P, Hanson R D, and Filisko F E (1996), "Electrorheological dampers, Part I: Analysis and design", *Journal of Applied Mechanics*, 63, 669-675.

[55] Peel D J and Bullough W A (1994), "Prediction of ER valve performance in steady flow", *Proceedings of the Institution of Mechanical Engineers, Part C: Journal of Mechanical Engineering Science*, 208, 253-266.

[56] Phillips R W (1969), "Engineering applications of fluids with a variable yield stress", *DEng Thesis*, Department of Mechanical Engineering, University of California at Berkeley.

[57] Wereley N M and Pang L (1998), "Nondimensional analysis of semi-active electrorheological and magnetorheological dampers using approximate parallel plate models", *Smart Materials and Structures*, 7(5), 732-743(12).

[58] Lee D-Y, Choi Y-T, and Wereley N M (2002), "Performance analysis of ER/MR impact damper systems using Herschel-Bulkley model", *Journal of Intelligent Material Systems and Structures*, 13(7-8), 525-531.

[59] Lee D-Y and Wereley N M (2000), "Quasi-steady Herschel-Bulkley analysis of electro- and magneto-rheological flow mode dampers", *Journal of Intelligent Material Systems and Structures*, 10(10), 761-769.

[60] Wang X and Gordaninejad F (2000), "Flow analysis of field-controllable, electro- and magneto-rheological fluids using Herschel-Bulkley model", *Journal of Intelligent Material Systems and Structures*, 10(8), 601-608.

[61] Dimock G A, Yoo J-H, and Wereley N M (2002), "Quasi-steady Bingham biplastic analysis of electrorheological and magnetorheological dampers", *Journal of Intelligent Material Systems and Structures*, 13(9), 549-559.

[62] Lord Corporation (2006), "MR seat damper (RD-1005-3)", http://www.lord.com/Default.aspx?tabid=2068&pid=3.

[63] Sims N D, Peel D J, Stanway R, Johnson A R, and Bullough W A (2000), "The electrorheological long-stroke damper: A new modelling technique with experimental validation", *Journal of Sound and Vibration*, 229(2), 207-227.

[64] Stanway R, Sproston J L, and El-Wahed A K (1987), "Non-linear modelling of an electro-rheological vibration damper", *Journal of Electrostatics*, 20, 167-184.

[65] Gamota D R and Filisko F E (1991), "Dynamic mechanical studies of electro-rheological fluids", *Journal of Rheology*, 35, 399-426.

[66] Spencer Jr. B F, Dyke S J, Sain M K, and Carlson J D (1997), "Phenomenological model for magnetorheological dampers", *Journal of Engineering Mechanics*, 123(3), 230-238.

[67] Dominguez A, Sedaghati R, and Stiharu I (2004), "Modelling the hysteresis phenomenon of magnetorheological dampers", *Smart Materials and Structures*, 13(6), 1351-1361.

[68] Giuclea M, Sireteanu T, Stancioiu D, and Stammers C W (2004), "Model parameter identification for vehicle vibration control with magnetorheological dampers using computational intelligence methods", *Proceedings of the Institution of Mechanical Engineers, Part I: Journal of Systems and Control Engineering*, 218(7), 569-581.

[69] Vavreck A N (2002), "Single-stage magnetorheological damper parameter estimation", *Smart Materials and Structures*, 11(4), 596-598.

[70] Kamath G M and Wereley N M (1997), "Nonlinear viscoelastic-plastic model for electrorheological fluids", *Smart Materials and Structures*, 6(3), 351-359.

[71] Gavin H P, Hanson R D, and Filisko F E (1996), "Electrorheological dampers, Part II: Testing and modelling", *Journal of Applied Mechanics*, 63, 676-682.

[72] Choi S-B, Lee S-K, and Park Y-P (2001), "A hysteresis model for the field-dependent damping force of a magnetorheological damper", *Journal of Sound and Vibration*, 245(2), 375-383.

[73] Chang C-C and Roschke P (1999), "Neural network modelling of a magnetorheological damper", *Journal of Intelligent Material Systems and Structures*, 9(9), 755-764.

[74] Sims N D, Holmes N J, and Stanway R (2004), "A unified modelling and model updating procedure for electrorheological and magnetorheological dampers", *Smart Materials and Structures*, 13, 100-121.

[75] Dyke S J, Spencer B F J, Sain M K, and Carlson J D (1998), "Experimental study of MR dampers for seismic protection", *Smart Materials and Structures*, 7(5), 693-703.

[76] Jansen L M and Dyke S J (2000), "Semi-active control strategies for MR dampers: Comparative study", *Journal of Engineering Mechanics*, 126(8), 795-803.

[77] Yi F, Dyke S J, Caicedo J M, and Carlson J D (2001), "Experimental verification of multi-input seismic control strategies for smart dampers", *Journal of Engineering Mechanics*, 127(11), 1152-1164.

[78] Yoshida O and Dyke S J (2004), "Seismic control of a nonlinear benchmark building using smart dampers", *Journal of Engineering Mechanics*, 130(4), 386-392.

[79] Xu Z D, Shen Y P, and Guo Y Q (2003), "Semi-active control of structures incorporated with magnetorheological dampers using neural networks", *Smart Materials and Structures*, 12(1), 80-87.

[80] Guo D L, Hu H Y, and Yi J Q (2004), "Neural network control for a semi-active vehicle suspension with a magnetorheological damper", *Journal of Vibration and Control*, 10(3), 461-471.

[81] Atray V S and Roschke P N (2004), "Neuro-fuzzy control of railcar vibrations using semi-active dampers", *Computer-Aided Civil and Infrastructure Engineering*, 19(2), 81-92.

[82] Craft M J, Buckner G D, and Anderson R D (2003), "Fuzzy logic control algorithms for Magneshock semi-active vehicle shock absorbers: Design and experimental evaluations", *SPIE Annual International Symposium on Smart Structures and Materials: Modelling, Signal Processing, and Control*, 5049, 577-588.

[83] Choi S-B, Lee H-S, and Park Y-P (2002), "H_∞ control performance of a full-vehicle suspension featuring magnetorheological dampers", *Vehicle System Dynamics*, 38(5), 341-360.

[84] Du H, Yim Sze K, and Lam J (2005), "Semi-active H_∞ control of vehicle suspension with magneto-rheological dampers", *Journal of Sound and Vibration*, 283(3-5), 981-996.

[85] Lam A H F and Liao W H (2003), "Semi-active control of automotive suspension systems with magneto-rheological dampers", *International Journal of Vehicle Design*, 33(1-3), 50-75.

[86] Han S S, Choi S B, Park J S, Kim J H, and Choi H J (2003), "Robust sliding mode control of an electrorheological suspension system with parameter perturbations", *International Journal of Vehicle Design*, 33(1-3), 279-295.

[87] Choi Y T and Wereley N M (2003), "Vibration control of a landing gear system featuring electrorheological/magnetorheological fluids", *Journal of Aircraft*, 40(3), 432-439.

[88] Simon D and Ahmadian M (2001), "Vehicle evaluation of the performance of magnetorheological dampers for heavy truck suspensions", *Journal of Vibration and Acoustics*, 123, 365-375.

[89] Choi S-B, Song H J, Lee H H, Lim S C, Kim J H, and Choi H J (2003), "Vibration control of a passenger vehicle featuring magnetorheological engine mounts", *International Journal of Vehicle Design*, 33(1-3), 2-16.

[90] Kim B and Roschke P N (1999), "Linearization of magnetorheological behavior using a neural network", *Proceedings of the 1999 American Control Conference,San Diego, CA, USA*, 6, 4501-4505.

[91] Chang C-C and Zhou L (2002), "Neural network emulation of inverse dynamics for a magnetorheological damper", *Journal of Structural Engineering*, 128(2), 231-239.

[92] Wang D H and Liao W H (2005), "Modelling and control of magnetorheological fluid dampers using neural networks", *Smart Materials and Structures*, 14(1), 111-126.

[93] Xia P-Q (2003), "An inverse model of MR damper using optimal neural network and system identification", *Journal of Sound and Vibration*, 266(5), 1009-1023.

[94] Sims N D, Peel D J, Stanway R, Bullough W A, and Johnson A R (1999), "Controllable viscous damping: An experimental study of an electrorheological long stroke damper under proportional feedback control", *Smart Materials and Structures*, 8, 601-605.

[95] Sims N D, Stanway R, Peel D J, Bullough W A, and Johnson A R (2000), "Smart fluid damping: Shaping the force/velocity response through feedback control." *Journal of Intelligent Material Systems and Structures*, 11, 945-949.

[96] Sims N D, Stanway R, and Johnson A R (2001), "Experimental testing and control of an ER long-stroke vibration damper", *SPIE Annual International Symposium on Smart Structures and Materials: Smart Systems for Bridges, Structures and Highways*, 4330, 218-227.

[97] Besinger F H, Cebon D, and Cole D J (1991), "Experimental investigation into the use of semi-active dampers on heavy lorries", *Vehicle System Dynamics Proceedings of 12th IAVSD Symposium on Dynamics of Vehicles on Roads*, 57-71.

[98] Choi S-B and Han Y-M (2003), "MR seat suspension for vibration control of a commercial vehicle", *International Journal of Vehicle Design*, 31(2), 202-215.

[99] Lee H-S and Choi S-B (2000), "Control and response characteristics of a magneto-rheological fluid damper for passenger vehicles", *Journal of Intelligent Material Systems and Structures*, 11(1), 80-87.

[100] Lafitte A, Mikulowski G, Remmers L, and Wolejsza Z (2005), "State of the art in landing gear shock absorber design/design requirements", *ADLAND Internal Report*.

[101] Currey N S (1988), *"Aircraft Landing Gear Design: Principles and Practices"*, American Institute of Aeronautics and Astronautics, Inc.

[102] Milwitzky B and Cook F E (1952), "Analysis of landing-gear behavior", *NACA Report*, 1154.

[103] Lafitte A and Gosselin O (2005), "Technical data for large-scale telescopic and levered landing gears", *Personal communication*, Messier Dowty, Zone Aèronautique Louis Brèguet, BP 133, 78148 Vélizy Cedex, France, http://www.messier-dowty.com/.

[104] Wahi M K (1976), "Oleopneumatic Shock Strut Dynamic Analysis and its Real-Time Simulation", *Journal of Aircraft*, 13(4), 303-308.

[105] Wahi M K (1976), "Oil compressibility and polytropic air compression analysis for oleopneumatic shock struts", *Journal of Aircraft*, 13(7), 527-530.

[106] Reddy J P, Nagaraj V T, and Ramamurti V (1984), "Analysis of a semi-levered suspension landing gear with some parametric study", *Journal of Dynamic Systems, Measurement and Control*, 106(3), 218-224.

[107] Yadav D and Ramamoorthy R P (1991), "Nonlinear landing gear behavior at touchdown", *Journal of Dynamic Systems, Measurement and Control*, 113(4), 677-683.

[108] Flugge W (1952), "Landing-gear impact", *NACA Technical Note*, 2743.

[109] Schnitzer E (1956), "Band-pass shock and vibration absorbers for application to aircraft landing gear", *NACA Technical Note*, 3803.

[110] Schnitzer E (1958), "Experimental evaluation of low-band-pass landing-gear shock absorber for pulse loadings", *NACA Technical Note*, 4387.

[111] McGehee J R and Carden H D (1976), "A mathematical model of an active control landing gear for load control during impact and roll-out", *NASA Technical Note*, NASA TN D-8080.

[112] Ross I and Edson R (1979), "An electronic control for an electro-hydraulic active control aircraft landing gear", *NASA Contractor Report*, 3113.

[113] Ross I and Edson R (1982), "An electronic control for an electro-hydraulic active control landing gear for the F-4 aircraft", *NASA Contractor Report*, 3552.

[114] Six M F, Magnac G, and Le Letty R (2004), "Cedrat Technologies' annual report", *Internal ADLAND report*, http://smart.ippt.gov.pl/adland/.

[115] Wereley N M, Kamath G M, and Madhavan V (2000), "Hysteresis modelling of semi-active magnetorheological helicopter dampers", *Journal of Intelligent Material Systems and Structures*, 10(8), 624-633.

[116] Batterbee D C, Sims N D, Stanway R, and Zbigniew W (2005), "Magnetorheological landing gear. Part 1: A design methodology", *Smart Materials and Structures*, Submitted.

[117] Batterbee D C, Sims N D, Stanway R, and Wolejsza Z (2005), "Design and performance optimisation of magnetorheological oleopneumatic landing gear", *SPIE Annual International Symposium on Smart Structures and materials: Damping and Isolation*, 5760-10.

[118] Batterbee D C, Sims N D, Wolejsza Z, and Lafitte A (2006), "Magnetorheological landing gear design: A feasibility study for small and large-scale aircraft", *ISMA International Conference on Noise and Vibration Engineering - Active Vibration Control and Smart Structures*, Submitted, September 18th-20th, Leuven, Belgium.

[119] Sims N D (2000), "Modelling and control of an electrorheological long-stroke vibration damper", *PhD Thesis*, The University of Sheffield, Department of Mechanical Engineering.

[120] Kinsler L E and Frey A R (1962), *"Fundamentals of Acoustics"*, 2nd Edition, John Wiley and Sons.
[121] Zbigniew W (2004), "Data sheet for Aeroshell 41", *Personal communication*, The Institute of Aviation, Al. Krakowska 110/114, 02-256 Warsaw, Poland, http://www.ilot.edu.pl/.
[122] Massey B (1998), *"Mechanics of Fluids"*, 7th Edition, Stanley Thornes Ltd.
[123] Rosenfeld N C and Wereley N M (2004), "Volume constrained optimization of magnetorheological and electrorheological valves and dampers", *Smart Materials and Structures*, 13, 1303-1313.
[124] Ahmadian M and Norris J A (2004), "Rheological controllability of double-ended MR dampers subjected to impact loading", *SPIE Annual International Symposium on Smart Structures and Materials: Damping and Isolation*, 5386-20.
[125] Zbigniew W (2004), "Experimental drop test data on the nose landing gear of the I-23. Drop test No. p086." *Personal communication*, The Institute of Aviation, Al. Krakowska 110/114, 02-256 Warsaw, Poland, http://www.ilot.edu.pl/.
[126] Bõse H (2004), "Data sheet for AD57 and AD275 MR fluid", *Personal communication*, Fraunhofer-Institut für Silicatforschung ISC, Neunerplatz 2, D-97082 Würzburg, http://www.isc.fraunhofer.de/.
[127] Stringer J D (1976), *"Hydraulic Systems Analysis"*, The Macmillan Press Ltd.
[128] FEMM (2005), *Version 3.4.2*, Foster-Miller, Inc., 350 Second Avenue, Waltham, MA 02451, USA, http://femm.foster-miller.net/index.html.
[129] Carlson J D (2002), "Permanent-electromagnet systems ("magnetic cancellation")", *Lord Corporation Engineering Note*, http://literature.lord.com/root/other/rheonetic/Permanent_Electromagnet_Systems.pdf.
[130] Batterbee D C, Sims N D, Stanway R, and Rennison M (2005), "Magnetorheological landing gear. Part 2: Validation using experimental data", *Smart Materials and Structures*, Submitted.
[131] Socata Aircraft, North Perry Airport, 7501 Pembroke Road, Pembroke Pines, FL 33023, http://www.socata.org/.
[132] RDP Electronics Ltd, Grove Street, Heath Town, Wolverhampton, WV10 0PY, United Kingdom, http://www.rdpe.com.
[133] Fraunhofer Institut Silicatforschung (2006), http://www.isc.fraunhofer.de/.
[134] Instron Structural Testing Systems, 825 University Ave., Norwood, MA 02062-2643, USA, http://www.instron.com.
[135] Moog Inc., Jamison Road, East Aurora, New York 14052, USA, http://www.moog.co.uk/noq/%5Fseries%5F%5Fc328/.
[136] Kepco Inc., 131-138 Sanford Avenue, Flushing, NY 11352, USA, www.kepcopower.com/bop.htm.
[137] xPC Target (2002), *The MathWorks, Inc., 3 Apple Hill Drive, Natick, MA*,
[138] National Instruments, 11500 N Mopac Expwy Austin, TX 78759-3504, USA, www.ni.com.
[139] Cedrat and Cedrat Technologies, Chemin de Malacher, 38246 Meylan, France, http://www.cedrat.com/.
[140] Robson J D (1979), "Road surface description and vehicle response", *International Journal of Vehicle Design*, 1(1), 25-35.

[141] Cebon D and Newland D E (1984), "The artificial generation of road surface topography by the inverse FFT method", *Proceedings of the 8th IAVSD Symposium on the Dynamics of Vehicles on Roads and Railway Tracks*, Cambridge, Massachussets, Swets and Zeitlinger, 29-42.

[142] Batterbee D C and Sims N D (2005), "Vibration isolation using smart fluid dampers: A benchmarking study." *Smart Structures and Systems*, 1(3).

[143] Batterbee D C and Sims N D (2004), "Skyhook damping with linearised magnetorheological dampers", *SPIE Annual International Symposium on Smart Structures and Materials: Damping and Isolation*, 5386.

[144] Sims N D and Wereley N M (2003), "Modelling of smart fluid dampers", *SPIE Annual International Symposium on Smart Structures and Materials: Passive Damping and Isolation*, 5052, 163-175.

[145] Welch P D (1967), "The use of fast Fourier transform for the estimation of power spectra: A method based on time averaging over short, modified periodograms", *IEEE Trans. Audio Electroacoust*, AU-15, 70-73.

[146] Redfield R C and Karnopp D C (1989), "Performance sensitivity of an actively damped vehicle suspension to feedback variation", *Journal of Dynamic Systems, Measurement and Control*, 111, 51-60.

[147] Besinger F H, Cebon D, and Cole D J (1995), "Damper models for heavy vehicle ride dynamics", *Vehicle System Dynamics*, 24, 35-64.

[148] Carlson J D (2003), "MR piston detail", *Personal communication*, Lord Corporation, Materials Division, 406 Gregson Drive, Cary, NC 27511.

[149] Plummer A (2004), "Instron/IST servohydraulic models", *Personal communication*, Instron Ltd, Coronation Road, High Wycombe, Bucks, HP12 3SY, UK, www.instron.com.

[150] Carrera MagneShock, , http://carreracustom.com/Gen1.html.

[151] Batterbee D C and Sims N D, "Hardware-in-the-loop-simulation of magnetorheological dampers for vehicle suspension systems", *Proceedings of the Institution of Mechanical Engineers, Part I: Journal of Systems and Control Engineering*, Accepted(Special issue article).

[152] Batterbee D C, Sims N D, and Plummer A (2005), "Hardware-in-the-loop-simulation of a vibration isolator incorporating magnetorheological fluid damping", *2nd ECCOMAS Thematic Conference on Smart Structures and Materials*, Lisbon, Portugal.

[153] Holmes N J (2003), "Active suspension for the formula student car - HILS hardware", *Thesis submitted to the University of Sheffield in partial fulfilment for the degree of Master of Engineering.*

[154] Batterbee D C and Sims N D (2003), "Feedback control strategies for MR vehicle suspension systems", *AMAS/ECCOMAS/STC Workshop on Smart Materials and Structures - SMART'03*, Jadwisin, Poland.

[155] Hughes E (1995), *"Electrical Technology"*, 7th edition: Revised by I McKenzie Smith, Addison Wesley Longman Limited.

[156] Ahmadian M and Norris J A (2003), "High-velocity behaviour of magnetorheological fluids", *SPIE Annual International Symposium on Smart Structures and materials: Damping and Isolation*, 5386-20.

[157] Gavin H P (2002), "Multi-duct ER dampers", *Journal of Intelligent Material Systems and Structures*, 12(5), 353-366.

[158] Worden K, Manson G, Lord T M, and Friswell M I (2005), "Some observations on uncertainty propagation through a simple nonlinear system", *Journal of Sound and Vibration*, 288(3), 601-621.

[159] Sims N D (2006), "Limit cycle behaviour of smart fluid dampers under closed-loop control", *Journal of Vibration and Acoustics*, 128, 413-428.

Appendix A: Abstracts of journal publications and submissions

MAGNETORHEOLOGICAL LANDING GEAR. PART 1: A DESIGN METHODOLOGY

D C Batterbee[†], N D Sims[†], R Stanway[†], and Zbigniew Wolejsza[‡]

[†]Department of Mechanical Engineering, The University of Sheffield, Sheffield, S1 3JD, UK.

[‡]The Institute of Aviation, Al. Krakowska 110/114, 02-256 Warsaw, Poland.

ABSTRACT

Aircraft landing gears are subjected to a wide range of excitation conditions, which result in conflicting damping requirements. A novel solution to this problem is to implement semi-active damping using magnetorheological (MR) fluids. This paper presents a design methodology that enables an MR landing gear to be optimised, both in terms of its damping and magnetic circuit performance, whilst adhering to stringent packaging constraints. Such constraints are vital in landing gear, if MR technology is to be considered as feasible in commercial applications.

The design approach focuses on the impact or landing phase of an aircraft's flight, where large variations in sink speed, angle of attack and aircraft mass makes an MR device potentially very attractive. In this study, an equivalent MR model of an existing aircraft landing gear is developed. This includes a dynamic model of an MR shock strut, which accounts for the effects of fluid compressibility. This is important in impulsive loading applications such as landing gear, as fluid compression will reduce device controllability. Using the model, numerical impact simulations are performed to illustrate the performance of the optimised MR shock strut, and hence the effectiveness of the proposed design methodology. Part 2 of this contribution focuses on experimental validation.

MAGNETORHEOLOGICAL LANDING GEAR. PART 2: VALIDATION USING EXPERIMENTAL DATA

D C Batterbee, N D Sims, R Stanway, and M Rennison

Department of Mechanical Engineering, The University of Sheffield, Sheffield, S1 3JD, UK.

ABSTRACT

Aircraft landing gears are subjected to a wide range of excitation conditions with conflicting damping requirements. A novel solution to this problem is to implement semi-active damping using magnetorheological (MR) fluids. In Part 1 of this contribution, a methodology was developed that enables the geometry of a flow mode MR valve to be optimised within the constraints of an existing passive landing gear. The device was designed to be optimal in terms of its impact performance, which was demonstrated using numerical simulations of the complete landing gear system. To perform the simulations, assumptions were made regarding some of the parameters used in the MR shock strut model. In particular, the MR fluid's yield stress, viscosity, and bulk modulus properties were not known accurately. Therefore, the present contribution aims to validate these parameters experimentally, via the manufacture and testing of an MR shock strut. The gas exponent, which is used to model the shock strut's non-linear stiffness, is also investigated. In general, it is shown that MR fluid property data at high shear rates is required in order to accurately predict performance prior to device manufacture. Information regarding the likely variation in fluid properties between batches is vital. Furthermore, the study illustrates how fluid compressibility can have a significant influence on the device time constant, and hence potential control strategies.

Vibration isolation with smart fluid dampers: a benchmarking study

D C Batterbee and N D Sims

Department of Mechanical Engineering, The University of Sheffield,

Sheffield, S1 3JD, UK.

ABSTRACT

The non-linear behaviour of electrorheological (ER) and magnetorheological (MR) dampers makes it difficult to design effective control strategies, and as a consequence a wide range of control systems have been proposed in the literature. These previous studies have not always compared the performance to equivalent passive systems, alternative control designs, or idealised active systems. As a result it is often impossible to compare the performance of different smart damper control strategies.

This article provides some insight into the relative performance of two MR damper control strategies: on/off control and feedback linearisation. The performance of both strategies is benchmarked against ideal passive, semi-active and fully active damping. The study relies upon a previously developed model of an MR damper, which in this work is validated experimentally under closed-loop conditions with a broadband mechanical excitation. Two vibration isolation case studies are investigated: a single-degree-of-freedom mass-isolator, and a two-degree-of-freedom system that represents a vehicle suspension system. In both cases, a variety of broadband mechanical excitations are used and the results analysed in the frequency domain. It is shown that although on/off control is more straightforward to implement, its performance is worse than the feedback linearisation strategy, and can be extremely sensitive to the excitation conditions.

Hardware-in-the-loop simulation of magnetorheological dampers for vehicle suspension systems

David C Batterbee and Neil D Sims

The University of Sheffield

Dynamics Research Group, Department of Mechanical Engineering,

Mappin St, Sheffield S1 3JD, UK

ABSTRACT

Magnetorheological (MR) fluids provide an elegant means to enhance vibration control in primary vehicle suspensions. Such fluids can rapidly modify their flow characteristics in response to a magnetic field, so they can be used to create semi-active dampers. However, the behaviour of MR dampers is inherently non-linear and as a consequence, the choice of an effective control strategy remains an unresolved problem.

Previous research has developed a method to linearise the damper's force/velocity response, to allow implementation of classical control techniques. In the present study, this strategy is used to implement skyhook damping laws within primary automotive suspensions. To simulate the vehicle suspension, a two-degree-of-freedom quarter car model is used, which is excited by realistic road profiles. The controller performance is investigated experimentally using the hardware-in-the-loop-simulation (HILS) method. This experimental method is described in detail and its performance is validated against numerical simulations for a simplified problem.

The authors demonstrate that feedback linearisation can provide significant performance enhancements in terms of passenger comfort, road holding, and suspension working space compared to other control strategies. Furthermore, feedback linearisation is shown to desensitise the controller to uncertainties in the input excitation such as changes in severity of the road surface roughness.

Appendix B: Derivation of the mass flow continuity equation

With reference to Figure B.1, the mass flow continuity on a fluid control volume is:

$$\frac{d}{dt}(m) = \frac{d}{dt}(\rho v) = \rho_i Q_i - \rho_o Q_o \tag{B.1}$$

where v is the current volume of the CV (which changes according to the position of the piston), and subscripts 'i' and 'o' denote 'in' and 'out' respectively.

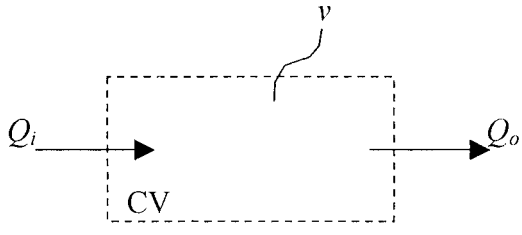

Figure B.1: Fluid control volume (CV).

Also:

$$\frac{d}{dt}(\rho v) = \rho \frac{dv}{dt} + v \frac{d\rho}{dt} \tag{B.2}$$

The degree of compressibility of a fluid is characterised by the bulk modulus β, which is defined by the equation [122]:

$$\beta = \rho \frac{dP}{d\rho} \tag{B.3}$$

Next, substitution of Eq.B.3 into Eq.B.2 gives:

$$\frac{d}{dt}(\rho v) = \rho\left(\frac{dv}{dt} + \frac{v}{\beta}\frac{dP}{dt}\right) \tag{B.4}$$

Finally, by combining Eq's B.1 with B.4 and assuming constant density, the general mass flow continuity equation accounting for fluid compressibility is:

$$\frac{dv}{dt} + \frac{v}{\beta}\frac{dP}{dt} = Q_i - Q_o \tag{B.5}$$